Charge Generation and Recombination in Hybrid Organic/Inorganic Solar Cells

Max Planck Graduate Center
mit der Johannes Gutenberg-Universität Mainz

Michael Meister

Dissertation

zur Erlangung des Grades eines
„Doktor rerum naturalium (Dr. rer. nat.)"
der Fachbereiche:
08 - Physik, Mathematik und Informatik
09 - Chemie, Pharmazie und Geowissenschaften,
10 – Biologie,
Universitätsmedizin
der Johannes Gutenberg-Universität Mainz

I hereby declare that I wrote this dissertation submitted without any unauthorized external assistance and used only sources acknowledged in the work. All textual passages which are appropriated verbatim or paraphrased from published and unpublished texts as well as all information obtained from oral sources are duly indicated and listed in accordance with bibliographical rules. In carrying out this research, I complied with the rules of standard scientific practice as formulated in the statutes of the Johannes Gutenberg-University Mainz to insure standard scientific practice.

Michael Meister

Summary

This thesis deals with the investigation of exciton and charge dynamics in hybrid solar cells by time-resolved optical spectroscopy. Quasi-steady-state and transient absorption spectroscopy, as well as time-resolved photoluminescence spectroscopy, were employed to study charge generation and recombination in solid-state organic dye-sensitized solar cells, where the commonly used liquid electrolyte is replaced by an organic solid hole transporter, namely 2,2′7,7′-tetrakis-(N,N-di-p-methoxyphenyl-amine)-9,9′-spirobifluorene (spiro-MeOTAD), and polymer-metal oxide bulk heterojunction solar cells, where the commonly used fullerene acceptor [6,6]-phenyl C61 butyric acid methyl ester (PCBM) is replaced by zinc oxide (ZnO) nanoparticles. By correlating the spectroscopic results with the photovoltaic performance, efficiency-limiting processes and processes leading to photocurrent generation in the investigated systems are revealed.

It is shown that the charge generation from several all-organic donor-π-bridge-acceptor dyes, specifically perylene monoimide derivatives, employed in solid-state dye-sensitized solar cells, is strongly dependent on the presence of a commonly used additive lithium bis(trifluoromethanesulphonyl)imide salt (Li-TFSI) at the interface.

Moreover, it is shown that charges can not only be generated by electron injection from the excited dye into the TiO_2 acceptor and subsequent regeneration of the dye cation by the hole transporter, but also by an alternative mechanism, called preceding hole transfer (or reductive quenching). Here, the excited dye is first reduced by the hole transporter and the thereby formed anion subsequently injects an electron into the titania. This additional charge generation process, which is only possible for solid hole transporters, helps to overcome injection problems.

However, a severe disadvantage of solid-state dye-sensitized solar cells is revealed by monitoring the transient Stark effect on dye molecules at the interface induced by the electric field between electrons and holes. The attraction between the negative image charge present in TiO_2, which is induced by the positive charge carrier in the hole transporter due to the dielectric contrast between the organic spiro-MeOTAD and inorganic titania, is sufficient to attract the hole back to the interface, thereby increasing recombination and suppressing the extraction of free charges.

By investigating the effect of different dye structures and physical properties on charge generation and recombination, design rules and guidelines for the further advancement of solid-state dye-sensitized solar cells are proposed.

Finally, a spectroscopic study on polymer:ZnO bulk heterojunction hybrid solar cells, employing different surfactants attached to the metal oxide nanoparticles, was performed to understand the effect of surfactants upon photovoltaic behavior. By applying a parallel pool analysis on the transient absorption data, it is shown that suppressing fast recombination while simultaneously maintaining the exciton splitting efficiency by the right choice of surfactants leads to better photovoltaic performances. Suppressing the fast recombination completely, whilst maintaining the exciton splitting, could lead to a doubling of the power conversion efficiency of this type of solar cell.

Zusammenfassung

In dieser Arbeit wurde die Dynamik von Exzitonen und Ladungen in hybriden Solarzellen mittels zeitaufgelöster optischer Spektroskopie untersucht. Insbesondere kamen quasi-Gleichgewichts- und transiente Absorptionsspektroskopie sowie zeitaufgelöste Photolumineszenzspektroskopie zum Einsatz, um die Ladungsträgergeneration und -rekombination in Feststoff-Farbstoffsolarzellen zu untersuchen, bei welchen der häufig verwendete Flüssigelektrolyt durch den organischen Lochtransporter 2,2′7,7′-tetrakis-(N,N-di-p-methoxyphenylamin)-9,9′-spirobifluoren (spiro-MeOTAD) ersetzt wurde. Weiterhin wurden Polymer:Metalloxid Hybridsolarzellen, bei welchen der in organischen Solarzellen übliche Fulleren-Akzeptor (6,6)-Phenyl-C61-Butyrsäure-methylester (PCBM) durch Zinkoxid (ZnO) Nanopartikel ersetzt wurde, untersucht. Die Korrelation der spektroskopischen Ergebnisse mit der photovoltaischen Effizienz ermöglichte es die effizienzlimitierenden Prozesse und die Prozesse, welche zur Fotostromerzeugung führen, zu identifizieren.

Dabei wurde deutlich, dass die Ladungsträgergeneration verschiedener Donor-Akzeptor-Farbstoffe, insbesondere von Perylen-Monoimid Derivaten, in Feststoff-Farbstoffsolarzellen stark von der Anwesenheit des Additivs Lithium bis(trifluoromethansulphonyl)imid (Li-TFSI) an der Grenzfläche abhängt.

Darüber hinaus wurde ein zum üblichen Ladungsgenerationsmechanismus alternativer Reaktionsweg untersucht, der sogenannte vorgezogene Lochtransfer, auch reduktives Löschen genannt (*preceding hole transfer* oder *reductive quenching*). Hierbei werden Ladungen nicht wie herkömmlich durch Elektroneninjektion vom angeregten Farbstoff in den TiO_2-Akzeptor und nachfolgende Regeneration des Farbstoffkations erzeugt, sondern der angeregte Farbstoff wird zunächst durch den Lochtransporter reduziert und das dadurch erzeugte Farbstoffanion injiziert daraufhin ein Elektron in das Metalloxid. Dieser zusätzliche Ladungsgenerationsmechanismus ist nur bei Verwendung fester

Lochleiter möglich und es konnte gezeigt werden, dass er durchaus zur Ladungsgeneration und damit zur Überwindung von Injektionsproblemen beiträgt.

Ein großer Nachteil fester organischer Lochleiter konnte indes auch identifiziert werden. Die Beobachtung des transienten Starkeffekts von Farbstoffmolekülen an der Grenzfläche zwischen Lochleiter und Titandioxid, hervorgerufen durch das elektrische Feld zwischen Elektronen und Löchern, zeigte, dass die Anziehungskraft zwischen der negativen Bildladung im TiO_2, hervorgerufen durch die positive Ladung (das Loch) im Lochleiter und den dielektrischen Kontrast zwischen dem organischen spiro-MeOTAD und dem anorganischen Titandioxid, bereits genügt, um den positiven Ladungsträger zurück zur Grenzfläche zu ziehen. Dieser Effekt verstärkt die Rekombination und unterdrückt somit die Extraktion von Ladungen.

Durch die Untersuchung der Auswirkung verschiedener Farbstoffstrukturen und deren physikalischer Eigenschaften auf die Ladungsträgergeneration und –rekombination wurden weiterhin Struktur-Eigenschafts-Beziehungen erarbeitet und Richtlinien für die Weiterentwicklung von Feststoff-Farbstoffsolarzellen entwickelt.

Zu guter Letzt wurden Polymer:ZnO *Bulk-Heterojunction* Hybridsolarzellen mit verschiedenen an die Metalloxidnanopartikel gebundenen Tensiden spektroskopisch untersucht, um deren unterschiedliches photovoltaisches Verhalten zu verstehen. Mit Hilfe einer Parallel-Pool-Analyse der mit transienter Absorptionsspektroskopie erhaltenen Daten konnte gezeigt werden, dass das Unterdrücken schneller Rekombination bei gleichzeitiger Aufrechterhaltung der Exzitonen-Trennungseffizienz durch die Tenside zu einem höheren Fotostrom führt. Die gänzliche Unterdrückung der schnellen Rekombination, bei gleichzeitiger Aufrechterhaltung der Exzitonen-Trennung, würde zu einer Verdopplung der Effizienz bei dieser Art von Solarzellen führen.

Danksagung

The acknowledgements are only contained in the printed original.

Contents

1

Introduction

The growing demand for energy and the increasing threat of global warming due to massive CO_2 emission (in 2011 CO_2 emissions reached a new global record high [1]) are tremendous future challenges for mankind. Harvesting the solar energy supplied by the sun is a key approach to providing green and sustainable energy, as the solar energy striking the Earth's surface per year is estimated to be about 6700 times the annual world primary energy consumption in 2008, which is expected to grow by more than 50% by 2035 [2, 3]. Thus, solar power is a - if not the most - promising alternative for carbon-free energy production [4]. Photovoltaics (PV), the direct generation of electricity from sunlight, is one of the technologies that can help to reduce carbon emission from electrical energy generation paving the way to clean energy production. PV is predicted to be able to contribute 11% towards global electricity production in 2050 [5]. This can only be achieved if all existing PV technologies are further improved and new technologies are developed.

Two promising emerging technologies for PV electricity generation are organic photovoltaics (OPV) and dye-sensitized solar cells (DSCs), devices which can potentially be produced at low cost. They have already entered the market in niche applications [5], some of which are shown in Figure 1.

Compared to traditional silicon-based or other inorganic solar cells, both OPV and DSCs have the advantages of material diversity, abundance, and open up the possibility of printing and large-scale fabrication even on flexible sub-

Figure 1: Some products already contain DSCs, e.g. a wireless tablet keyboard "Folio" from Logitech [7] or, as shown here, G24i Bicycle Panniers with DSCs. Reprinted with permission from [8]. Copyrigth 2013 G24i Power, Ltd.

strates. Moreover, their low weight and low material consumption as well as a less energy-intensive production can lead to low production costs and short energy payback times of less than a year. Additional advantageous features of OPV or DSCs are a broad scope for design, with the ability to modify aspects such as transparency and color. [6] Furthermore, DSCs are promising for indoor or diffuse light applications, as the devices exhibit higher efficiencies under diffuse and weak illumination than silicon-based solar cells. The use of abundant and non-toxic materials is advantageous, especially compared to inorganic thin film CdTe or CIGS solar cells.

However, the efficiencies and stability of OPV and DSCs are still major drawbacks compared to conventional inorganic PV technologies, and at present they do not compete commercially. Liquid electrolyte DSCs have the problem that, apart from the stagnation of the already rather high efficiencies around 10 % since they were first introduced, due to the use of corrosive and volatile iodide-based electrolytes, the devices need to be sealed leading to increased costs for substrates and encapsulation. This leaves little financial scope to achieve competitive prices per Watt-peak. [9] Solid-state DSCs [10] have the advantage of not using any liquid electrolyte, leading to fewer constraints for encapsulation, and a possible route to cost reduction. Although the recently published record efficiencies of 7.2% [11] and 8.5% [12], for organic and inorganic hole transporters respectively, are promising, solid-state DSCs still lag behind their liquid analogues. For organic hole transporters, some reasons for the deficit have already been identified such as increased or faster recombination [13] and insufficient pore-filling [14, 15], requiring thinner layers and resulting in inferior light harvesting [9]. By using organic dyes with high molar extinction coefficients, light harvesting can be increased, but efficiencies still lag behind the much thicker liquid electrolyte cells. Thus, it is important to gain a better understanding of the efficiency constraints in solid-state DSCs. In this thesis, this issue is addressed by steady-state and time-resolved optical spectroscopy, used to investigate charge generation and recombination processes. In particular, transient absorption spectroscopy, already proven to be a powerful tool to study charge generation and recombination in organic solar cells [16], is applied to investigate these important processes in DSCs. This thesis deals with the spectroscopic investigation of two material systems for application in OPV. Firstly, perylene and naphthalene imide dyes designed for solid-state DSCs are studied. Furthermore, the study is extended to hybrid solar cells comprising a blend of a conjugated polymer with metal oxide nanoparticles.

This thesis consists of five chapters. In the present chapter, a brief introduction to dye-sensitized and hybrid solar cells is presented. The motivation for the development of these novel types of photovoltaic solar cells is given, as well as the motivation and aim of the presented work.

In chapter two (Background) the basic theoretical framework for the thesis is presented, including reviews of the current status of research. First, the fundamentals of the electronic structure of organic conjugated molecules are presented. Here, the concept of donor-acceptor molecules is briefly introduced, followed by the theoretical background of light absorption and emission. This section aims to give a basic understanding of the origins of typical absorption and emission spectra of conjugated molecules along with typical measures and quantities of the absorption strength. Additionally, the influence of an electric field on absorption and emission (Stark effect) is reviewed. Furthermore, the inorganic components of hybrid and dye-sensitized solar cells, semiconducting metal oxides, are discussed, especially focusing on the origin of semiconductivity in these materials. Before the basic concepts of excitonic solar cells and a detailed picture of the function of dye-sensitized and hybrid solar cells and their components is given, the theoretical basis of electron transfer is introduced. Finally a brief introduction to laser spectroscopy is given, including the generation of ultrashort pulses and supercontinuum white-light and the basics of photoinduced absorption spectroscopy.

Chapter three (Experimental Techniques) introduces the experimental methods employed within this thesis. A typical preparation method for solid-state dye-sensitized solar cells is described. The electronic and optical measurement principles are presented, including the type of data that is typically acquired and the nature of the experimental setups.

In chapter four (Results & Discussion), all experimental results are presented and discussed in detail. As the results and discussions within the framework of this thesis were partially submitted to or published in peer reviewed journals, this chapter is a collection of the relevant submitted or published articles extended by further, unpublished or unsubmitted results.[1] The first article covers spectroscopic investigations of charge generation in a perylene imide based solid-state DSC, unveiling a second charge generation mechanism that might help solid-state DSCs to reach higher efficiencies. Supplemental information and measurements, together with a similar study on a naphthalene imide dye, are presented thereafter. Another thus far unpublished optical study deals with two perylene imide dyes differing only in a side group. It reveals that energy levels measured in solution do not necessarily reflect the situation in the solar cell, where dipole moments and additives play an important role. A second manuscript describes a possible interpretation of Stark effect kinetics leading to the conclusion that recombination and charge trapping plays a stronger role in solid-state DSCs compared with their liquid analogues. Finally, a spectroscopic investigation of a polymer metal oxide nanoparticle blend is presented, with indications for possible recombination mechanisms leading to

---

[1] In accordance with the MPGC examination regulations §11.1.

decreased power conversion efficiencies. A complete overview of all scientific contributions in the framework of this thesis can be found in the list of scientific contributions on page 229.

Within chapter five (Conclusions & Outlook), the results of this thesis are summarized and an overall conclusion is presented together with an outlook that provides suggestions for future work to further improve the understanding and performance of the solar cells presented in this thesis.

2

Background

The following chapter provides background information relevant to this thesis and places it within the context of current research. Beginning with fundamental light-matter interactions and electronic properties of organic materials, the current understanding of the microscopic processes in solar cells are introduced. Based thereupon, the basic concepts of organic (excitonic) photovoltaics are outlined, with a focus on dye-sensitized and hybrid solar cells, the device concepts that were mainly investigated in this thesis. In this context, current developments and record efficiencies of these types of solar cells are reviewed. Finally, some general background information about ultrafast laser spectroscopy, and transient absorption spectroscopy in particular, is presented.

2.1 Electronic and Optical Properties of Conjugated Organic Materials

2.1.1 Electronic Structure and States of Conjugated Materials

Conjugated organic materials, the active components in organic electronics, are based on carbon and their electronic properties are determined by its electronic configuration and types of bonding. A carbon atom has four valence electrons in the configuration $2s^22p^2$, with two unpaired electrons in two p orbitals. The energy difference between 2s and 2p orbitals is on the order of covalent bonding energies, making it energetically favorable for carbon to rearrange the electrons in hybridised orbitals when forming covalent bonds. Hybrid orbitals are formed by linear combination of the wavefunctions of the atomic orbitals (LCAO). In carbon the relevant orbitals are the 2s, $2p_x$, $2p_y$ and $2p_z$ orbitals, and the energy needed to promote the 2s electrons to a higher level is compensated by the formation of stable bonds. For organic semiconductors, sp^2-hybridisation is by far the most important. The s- and two p-orbitals , e.g. s, p_x and p_y, are hybridized and form in-plane σ-bonds, whereas the remaining p-orbital (p_z) forms an out-of-plane π-bond. When several carbon atoms are covalently bonded with sp^2-hypridisation, the p_z-orbitals of each carbon atom overlap with the neighboring p_z-orbitals and delocalized π-bonds are formed. This delocalization of one electron per carbon atom is usually termed conjugation. The conjugation, usually represented as alternating double and single bonds in the structural formula, is the origin of conductivity and the optoelectronic properties of molecules. [17, 18] The example of benzene is shown in Figure 2.

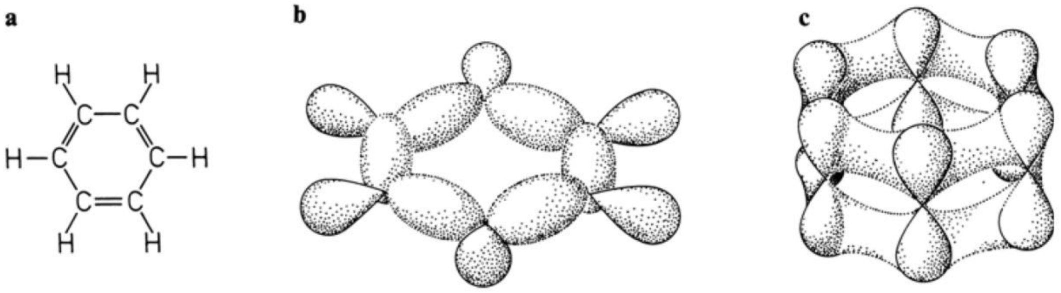

Figure 2: Benzene (a), an example of a conjugated and aromatic molecule, with carbon-carbon and carbon-hydrogen σ-bonds in-plane (b) and carbon-carbon π-bonds out-of-plane (c) that form the conjugated π- electron system. Reprinted with permission from figure 5.1, page 81 in [18]. Copyright 2006 Springer-Verlag.

In conjugated materials, the highest energy orbital containing bonding π-electrons is termed the highest occupied molecular orbital (HOMO). The next higher energy orbital that is unoccupied is an anti-bonding π^*-orbital, referred to as the lowest unoccupied molecular orbital (LUMO). By analogy with inorganic semiconductors, the HOMO-LUMO difference is often referred to as the band gap. In a first approximation, a larger π-system leads to a lower HOMO-

LUMO difference, which can in a simple picture be compared to the excitations of electrons in a box-potential. The HOMO-LUMO energy picture is a single particle picture that describes energy levels of single electrons in the potential of the nucleus with core electrons. The HOMO energy is essentially the energy needed to remove one electron to the vacuum level (ionization potential IP). The LUMO is a measure for the electron affinity.

2.1.2 Electronic Excitations in Molecules: Excitons and Charge-Transfer States

Upon excitation, one electron of the HOMO is promoted to the LUMO. The resulting excited state can be described as a bound state of the electron in the higher state with the remaining cationic molecular core (defect-electron or hole, by analogy with inorganic semiconductors). Such an excitation can be described as a neutral quasi-particle called an exciton. A crucial difference between organic and inorganic semiconductors results from the magnitude of the Coulomb binding energy between the electron and hole within this quasi-particle. This binding energy is neglected in the simple HOMO-LUMO picture presented previously. In organic molecules, the exciton is localized on one molecule (Frenkel exciton), it is strongly bound due to the relatively low dielectric constant ($\varepsilon \sim 3$) and the proximity of the charges. In contrast, in inorganic semiconductors, which have a higher crystallinity, the so called Mott-Wannier excitons are delocalized over several lattice constants. The higher dielectric constant ($\varepsilon > 10$) additionally results in a better screening between electron and hole, so that excitons are weakly bound and as a result are already split below room temperature. [19, 20]. Frenkel excitons can move from one molecule to another by hopping energy transfer (Förster resonance energy transfer and Dexter energy transfer), which is typically termed exciton diffusion. A schematic representation of Frenkel and Mott-Wannier excitons is given in Figure 3.

The difference in binding energy between Frenkel and Mott-Wannier excitons distinguishes the inorganic from the organic solar cells: Whereas the Mott-

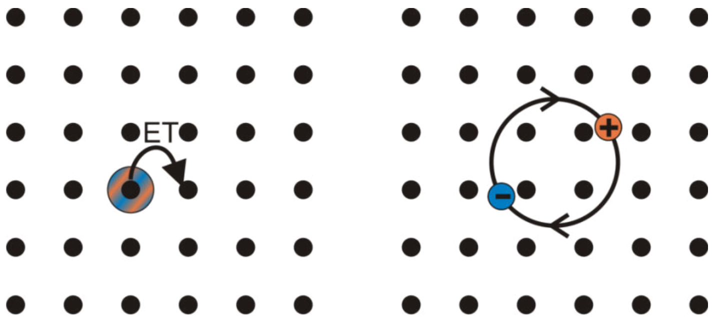

Figure 3: Schematic representation of a Frenkel (left) and a Mott-Wannier (right) exciton. Frenkel excitons are localized at a molecule and strongly bound, whereas Mott-Wannier excitons are delocalized in the lattice and weakly bound. Frenkel excitons can hop from one molecule to another by energy transfer (ET).

Wannier excitons in inorganic semiconductors are already split at room temperature, the Frenkel excitons in organic semiconductors such as conjugated molecules or polymers are still strongly bound. In order to overcome this binding energy, organic photovoltaic devices usually employ a heterojunction of an electron donor (e.g. dye, polymer) and an electron acceptor (e.g. fullerene, metal oxide, polymer). The energy levels are chosen in a way that the exciton binding energy is compensated by the energy gained due to a charge transfer from the donor to the acceptor material (see section 2.2.1).

In order to completely describe the electronic state of an excited molecule including the exciton binding energy, the complete multi-electron molecular quantum state and its energy including the spins of the valence electrons have to be considered (see Figure 4). The states are named after the multiplicity of the combination of electron spins as singlet, triplet etc. This representation is very valuable when optically induced electronic transitions are illustrated in a simple picture that will be described in section 2.1.3.

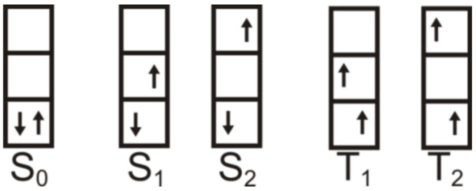

Figure 4: Spin state representation. Each quantum state is represented by a box. The states are named after the multiplicity of the combination of electron spins: singlet ground state (S_0), singlet states at higher excitations (S_1, S_2) and triplet states at higher excitations (T_1, T_2).

Nevertheless, for reasons of simplification HOMO and LUMO are typically considered when two materials are brought together to form a donor-acceptor complex for charge photogeneration (see chapter 2.2).

A class of very interesting molecules are donor-acceptor type molecules, where an electron donating group is covalently bound to an accepting group so that the electron density (charge distribution) is unevenly distributed over the molecule in the ground state, leading to a ground state dipole moment. This can be further enhanced in the excited state, if an intramolecular charge transfer occurs resulting in a partial positive charge on the donor and negative charge on the acceptor unit. Such intramolecular charge-transfer states lead to even higher dipole moments [18]. The difference between the dipole moments in the ground and excited state is important in interpreting the results of optical spectroscopy in terms of a Stark effect (see section 2.1.4 and 2.3.6).

2.1.3 Electronic Transitions: Light Absorption and Emission

Light-matter interaction is governed by optically triggered transitions between energy levels. Excitations of molecules are subdivided in two parts as a consequence of the Born-Oppenheimer approximation, which states that electronic and nuclear motion can be separated, and is justified by the fact that the electron motion is much faster than nuclear motion due to their lower mass. Therefore, the following types of transitions can be distinguished: i) Electronic excitations, meaning the transition of an electron into higher electronic energy levels in the effective potential of the nuclei and core electrons with energy differences corresponding to the visible or higher energy part of the electromagnetic spectrum; and ii) vibrational (and rotational) excitations, the stimulation of relative movements (vibrations) of the nuclei in the effective potential originating from nuclei and electrons, corresponding to the infrared and lower energy part of the electromagnetic spectrum. Both excitations can influence each other (electron-phonon-coupling).

Three types of electronic transitions can be distinguished: (induced) absorption, induced or stimulated emission and spontaneous emission. The latter process appears without external stimulation. The rates for these processes can be described by the Einstein coefficients. The rate for the two induced processes is the same ($B_{12} = B_{21}$), whereas the spontaneous emission rate is proportional to the induced rates and the energy difference of the two states ($A_{21} \propto \Delta E^3 B_{21}$). Stimulated emission, required for lasing, is achieved, when a population inversion is created (i.e. if the number of populated states in the higher energy level exceeds the number in the lower energy level).

An optically induced electronic transition from an initial to a final state occurs mainly through the dipolar interaction of the electrons with the electric field of the light. Such a transition is characterized by the transition dipole moment.

$$\vec{M}_{if} =< \Psi_f \left| \vec{M} \right| \Psi_i >= \int_{-\infty}^{\infty} \Psi_f^* \vec{M} \Psi_i dV \, , \tag{2.1}$$

where $\vec{M} = e\vec{r}$ is the electric dipole operator with e the elementary charge and $\vec{r}$ the position operator. Ψ_x are the full wavefunction solutions of the Schrödinger equation of the initial ($x = i$, e.g. ground state) and final state ($x = f$, e.g. first excited state). The transition probability is given by its absolute square $\left|\vec{M}_{if}\right|^2$. Using the Born-Oppenheimer approximation, the complete wavefunction can be subdivided into electronic (φ) and nuclear (vibronic, χ) parts. The complete wavefunction also includes a description of the spin-state S: $\Psi = \varphi \cdot \chi \cdot S$. The dipole operator only operates on the electronic wavefunctions, so that

$$\left|\vec{M}_{if}\right|^2 = \left|< \varphi_f |\vec{M}| \varphi_i >\right|^2 \cdot \left|< \chi_f | \chi_i >\right|^2 \cdot \left|< S_f | S_i >\right|^2 . \tag{2.2}$$

If one term is zero, the transition is forbidden. As a result, several selection rules can be derived for optical dipolar transitions: In order for the integral $< \varphi_f \left| \vec{M} \right| \varphi_i >= \int_{-\infty}^{\infty} \varphi_f^* \vec{M} \varphi_i dV$ to be non-zero, the product $\varphi_f^* \vec{M} \varphi_i$ needs to be an even function. As $\vec{M}$ is an odd operator ($M(-\vec{r}) = -M(\vec{r})$), the electronic wavefunctions of initial and final state need to have different symmetries. Moreover, in order for the integral to be large, the spatial overlap between φ_i

and φ_f has to be high, meaning that transitions between orbitals of the same origin are most likely ($\sigma \rightarrow \sigma^*, \pi \rightarrow \pi^*$). The second term $\left|< \chi_f | \chi_i >\right|^2$ is called Franck-Condon factor and takes into account the overlap of the nuclear wavefunctions in the initial and final electronic state. This factor determines the vibronic features of the spectrum that occur upon photon absorption, when together with the electronic excitation a quantized vibrational state of the nuclei in the binding potential is excited. A typical potential for nuclei in a molecule is depicted in Figure 5, where the potential energy (-surface) is plotted against the nuclear configuration coordinate q, which is a measure for the internuclear distances (in a diatomic molecule it is the internuclear distance). Upon excitation of an electron, the bonding strength changes, altering the potential surface (usually it shifts to larger q as an electron is promoted into an antibonding orbital). The Franck-Condon-principle states that a transition of an electron is usually much faster than the response of the nuclei (similar to the Born-Oppenheimer approximation, this is justified by the much higher mass of the nuclei) and thus in this diagram an electronic transition is always vertical. The Franck-Condon factor is largest, that is, the transition is most likely into the state where the position probability of the nuclei is most similar in the electronic ground and excited state. In Figure 5 this would be the 0→2 transition.

Finally, the last term in the transition dipole moment $\left|< S_f | S_i >\right|^2$ is only nonzero when initial and final states have the same spin state. Thus, a transition between a pure singlet and pure triplet is strictly forbidden. However, in real molecules mixed states are present due to spin orbit coupling. This can lead to intersystem crossing, especially if heavy atoms are included, resulting in transitions which change the spin state.

In order to fully understand absorption and emission spectra at room temperature, the empirical rules of Kasha have to be applied: Absorption from the zero vibrational level of the ground state has the highest probability (due to the Boltzmann distribution, this state has the largest occupancy) and emission originates with the highest probability from the zero vibrational level of the

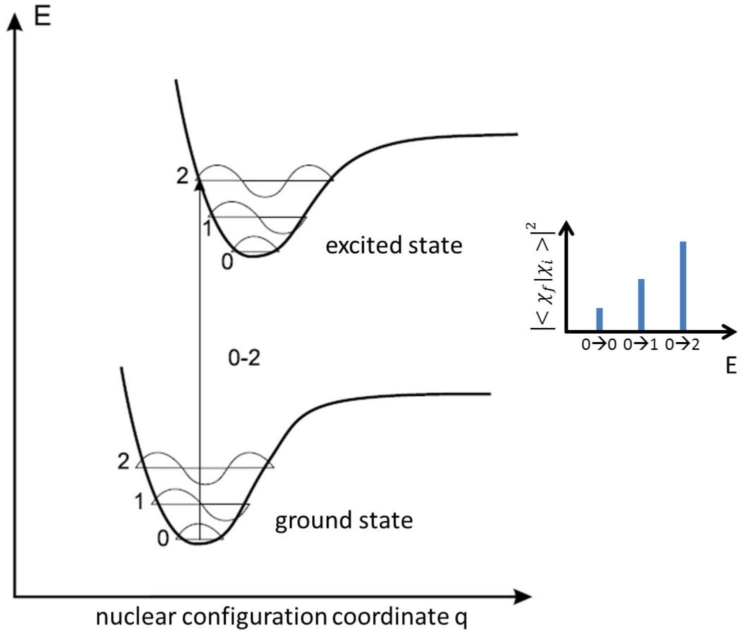

Figure 5: Franck-Condon principle. The transition between states where the nuclear wavefunction overlap is largest corresponds to the strongest vibronic band. Adapted from [21]

excited state, as vibrational relaxation (internal conversion) is faster than the typical lifetime of an electronically excited state. Singlet state emission is called fluorescence and triplet state emission (longer lived due to the forbidden spin transition) is termed phosphorescence. The rules of Kasha explain the often observed mirror symmetry of absorption and emission. A typical scheme of possible transitions together with spectra and time constants is depicted in Figure 6. The Jablonski diagram shows electronic and vibronic states and the most probable transitions. However, it contains no information about the relative strength of the transitions, as no information about the origins of the electronic and vibronic states is given.

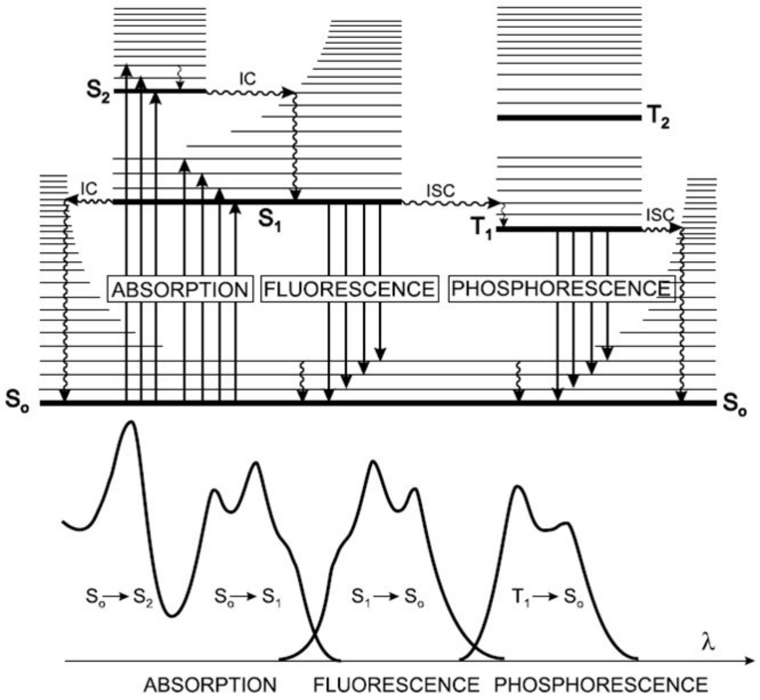

CHARACTERISTIC TIMES

absorption	10^{-15} s
vibrational relaxation	10^{-12}-10^{-10} s
lifetime of the excited state S_1	10^{-10}-10^{-7} s → fluorescence
intersystem crossing	10^{-10}-10^{-8} s
internal conversion	10^{-11}-10^{-9} s
lifetime of the excited state T_1	10^{-6} -1 s → phosphorescence

Figure 6: Jablonski diagram with electronic and vibronic states and the most probable transitions together with typical spectra and characteristic lifetimes. Non-radiative decay channels, such as intersystem crossing (ISC) and internal conversion (IC) are also depicted. Reprinted with permission from chapter "Characteristics of Fluorescence Emission" in [21]. Copyright 2012 Wiley-VCH Verlag GmbH & Co. KGaA.

Quantities Characterizing Absorption

A dimensionless quantity that describes the absorption strength is the oscillator strength f that is directly related to the transition dipole moment:

$$f = \frac{8\pi^2}{3} \frac{m_e \Delta E}{h^2 e^2} \left|\vec{M}_{if}\right|^2 . \tag{2.3}$$

The transition dipole moment and oscillator strength are related to the Einstein coefficients by $f \propto \Delta E \; B_{12}$. Light absorption by molecules with a molar concentration C in a homogeneous sample of thickness x is described by the

Beer-Lambert law: $\log\left(\frac{I_0}{I}\right) = \varepsilon C x$ (or $I = I_0 e^{-\alpha x}$, with $\alpha = \ln(10)\,\varepsilon C$, the absorption coefficient), where I_0 and I are the incoming and transmitted light intensities, respectively. ε is the molar decadic extinction coefficient and is directly related to the oscillator strength by a spectral integration $f \propto \int \varepsilon(E) dE$. $A = \varepsilon C x$ is referred to as the absorbance or optical density of a sample and is usually the quantity measured in UV-VIS absorption spectroscopy. Another measure for the absorption ability of a molecule is the absorption cross section σ, which is defined as $\sigma = \frac{\alpha}{N} = \frac{\varepsilon \ln(10)}{N_A}$, where N is the atomic density and N_A is the Avogadro constant. [18, 21]

Emission: Time Dependence

The decay dynamics of excited states are governed by the nature of the excited states and their possible transitions (fluorescence, internal conversion, intersystem crossing etc.). As spontaneous decay processes are statistical decays, the change of population n_i of a state i with time is proportional to the population: $\frac{dn_i}{dt} = -\sum_j k_j\, n_i$. The solution of this differential equation with an initial population of $n_i(t = 0) = n_{i0}$ is $n_i(t) = n_{i0} e^{-\sum_j k_j t}$. The state depopulation follows a mono-exponential function with the rate $\sum_j k_j$. Here, the k_j's are the transition probabilities per time for each decay, e.g. determined by Fermi's golden rule, [18] and for example for spontaneous emission given by the Einstein coefficient A_{21}. [21] The lifetime τ_i of the state is defined as the mean time $\tau_i = \left(\sum_j k_j\right)^{-1}$, at which the population reaches $n_i(\tau_i) = n_{i0}/e$. For instance in photoluminescence measurements the observed excited state lifetime is given by $\tau_{PL} = (k_r + k_{nr})^{-1}$, where k_r is the sum of radiative decay channel rates and k_{nr} the sum of all non-radiative decay channel rates. The photoluminescence quantum efficiency (PLQE), which is the number of emitted photons per absorbed photons (that is, the fraction of excited states that decay radiatively), is then $\Phi_{PL} = \frac{k_r}{k_r + k_{nr}}$. For more complicated systems where several states exist at the same time, sequential decays occur or the rates are no longer time independent, and thus the simple mono-exponential behavior is no longer valid. In this case multi- or stretched exponential decays can be observed. [21, 22]

2.1.4 The Stark Effect

The Stark effect describes the influence of an electric field on the energy levels of atoms or molecules and is the electric analogue to the magnetic Zeeman effect. Discovered in 1913 by Johannes Stark [23], the Stark effect describes how an electric field can lead to the splitting of normally degenerate states and shifts in their energy levels. These shifts can be observed in optical (electronic) as well as vibrational transitions. The Stark effect can be subdivided into two parts: The linear and quadratic Stark effect. The linear Stark effect can only be observed for atoms or molecules whose states have a permanent dipole moment. It depends on the orientation of the electric field towards these dipole moments and can influence energy levels as

$$\Delta E = -\vec{\mu} \cdot \vec{F} \, , \tag{2.4}$$

where ΔE is the change in energy of the state with permanent dipole moment $\vec{\mu}$ caused by the applied electric field $\vec{F}$: An electric field parallel to the dipole moment shifts the energy level to more negative energies, as the state becomes energetically more favorable; an antiparallel field has the opposite effect and shifts the energy level to more unfavorable (higher) energies. An electric field having no component parallel or antiparallel to the dipole moment has no effect on the energy levels (see energies of E_{Ex} in Figure 7, left scheme). Electronic and vibronic transitions are affected when the dipole moment changes from ground to excited state $\Delta\vec{\mu} = \vec{\mu}_{ex} - \vec{\mu}_{gs}$, depicted in Figure 7. The quadratic Stark effect can be understood as an interaction of the electric field with the field-induced dipole moment due to the polarizability of the state. The induced dipole scales linearly with the field $\vec{\mu}_{pol} \propto \hat{\alpha}\,\vec{F}$, where $\hat{\alpha}$ is the polarizability tensor and $\vec{F}$ the electric field. The energy shift is then $\Delta E \propto \vec{F}\hat{\alpha}\vec{F}$, which scales quadratically with the applied electric field [24, 25]. Due to the change in ener-

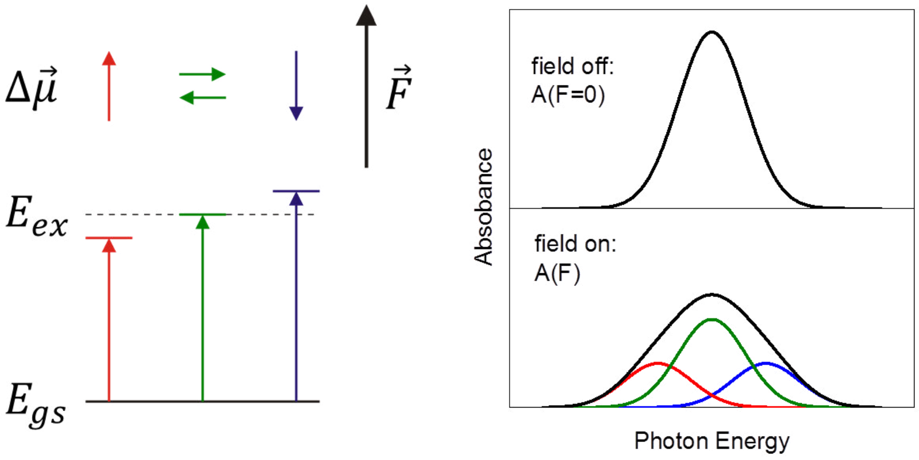

Figure 7: Schematic of an isotropic Stark effect on transitions due to a change in the electric dipole moment from ground to excited state $\boldsymbol{\Delta\vec{\mu}}$ leading to absorption changes in the presence of an external electric field $\boldsymbol{\vec{F}}$. For simplicity, a vanishing dipole moment in the ground state is assumed. Vectors corresponding to $\boldsymbol{\Delta\vec{\mu}}$ parallel, perpendicular and antiparallel to $\boldsymbol{\vec{F}}$ are shown in red, green and blue, respectively. The excited state energy $\boldsymbol{E_{ex}}$ shifts by $\boldsymbol{\Delta E_{ex}} = -\boldsymbol{\Delta\vec{\mu}} \cdot \boldsymbol{\vec{F}}$. For an isotropic sample this leads to a spectral broadening (black spectrum). Adapted from [25].

gy levels and electron distribution on application of an electric field, the transition dipole moment in equation (2.2) is altered ($|\varphi_i>$ and $|\varphi_f>$ are differently affected by the field depending on their dipole moment). The Stark effect thus affects optical transitions in terms of energy and oscillator strength. Indications of Stark effects in optical transitions and spectroscopy and their relevance for transient absorption measurements especially for donor-acceptor molecules are explained in greater detail in section 2.3.6.

One consequence of the Stark effect is the so-called solvatochromism or solvent relaxation. In a polar solvent, the absorption and emission spectra are different compared to a less polar solvent due to the reorganization of the dipoles of the polar solvent around the dipole of the dissolved molecule. The additional field created by the solvent shell shifts the energy levels and leads to changes in the transition energies, observable as spectral shifts. [26]

2.1.5 Semiconducting Metal Oxides

Transition metal oxides can have semiconducting or metallic electronic properties. The band structure in transition metal oxides arises as a result of the interaction of empty, partially filled or filled d-orbitals with the oxygen 2p-orbital. In a simplified picture of pure ionic interactions between oxygen and metal, the oxygen 2p orbital is filled and forms the valence band, while the empty (semiconductor/insulator) or partially filled (conductor) metal d-orbitals provide the conduction band. In DSCs, titanium(IV)dioxide (TiO_2, titania) is one of the most important transition metal oxides and is used as an electron acceptor. In the case of TiO_2, Ti^{4+} is situated at the center of an octahedron of six O^{2-} and has no d-electrons. TiO_2 is therefore a semiconductor, since the valence band is empty. TiO_2 has a partially covalent character in addition to the pure ionic interactions, which reduces the band gap of the material to around 3 eV. The TiO_2 valence band contains bonding combinations of titanium d- and oxygen p-orbitals, whereas the conduction band contains antibonding “metal-d” band combinations. This can be explained within the ligand field theory, a molecular orbital theory that not only takes into account the electric field of the ligands acting on the metal center and accounting for the ionic bonding character, but also orbital interactions of the metal center with the ligand orbitals, accounting for the covalent bonding character. [27]

Titania has three stable crystal conformations: rutile, anatase and brookite. Anatase and rutile differ mainly through distortion of the octahedron. For solar cell applications anatase has proven to be the best structure [6] and its unit cell is depicted in Figure 8. TiO_2 is an n-type semiconductor. The n-type character is a result of oxygen vacancies or interstitial titanium that adds extra electron states close to the conduction band leading to n-doping [27, 28]. A diverse range of nano-structures of TiO_2 (and metal oxides in general) can be prepared by a variety of techniques. Among the most commonly used methods such as hydrothermal, sol-gel, micelle, microwave or sonochemical approaches, hy-

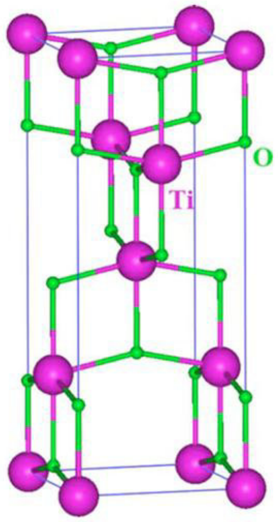

Figure 8: Unit cell of anatase TiO_2. Six O^{2-} coordinate one Ti^{4+} in a distorted octahedron. Adapted from [28]. Copyright 2006 by the American Physical Society.

drolysis of an organic titanium precursor followed by hydrothermal treatment is the most widely used. [6]

2.1.6 Electron Transfer Processes

A key step in charge photogeneration in DSCs and OPV devices is the transfer of an electron from donor to acceptor. Electron transfer processes and exciton quenching through dissociation are highly complicated processes influenced by several factors such as binding energies, orbital overlap and shape, reorganization energies, energy level differences and many others. A simplified approach to describe (photoinduced) charge-transfer processes is based on non-adiabatic transfer or Marcus' theory. [29] The following simple description (according to [30]) gives an insight into the possible dependences of transfer rates on the above mentioned parameters. Marcus' theory describes non-adiabatic electron transfer processes semi-classically. The donor and acceptor state energy surfaces are described as intersecting harmonic oscillators with a parabolic potential as a function of the generalized reaction coordinate q that represents the motion of all nuclei, see Figure 9.

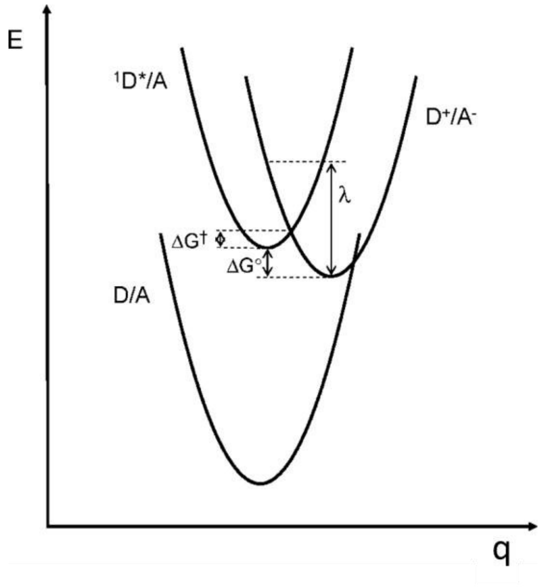

Figure 9: Potential energy surfaces for donor/acceptor (D/A) systems. q is the generalized reaction coordinate that represents the motion of all nuclei in the system. Reprinted with permission from [30]. Copyright 2010 American Chemical Society.

Electron transfer occurs at the intersection of both parabolas, with an activation energy of $\Delta G^{\dagger} = \frac{(\lambda+\Delta G^0)^2}{4\lambda}$, defined by the Gibbs free energy ΔG^0 and the reorganization energy λ, which accounts for the energy needed to bring the acceptor into the equilibrium geometry of the product (in terms of structure and environment). The rate constant can then be calculated by Fermi's golden rule as:

$$k_{ET} = \frac{|V_{DA}|^2}{\hbar}\sqrt{\frac{\pi}{kT\lambda}}\, e^{-\frac{(\Delta G^0-\lambda)^2}{4\lambda kT}}, \tag{2.5}$$

where $|V_{DA}|^2$ denotes the electronic coupling between donor and acceptor depending on the electronic wavefunctions' overlap. In the non-adiabatic case, this coupling is small compared to the reorganization energy. This implies that electron transfer occurs with a much lower rate than the nuclear vibration. It is a semi-classical theory, as it assumes the continuous Boltzmann distributed states of the harmonic oscillator but includes quantum mechanics through Fermi's golden rule. Further quantization by using discrete states for the harmonic oscillator leads to some modifications that will not be discussed further here. [31] The Marcus rate expression implies, that upon increasing the Gibbs free energy ΔG^0, the rate increases until ΔG^0 is equal to the reorganization energy λ. Here the fastest possible transfer occurs and a further increase of ΔG^0 leads to lower rates (Marcus inverted region). In more quantum mechanical models, this inverted region is less pronounced. [32] For non-discrete acceptor states like in inorganic semiconductors, many acceptor potential surfaces are available. The rate needs then to be extended by integrating over the density of acceptor states and their free energy. [30]

2.2 Photovoltaics

"I'd put my money on the sun and solar energy. What a source of power! I hope we don't have to wait until oil and coal run out before we tackle that."

(Thomas Alva Edison)

2.2.1 General Aspects: Excitonic Solar Cells

Organic and dye-sensitized photovoltaic cells differ from conventional inorganic p-n-junction solar cells, primarily due to the difference in exciton binding energy discussed in section 2.1.2. The free charges are not directly created by excitation but are rather bound in a Frenkel exciton state, which needs to be split by the input of additional energy to overcome the exciton binding energy. The splitting is usually obtained at a heterointerface between donor and acceptor, towards which the excitons might have to diffuse. Thus, the term excitonic solar cell adequately outlines the difference between these devices and the widely known inorganic p-n-junction solar cells [33], where the exciton is very weakly bound (meV) and is already separated by the thermal energy. In inorganic solar cells, the p-n-junction allows the free charges to drift in the internal electric field to the respective electrodes (see Figure 10, left). In contrast, in the excitonic solar cell, the more strongly bound exciton needs to be split into free charges at an interface between a donor and an acceptor (Figure 10, right) and the charges subsequently drift or diffuse to the electrodes.

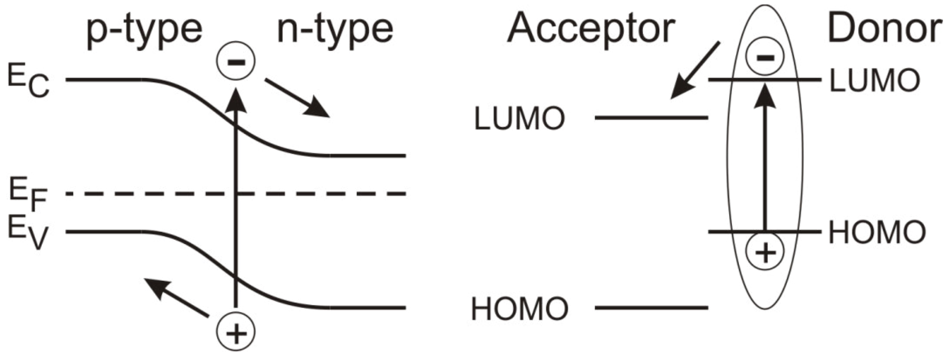

Figure 10: Inorganic solar cell (left) and excitonic solar cell (right) energy levels. In contrast to the inorganic solar cell, the excitonic solar cell exhibits a strongly bound exciton that needs to be split at an interface.

Examples of excitonic solar cells include: all organic bulk heterojunction (BHJ) solar cells (e.g. polymer:polymer [34], polymer:fullerene [35] or small molecule:fullerene solar cells [36]), hybrid solar cells (e.g. polymer-metal oxide BHJ solar cells [37]) and dye-sensitized solar cells (employing either a solid-state [11] or a liquid-electrolyte hole transporter [38]). All these types have in common that the initially bound exciton is split at an interface. As the exciton diffusion length in organic materials is typically not very long (some ten nanometers, depending on the material [30, 39]), excitons need to be created close to the interface in order to be split. Hence, the interfacial area is typically strongly increased by using mesoporous structures or bulk heterojunctions instead of bilayers and flat interfaces. The main difference between the types of excitonic solar cells introduced above is that in dye-sensitized solar cells (DSCs), the light harvesting is separated from the charge transport. DSCs are ternary systems; charge transport and light absorption take place in separate materials. In contrast, in binary blend BHJs charge transport and light absorption are usually accomplished in one or both of the blend components.

2.2.2 Charge Generation and Recombination

For an exciton to be split into charges, a driving force is needed, that is provided by the donor-acceptor interface (see sections 2.1.2 and 2.2.1). Upon exciton splitting, it is possible that an interfacially bound intermolecular charge-transfer state, also called geminate pair, is formed, in which the electron and hole originate from the same initial excitation. Recombination of this state is usually much slower than its generation, as it lies in the Marcus-inverted region. [6] The recombination rate of geminately bound charge pairs does not depend on the density of created states as it is a monomolecular process. As soon as free charges are created, e.g. upon electron injection into the acceptor, recombination of free charge carriers (non-geminate pairs) is limited by the probability of the two oppositely charged species meeting at the interface. In this case, the recombination rate depends on the charge density, as the probability of two charges meeting increases with higher carrier density. Free charge carrier recombination is usually slower than geminate recombination; however, at very high densities it can approach the same timescales. [30] In DSCs, the recombination of free charges is additionally hindered, as the dye layer represents a tunneling barrier for the charges. Faster recombination is possible, when the dye layer has voids and thus allows direct recombination. A possible way to explain charge recombination in DSCs is by using a model that accounts for trap states in TiO_2 as the main mediators for recombination which can explain the intensity dependent recombination rates of injected carriers. [40, 41]

2.2.3 Dye-sensitized Solar Cells

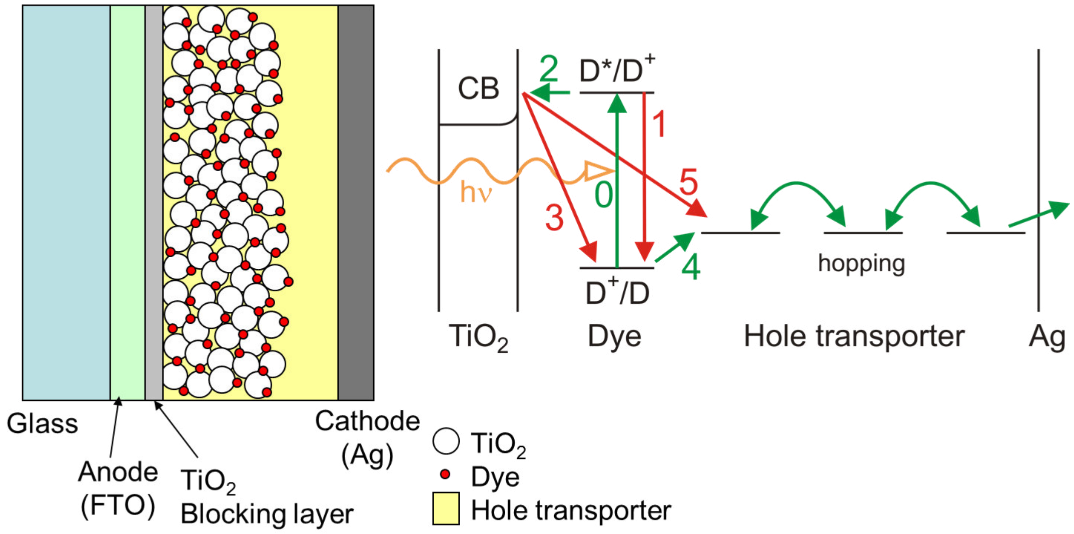

Figure 11: Schematic architecture of a dye-sensitized solar cell (left) and simplified energy level diagram and working principle. Processes indicated in green are beneficial for solar cell performance, whereas red processes indicate loss mechanisms. 0 photon absorption; 1 exciton recombination; 2 electron injection; 3 electron-dye-cation recombination, 4 dye regeneration; 5 electron-hole recombination.

Dye-sensitized solar cells are hybrid solar cells that combine inorganic semiconductors as electron acceptors with organic or metal-organic complexes as sensitizers, and employ charge transport materials of several kinds. The typical layout of a dye-sensitized solar cell is depicted in Figure 11. Apart from the substrate (glass) and electrode (typically fluorinated tin oxide as transparent conducting oxide and a metal electrode as back contact), it comprises a mesoporous structure of a metal oxide semiconductor sensitized by a dye and incorporated by a hole transporter.

Working Principle: Separation vs. Recombination

A simplified picture of the charge separation and losses in DSCs is given in Figure 11, right panel. Upon light absorption an exciton is formed on the dye (0). The first potential loss process is exciton recombination prior to exciton splitting (1). The exciton is split by electron transfer to the conduction band (2) of the semiconductor, which is usually a sub- picosecond process [42]. This is much faster than the typical exciton recombination time and is thus usually very efficient. However, when the injection is slowed down (e.g. when injection occurs from triplet states), exciton recombination competes with injection, and the splitting efficiency can be reduced [43]. The remaining dye cation is regenerated by the hole transporter (4) if it does not recombine with the electrons in the conduction band beforehand (3). In order to achieve a high efficiency of the hole transfer reaction, again the regeneration needs to be faster than the electron-dye-cation recombination, which can occur on the order of nano- to milliseconds, depending on the material and environment [41, 44, 45]. In a liquid electrolyte cell, a diffusion limited redox reaction takes place, with reaction times of typically nano- to a few microseconds [46]. With solid hole transporters, hole transfer occurs on much faster timescales, down to picoseconds [47]. Finally, the separated charges have to move to the electrodes in the respective materials. In the semiconductor, this process is mainly due to an electron concentration gradient and thus diffusion [48]. The transport itself is usually explained by a multiple trapping model [6]. Similarly, in the hole conductor, charge transport is driven by diffusion. Whereas in liquid electrolytes the charge transport corresponds to the diffusion of charged molecules, i.e. mass transport, in the solid state it is usually a charge-transfer hopping mechanism. Charge recombination of free electrons and holes (5) is strongly suppressed in the most efficient liquid electrolyte cells due to screening of the charges in the electrolyte, and thus exhibits time constants of 1-20 ms [49, 50], whereas in solid materials and other hole transporters the recombination can be much faster [51]. Finally, the charge carriers are extracted at the electrodes. With liquid electrolytes a catalytically active electrode (usually Pt) aids the redox reaction. In solid-state cells, charge extraction occurs electronically by injection into the electrodes. A final loss mechanism is the recombination of electrons in the transparent conductive oxide (TCO)-electrode with holes in the hole transporter, if both are in direct contact. This is avoided by introducing a hole blocking layer on top of the TCO, preventing direct contact between hole transporter and TCO-electrode. This layer is typically a compact TiO_2 layer and is especially important in solid-state cells [52].

Metal Oxide Semiconductor Acceptors

The acceptor in a DSC is usually made of a wide band gap metal oxide semiconductor. By far the most studied is TiO_2 [53], but others such as ZnO [54] or (surface modified) SnO_2 [55, 56] are also investigated. However, these have not yet reached the efficiencies of TiO_2. The mesoporosity is essential, as due to the much higher surface area (about 1000 times surface area increase compared to a flat film [6]), the absorbance is strongly enhanced because more dye molecules are adsorbed in the layer. Other more ordered structures like nanorods or nanotubes [57] are currently being developed but have not yet outperformed the mesoporous electrodes. Crystallinity is desirable, as the main task of the metal oxide is, apart from accepting electrons, to transport the charge carriers to the electrode. Compared to crystalline silicon or thin film technologies like CIGS, metal oxide semiconductors are easy and cheap to produce, abundant, non-toxic, stable and require less energy in their preparation. TiO_2, for example, is widely used in mass products like sunscreen, toothpaste, and even as an additive for food (E171) [6].

Sensitizing Dyes

The dye attached to the metal oxide plays the important role of light absorption. The sensitizing dye has to fulfill several requirements: i) it should absorb as much of the incoming solar spectrum as possible; ii) it needs an anchoring group that binds to the metal oxide surface (e.g. -COOH, $-H_2PO_3$); iii) the energy levels should fit to the metal oxide and hole transporter, i.e. the excited state should be higher than the conduction band edge of the oxide and the oxidized state level should be deeper than the redox level/HOMO of the hole transporter. Photostability of the dye is also desired. Metal complexes, in particular Ru-complexes have shown the highest efficiencies in liquid electrolyte [58, 59] and solid-state [13, 60] DSCs. However, due to the scarcity of Ru, other metal centered complexes like porphyrins [11, 38] and metal-free organic dyes [61] are advancing as they are abundant and modifiable by synthesis, resulting in for example higher molar extinction coefficients and spectral tunability. The general approach for organic dyes is to use a push-pull donor-π-bridge-acceptor type structure (D-π-A). The acceptor part, which mainly carries the negative charge in the excited state, is connected to the anchoring group and thus injects the electron into the semiconductor conduction band after excitation. The positive partial charge in the excited and oxidized state is located on the donor and thus is close to the hole transporter, promoting the dye regeneration. The dye itself therefore promotes charge transfer via an intramolecular charge-transfer state [6].

Perylene imides have attracted particular interest for use in DSCs, as they combine excellent photostability, electronic and optical properties and are of industrial relevance, for instance as color pigments [62]. Perylene imides show reasonably good performances in organic photovoltaics [63] and as D(-π)-A structures in DSCs, especially in combination with solid-state hole transporters [64]. The characteristic perylene imide structure is depicted in Figure 12, indicating the substitution sites and typical positions of donor, spacer, and acceptor. The donor is usually an alkyl- or arylamine in the *peri*-position. Not only does the intramolecular charge transfer help charge separation, but the push-pull system is also beneficial for light harvesting as it usually broadens the absorption spectrum [62]. By modifying the structure and positions of donors, spacers and acceptors, HOMO and LUMO levels can be easily tuned. For example, a donor directly connected to the perylene at the *bay*-position pushes both the HOMO and the LUMO to higher energies. Apart from the anchoring group, it is also important to consider the bulkiness of the dye (especially of the donor group), as it might influence the interaction with the hole transporter, and can help to avoid aggregation of the dye and direct contact between hole transporter and semiconductor, thereby hindering recombination. Finally, the spacer influences the interaction of donor and acceptor and thus the absorption spectrum, depending on whether it enhances the conjugation of the perylene or separates the donor from the acceptor [62].

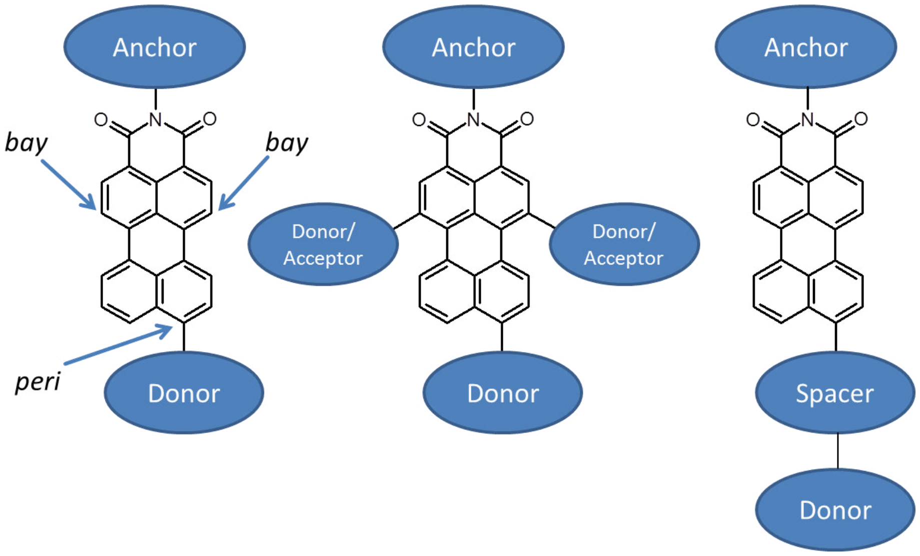

Figure 12: Perylene monoimide based dyes for DSCs and substitution sites. The perylene monoimide moiety serves as an acceptor in the push-pull geometry. Donor refers to electron-donating groups, whereas acceptor refers to electron-withdrawing groups. Adapted from [62].

With the anchor, the dye has to bind to the metal oxide surface. Several different modes are conceivable. In particular, covalent binding, electrostatic (ionic) binding, hydrogen bonding and physisorption through van der Waals forces or entrapment inside the pores are possible. The typical binding modes of carboxylic acid anchors are summarized in Figure 8. [6]

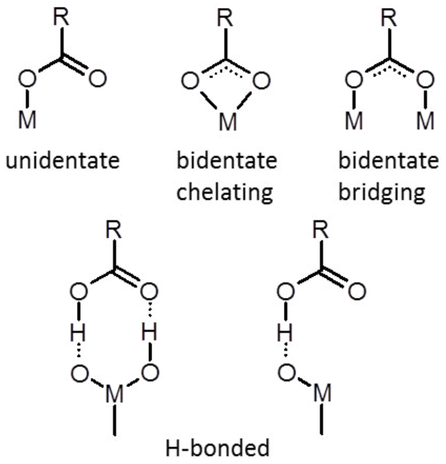

Figure 13: Typical binding modes of the carboxylic acid anchor groups to the metal oxide. M refers to the metal. Adapted from [6].

Hole Transporter

The hole transporter and reducing agent of the dye cation is the third important component in the ternary blend. The original Grätzel-cell is based on a liquid electrolyte using an iodide/iodine redox couple [53]. Electrolytes based on this couple are still among the most efficient reducing agents in DSCs [9]. However, for industrial and technical applications a corrosive and volatile liquid electrolyte is not optimal as it needs to be properly sealed and the danger of leakage is always present, if the cell structure is not sufficiently robust. Therefore, other hole transporters, such as less corrosive reagents [38], polymer or gel electrolytes [65, 66], ionic liquids [67, 68] and organic and inorganic solid hole transporters, have been developed. The latter are most promising for industrial applications. Among the solid hole transporters, several approaches have been pursued. Until recently, inorganic solids have not played an important role, but by using $CsSnI_3$ doped with SnF_2, Chung et al. recently achieved efficiencies approaching liquid electrolyte performances [12]. Two classes of organic compounds are currently investigated: conducting polymers and molecular hole conductors. Conducting polymers such as P3HT can be used as a hole transporter and absorber at the same time, leading to promising efficiencies [69] (see also 2.2.4 Hybrid Solar Cells). The most studied small molecule hole transporter is (2,2′7,7′-tetrakis-(N,N-di-p-methoxyphenylamine)-9,9′-spirobifluorene (spiro-MeOTAD, Figure 14) [10, 11]. One of the biggest issues with solid hole transporters is inefficient filling of the pores in the mesoporous metal oxide [14, 15], as they are usually deposited from solution. This, in combination with faster recombination [13], limits the thickness of the films to a few µm, about one fifth of the thickness of the liquid analogues, thereby causing inferior light harvesting. Hence, organic dyes are particularly interesting for solid-state cells, as higher molar extinction coefficients can be achieved. Additional attempts to tackle the pore filling problem are to employ other deposition methods, e.g. melts or concentrated solutions [70]. Ionic additives, such as Li salts and 4-*tert*-butylpyridine (tBP), see Figure 14, also have a significant impact on organic solid-state DSCs' performances. In fact, they essentially do not work without additives [10]. Several effects are attributed to the additive including i) suppression of recombination [52], ii) modification of acceptor and donor states [71, 72] and iii) improving the hole mobility [73]. A novel additive recently led to a record efficiency for spiro-MeOTAD DSCs [11], underlining the importance of additives. However, the development and study of novel hole transporters is also of utmost importance, because there is still a lot of room for improvement, and hole conductors have to date been underdeveloped compared with liquid electrolytes [9].

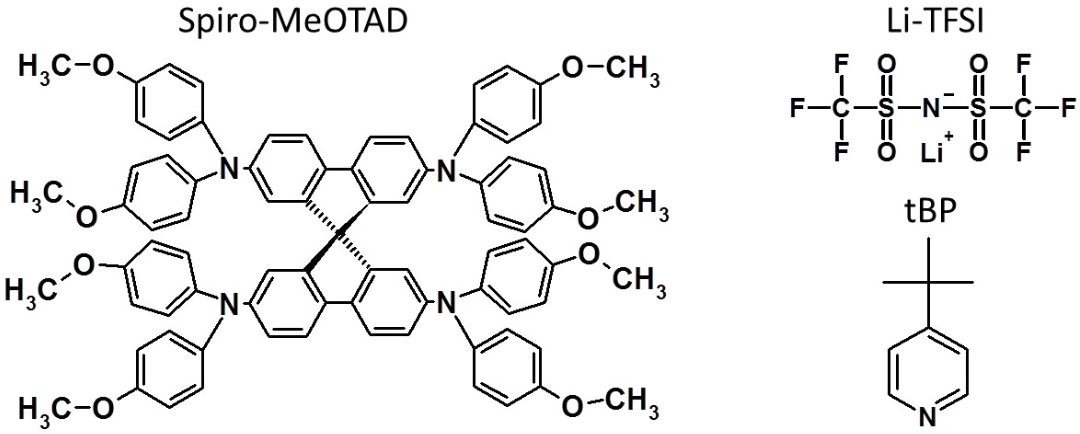

Figure 14: Chemical structures of the hole transporter spiro-MeOTAD and the additives Li-TFSI and tBP.

Current Status: Highest Efficiencies and Open Questions

The highest efficiencies published to date for selected material compositions are summarized in Table 1. There is still room for improvement, and understanding of the different steps that lead to high power conversion efficiencies is needed. The most important issues that have to be addressed are i) novel charge generation mechanisms, ii) suppression of recombination, iii) increase of light harvesting (with thicker films in solid-state DSCs due to better pore filling; stronger absorbing dyes; light management), and iv) reducing the loss-in potential (the difference between band gap of the ab-

Table 1: Record efficiencies under 1 sun AM1.5-G for different DSC types.

Hole transporter	Dye	Efficiency	J_{SC} /mA	V_{OC} /mV	FF	
$Co^{(II/III)}$-complex	Zn-porphyrin	12.3%	17.7	935	0.74	[38]
I_3^-/I^-	Ru-complex	11.5%	20.1	743	0.77	[74]
Spiro-MeOTAD	Triarylamine	7.2%	9.5	986	0.76	[11]
$CsSnI_3$	Ru-complex	8.5%	15.9	723	0.74	[12]

sorber divided by the elementary charge and the open circuit voltage, V_{OC}) by careful design and matching of the energy levels of all materials. [9]

With regard to solid-state DSCs in particular, a lot of questions remain unresolved and are currently being investigated with respect to how efficiency can be increased. Among the most important are: What is the minimum driving force needed for charge separation to minimize the loss-in potential, and how red can the dye absorb to still maintain efficient charge generation? What is the role of additives and how can control of these effects be achieved? How can recombination be decreased?

Other Approaches

It is worth mentioning that a lot of other problems are also currently being addressed to improve efficiencies. Apart from optimizing the above mentioned components, i.e. metal oxide, dye and hole transporter with additives, other parts of the solar cell have to be improved as well, such as the hole blocking layer [75], light management by scattering layers or plasmonic effects [76] and the use of dye cocktails (energy relay dyes and co-adsorption) [77-79] as well as quantum dot sensitized solar cells [80]. P-type DSCs, where the metal oxide serves as electron donor, both alone and in combination with n-type cells as tandem cells, are also being investigated. [81] Furthermore, organometal halide perovskite based materials have recently attracted attention as replacements for the dye and the electron acceptor in all solid-state mesoporous devices, reaching power conversion efficiencies as high as 11 %. [82, 83]

2.2.4 Hybrid Solar Cells: Metal Oxide Bulk Heterojunction (BHJ)

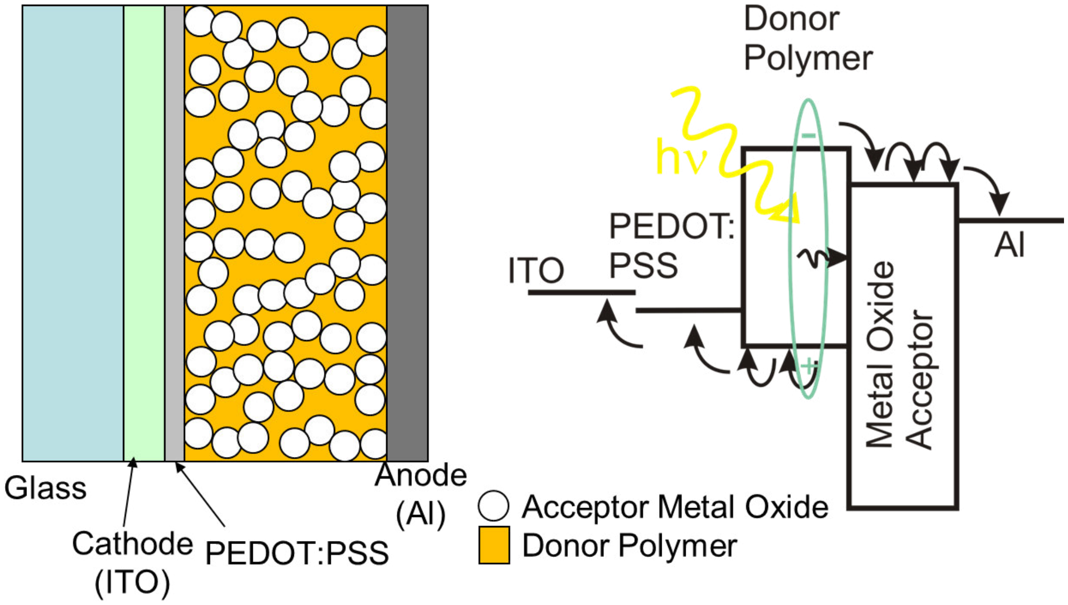

Figure 15: Schematic of a metal oxide-polymer hybrid solar cell (left) and working principle (right). Incident light creates a bound exciton in the polymer, which has to diffuse to an interface with the metal oxide where it is split into charges. The charges then have to be transported to and extracted at the electrodes.

Similar to the fullerene derivatives used in polymer:fullerene BHJ solar cells, metal oxide nanoparticles can be used as acceptors, with the electron donor being a polymer that in this case also transports the holes. Using inorganic acceptor materials is advantageous, as they combine ease of synthesis and tunability of morphological (particles, rods, tetrapods) and electronic (band gap) properties. [84] Together with the high dielectric constant of inorganic materials, which should in principle lead to a better splitting of excitons and a lower attraction between separated charges, inorganic nanoparticles are promising acceptors. The typical geometry of a hybrid BHJ device is depicted in Figure 15. The structure is similar to solid-state DSCs, employing a polymer as hole transporter, but without the sensitizer, whose function is adopted by the donor polymer. The preparation can differ from DSCs, as the polymer and nanoparticles are usually first mixed and then deposited at the same time. The morphology is thus controlled by the deposition method and the properties of the individual components.

Working Principle

The working principle and steps leading to charge transfer in a hybrid solar cell are schematically shown in the right panel of Figure 15 [30]. The polymer absorbs light and an exciton is formed which must diffuse to an interface between polymer and nanoparticle to be split. The electron is injected into the metal oxide and the hole and electron drift-diffuse to the respective electrodes. Recombination losses can occur in all steps: exciton recombination prior to splitting, interfacial geminate electron-hole recombination of the newly created but bound state at the interface, and electron-hole recombination of already spatially separated free charges.

Current Status

Several inorganic semiconducting nanostructures such as CdSe (nanorods with P3HT, η =1.7%) [85], CdS (quantum dots with P3HT nanowires, η =4.1%) [86], PbS (nanocrystals with low band gap polymer PDTPBT, η =3.8%) [87], TiO_2 (nanorods with P3HT, η =1.14%) [88] and ZnO (network with P3HT, η =2.0% [37], nanoparticles with MDMO-PPV, η =1.6% [89]) have been applied in hybrid BHJ solar cells. ZnO and TiO_2 have attracted particular interest, as they combine favorable electronic properties and ease of synthesis with biocompatibility, non-toxicity and cheapness [90]. Approaches to increase the performance include modification of the metal oxide by surfactants [91], control of the morphology or (energetic) interface modification [92] and modification of the organic compound, as well as intermediate structures between DSCs and BHJs [90].

2.3 Laser Spectroscopy

This section gives a short and qualitative introduction to the generation of ultrashort laser pulses, their amplification, white-light generation and optical parametric amplification, mentioning the most important effects and technologies. Further more detailed information can be found in the literature [93-96]. These processes are utilized for the ultrafast spectroscopy applied in this thesis. Finally, photoinduced absorption spectroscopy is introduced and the interpretation of the signals is outlined.

2.3.1 Ultrashort Pulse Generation

Ultrashort laser pulses are realized by the superposition of laser beams with different frequencies with a fixed phase relation (mode locking). An example for the superposition of up to eight waves is shown in Figure 16. The product of spectral bandwidth f_B and pulse length Δt is constant, and for a Gaussian spectral shape (chirp free) given by $f_B \Delta t = 0.4413$. This theoretical limit implies that the broader the bandwidth of the participating waves is, in other words the more frequencies participate, the shorter the pulses can get. On the other hand it implies that ultrashort pulses always have a broad spectral bandwidth.

Mode locking can be realized actively and passively. Passive mode locking leads to the shortest available pulses. It is essentially based upon saturable absorbers in the resonator that allow only the highest intensities that saturate the absorption to pass. The most common passive mode locking technique employed in fs-laser systems uses the Kerr Lens Mode Locking (KLM). Here, the intensity dependent index of refraction - a third order non-linear effect causing the index of refraction of the medium to be dependent on the light intensity, the so-called optical Kerr effect - causes self-focusing in the highly non-linear gain medium which is used to geometrically separate the high intensity (self-focused, mode locked) parts of the beam from the rest (back light and unlocked light) e.g. by an aperture. Titanium Sapphire has proven to be one of the best media for ultrashort pulse creation, as it combines a strong self-focusing with a

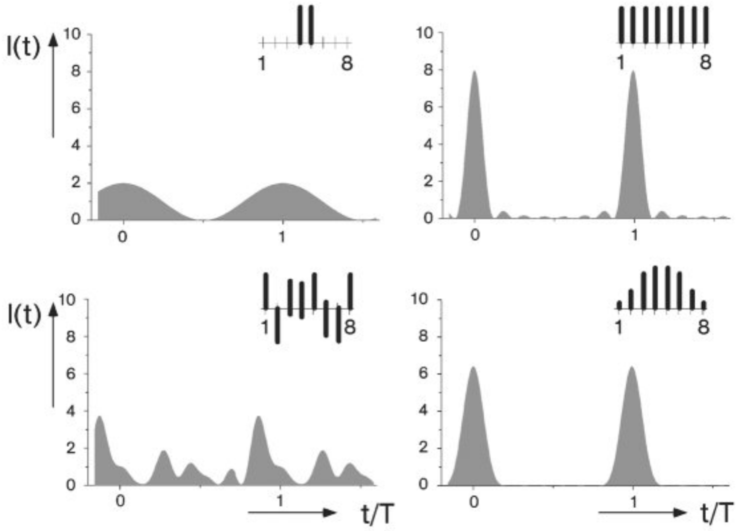

Figure 16: Principle of the generation of ultrashort pulses by superposition of waves with different frequencies. The graphs show the resulting light intensity profile with time. The subsets indicate the relative amplitudes and phases of the participating modes. In the top left graph the superposition of two waves with different frequencies, similar amplitude and constant phase relation is shown. The top right panel shows a similar superposition of eight waves with different frequencies, leading to short pulses. The lower right shows a similar situation with a Gaussian distribution of intensities and mode-locked phases, coming closest to the situation in a real resonator. In contrast, the lower left panel shows superposition of the same waves without mode-locking and fixed amplitudes leading to a noisy output. Reprinted with permission from figure 8.16, page 326 in [97]. Copyright 2008 Vieweg+Teubner.

good gain medium in one material. Due to chromatic dispersion and the frequency dependence of the Kerr effect, the pulses exhibit chirp, that is, the temporal displacement of different wavelengths. Chirp prolongs the pulse. In order to achieve shorter pulses, the chirp has to be compensated by compression of the pulse using e.g. dielectric mirrors (chirped mirrors) or a pair of diffraction gratings or prisms. [96, 97]

2.3.2 Ultrashort Pulse Amplification

Amplification of ultrashort laser pulses to higher energies per pulse is desirable if one single laser system is used to feed several experiments, or if further pulse modifications are needed (e.g. wavelength conversion in an optical parametric amplifier, white-light generation or other non-linear processes). In general, amplification of a seed laser is achieved by coupling it into an electrically or optically pumped gain medium. The most effective amplification of ultrashort pulses is provided by the use of regenerative amplifiers shown in Figure 17. Here, the gain medium (typically Ti:sapphire) is placed in an optical resonator combined with an optical switch for out-coupling (usually an electro-optic modulator such as a Pockels cell) that allows control of the number of round trips for the multi-pass amplification. For highest amplification, the repetition rates are usually reduced with a pulse-picker (e.g. also a Pockels cell) at the entrance of the resonator, which is opened for a time shorter than the round trip time, typically in the kHz regime. The gain medium is in this case pumped by a Q-switched laser working at the same repetition rate. High pump energies of ultrashort pulses can however lead to damage of optics, especially in the amplification medium. Therefore the original short laser pulse is temporally stretched in a grating expander arrangement before it enters the amplifier. The amplifier output is then recompressed to its original femtosecond pulse shape. A similar approach is used in the amplifier system used for this thesis as described in section 3.5.2. [94, 96, 97]

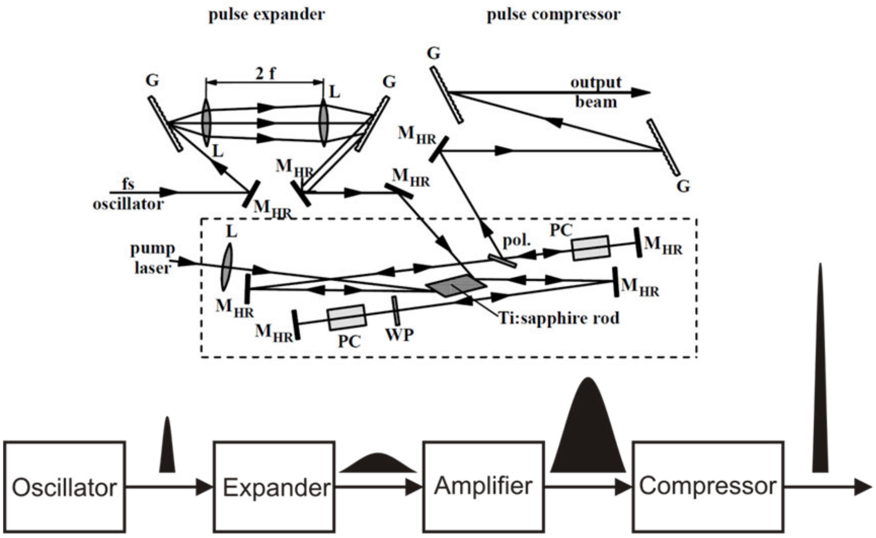

Figure 17: Regenerative amplifier with stretcher (expander) and compressor as explained in the text. The working principle is shown in the flow diagram [97]. After pulse expansion the pulse enters the amplifier cavity, which is marked by the dashed box. The mirrors M_{HR} define the resonator and after a certain amount of passes, the pulse is out-coupled via the Pockels cell PC and the pulse is recompressed. G: grating; L: lens; WP: waveplate; pol.: polarizer. Reprinted with permission from figure 6.93, page 483 in [94]. Copyright 2007 Springer-Verlag.

2.3.3 Supercontinuum White-Light Generation

When a strong ultrashort laser pulse is focused into a highly non-linear medium (e.g. sapphire Al_2O_3), it is possible to create coherent supercontinuous white-light (see Figure 18 top). With optical fibers made of highly non-linear materials, white-light generation can even be achieved with much lower pulse energies. The white-light is generated through a combination of non-linear processes, for femtosecond pulses mainly due to self- and cross-phase modulation, four-wave mixing and stimulated Raman scattering. Self-phase modulation occurs, similar to self-focusing, due to the optical Kerr effect. The intensity dependent change in refraction affects the temporal structure of the pulse and leads to a frequency chirp, that is, a change in frequency within the pulse (see Figure 18 bottom). Together with the above-mentioned processes, broad white-light can be generated ranging e.g. from 400 to 1800 nm depending on the non-linear medium and the wavelength of the seed pulse.

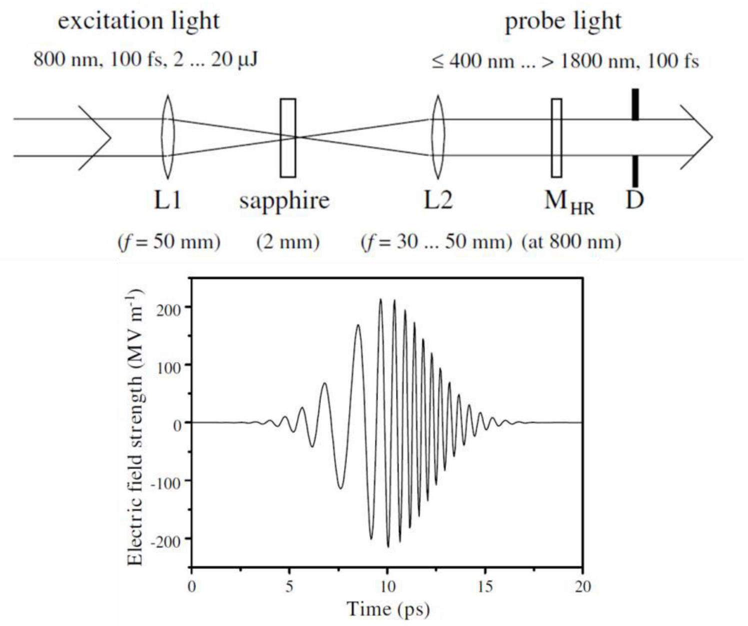

Figure 18: Top: White-light generation with femtosecond laser pulses. The excitation light of a Ti:Sa oscillator is focused (L1) into a sapphire plate. Coherent white-light is generated as a result of non-linear effects within the sapphire plate and is then collimated (L2). The pump laser is filtered out (M_{HR}). Bottom: Schematic of self-phase modulation leading to frequency chirp of a short laser pulse in a non-linear medium due to the optical Kerr effect, broadening the bandwidth of the pulse. Both reprinted with permission from figure 7.32, page 590 and figure 4.30, page 220 in [94]. Copyright 2007 Springer-Verlag.

2.3.4 Optical Parametric Amplification

In the previous sections, it was explained how ultrashort pulses of a single wavelength (usually 800 nm for a Ti:sapphire fs-oscillator) are generated and amplified and how a supercontinuum white-light can be generated. However, for the ultrafast spectroscopy experiments employed in this thesis, pulses of a particular wavelength had to be used as pump pulses to excite the sample, and to generate a white-light supercontinuum in the desired wavelength range (see section 3.5.2). These pulses are usually created by converting the 800 nm pulse to the desired wavelength in an optical parametric amplifier (OPA). The basic principle of optical parametric amplification is outlined in Figure 19. A signal and higher frequency strong pump pulse are overlapped in a non-linear medium such as BBO (with overall intensities reaching the non-linear regime), and by appropriate phase matching, the signal can be amplified at the expense of the pump. Additionally, a so called idler beam is generated, having the difference frequency of pump and signal due to the requirement for energy conservation. Phase matching means that the interacting waves (incident and newly generated) in the medium have a constant phase relation along the propagation direction, so that all parts of the medium along the propagation direction add up constructively to contribute to the desired conversion process. This is usually obtained by exploiting the birefringence of the crystal and by adjusting the crystal orientation and the polarizations of the beams in a suitable way [96]. In order to have access to a large variety of wavelengths, commercially available systems use a supercontinuum white-light to seed the OPA. By adjusting the phase matching and delay between pump and white-light, the desired signal and idler wavelength that are amplified can be chosen within some boundaries. Combining this with additional sum frequency mixing of signal or idler with the pump, and second or fourth harmonic generation, a broad wavelength range from the UV to the IR can be accessed. [94]

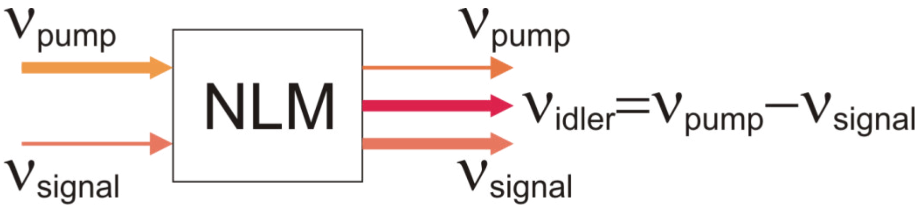

Figure 19: Basic principle of an optic parametric amplifier (OPA). The signal and a strong pump are overlapped in a non-linear medium (NLM). With suitable phase matching, the signal can be amplified at the expense of the pump and an additional idler beam is generated at the difference frequency of pump and signal (due to the requirement for energy conservation). Adapted from [94]

2.3.5 Photoinduced Absorption Spectroscopy: General Aspects

Photoinduced absorption spectroscopy records spectra of excited states of optically active materials, such as conjugated organic molecules. The experimental implementation is described in chapter 3.5. Here, the typical signals and data analysis are introduced. The measured quantity $\Delta T/T$ is the change in transmission of a sample upon excitation with a pump light ΔT, normalized to the ground state transmission of the sample T. The change in absorbance ΔOD is directly related to $\Delta T/T = 10^{-\Delta OD} - 1$. Several signals of different origin can typically be observed:

Ground state bleach (GSB): This is a positive $\Delta T/T$-signal in the wavelength region of the ground state absorption of the sample. As the ground state is less, and the excited states are more populated due to the effect of the pump pulse, less light is absorbed in the sample compared to the ground state, leading to a higher transmission. The GSB is usually used to monitor the ground state recovery and its dynamics represent the sum of all excited states.

Stimulated emission (SE): Stimulated emission can be observed as a positive $\Delta T/T$-signal in the wavelength region of the fluorescence. Due to the population of fluorescent excited states by the pump, the probe light can stimulate a radiative decay into the ground state. This additional emission in the respective wavelength region leads to a positive “transmission change”. It can be used to track primary emissive excitations.

Photoinduced absorption (PA): This refers to excited state absorptions arising from transitions from the excited states to even higher excited states. It can be of several origins, including primary excitations, charge-transfer states, free charges, triplets or any other species formed upon interaction of the sample with the pump light.

The typical wavelength regions and the schematically illustrated origins of the above mentioned signals are shown in Figure 20.

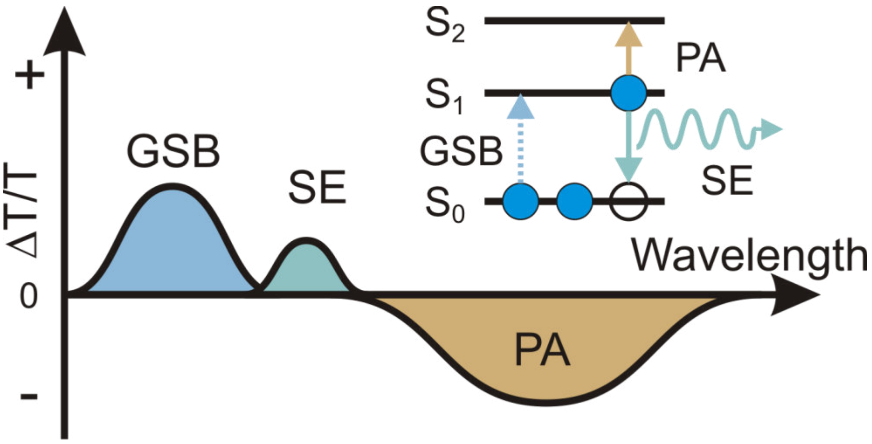

Figure 20: Typical photoinduced absorption signals and schematic representation of the processes (inset): GSB, ground state bleach, the dotted arrow indicates fewer transitions; SE, stimulated emission, the wavy arrow indicates an emitted photon; PA, photoinduced absorption.

In the linear absorption regime, disregarding coherent and non-linear effects, the signals obey the Beer-Lambert law, and are proportional to the number of absorbing species. In the small signal approximation,

$$\frac{\Delta T}{T}(\lambda, t) = -\sum_{i,f} \sigma_{if}(\lambda)\Delta N_i(t) d\,. \tag{2.6}$$

Here, i and f depict the initial and final states of the probed transition, $\sigma_{if}(\lambda)$ is the cross section of the transition $i \rightarrow f$ in cm^2, and is negative for upward transitions (absorption) and positive for downward transitions (emission), ΔN_i is the population change of state i due to the pump and d the thickness of the measured film [98]. In this regard, the GSB refers to $0 \rightarrow f$ transitions, the SE to $f \rightarrow 0$ transitions (where emission is allowed) and the PA to $i \rightarrow f$ with $i \neq 0$.

If σ is known, the signal amplitude is a direct measure of the population. In order to gain insight into the underlying processes, rate expressions can be employed describing the fate of the participating excited states, and the overall signal can be described by equation (2.6). In time-resolved measurements, rates and mechanisms of excited state formation and decay can be determined. The time resolution is limited by the length of the laser pulses, in a typical ultrafast pump-probe experiment down to tens of femtoseconds.

2.3.6 Observing Stark Effects with Photoinduced Absorption Spectroscopy

In section 2.1.4 the Stark effect was introduced and described as the influence of an electric field on optical transitions by modulation of their oscillator strength and transition energy. In dye-sensitized solar cells, charges are created upon illumination, and generate an electric field across the metal oxide-dye-hole transporter interface. After complete charge separation, the dyes are in the ground state and should not contribute to a photoinduced absorption or bleach signal. However, strong signals can be still observed that are assigned to a change of the ground state absorption of the dyes due to the electric field of the charges. This is of particular importance for donor-acceptor dyes that exhibit a strong change of the electric dipole moment between ground and excited state. [71, 99, 100]

The $\Delta T/T$-signal represents the change in transmission upon excitation. In the case that the sample exhibits a Stark effect, the photoinduced formation of charges has a similar effect to the application of an external electric field. Thus, photoinduced absorption spectroscopy effectively probes the difference in transmission with and without a field. Figure 21 shows a schematic representation of the situation at the interface with charges present. Here, the Stark effect is anisotropic as the field always points in one direction with respect to the dipole moment change, due to the interfacial geometry. In contrast to the situation depicted in section 2.3.6, Figure 7, where the electric field-induced absorption shifts to the red and the blue due to the isotropic geometry, here,

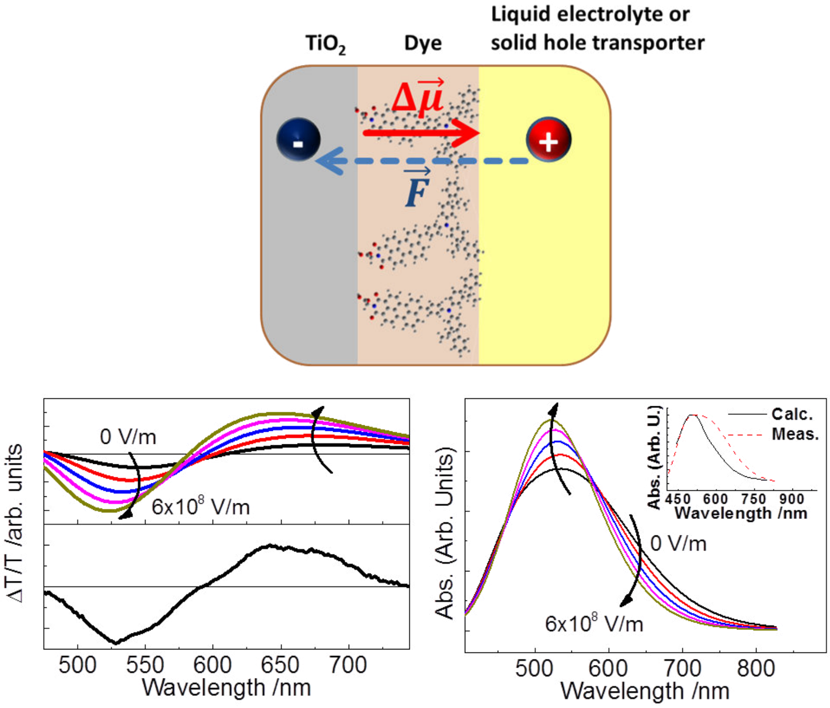

Figure 21: Origin of Stark features in photoinduced absorption measurements on DSCs. The top sketch shows the anisotropic situation at the interface, where the field $\vec{F}$ and the dipole moment change $\Delta\vec{\mu}$ are always similarly oriented with respect to each other. This leads to changes in the absorption of the dyes affected by the field as depicted in the lower right graph. The spectra were calculated with TDDFT. [101]The inset shows a comparison of the calculated absorption spectrum in vacuum with the observed spectrum on TiO$_2$. The change in absorption due to the field leads to transient absorption features as shown in the lower left graph.

the absorption maximum shifts only to the blue (note that the electric field points from the positive to the negative charge, whereas the dipole moment points from the dipole's negative charge to the positive), as the excited state is energetically less favorable (higher in energy) than the ground state. This leads to an increase of the transition energy. The oscillator strength can also be influenced. The two bottom graphs in Figure 21 depict the change in absorption as derived from quantum chemical time-dependent density functional theory (TDDFT) calculations, [101] and the implication for photoinduced absorption signals along with the observation by the experiment. Further information can be found in section 4.4.

3

Experimental Techniques

In this chapter, the most important experimental techniques and methods employed in this thesis are presented and explained. For detailed experimental details, especially sample preparation, the reader is encouraged to consult the experimental sections of the manuscripts presented in the Results and Discussion chapter 4.

3.1 Standard Sample Preparation

3.1.1 Solar Cells

The standard preparation of solid-state dye-sensitized solar cells is usually conducted in several steps including substrate cleaning and treatment followed by several coating procedures. Here, a typical recipe for a functioning solar cell is presented. For different materials, the recipes might differ; if the preparation of samples used in the results part deviated from the way presented here, it will be mentioned.

The substrates used are typically standard glass substrates coated with a transparent conductive oxide (TCO), such as fluorinated tin oxide (FTO) or indium tin oxide (ITO). Due to the high temperature sintering steps required for DSCs, the TCO of choice is usually FTO due to its superior stability at high temperatures. For devices not employing a high temperature treatment ITO is usu-

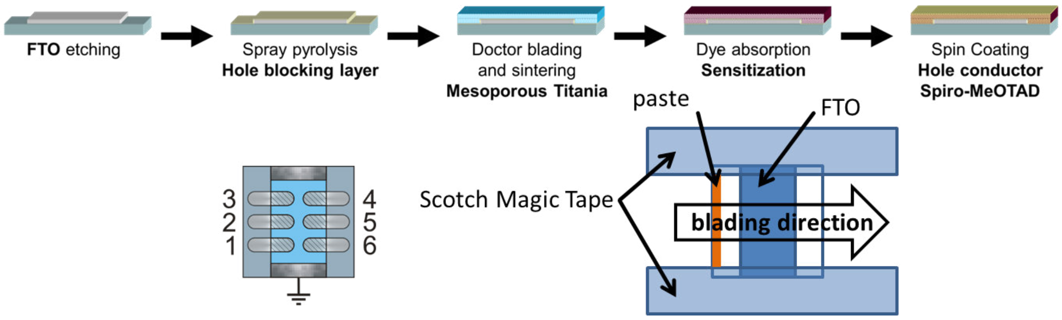

Figure 22: Typical solar cell preparation steps and outline of a sample with six pixels. The substrate dimension is 24x24 mm². The TCO-stripe is shown in light blue, electrodes are grey/metallic. The active area of one pixel is defined as the overlap of TCO and metal electrode (shaded area) and has a surface area of about 14 mm². The lower right scheme shows the geometry of the doctor-blading technique for the mesoporous TiO_2 layer.

ally the TCO of choice, as it has a lower sheet resistance and surface roughness. A typical preparation cycle developed within this thesis is depicted in Figure 22. First, the 24x24 mm sized FTO substrate (Pilkington TEC-15) was etched so that a 12 mm stripe in the middle of the substrate remained. Therefore, the sample was protected with a polyimide tape and the FTO was etched with zinc powder and 4M hydrochloric acid. A well-defined TCO stripe is needed to get a distinct pixel size, determined by the overlap of top electrode and TCO. Subsequently, several cleaning steps were conducted, including Hellmanex and organic solvent treatment (using either ethanol or 2-propanol) in an ultrasonic bath. A dry nitrogen flow was used to remove residual solvent. A final cleaning step was performed by treatment for 10 min with an argon plasma at 0.2 mbar, created by 300 W microwave power. Afterwards, the compact TiO_2 hole blocking layer was applied by spray pyrolysis. In this step, the samples were heated to 450 °C on a hotplate (Harry Gestigkeit GmbH PZ28-3TD) and successively sprayed with a dilute (1:10 by volume) solution of Diisopropoxytitanium bis(acetylacetonate) in ethanol, employing a glass atomizer (Glaskeller Art Nr. 12.159.603). This was manually operated, corresponding to sprays of about 1 s, requiring about 50 sprays to yield an 80 nm thick compact TiO_2 layer. The distance between sample and spray nozzle did not exceed 10 cm and the samples were coated as uniformly as possible. An interval of at least 10 s was taken between each spray to allow the solvent to evaporate, the organic to be pyrolized and the sample to return to the reaction temperature of 450 °C. After cooling down, the mesoporous titania layer was applied using a TiO_2 paste. In order to yield a thickness of about 2.2 µm, the paste (Dyesol DSL-18NR-T) was diluted with ethanol in a ratio of 1 g : 1.5 ml and shaken or stirred until homogeneous. Adhesive tape (Scotch Magic tape) was used as a spacer and to protect the FTO electrode for contacting it later. The TiO_2 paste was applied by doctor-blading: A small stripe of paste (about 40 µL) was applied to one side of the sample and spread over the sample by using the tape as a spacer and a plane rigid trowel (e.g. a microscopy glass slide or a glass stick) in a smooth movement at a rate of about 2 cm/s. To allow the paste to settle, it was left in a petri dish for 1 min and subsequently placed on a hotplate at 70 °C to avoid any further spreading. After all substrates were coated, the films were sintered with the temperature ramp shown in Table 2. After cooling, the samples were treated in a 70 °C dilute aqueous $TiCl_4$ solution (40 mM) for one hour, followed by another sintering step at 500 °C for 45 min.

Table 2: Temperature ramp used for sintering the mesoporous TiO_2 film.

Rise time	Temperature	Dwell time
10 min	100 °C	10 min
5 min	150 °C	10 min
10 min	325 °C	30 min
5 min	400 °C	5 min
5 min	500 °C	30 min

For dye adsorption, the samples were left to cool to 70 °C and immersed in the dye solution. Depending on the dye, various solvents were used. A few examples are given in Table 3. Typical concentrations were 0.3-0.5 mM. The dye soaking usually takes several hours, up to a day. When the samples were taken out of the dye solution, dye molecules not adsorbed to the metal oxide were removed by rinsing the samples thoroughly with the particular solvent used for sensitization.

Table 3: Typical solvents for different dyes.

Dye compound	Examples	Solvent
Ru-complexes	Z907, N719	Acetonitrile:tert-butanol 1:1vol
Organic compounds	Naphthalene or perylene-based	Dichloromethane or ortho-xylene

The hole transporter of choice was 2,2′7,7′-tetrakis-(N,N-di-p-methoxyphenyl-amine)-9,9′-spirobifluorene (spiro-MeOTAD, Merck SHT-263 Livilux, Figure 14). It was dissolved in chlorobenzene at concentrations of 160-200 mg/ml, and heated to 100 °C to fully dissolve. Several additives can be added to the hole transporter solution. The most important additive, and the main one used in this thesis, is lithium bis(trifluoromethanesulphonyl)imide salt (Li-TFSI, Figure 14), which was predissolved in acetonitrile (170 mg/ml, 0.6 M) or cyclohexanone (85 mg/ml, 0.3 M) and added as 4 mol Li-TFSI per 33mol of spiro-MeOTAD to the hole transporter solution (corresponding to 15 µL of the 0.6 M acetonitrile solution per 73 mg of spiro-MeOTAD). Another additive commonly used, especially for Ru-sensitized solar cells, is 4-*tert*-butylpyridine (tBP, Figure 14), which was directly added as 7 µL per 73 mg of spiro-MeOTAD to the hole transporter solution. About 65 µL of the hole transporter solution was spin coated onto each solar cell substrate. However, after the application of the solution to the substrate and before spin coating, it was left to infiltrate the mesoporous structure for 30 s to 1 min. Finally, the excess solution was spun away at 1000 rpm for 5 s followed by 1500 rpm for 30 s. The silver top electrodes were evaporated using an evaporation mask depicting the desired electrode pattern. A 200 nm silver layer was evaporated with a deposition rate not exceeding 0.3 nm/s. It was beneficial to evaporate the first 50 nm with a rate lower than 0.15 nm/s. Finally, the FTO was uncovered at the edges where it needed to be contacted by mechanically scratching off the spiro-MeOTAD and TiO_2 compact layer. For a better contact during measurement, the electrodes were covered with a silver paste at the contact site.

3.1.2 Spectroscopy Samples

Spectroscopy samples were typically prepared on quartz substrates instead of FTO coated glass. The recipe was similar to the solar cell preparation. In order to obtain different material compositions, one or the other of the individual components was not applied to the sample. For example, for samples with Li-TFSI but without hole transporter, the hole transporter was replaced by the same volume of the solvent chlorobenzene in the spin coating solution, to yield a roughly similar Li-TFSI concentration on the sample. The TiO_2 thicknesses were adjusted to yield absorbances suitable for spectroscopy measurements (optical densities of between 0.3 and 0.8). Samples in which TiO_2 was replaced by Al_2O_3 were prepared by pasticising a standard mesoporous Al_2O_3 dispersion (Sigma-Aldrich, <50 nm particle size, 20 wt. % in isopropanol) with terpineol, ethanol and ethyl cellulose according to Ito *et al.* [102]. 300 mg terpineol and 1250 µl ethanol were added to 500 µl dispersion and mixed into 50 mg ethyl cellulose solution. The ethyl cellulose stock solution was prepared using 0.75 mg of a higher and 0.75 mg of a lower viscosity ethyl cellulose (Sigma-Aldrich: "viscosity 46 cP, 5 % in toluene/ethanol 80:20 (lit.), extent of labeling: 48% ethoxyl" and "viscosity 10 cP, 5 % in toluene/ethanol 80:20 (lit.), extent of labeling: 48% ethoxyl", respectively) in 15 ml ethanol. The paste mixture was shaken for several hours to achieve the desired homogeneity. It was then applied in a similar way as the TiO_2 paste, i.e. by doctor blading.

3.2 J-V Characterization of Solar Cells

The figure of merit for photovoltaic devices is their power conversion efficiency η, which is defined as the ratio of the electrical power of the solar cell at the maximum power point P_{MPP} and the optical power used to illuminate the device P_{in}^{opt}: $\eta = \frac{P_{MPP}}{P_{in}^{opt}}$. Typically, a solar cell is characterized by a J-V curve, obtained by measuring the dependence of the output current on the voltage applied to the electrodes under solar illumination. A typical J-V curve is shown schematically in Figure 23. It can be described by three main parameters:

1) the open circuit voltage V_{OC}, being the voltage where the net current is zero in the solar cell $V_{OC} = V(J = 0)$,
2) the short circuit current density J_{SC}, being the maximum current in the solar cell at zero voltage $J(V = 0)$, and
3) the fill factor FF, which is a dimensionless parameter, defined as the ratio of the actual maximum power density at the maximum power point and the theoretically possible maximum power density defined by the product of V_{OC} and J_{SC} which would be the maximum power point if no losses were present and the J-V curve had a rectangular shape: $FF = \frac{P_{MPP}}{V_{OC} J_{SC}}$.

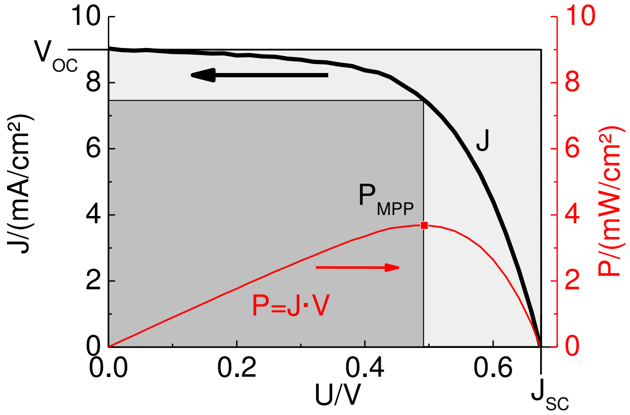

Figure 23: Typical J-V curve of a solar cell with characteristic parameters. The fill factor FF is defined as the ratio between the dark grey surface area (corresponding to P_{MPP}) and the light grey surface area (corresponding to $\boldsymbol{J_{SC} \cdot V_{OC}}$).

In order to simulate the performance of a solar cell under illumination by the sun, a standardized solar spectrum was used. The classification of this spectrum is AM1.5G (also known as ASTM G173-03 from the American Society for Testing and Materials [103]), which describes a standard spectrum of the sun after passing through 1.5 atmosphere thickness, corresponding to a solar zenith angle of 48.2°. This spectrum is depicted in Figure 24. The illumination of one sun is defined as an overall light surface power density of 100 mW/cm^2 (=1000 W/m^2).

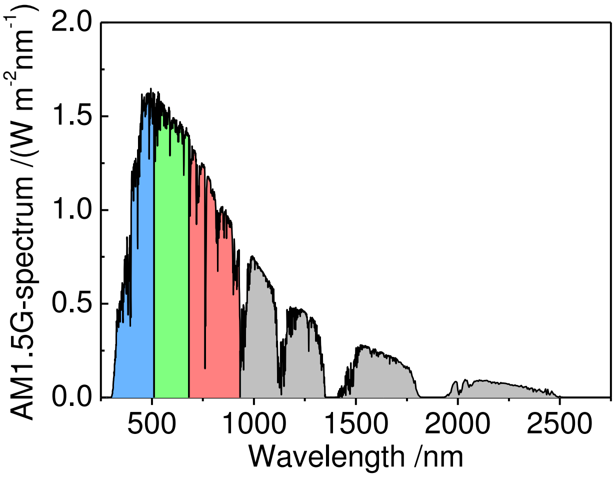

Figure 24: AM1.5G standard solar spectrum [103]. Each colored area corresponds to 25% of the total power density. [104]

The solar cells characterized within this work were measured under AM1.5G solar conditions generated by a xenon arc lamp with suitable filtering (LOT-Oriel Low Cost Solar Simulator). J-V curves were recorded with a Keithley 2400 digital source-measure unit controlled by LabVIEW (National Instruments) based software. In order to calibrate the light power output to one sun, a silicon reference solar cell (RERA Systems) was used.

3.3 External and Internal Quantum Efficiency

The external quantum efficiency or EQE (also known as incident photon to current efficiency, IPCE) measures the spectrally resolved number of electrons N_{el} extracted per *incoming* photons N_{ph}: $EQE(\lambda) = \frac{N_{el}(\lambda)}{N_{ph}(\lambda)}$, whereas the internal quantum efficiency (IQE) measures the number of electrons extracted per *absorbed* photons N_{abs}: $IQE(\lambda) = \frac{N_{el}(\lambda)}{N_{abs}(\lambda)}$. The EQE is determined by measuring the short circuit current (I_{SC}) as a function of the wavelength of the incident light. This is realized by using monochromatic white-light, which is guided onto the sample in such a way that the light spot is smaller than the pixel. Using a spectrally calibrated reference photodiode (photodiode with known $EQE_{Ref}(\lambda)$), the absolute number of incident photons for each wavelength can be calculated. By measuring the I_{SC} of the solar cell under the same conditions, the EQE can be determined as $EQE_{Sample}(\lambda) = \frac{I_{SC}^{Sample}(\lambda)}{I_{SC}^{Ref}(\lambda)} EQE_{Ref}(\lambda)$. For the internal quantum efficiency, the absolute number of photons absorbed in the sample has to be known, which usually is not simple to determine as interference effects, reflection, scattering and parasitic absorption of non-photoactive layers contribute unknown losses. The absorbance of the sample is measured in reflection and has to be corrected for the losses. This can be approximated by using an integrating sphere to measure the absorbance of samples with different constitutions to account for the different layers. If the corrected absorbance determined in reflection $A(\lambda)$ of the sample is known, the IQE is determined as $IQE = \frac{EQE}{1-10^{-A}}$. However, due to the above mentioned uncertainties, the IQE is usually a very error-prone value and should thus be considered an approximation.

3.4 Time-Resolved Photoluminescence Spectroscopy

Working Principle

Time-resolved photoluminescence spectra and kinetics were recorded using a Hamamatsu Streak Camera system. The principle of a streak camera is depicted in Figure 25. The sample is excited with a short laser pulse. The emitted fluorescent light is collected with a telescope and focused on a spectrograph, where the light is diffracted and spectrally resolved in the x-axis (parallel to the table and perpendicular to the incoming light). The spectrally resolved photons are then converted by a photocathode into electrons. The electrons witness a time-dependent electric field in the y-axis (perpendicular to the table and the incoming light), which is triggered in a way that, depending on the time the photons arrive at the cathode (the electrons are created), the electrons are deflected to a different extent. The field thus sorts the electrons in the y-axis depending on their time of creation. Finally the electrons are converted back into photons on a phosphorescent screen and detected with a two dimensional CCD camera. The recorded streak image shows the spectral resolution in the x-axis and the temporal information on the y-axis.

Setup

There were two time modes available for the measurements presented in this thesis; one with a resolution down to a few picoseconds and a maximum time range of two nanoseconds (fast sweep) and a second with a time resolution down to a few hundred picoseconds and a maximum time range limited by the repetition rate of the excitation source (slow sweep). Excitation was provided depending on the measuring mode. For fast sweep experiments a Ti:Sapphire ultrafast laser system (Coherent Mira 900-Dual fs-ps-Oscillator) with a repetition rate of 80 MHz and a pulse length of 100 fs pumped by a diode pumped solid-state laser (Coherent Verdi V8) was used. The 800 nm output was frequency doubled using a BBO crystal to achieve the excitation wavelength of 400 nm. For the slow sweep measurements, a Fianium fiber laser supercontinuum source (SC450-2) was used, which provides a white laser light (460-2200 nm) with a pulse width of 6 ps and a fundamental repetition rate of 20 MHz, that was typically derated by an implemented pulse picker to 1 MHz. The desired excitation wavelength was filtered out of the white-light using an acousto-optical modulator (AOM, Fianium AOTF).

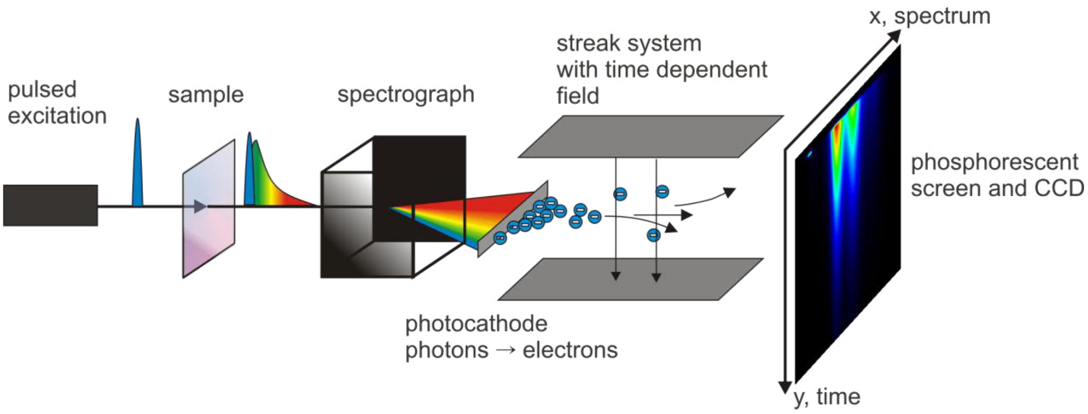

Figure 25: Schematic and working principle of the streak camera system further explained in the text.

3.5 Photoinduced Absorption

Photoinduced absorption spectroscopy records changes in the absorption (transmission) of an optically active sample due to an excitation stimulus. Changes in transmission originate from excited states that are generated due to the stimulus. In principle, transmission changes can be induced by external stimuli of different origins (e.g. electrical, optical or even thermal), though photoinduced absorption generally refers to a change induced by an optical stimulus. Two modes of optical photoinduced absorption spectroscopy were employed, namely quasi-steady-state photoinduced absorption and transient absorption spectroscopy.

3.5.1 Quasi-steady-state Photoinduced Absorption Spectroscopy

Working Principle

In quasi-steady-state photoinduced absorption spectroscopy (PIA) the sample is continuously probed by a monochromatic probe light. Additionally a modulated (typically rectangular) strong monochromatic light is used as an excitation source. The change in transmission due to the excitation is recorded with a lock-in amplifier operating at the frequency of the excitation modulation. Hence, a very good signal-to-noise level can be obtained. By scanning the monochromatic light through the available spectrum, spectral information is acquired.

In Figure 26 the principle of the measurement is depicted. The chopped excitation source modulates a transmission change $\Delta T_{PIA}(\lambda)$ on the ground state transmission spectrum $T(\lambda)$, due to optically created long-lived excited states like charges or triplets. This modulation is filtered out by a lock-in amplifier. A lock-in amplifier is essentially a very good band-pass filter that discriminates a signal of the same frequency as the reference signal from any background or other signals. The output of the lock-in is proportional to the amplitude of the signal oscillating at the reference frequency.

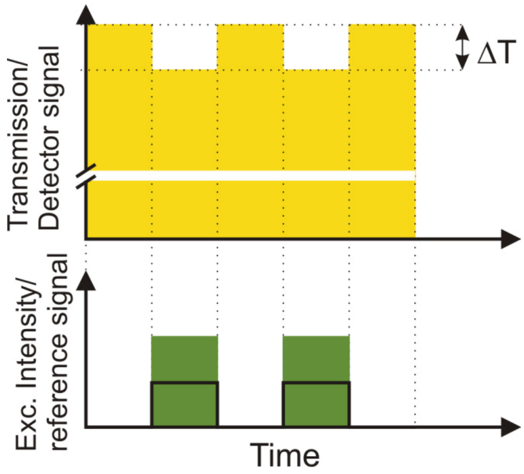

Figure 26: Principle of quasi-steady-state photoinduced absorption spectroscopy. The lower graph depicts the excitation intensity plotted with respect to time. Due to the chopping or electronic triggering, the excitation is switched on and off at the same frequency that is used as a reference for the lock-in. The transmission of the sample at one particular wavelength depicted in the upper graph is modulated due to the additional absorption of long-lived excited states like charges created by the excitation light. The lock-in filters this small difference (typically <0.1%) out of the huge transmission background.

In this measurement the input signal is the output voltage of an amplified detector, being a measure for the transmission of the sample. In order to account for the different spectral responsitivity of the whole setup (e.g. due to the white-light spectrum, the monochromator efficiency and the spectral response of the detector), the relative change of the transmission $\Delta T_{PIA}/T\ (\lambda)$ for each wavelength is calculated. The transmission spectrum $T(\lambda)$ is recorded prior to the PIA scan with the same setup by chopping the probe-light and recording the transmission with the lock-in amplifier. To account for any photoluminescence or scattered pump light in the respective wavelength regions, the PIA signal is corrected for each wavelength, by measuring the signal under excitation illumination but without the continuous probe-light. This correction spectrum $\Delta T_{PL}(\lambda)$ is subtracted from the PIA signal to yield the final PIA spectrum: $\frac{\Delta T_{PIA}(\lambda)-\Delta T_{PL}(\lambda)}{T(\lambda)}$. Due to the limited excitation repetition frequency (usually below 1 kHz) and the quasi-steady state, only long-lived (~µs) excited states can be observed. The PIA measurement is a very straight-forward measurement to obtain spectra of charges and triplets, and to get first impressions of the possibility to optically create long-lived states in the sample. It is essential to collect this information about the spectral shape and the region of interest, before the more sophisticated transient absorption technique is used.

Setup

A schematic of the setup developed and installed as a part of this thesis is shown in Figure 27. The continuous probe white-light was generated by a 100 W tungsten halogen light source (Müller Elektronik Optik DUO150). It passed through a monochromator (LOT Oriel Omni-λ 300) equipped with three gratings for three wavelength regions to cover the entire spectrum from 500 nm up to 4500 nm (1200 lines/mm, 500 nm blaze; 600 lines/mm, 1000 nm blaze; 300 lines/mm, 3 μm blaze). The sample was placed at an angle of around 45° in an optical cryostat (Oxford Instruments Optistat CF). The cryostat allows measurements in vacuum or controlled atmosphere in temperatures down to 77 K (cooling agent liquid nitrogen) or even 4 K (cooling agent liquid helium). For low temperature measurements, helium was used in the sample chamber as a heat transfer agent. The probe light passed through the sample into a second monochromator, with the same configuration and set to the same wavelength as the first monochromator. The second monochromator assures that only the set probe wavelength reaches the attached detector, and that scattered pump and photoluminescence is suppressed. Three different detectors were used for the three accessible wavelength regions: For the visible region (500-1100 nm), an amplified silicon detector (Thorlabs PDA 100A) was employed, the near infrared region (900-1700 nm) was detected by an amplified germanium detector (Thorlabs PDA 50B) and for the infrared part of the spectrum (1700-4500 nm) an amplified nitrogen-cooled indium antimonide detector (Teledyne-Judson J10D) was used. The amplified detector signal was fed into a dual channel lock-in (EG&G Princeton Applied Research Model 5210). The lock-in reference was either provided by a standard function generator (Kontron Messtechnik Model 8201), if the pump source could be controlled electronically, or by an optical chopper (Thorlabs MC1000A). Several optical

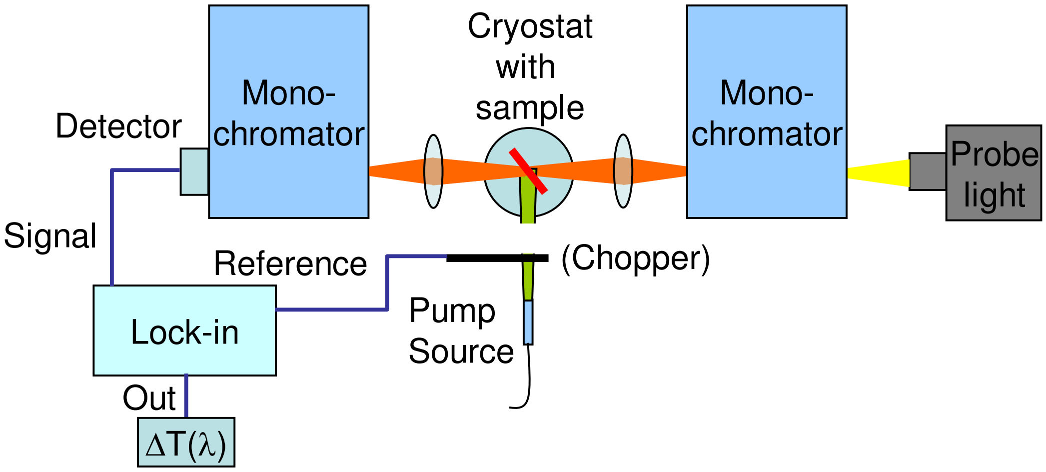

Figure 27: Schematic setup of the quasi-steady-state photoinduced absorption spectrometer.

pumps were available: For UV excitation a UV-LED (Hamamatsu LC-L2) operating at 365 nm was employed, visible excitation was provided by a high power green LED (Newport LED-527-HP) centered at 527 nm and a red (633 nm) helium-neon laser (JDSU Model 1145P). For near-infrared excitation, a diode laser working at 808 nm was installed (Topag LDT-808-150GCB). The excitation illuminated the sample at an angle of about 90° with respect to the probe light, whereas the sample was tilted by an angle of about 45° with respect to the probe light. The phase of the lock-in was adjusted in such a way that the excitation signal at the excitation wavelength was positive in the X channel (in-phase channel) and that the Y channel (out-of-phase channel) was zero. The overall signal was finally determined by calculating the absolute value of the two channels, defined as $\operatorname{sgn}(X)\sqrt{X^2+Y^2}$. By varying the excitation frequency, additional temporal information can be extracted from the data by comparing the X and Y channels or the signal amplitude and by solving a photophysical model in a quasi-steady state implying a periodic generation and for example charge recombination [105, 106] or assuming a signal decay and transforming it from the time to the frequency domain [107]. However, these methods were not used within this work and are thus not further illustrated.

Data Processing

The quantity usually considered in this work is the absolute value of the two channels. In order to compare different samples with varying absorbance and different excitation sources, the signal was normalized to the flux of absorbed photons $\Phi_{abs} = \frac{I_0 \lambda_{exc}}{h\,c}\left(1 - 10^{-A(\lambda_{exc})}\right)$. Here, I_0 is the incoming excitation intensity (dimension W/m^2), λ_{exc} is the excitation center wavelength, $A(\lambda_{exc})$ is the absorbance of the sample at λ_{exc}, h is the Planck constant and c the speed of light. For comparing signals, all constant parameters can be neglected. In case of the same excitation source and setup, the normalization factor is reduced to $\left(1 - 10^{-A(\lambda_{exc})}\right)$. Again, similar to the internal quantum efficiency, the absorbance of the sample has to be known. However, if the samples have the same geometry (layer thickness, substrate etc.) and only differ for example in the sensitizing dye, it is reasonable to use the absorbance obtained by a UV-VIS absorption experiment in transmission, because scattering and parasitic absorption can be assumed to be similar in the samples and much smaller than the total absorbance. In addition, the PIA measurement was also performed in transmission. A typical PIA spectrum is depicted in Figure 20 on page 41. Stimulated emission is usually not observed in the quasi-steady-state measurement as it originates from primary excited states that are too short-lived to be detected with this technique.

3.5.2 Transient Pump-Probe Photoinduced Absorption Spectroscopy

Working Principle

Transient absorption (TA) spectroscopy is a pump-probe technique, which, in contrast to quasi-steady-state PIA, uses ultrashort laser pulses to excite and probe the sample. A supercontinuum white-light laser pulse is used as a probe, whereas a monochromatic pulse adjusted to the ground state absorption of the sample is used as a pump. The probe pulse is focused on the sample and the transmitted light is diffracted in a spectrograph onto an array detector, which allows the whole spectrum for each probe pulse to be recorded. In order to obtain the change in transmission caused by the optical excitation normalized to the ground state transmission $\Delta T/T$, the transmission of the sample in the absence of the pump pulse is subtracted from the transmission after a pump was present and then divided by the same transmission in the absence of the pump $\frac{\Delta T}{T} = \frac{T_{pump\ on} - T_{pump\ off}}{T_{pump\ off}}$. In order to achieve a reasonable signal to noise ratio, these spectra have to be averaged over typically thousands of shots. By varying the time delay between pump and probe, spectra at different delay times can be recorded. This delay can be achieved by changing the optical path length between the two pulses with a delay stage (short time range or "short delay"). A path of 1 mm corresponds to a time delay of 3.3 ps. By using an electronically triggerable, e.g. an actively Q-switched, laser as the pump pulse source, the time delay can be achieved with an electronic delay generator, and much longer delay times can be covered (ns-µs or "long delay").

Setup

Figure 28 shows a schematic of the TA setup. The fundamental 800 nm, 100 fs laser pulses were generated by a one-box Ti:Sapphire laser system (Coherent Libra HE), that delivers a pump energy of 3.5 mJ per pulse with a repetition rate of 1 kHz. The output was coupled into two optical parametric amplifiers (OPA, Coherent OPerA Solo Topas system), which convert the incoming laser pulse into wavelengths reaching from 285 nm to 2600 nm. The output of Topas 2 was used as a seed to generate a supercontinuum white-light. To generate this white-light, the seed was focused into a nonlinear medium like Sapphire (Al_2O_3, c-cut 3 mm thick) causing self-phase modulation and other nonlinear effects (see 2.3.3) and creating a spectrally broad white-light pulse. The seed wavelength was selected depending on the desired wavelength region of the white-light. For the visible to NIR spectral region (450-1000 nm), the seed was set to 1300 nm (signal of the Topas), whereas for the NIR to IR spectral region (1100-2000 nm), the seed was set to 2100 nm (idler of the Topas).

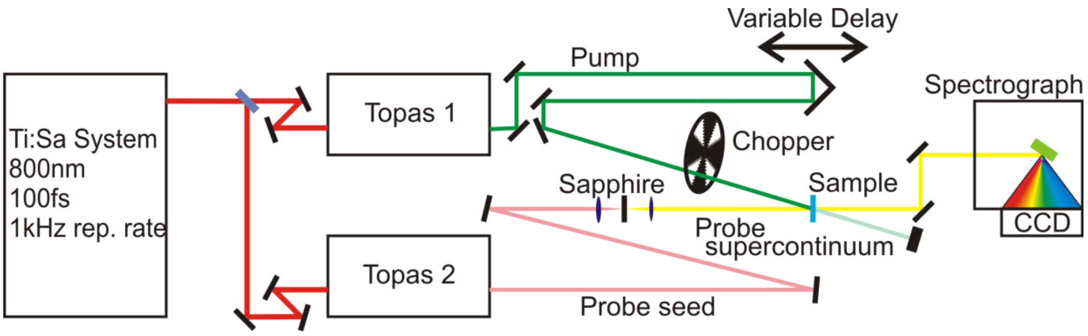

Figure 28: Schematic setup of transient absorption spectroscopy.

Other nonlinear media are also applicable like yttrium-aluminium-garnet (YAG) or yttrium vanadate (YVO_4), which have to be seeded with other wavelengths to achieve the desired stable spectrum. The white-light was focused on the sample and detected with a spectrograph employing a linear 512 or 256 pixel silicon photodiode NMOS array (Hamamatsu NMOS linear image sensor S3901-256/512) for the visible and a Peltier-cooled 512 pixel long linear extended InGaAs array (Entwicklungsbüro Stresing) for the NIR spectral region. For the short delay measurements, the pump beam was generated using Topas 1. Depending on the desired pump wavelength, usually the sum frequency of signal (470-535 nm) or idler (533-613 nm), second harmonic signal (565-810 nm) or idler (793-1130 nm) or fourth harmonic signal (285-405 nm) or idler (400-480 nm) were used. The pump was guided over a mechanical delay stage (Newport, 600 mm travel range, up to 1200 mm optical path length corresponding to up to 4 ns time delay) and chopped at a frequency of 500 Hz to block every second pulse before it was focused on the sample. As the detectors are read out at 1 kHz, adjacent diode readings corresponding to the transmission of the sample after an excitation pulse and without an excitation pulse can thus be used to calculate $\Delta T/T$. The pump spot was chosen to be larger than the probe in order to have a defined excitation density. For the long delay measurement from 1 ns to 1ms with a time resolution of 600 ps, an actively Q-switched Nd:YVO_4 laser (AOT Ltd. MOPA) operating at 532 nm was used. The electronical delay was provided by an electronic delay generator (Stanford Research Systems DG535). The polarization for both pump modes was set to magic angle (54.7°) relative to the white-light polarization in order to avoid contributions from polarization relaxation effects in the kinetics.

Data Processing

A typical recording is depicted in Figure 29. The results are displayed in a two dimensional matrix containing the time and spectral information, whereas the values of the matrix correspond to the $\Delta T/T$-value. Thus, slices parallel to the time axis result in kinetics at the respective wavelength and slices parallel to the wavelength axis result in a spectrum at the respective time. The typical spectral features are explained in chapter 2.3.4 and Figure 20. Two corrections had to be applied to the data: a background correction and, for the spectra at short times, a chirp correction. The background correction is needed if the sample has a strong fluorescence or scatters the pump, and if the wavelengths affected are within the measurement range. As the detectors are sensitive during most of one readout cycle, almost all incident light is detected. If the sample strongly scatters or fluoresces, some part of the scattered pump or the pump-induced fluorescence hits the detector. As these signals only occur when the pump is on, they will be present in the $\Delta T/T$-signal as a background independent of the pump-probe delay. Therefore, the background, which is defined

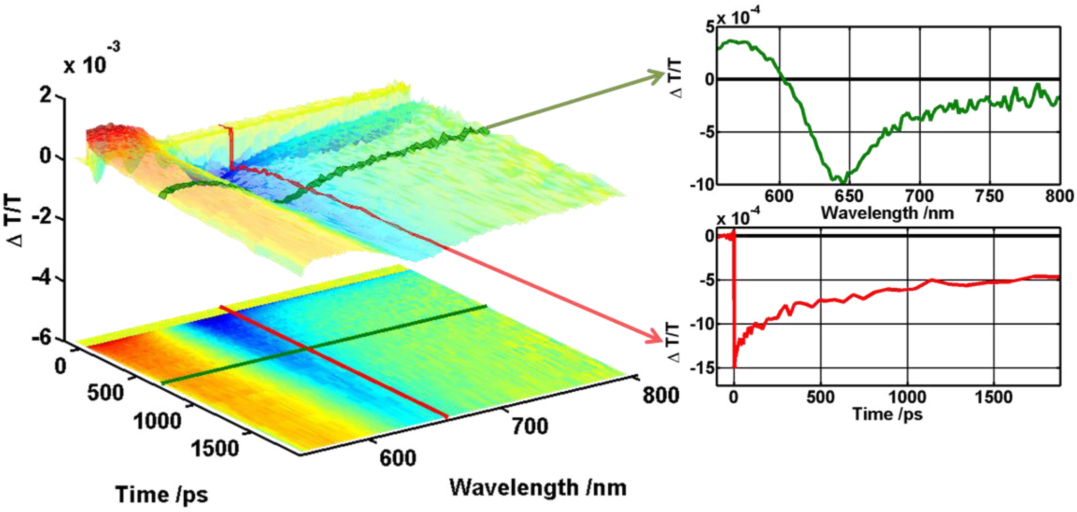

Figure 29: Typical result of a transient absorption experiment. The two dimensional matrix contains the $\boldsymbol{\Delta T/T}$ values for each time and wavelength. Slices parallel to the respective dimension result in spectra at the respective times (top right graph, green) or in kinetics at the respective wavelengths (lower right graph, red).

as any spectral feature that is visible before zero time, can be subtracted. The second correction is due to chirp of the white-light, which is visible in the earliest spectra after zero time. Chirped white-light means that not all wavelengths arrive at the sample at the same time. Chirp can arise when the white-light travels through media that have a wavelength dependent dispersion. The chirp correction is essentially a zero time correction for each wavelength's kinetic. One way to correct for the chirp is to look at a signal that is instantaneously present when pump and probe arrive on the sample at the same time. The initial rise of the signal that corresponds to the zero time will depend on the wavelength and can be fitted with a polynomial to obtain a wavelength dependent zero time correction, see Figure 30. Additionally it might be necessary to shift the whole data with respect to time, to assure that zero time corresponds to the signal emergence, i.e. when pump and probe reach the sample simultaneously.

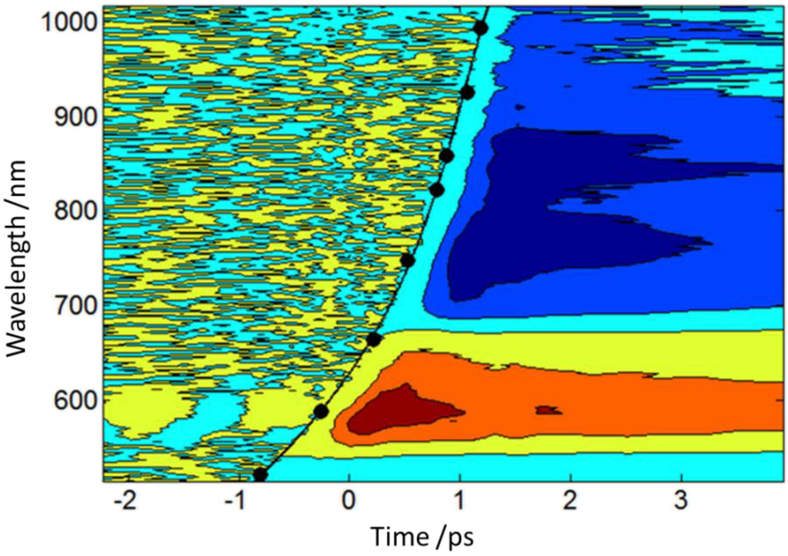

Figure 30: Chirp correction by fitting the initial rise of a signal. The color refers to the signal (red positive, blue negative), the chirp function is shown as a black line. Each wavelength is then corrected for a zero time corresponding to the fitted chirp function, which is a polynomial.

4

Results & Discussion

The experimental results obtained with the techniques introduced in chapter three are presented and discussed in the context of the recent literature. Most of the results were submitted to or published in peer-reviewed journals at the time this thesis was written and are thus presented as manuscripts including the supporting information.[1] Further supplementary results are presented as additional subsections. A complete list of scientific contributions can be found on page 229.

4.1 Two Channels for Charge Generation in Perylene Monoimide Solid-state Dye-Sensitized Solar Cells

The following manuscript was submitted to the Journal of the American Chemical Society and rejected after revision. A revised version was submitted to Energy & Environmental Science and the revision was still in progress at the time this thesis was printed.

---

[1] In accordance with the MPGC examination regulations §11.1.

Two Channels of Charge Generation in Perylene Monoimide Solid-State Dye-Sensitized Solar Cells

Michael Meister[§&], Ian A. Howard[*§&], Björn Baumeier[+], Henrike Wonneberger[$], Neil Pschirer[$], Rüdiger Sens[$], Ingmar Bruder[$], Chen Li[€], Klaus Müllen[€], Denis Andrienko[+] and Frédéric Laquai[*,§]

[&]These authors contributed equally to this work.

[§]Max Planck Research Group for Organic Optoelectronics, [€]Synthetic Chemistry Group, [+]Polymer Theory Group, Max Planck Institute for Polymer Research, Ackermannweg 10, D-55128 Mainz, Germany

[$]BASF SE, GVE/E - J542, 67056 Ludwigshafen, Germany

KEYWORDS Dye-Sensitized Solar Cell, Solid-State Hole Transporter, Charge Generation.

ABSTRACT: The mechanism of charge generation in solid-state dye-sensitized solar cells using triarylamine-substituted perylene monoimide dyes is studied by quasi steady-state and Vis-NIR broadband pump-probe transient absorption spectroscopy. The experiments demonstrate that photoinduced electron injection into the TiO2 can only occur when Li^+, from the commonly used Li-TFSI additive salt, is present on the TiO2 surface. Incomplete surface coverage by Li^+ means that some dye excitons cannot inject their electron into the TiO2. However, herein we directly observe that these dye excitons can create free charges by a second pathway: namely the reduction of the photoexcited state (reductive quenching) by the solid-state hole transporter spiro-MeOTAD followed by the now energetically favorable electron injection into the TiO2 from the resultant dye anion. The second pathway for charge generation is significant, it enhances the quantum efficiency of charge generation from 68 % to over 80 %. For NIR absorbing dyes in which the driving force for electron injection from the exciton is further reduced, this second pathway could be exploited to maintain high quantum efficiency and achieve overall enhancements in device performance.

1 Introduction

Dye-sensitized solar cells (DSCs) are promising photovoltaic devices for solar energy conversion in the current quest for sustainable sources of electrical energy. Since their invention in 1991,[1] the power conversion efficiency of liquid-electrolyte based solar cells has increased steadily mainly due to design of dye molecules and redox partners with current record efficiencies now up to 12.3 %.[2] Although the record solar cells use a less corrosive cobalt-based liquid electrolyte instead of the common iodide-iodine redox couple, the use of a liquid electrolyte to achieve hole transport limits their employment in large-scale industrial production. Many research groups currently try to replace the liquid electrolyte by a solid-state hole transporter, however, efficiencies still lag behind the liquid-electrolyte analogues for reasons not yet entirely understood. Several approaches have been pursued including inorganic,[3] polymer-based[4] and organic small molecule hole transport materials. Efficiencies as high as 7.2 % have been reported for the latter,[5] employing 2,2′,7,7′-tetrakis(N,N-di-p-methoxyphenylamine)-9,9′-spirobifluorene (spiro-MeOTAD)[6] as the solid-state hole transport material. The mesoporous TiO2 layer must be thinner in solid-state DSCs (i.e. only a few μm thick) than in liquid-electrolyte cells[7] and thus it is very important to use dyes with strong absorption and high surface coverage leading to maximized harvesting of the incident solar light. In this respect organic dyes are excellent candidates[5] due to their high molar extinction coefficients. In particular perylene monoimides, which have excellent photo and thermal stability and are often used as color pigments,[8] have attracted significant attention as sensitizers in dye-sensitized solar cells, as electron transporters in bulk heterojunction solar cells,[9] and also as high mobility charge transport materials in organic field-effect transistors.[10] High efficiencies in solid-state DSCs have already been achieved by using perylene imide derivatives of a donor-spacer-acceptor type structure.[11] However, there are currently only very few studies addressing the mechanism of charge generation in solid-state organic (metal-free) dye-sensitized solar cells in general and in perylene-based dye-sensitized cells in particular.[12-14] We note that recent results achieved using inorganic perovskite coatings as a sensitizer/hole-transport material have achieved very impressive power conversion efficiencies exceeding 10 %.[3,15,16]

The cascade of processes leading to charge generation after absorption of a photon by the dye is often described as i.) electron injection from the excited state of the dye into the TiO2 conduction band followed by ii.) regenera-

$$\text{(I)}\ \mathrm{S + D^* + TiO_2 \rightarrow S \ + D^+ + TiO_2^- \ \rightarrow S^+ + D + TiO_2^-}$$

$$\text{(II)}\ \mathrm{S + D^* + TiO_2 \rightarrow S^+ + D^- + TiO_2 \ \ \rightarrow S^+ + D + TiO_2^-}$$

Figure 1. Two possible types of charge generation in solid-state dye-sensitized solar cells. S is the spiro hole transport material, D is the dye, TiO2 is the titania, +/- indicates cation/anion and * indicates exciton. In type I, the electron is injected from the excited dye to the TiO2 which is then regenerated by the hole transporter (I). In type II charge generation, the electron is first transferred from the hole transporter to the excited dye and subsequently injected into the TiO2 (II).

tion of the dye cation remaining after electron injection by the hole transport material or liquid electrolyte,[17] which hereafter we address as type I charge generation (see Figure 1). In fact, in liquid electrolyte cells this type I pathway for charge generation is the only one possible, because the regeneration of the dye cation is diffusion-limited and hence occurs typically on a timescale of nano- to microseconds, i.e. much slower than electron injection, which can lead to a photocurrent loss, if the recombination of electron and dye cation is on a similar timescale.[17] In solid-state dye-sensitized cells type I charge generation is not necessarily the only mechanism for charge separation. In fact, a second mechanism named reductive quenching has already been proposed.[13] In solid-state cells, the hole transporter is in close proximity to the dye and thus electron transfer from the hole transporter to the photoexcited state of the dye (equivalently described as hole injection from the photoexcited dye into the hole transport material) could take place on the timescale of a few picoseconds.[12] In this case, a second pathway of free charge generation is opened, which is reduction of the excited state of the dye by the hole-transporter followed by electron injection from what is now a dye anion into the titania nanoparticles. We note that the injection of the electron from the dye anion can be significantly more energetically favorable than injection of the electron from the dye exciton. Hereafter, we call this mechanism type II charge generation (see Figure 1). We hypothesize that if type I charge generation is impeded, type II charge generation could take over and help deliver a higher overall quantum efficiency for charge generation. After being hypothesized by Snaith et al.[13] type II charge generation has been discussed in relationship to perylene imide dyes.[14] However, to the best of our knowledge, direct experimental evidence demonstrating that type II charge generation occurs in solid-state dye-sensitized solar cells has not been presented yet. This direct evidence for type II charge generation is presented herein, where we show that it plays an important role in determining the quantum efficiency of charge generation in this dye system where electron injection from the dye exciton into the TiO2 is borderline. In fact, *our key finding is that for the dye used in this study the electron injection from a dye exciton requires the presence of nearby surface-localized Li^+ cations from the often used additive Bis(trifluoromethane)sulfonimide lithium salt (Li-TFSI). When these cations are not in the direct vicinity of a dye exciton it cannot participate in type I charge generation, but it can still participate in type II charge generation meaning that a significant fraction of the non-Li^+-affected excitons also eventually lead to free charges allowing the cell a good overall quantum efficiency*.

2 Results and Discussion

2.1 Device performance

Figure 2 shows the chemical structures of the perylene imide derivative used as sensitizer and the solid-state hole transport material spiro-MeOTAD along with typical J-V characteristics of devices. We could achieve power conversion efficiencies as high as 4 % with this particular material system. The maximum photon to electron conversion efficiency (internal quantum efficiency, IQE) of this dye was found to be about 67%. In this system, as in many others, the additive Li-TFSI plays an important role for the device efficiency, since it influences not only the charge transport properties of the hole transport material,[18] but also, as we will see in the following section, the injection efficiency of electron transfer from the dye into the TiO2.

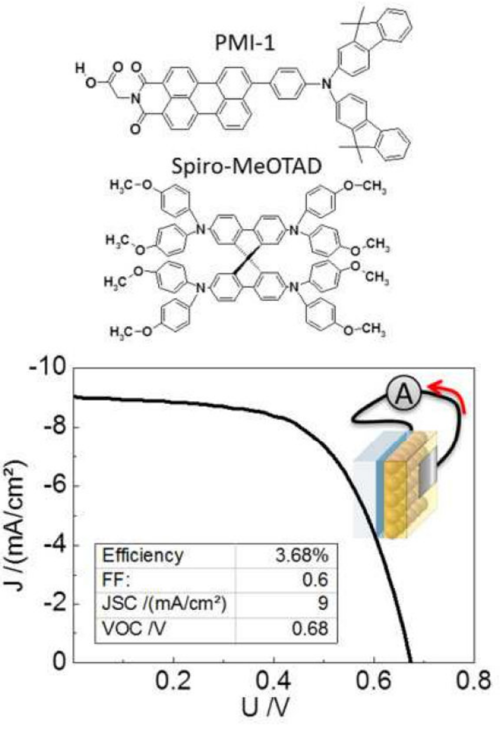

Figure 2. Chemical structures of the perylene monoimide sensitizer PMI-1 (top) and of the hole transport material spiro-MeOTAD (middle). Typical J-V-characteristics of a dye-sensitized solar cell are depicted in the bottom graph. The inset shows a schematic of a solid-state DSC comprised of a glass substrate, a transparent conductive layer (FTO), a dyed mesoporous TiO2 layer incorporated with the solid hole transporter and a silver counter electrode.

2.2 Optical spectroscopy

2.2.1 Samples

In order to understand the role of type I and type II charge generation we used steady-state, quasi-steady state, and time-resolved optical spectroscopy to investigate a sequence of three samples consisting of: 1) dye attached to titania, 2) dye attached to titania in presence of Li-TFSI, and 3) a 'full' solar cell structure with the hole transporting material and Li-TFSI but omitting the metal electrode.

2.2.2 Quasi-Steady-State Photoinduced Absorption

Quasi steady-state photoinduced absorption (PIA) records the change of absorption of a sample due to long-lived photoinduced excited states, such as charges created in dye-sensitized solar cells.[19] Figure 3 depicts the steady-state PIA spectra of the three samples. In sample 1, the surface bound dye without the Li-TFSI additive, no photoinduced signal was observed indicating that no long-lived charges are created in this sample. In contrast, sample 2 which is identical to sample 1 except that the Li-TFSI is added, showed a strong induced absorption due to long-lived charges. The charge-induced absorption spectrum shows a positive signal in the higher energy region of the spectrum with a zero crossing at 760 nm (1.63 eV), which can be assigned to the ground state bleaching of those dye molecules that had successfully injected electrons into the TiO2 plus a Stark effect due to the influence of the fields of the photoinduced charges on the ground state absorption of the nearby dye molecules. A strong photo-induced absorption was observed in the near IR region peaking around 900 nm (1.38 eV), which extended further into the IR. This feature is very similar to that of the chemically oxidized dye (shown for comparison as the dashed gray line) supporting our assignment of this photo-induced spectrum to the creation of dye cations.

From the comparison of sample 1 and sample 2 by PIA we reach our first key conclusion: in this dye system, Li-TFSI must be present for electron injection from a dye exciton into the titania to occur.

In sample 3, when the hole transport material spiro-MeOTAD is also present, the induced absorption of the long-lived charges changes from that in sample 2. This is because the dye cation is reduced by hole transfer to the hole transport material in sample 3, so the long-lived states are the oxidized hole transport material and an electron in titania rather than the dye cation and electron in titania present in sample 2. Looking at the spectrum of sample 3 it is clear that the dye cation photoinduced absorption feature at 900 nm vanishes entirely, while a different photoinduced absorption feature peaking in the NIR region around 1550 nm (0.8 eV) emerges. This new absorption band can be assigned to the cation of the hole transport material spiro-MeOTAD by comparison with previously published results.[20-22] As the PIA of the dye cations was found to be entirely absent in the presence of spiro-MeOTAD, it appears that the pore filling was sufficient to regenerate virtually all oxidized dye molecules.

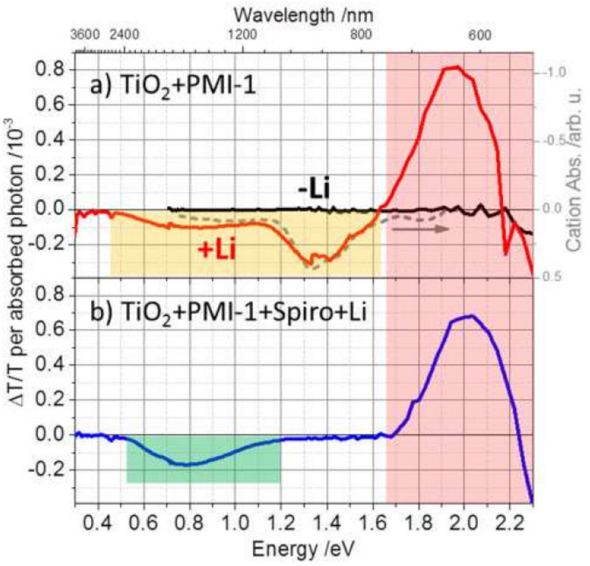

Figure 3. Quasi steady-state photoinduced absorption spectra of a) sample 1 (black line) and sample 2 (red line) along with the absorption spectrum of the chemically oxidized dye (dye cation) shown as a dashed gray line. Panel b) depicts the PIA spectrum of the device-like structure including the hole transporter spiro-MeOTAD and the additive Li-TFSI. Highlighted in red is the bleaching/Stark effect region, in yellow the dye cation absorption and in green the absorption of the spiro cation.

Since the regeneration of the dye cations restores the ground state of the dye molecules, a ground state bleaching caused by dyes in an excited state no longer exists, however the Stark effect on ground state dyes of the photoinduced field leads to a very strong positive signal in the short wavelength region (1.7 to 2.2 eV).[23]

This Stark effect has recently been examined in detail by us and others, in order to provide insight into the motion of charges near the interface.[23-25] In order to investigate the role of type I and type II mechanisms in the generation of the free charges in sample 3 we must turn to time-resolved spectroscopy, however *the PIA of sample 3 reveals a 2nd key conclusion, namely that pore-filling is good enough to allow complete dye regeneration, as no feature of the dye cation remains in the photoinduced absorption of sample 3.*

2.2.3 Steady-State Spectroscopy

The steady-state absorption spectra of sample 1,2 and 3 are presented in Figure 4a. The addition of Li-TFSI in sample 2 causes a change in the ground state absorption spectrum relative to that in sample 1. The absorption is broadened and red-shifted. Similarly in sample 3 a clear broadening and a red shoulder are observed. The effect of Li-TFSI on the absorption spectra can be explained by the Stark effect of Li^+ ions adsorbed to the titania surface.

Considering the Stark effect, i.e. the influence of an electric field on the ground state absorption, we note the following:[23] a zeroth order approximation would be that an electric field antiparallel to the change of the electric dipole moment $\Delta\mu$ of the dye shifts the absorption peaks to higher energies, whereas a field parallel to the change of the dipole moment causes shifts to lower energies. This would suggest that there is a parallel field present, at least in sample 2, and as shown in Figure 4 the field created by a surface adsorbed Li^+ ion is indeed parallel. The precise effect of field on absorption, taking into account both peak shifts and changes in oscillator strength (which are both found to be important) can be calculated by time-dependent density functional theory (TDDFT). Figure 4b shows the absorption spectrum as calculated for PMI-1 in the gas phase with and without a parallel applied electric field. Qualitatively the calculated Stark effect matches very well with the observed absorption changes, leading us to our 3rd key conclusion: *that the broad red shoulder observed in the absorption spectrum of sample 2 and 3 indicate that surface adsorbed Li^+ ions are present in both of these samples, and that these surface bound Li^+ ions create fields that lower the barrier for charge injection.*

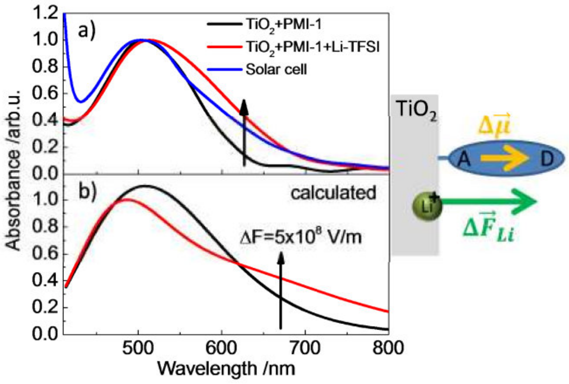

Figure 4. a) Absorption spectra of PMI-1 dyes attached to TiO2 in the absence and presence of Li^+-ions. Note the emergence of a shoulder in the absorption spectrum upon addition of Li-TFSI. b) Field-dependent absorption spectra of PMI-1 calculated by TDDFT. A positive change in electric field ($\boldsymbol{\Delta\vec{F}}$) corresponds to a field change pointing away from the TiO2 surface. Note that for a less negative field, i.e. a more positively charged TiO2, a shoulder at the red edge of the spectrum occurs. c) Comparison of the normalized absorption spectra of PMI-1 on titania in the absence of Li-TFSI, in the presence of Li-TFSI and in the device-like structure including spiro-MeOTAD and Li-TFSI. The sketch on the right side depicts schematically the positive change in electric field $\boldsymbol{\Delta\vec{F}}$ due to the Li^+-ions and the direction of the change in dipole moment from the ground to the excited state $\boldsymbol{\Delta\vec{\mu}}$.

2.2.4 Transient Absorption Spectra

Figure 5 compares the time-resolved absorption spectra of three samples in the time range from 1 ps to 3 ns. The transient pump-probe spectra of the 1st sample (dye on titania, upper panel) exhibit a positive signal in the short wavelength spectral region, which we assign to ground state bleaching. It then has a zero crossing at 600 nm followed by a broad photoinduced absorption at longer wavelength extending into the near-infrared spectral region. All features decayed within the observed time range of 3 ns without drastic change in spectral shape indicating that long-lived charges were not created in this sample in good agreement with the PIA results presented above. We stress that neither a negative PIA peak around 900 nm nor a Stark contribution in the visible is observed, meaning that no dye cations are created, so the transient signal recorded measures the return of dye excitons to the ground state under the influence of the titania surface environment. Consistent with our interpretation of the PIA, *no charges are created in sample 1 (which contains no Li-TFSI).*

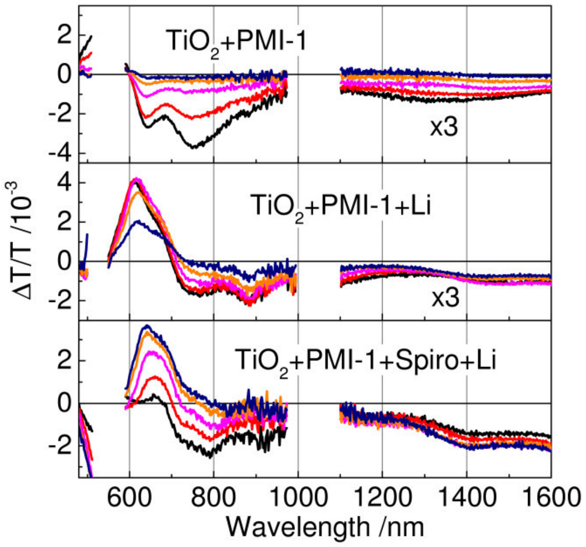

Figure 5. Transient absorption spectra (averaged over time) of PMI-1 adsorbed on TiO2 (sample 1, upper panel), with Li-TFSI (sample 2, middle panel) and in the device-like structure with Li-TFSI and spiro-MeOTAD (sample 3, bottom panel). Colors refer to mean delay times as follows: black: 1.25ps; red: 3.8ps; magenta: 34ps; orange: 335ps; violet: 3125ps.

In sample 2 (middle panel) the measured signal is substantially different. Firstly there is clear evidence that charges are created. The spectrum by 3 ns resembles strongly that of charges observed in the quasi-steady-state PIA spectroscopy. For a direct comparison of the PIA spectrum and 3 ns time-resolved spectrum of sample 2 please see the supporting online information. Also in the supporting information we measure the decay of this cation signal on the ns to ms timescale and find that its decay is consistent with carrier recombination kinetics. From this information it is clear that the excited states remaining in sample 2 after 3 ns are exclusively dye cations and electrons in titania, but the spectral evolution before 3 ns indicates that other species are present at earlier times. The pronounced peak at 770 nm at early times can be seen to be a feature of exciton induced absorption from comparison with sample 1. In sample 2 this peak is present in the short-delay spectra but disappears gradually from the longer-delay spectra. This indicates that some fraction of the population created after the instrument response of our spectrometer is in the exciton population pool and that this population fraction decays similarly to how it decays in sample 1. *So a 4^{th} key conclusion is that not all dye excitons can promptly inject an electron into the titania in sample 2.* In the further analysis we will find that these data from sample 2 are best described by two populations being present after the instrument response, one population of dye cations that are relatively long-lived (these are created by excitons which inject their electron into the titania within the instrument response of the system), and one population of excitons that then decay exactly as they did in sample 1 indicating that they are completely uninfluenced by Li-TFSI most likely because there is not any in their vicinity.

The TA spectra of sample 3 at early times in the visible wavelength region are quite similar to those of sample 2. Both spectra show Stark effect-induced features which dominate the visible wavelength region up to 750 nm. However there are also two important differences. Firstly, the negative feature observed at 900 nm in the spectra for sample 2 which can be ascribed to the dye cation are absent in the spectra of sample 3 after 2 ps. Also, the PIA of the oxidized spiro at 1550 nm quickly grows in then remains almost constant. This again confirms our quasi-steady state PIA conclusion that *pore-filling is sufficient for dye reduction, we see no fraction of dye cations that are not quickly reduced by hole transfer to nearby hole transport material.* Also in sample 3, the features of the exciton population, most clearly visible at the 770 nm photoinduced absorption peak no longer decay as they do in sample 1, but rather they disappear much more quickly. This indicates that the exciton population in sample 3 is quenched by a process not present in sample 1 or 2. *So in sample 3 the dye excitons that could not inject charges into the titania in sample 2 exhibit a shortened lifetime in sample 3 indicating that they can create charges by the now available type II mechanism.*

2.2.5 Introduction to Modeling of Transient Kinetics

In the preceding sections we have, amongst others, made the key conclusions that:

1. In sample 2 only some fraction, let us say *f*, of dye excitons can promptly inject an electron into the titania. The remaining 1-*f* excitons decay as they did in sample 1.
2. In sample 3 the remaining 1-*f* excitons no longer decayed as they did in sample 1, but rather where quenched through type II charge generation.

In the coming section we will consider the transient absorption data of sample 1 and sample 2 to estimate *f*, the fraction of dye excitons that participate in type I charge generation. We will then use a simple photophysical model to fit the transient absorption data of sample 3 from which we can extract how much the overall quantum efficiency of the device is increased by type II charge generation in the (1-*f*) dye excitons which cannot participate in type I charge generation.

2.2.6 Transient Kinetics: Sample 1 and 2 (determination of *f*)

The transient absorption kinetics of sample 1 are depicted in Figure 6a. We show three wavelength regions chosen to be useful for the comparison of sample 1, 2 and 3. Although in sample 1 excitons are the only species present, the wavelength regions chosen are selected so that when a mixture of excited state species is present good contrast between the species is achieved. In the 800-810 nm region dye excitons have the dominant cross-section, between 850-950 nm the dye cations have the dominant cross-section, and between 1400-1600 nm the spiro cations have the dominant cross-section.

In sample 1 the decay kinetics in these three wavelength regions are all due to the decay of dye excitons to the ground state. As already observed in the spectra the signals decayed to zero within the measured time range, indicating that no long lived charges were created. However, the kinetics of the wavelength regions identified are slightly different. We have measured the transient absorption decay of this dye in solution with a sequence of solvent of differing polarity (see SI). The decay time of the exciton and its absorption spectra was affected by the solvent polarity, indicating that the dielectric environment has an influence on the photoinduced spectrum of the dye exciton and its relaxation kinetics. This is not surprising, as the dye exhibits a strong donor-acceptor character and thus has high electric dipole moments. Based on this knowledge we interpret the transient absorption data of sample 1 in the following way. Due to the distribution of surface binding angles (i.e. how much the

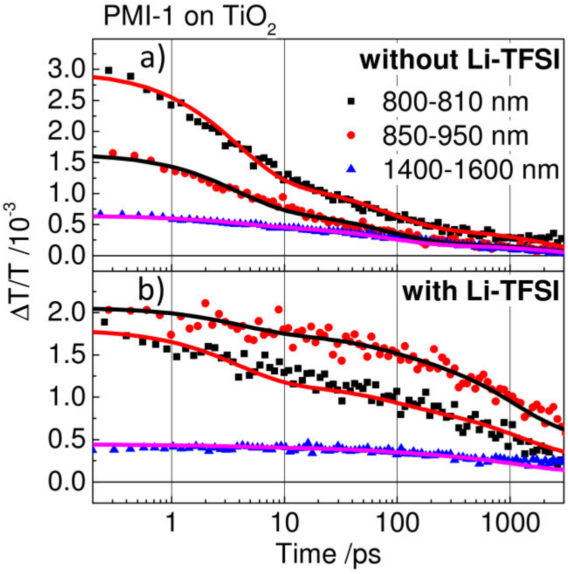

Figure 6. Transient absorption kinetics monitored at 805 nm (black squares), 900 nm (red circles) and 1500 nm (blue triangles), where the dye cation and dye excitons absorb, without (upper panel) and with Li-TFSI (lower panel) along with the fits (solid lines) according to the model explained in the text.

dye stands or lies on the surface) and the disorder of the titania surface[26] there are a variety of effective local dielectric environments that the dye excitons experience in sample 1. This inhomogeneously broadened distribution of dye excitons causes the measured decay to be non-exponential and also vary with wavelength.

Due to this inhomogeneous broadening, it is difficult to reconstruct exactly the population kinetics of exciton decay in sample 1 (at least without explicit knowledge of the distribution of cross-sections which is difficult to obtain).

However, without an explicit knowledge of the population kinetics in sample 1 we can still get an estimate for *f*. We can parameterize the signal from sample 1 somehow, let us call this parameterization $\Delta T/T^{P}_{s1}$, in order to express how a randomly distributed exciton population decays. We can then express the decay of sample 2 as shown in equation 1, where we assume that a fraction of the initial population *f* injects charges (due to the influence of Li-TFSI as already established) leading to a transient absorption signal $\Delta T/T_{charges}$, while the remaining *(1-f)* part of the population leads to the exciton decay signal that we have already parameterized.

$$\Delta T/T_{s2} = f\,\Delta T/T_{charges} + (1-f)\,\Delta T/T^{P}_{s1}\ . \qquad (1)$$

To parameterize the signal observed in sample 1 we fit the kinetic at each wavelength range to the sum of three exponentials ($\sum_{i=1}^{3} A_i^{\lambda} \exp(-k_i t)$). As shown in Figure 6 this provides an accurate representation of the signal.

We now must come up with a model for the contribution of the charge-generating fraction of the population. Due to the presence of the typical dye cation feature from the earliest times, we assume that the dyes that are affected by Li-TFSI inject faster than the response time of our spectrometer (>500 fs). Therefore we initially observe $f N_0$ dye cations $D^{+}_{+Li}(t)$. As already mentioned, we observe some recombination of dye cations with electrons in the TiO2 on the timescale of our experiment; this is seen in a decrease of the blue line between 100 and 1000 ps in Figure 6b. However, after longer times (1000 ps and longer), the signal levels off and the dye cations recombine on a much longer timescale (see SI). To account for this, we split the dye cations in two pools: one is prone to fast recombination (fraction s) with the rate $k_{D^+\to D}$ and the other (fraction $1-s$) does not recombine on the observed timescale. Considering the inhomogeneous broadening observed in the exciton population, we feel that this approximation of different lifetime scales for recombination is reasonable. Under these assumptions the transient absorption of the charges can be written as:

$$\Delta T/T_{charges,\ \lambda} = \mathrm{N}_0 d\, f \sigma_{\lambda,D^+}[s\ \exp(-k_{D^+\to D}\, t) + (1-s)]\ . \qquad (2)$$

Substituting equation 2 into equation 1 we can fit the transient absorption kinetics recorded for sample 2 with the free parameters *f*, *s*, $k_{D^+\to D}$, and also a dye cation cross section σ_{λ,D^+} for each wavelength region. $N_0 d$ is the number of absorbed photons per area (excitation density times thickness of the sample), determined by the pump fluence and the absorbance of the sample at the excitation wavelength. The result of the fit is shown in Figure 6b and the extracted parameters are summarized in Table 1. *The modeling of the transient absorption of sample 1 and sample 2 reveals a fraction f = 68 % of dye excitons that undergo type I charge generation. This means that 32% of dye excitons cannot generate charges by a type I mechanism in this dye system.* We also found that roughly 60 % of the charges created by the type I mechanism in sample 2 are susceptible to fast recombination, but we will see that when the hole transporter is added in sample 3 this quick recombination is suppressed so it does not affect device efficiency.

Table 1. Parameters obtained from analysis of the transient absorption of sample 1 and 2 described in the text.

Parameter	805 nm	900 nm	1500 nm
$N_0 d$ $/(10^{13} cm^{-2})$	$3.16 \pm .33$		$2.95 \pm .46$
${k_{D^+\to D}}^{-1}/ps$	1011 ± 117		
f	$0.68 \pm .02$		
s	$0.62 \pm .02$		
σ_{D^+} $/(10^{-17} cm^2)$	$3.49 \pm .06$	$6.87 \pm .11$	1.57 ± 0.04

The error of $N_0 d$ *was determined by Gaussian error propagation from the error prone results of fluence and absorbance. All other errors were determined from the fitting.*

2.2.7 Transient Kinetics: Sample 3 (quantum efficiency enhancement due to type II charge generation)

The device-like sample 3 now includes the hole transport material. This means that the dye cations created by ultrafast type I charge generation can now be reduced by transferring their holes to the hole transport material. Also it raises the possibility that the *(1-f)* remaining excitons are quenched by type II charge generation. The transient absorption kinetics of sample 3 are shown in Figure 7. The 1400-1600 nm kinetics show a very clear increase on the timescale from 2-20 ps indicating an increase in the population of holes on the hole transport material. This is strongly correlated with a decrease in the dye exciton photoinduced absorption (800-810 nm signal). *This correlated increase of the spiro cation absorption and decrease of the exciton photoinduced absorption, plus the fact that the dye cation regeneration has already taken place on the sub 2 ps timescale (see supporting information) indicates that type II charge generation occurs in the population of (1-f) excitons that do not undergo type I charge generation.*

In order to quantify the role of type II charge generation in the overall efficiency of charge generation we develop a simple population model to describe the population flows after 2 ps in sample 3. This model is summarized in Figure 7a. First, we assume that we can express the excitons with a single spectrum and decay rate to the ground state.

Although we know this is only approximately valid from the transient absorption data for sample 1, it is sufficient to obtain the rough estimate of the effect of type II charge generation that we wish. We then assume that the (*1-f*) excitons that do not undergo type I charge generation can be separated into two pools, those that can undergo type II charge generation (χ_{II}), and those $1-\chi_{II}$ that cannot (perhaps having an unfavorable orientation relative to the hole transport material for hole transfer). The component of excitons that cannot undergo type II generation is necessary to fit the decay in the visible spectra on the timescale of roughly 100 ps. The rate of hole transfer from the exciton to the hole transport material eventually creating free charges is given by $k_{D^*\to C}$, and the rate of exciton decay by k_{dec}. The transient absorption kinetics can then be simulated by:

$$\frac{\Delta T}{T}(t,\lambda) = N_0 d\,\Big\{\sigma_{\lambda,D^*}(1-f)\exp(-k_{dec}t)\,[(1-\chi_{II}) + \chi_{II}\exp(-k_{D^*\to C}\,t)] + \sigma_{\lambda,C}\Big[f + \frac{\chi_{II}(1-f)k_{D^*\to C}}{k_{dec}+k_{D^*\to C}}(1-\exp(-(k_{dec}+k_{D^*\to C})t))\Big]\Big\} \tag{3}$$

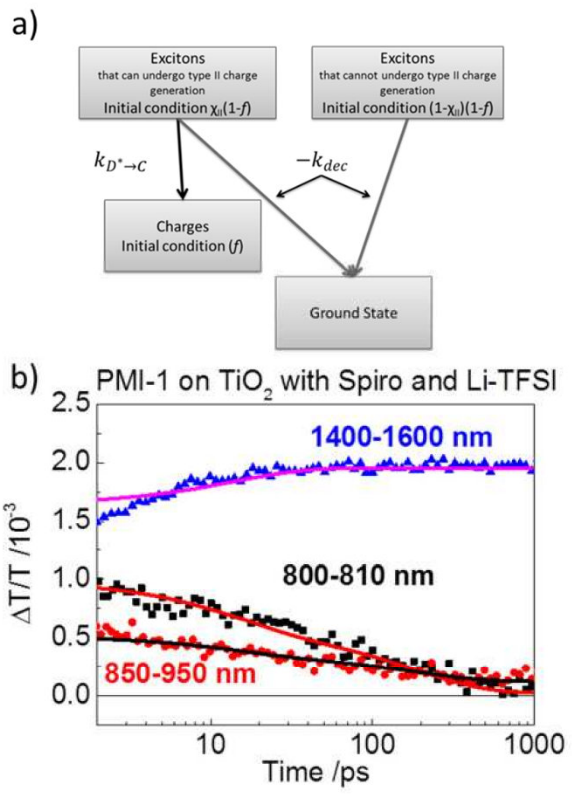

Figure 7. a) Model used to describe the data. b) Transient absorption kinetics of a solar cell probed in three distinct wavelength regions around 805 nm, 900 nm and 1500 nm, where the dye excitons, cations and the cation of the hole transporter dominate the photoinduced absorption, respectively. Along with the experimental data a fit to the model in a) and as described in the text is shown that was used to determine the possibility of preceding hole transfer (type II charge generation).

Where σ_{λ,D^*} and $\sigma_{\lambda,C}$ are the cross sections of the excitons and the charges (hole on hole transporter) in the wavelength region λ. f was fixed to 0.68, the value from the previous section. The free parameters were k_{dec}, $k_{D^*\to C}$ and χ_{II}, shared between all wavelength regions, and σ_{λ,D^*} and $\sigma_{\lambda,C}$, which were free for each wavelength region.

The fit is shown in Figure 7b and it is clear that the model can qualitatively describe the features of the data adequately. The parameters extracted from the fits are shown in Table 2.

The observation of the infrared transient absorption was critical in revealing the dynamics of type II charge generation, and highlights the utility of broadband spectroscopy for directly revealing population kinetics.

Table 2. Parameters obtained from fitting the transient absorption dynamics of the device-like sample 3 according to the model described in the text.

Parameter	805 nm	900 nm	1500 nm
$N_0 d$ $/(10^{13} cm^{-2})$	$1.78 \pm .20$		$1.88 \pm .26$
${k_{dec}}^{-1}/ps$	187 ± 20		
${k_{D^*\to C}}^{-1}/ps$	15 ± 3		
χ_{II}	$0.44 \pm .03$		
σ_{λ,D^*} $/(10^{-17} cm^2)$	$17.2 \pm .55$	$7.34 \pm .36$	$0^{+.89}_{-0}$
$\sigma_{\lambda,C}$ $/(10^{-17} cm^2)$	$0.16 \pm .06$	0.83 ± 0.06	12.8 ± 0.25
η	$81 \pm 1\,\%$		

The quantum efficiency of charge generation can be calculated as the fraction of excitons which generate charges as $\eta = f + \frac{\chi_{II}(1-f)k_{D^*\to C}}{k_{dec}+k_{D^*\to C}}$, where the second half of the expression gives the increase in efficiency due to the type II charge generation. Using the parameters obtained from the fit $\eta = 0.81$, with type II charge generation responsible for around 13% of the total charge generation. We note that this fit can also be performed with f as a free parameter (shared between the wavelengths). This fit is shown in the SI, and the extracted value for f is 0.53, $\eta = 0.71$, with then type II charge generation making a 20% contribution to the overall charge generation efficiency. *So, we conclude that although this modeling is not highly precise, it is certainly sufficient to demonstrate that the overall charge generation efficiency is high, in the region of 0.6-0.9, and that type II charge generation makes a not insignificant contribution, being on the order of 10-30% of the total charge generation.*

2.2.8 Kinetics of Spiro:Dye Blend (verification of type II charge generation)

In the previous section we asserted that type II charge generation (the transfer of a hole from the dye exciton on a surface-bound dye to the hole-transporting spiro) clearly occurred in sample 3, the solar cell structure. If this is

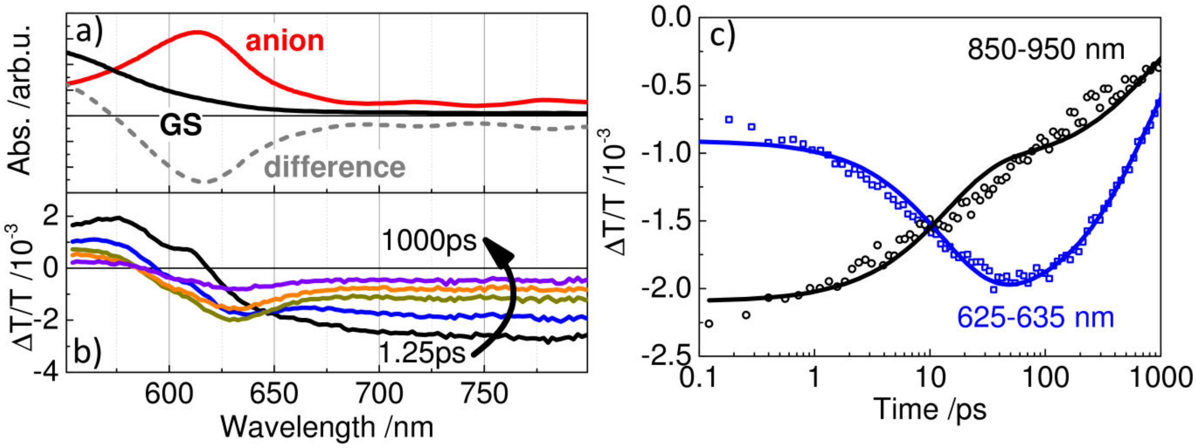

Figure 8. a) Absorption spectra of the ground state (GS, black) and chemically reduced dye (anion, red). The difference spectrum of ground state and anion (dashed grey line) reflects the expected anion-induced absorption signal in the transient absorption spectra. b) Transient absorption spectra of Spiro-MeOTAD:PMI-1 blend; colors refer to times as: black: 1.25 ps; blue: 11 ps; green: 103 ps; orange: 310 ps; purple: 934 ps. Note that after 11 ps the spectrum is very similar to the difference spectrum of ground state and cation-induced absorption (dashed grey line) in the upper panel. c) Transient absorption dynamics for two distinct wavelength regions, in which the absorption of the anion is very prominent (625-635nm) and in which the exciton absorption dominates the spectrum (900-1000nm) along with fits to the charge transfer and recombination model explained in the text. The extracted inverse rate for the charge transfer from dye excited state to spiro was $(\mathbf{14 \pm 1})$ ps and the inverse recombination rate turned out to be $(\mathbf{787 \pm 22})$ ps.

the case, then type II charge generation should also occur in a solid-state blend film prepared by spin-casting the dye co-dissolved with the hole-transporting material.[14] In Figure 8 we present transient absorption data for such a blend film alongside the spectrum of the dye chemically reduced by Lupasol™ treatment. The dye anion absorption peak at around 620 nm is very clear in the transient absorption data, indicating that photoinduced hole transfer indeed causes the creation of a dye anion in this spiro:dye blend.

In order to estimate the rate of type II charge-generation in the blend the data were fit to a two pool (excitons and charge-transfer states) model. The rate of quenching can be seen to be an order of magnitude greater than the dye exciton lifetime in solution, so with the approximation that $k_{Ex\to CT} \gg k_{Ex\to GS}$ the exciton population can be written as $Ex(t) = \exp(-(k_{Ex\to CT})\, t)$ and the charge-transfer state population as $CT(t) = \frac{k_{Ex\to CT}(\exp(-k_{CT\to GS}t)-\exp(-k_{Ex\to GS}\, t))}{k_{Ex\to CT}-k_{CT\to GS}}$.

Here, $k_{Ex\to CT}$ is the rate of hole transfer from the excited dye to the hole transporter spiro-MeOTAD, $k_{CT\to GS}$ is the recombination rate of the charge transfer state formed between the dye anion and the spiro cation. Applying this population model to the TA data results in the fits shown as the solid lines. The inverse rates were extracted to be $k_{Ex\to CT}^{-1} = (14 \pm 1)\,\text{ps}$ and $k_{CT\to GS}^{-1} = (787 \pm 22)\,\text{ps}$. Complete details of the fit and the extracted cross-sections are reported in the SI. The inverse rate of type II charge generation we extracted from sample 3 was $(15 \pm 3)\,\text{ps}$, which agrees well with the rate extracted in the blend film. *So examining the blend film gives unequivocal evidence of the formation of dye anions by type II charge generation, and supports our assertion that type II charge generation also occurs in sample 3 given the rate constants agree so well.* We note that we do not see the anion feature in sample 3 because anions created at the interface are quickly oxidized by electron injection into the TiO2 (and overlap with the Stark feature obscures any subtle presence).

3 Conclusions

We have investigated the use of a perylene monoimide dye in a solid-state dye-sensitized solar cell using steady state, quasi-steady-state, and time-resolved spectroscopy.

Quasi-steady state spectroscopy revealed that the presence of Li$^+$ at the interface was necessary for type I charge generation (electron injection from the excited dye into TiO2 and subsequent regeneration by the hole transporter), and further time-resolved measurements quantified that around 50-70% of dye excitons can undergo type I charge injection. Steady state spectroscopy revealed that Li$^+$ indeed does localize to an extent at the interface, and that the effect of this surface adsorbed Li$^+$ is to create a field that encourages electron injection into the titania.

Next, our broadband transient measurements allowed us to ascertain that type II charge generation (transfer of the hole from a dye exciton to the hole transport material followed by electron injection from the resulting dye anion into the titania, also known as reductive quenching) also occurs in the solar cell and is responsible for 10-

30% of the total charge generation. If the efficiency of type I generation is reduced, for example by red-absorbing dyes with lower-lying LUMOs, it is possible that systems relying on the (15 ± 3) ps inverse rate type II generation could still maintain high quantum efficiencies while extending absorption into the NIR.

ASSOCIATED CONTENT

Supporting Information.
Experimental section, further measurements including transient absorption and photoluminescence in solution and delayed (ns-µs) recombination dynamics as well as further details of the fitting procedure is available as supporting information. This material is available free of charge via the Internet at http://pubs.acs.org.

AUTHOR INFORMATION

Corresponding Author

laquai@mpip-mainz.mpg.de
ian.howard@mpip-mainz.mpg.de

Notes

The authors declare no competing financial interests.

Present Addresses

†If an author's address is different than the one given in the affiliation line, this information may be included here.

ACKNOWLEDGMENT

F.L. is very grateful to the Max Planck Society for funding a Max Planck Research Group. M.M. thanks the Max Planck Graduate Center with the University of Mainz (MPGC) for funding. I.A.H acknowledges a fellowship of the Alexander von Humboldt Foundation and a research scholarship of the Max Planck Society. We acknowledge financial support from the International Research Training Group 1404 and the SFB 625. F.L. and M.M. thank A. Petrozza for fruitful discussions.

REFERENCES

(1) O'regan, B.; Gratzel, M. Nature 1991, 353, 737-740.

(2) Yella, A.; Lee, H.-W.; Tsao, H. N.; Yi, C.; Chandiran, A. K.; Nazeeruddin, M. K.; Diau, E. W.-G.; Yeh, C.-Y.; Zakeeruddin, S. M.; Grätzel, M. Science 2011, 334, 629-634.

(3) Chung, I.; Lee, B.; He, J.; Chang, R. P. H.; Kanatzidis, M. G. Nature 2012, 485, 486-489.

(4) Chang, J. A.; Rhee, J. H.; Im, S. H.; Lee, Y. H.; Kim, H.-j.; Seok, S. I.; Nazeeruddin, M. K.; Gratzel, M. Nano Lett. 2010, 10, 2609-2612.

(5) Burschka, J.; Dualeh, A.; Kessler, F.; Baranoff, E.; Cevey-Ha, N.-L.; Yi, C.; Nazeeruddin, M. K.; Grätzel, M. J. Am. Chem. Soc. 2011, 133, 18042-18045.

(6) Bach, U.; Lupo, D.; Comte, P.; Moser, J. E.; Weissortel, F.; Salbeck, J.; Spreitzer, H.; Gratzel, M. Nature 1998, 395, 583-585.

(7) Schmidt-Mende, L.; Zakeeruddin, S. M.; Gratzel, M. Appl. Phys. Lett. 2005, 86, 013504.

(8) Li, C.; Wonneberger, H. Adv. Mater. 2012, 24, 613-636.

(9) Kamm, V.; Battagliarin, G.; Howard, I. A.; Pisula, W.; Mavrinskiy, A.; Li, C.; Mullen, K.; Laquai, F. Adv. Energy Mater. 2011, 1, 297-302.

(10) Huang, C.; Barlow, S.; Marder, S. R. J. Org. Chem. 2011, 76, 2386-2407.

(11) Cappel, U. B.; Karlsson, M. H.; Pschirer, N. G.; Eickemeyer, F.; Schöneboom, J.; Erk, P.; Boschloo, G.; Hagfeldt, A. J. Phys. Chem. C 2009, 113, 14595-14597.

(12) Bach, U.; Tachibana, Y.; Moser, J.-E.; Haque, S. A.; Durrant, J. R.; Gratzel, M.; Klug, D. R. J. Am. Chem. Soc. 1999, 121, 7445-7446.

(13) Snaith, H. J.; Petrozza, A.; Ito, S.; Miura, H.; Grätzel, M. Adv. Funct. Mater. 2009, 19, 1810-1818.

(14) Cappel, U. B.; Smeigh, A. L.; Plogmaker, S.; Johansson, E. M. J.; Rensmo, H. k.; Hammarström, L.; Hagfeldt, A.; Boschloo, G. J. Phys. Chem. C 2011, 115, 4345-4358.

(15) Kim, H.-S.; Lee, C.-R.; Im, J.-H.; Lee, K.-B.; Moehl, T.; Marchioro, A.; Moon, S.-J.; Humphry-Baker, R.; Yum, J.-H.; Moser, J. E.et al. Sci. Rep. 2012, 2.

(16) Lee, M. M.; Teuscher, J.; Miyasaka, T.; Murakami, T. N.; Snaith, H. J. Science 2012.

(17) Hagfeldt, A.; Boschloo, G.; Sun, L.; Kloo, L.; Pettersson, H. Chem. Rev. 2010, 110, 6595-6663.

(18) Snaith, H. J.; Gratzel, M. Appl. Phys. Lett. 2006, 89, 262114.

(19) Boschloo, G.; Hagfeldt, A. Inorg. Chim. Acta 2008, 361, 729-734.

(20) Brown, M. D.; Suteewong, T.; Kumar, R. S. S.; D'Innocenzo, V.; Petrozza, A.; Lee, M.; Wiesner, U.; Snaith, H. J. Nano Lett. 2010, 11, 438-445.

(21) Olson, C.; Veldman, D.; Bakker, K.; Lenzmann, F. Int. J. Photoenergy 2011, 2011, 513089.

(22) Cappel, U. B.; Gibson, E. A.; Hagfeldt, A.; Boschloo, G. J. Phys. Chem. C 2009, 113, 6275-6281.

(23) Cappel, U. B.; Feldt, S. M.; Schöneboom, J.; Hagfeldt, A.; Boschloo, G. J. Am. Chem. Soc. 2010, 132, 9096-9101.

(24) Ardo, S.; Sun, Y.; Staniszewski, A.; Castellano, F. N.; Meyer, G. J. J. Am. Chem. Soc. 2010, 132, 6696-6709.

(25) Meister, M.; Baumeier, B.; Pschirer, N.; Sens, R.; Bruder, I.; Laquai, F.; Andrienko, D.; Howard, I. A. 2012, submitted.

(26) Ardo, S.; Meyer, G. J. Chem. Soc. Rev. 2009, 38, 115-164.

4.1.1 Supporting Information

Experimental

Sample preparation

The solar cells and samples for spectroscopy were prepared in a similar manner. For solar cells laser-etched FTO coated glass (Pilkington TEC-15) was cleaned with different solvents and coated with a compact TiO_2 layer by spray pyrolysis. For the quasi steady-state PIA measurements quartz substrates were used instead. A 1.6µm thick mesoporous TiO_2 layer was applied by screen printing a terpineol diluted paste (Dyesol DSL 18NR-T) and subsequent sintering at 450 °C for 30 min. The temperature was ramped up within 45 min. The samples were left to cool down and immersed in a 20 mM aqueous $TiCl_4$ solution at 60 °C for 30 min followed by another sintering step at 450 °C. The TiO_2-coated substrates were pretreated with a surface modifier (ID662) and directly afterwards placed in a 0.5 mM dye solution in dichloromethane (DCM) for 1 h. After the dyeing step, the samples where thoroughly rinsed with DCM and dried in a nitrogen flow. Spiro-MeOTAD was dissolved in chlorobenzene at a concentration of 200 mg/mL. The solution was heated to 85 °C to aid dissolving. Li-TFSI was dissolved in cyclohexanone at a concentration of 0.3 M. The freshly prepared solution was added to the Spiro-solution yielding molar ratios of Spiro:Li-TFSI 33:4. The spiro film was prepared by spin coating the solution for 30 s at 2000 rpm after leaving the solution on the sample for about 1 min. Finally, a 200 nm thick silver electrode was evaporated on top.

Samples that contained only Li-TFSI (no Spiro) were prepared like the solar cells, but the hole transporter was replaced by solvent.

Solar Cell testing

J-V curves were measured using a LOT-Oriel solar simulator (class AAB) with an AM1.5G standard spectrum. The J-V curves were measured with a

Keithley 2600 SMU under 1 sun conditions calibrated with a Rera Systems reference solar cell. The active area was determined to 12.6mm^2 by measuring the overlap of the silver electrode with the TCO.

Internal quantum efficiencies were determined by measuring the external quantum efficiency and further correction for the amount of absorbed photons determined by diffuse reflection measurements.

Absorption and Photoluminescence

Absorption spectra were recorded in transmission with a Perkin Elmer Lambda 25 spectrophotometer. Photoluminescence was measured with a Hamamatsu streak camera system using a femtosecond laser (Coherent MIRA Duo) as excitation source. The 800 nm output of the oscillator was doubled in a BBO crystal to get 400 nm excitation.

The dye cation absorption was recorded in solution by chemically oxidizing the dye with Iron(III)chloride.

The dye anion spectrum was recorded by blending the dye into Lupasol™ (solvent: DCM) and drop casting the blend on a quartz substrate followed by UV illumination. Several absorption spectra were recorded with increasing illumination time, until no further change of the absorption could be observed.

Quasi-steady state photoinduced absorption spectroscopy

Quasi-steady-state photoinduced absorption spectroscopy (PIA) was performed in a pump–probe setup consisting of a 100 W tungsten-halogen lamp with a LOT-Oriel Omni-λ 300 monochromator providing the probe light and a Newport LED (LED-527-HP) emitting at 527 nm with a power density of ca. 100 mW cm^{-2} at the sample position used as the pump. The transmitted light was dispersed by a second (identical) monochromator and then detected by a photodetector. For measurements in the wavelength range from 550 to 1000 nm, an amplified silicon photodetector (Thorlabs PDA 100A) was employed, which was replaced by an amplified germanium detector (Thorlabs

PDA 50B) for the wavelength range from 900 to 1800 nm. For the IR spectral region (1700-4000 nm), an amplified nitrogen-cooled InSb detector (Teledyne Judson J10D) was used. The pump light was chopped at 317 Hz to induce changes in the transmission ΔT, which were measured by using a lock-in amplifier (EG&G Princeton Applied Research model 5210). Where necessary, the ΔT signal was corrected for photoluminescence and scattered pump. To calculate ΔT/T, the transmission was recorded prior to the PIA measurement. The sample was kept in air during the measurements.

Transient absorption spectroscopy

Transient absorption measurements were performed with a home-built pump-probe setup.[1] To measure a time range up to 4 ns with a resolution of ~100 fs, the output of a commercial titanium:sapphire amplifier (Coherent LIBRA HE, 3.5 mJ, 1 kHz, 100 fs) was split with one portion used to generate a 530-550 nm excitation pulse using a home-built narrowband non-collinear optical parametric amplifier (NOPA) and another used to generate a 1300 nm seed pulse (output of an optical parametric amplifier (Coherent OPerA Solo)) for white-light generation in the visible to NIR (500-1000nm) in a c-cut 3 mm thick sapphire window. For the redder NIR white-light (1200-2000nm), a 2100nm seed was used. A polished silicon substrate was added into the path of the white light to block the visible fraction of the supercontinuum. The variable delay of up to 4 ns between pump and probe was introduced by a broadband retroreflector mounted on a mechanical delay stage. The excitation pulse was chopped at 500 Hz, while the white-light pulses were dispersed onto a linear silicon (Hamamatsu NMOS linear image sensor S3901) or Peltier-cooled extended InGaAs (Entwicklungsbüro Stresing) photodiode array for the VIS and NIR light, respectively. The arrays were read out at 1 kHz. Adjacent diode readings corresponding to the transmission of the sample after an excitation pulse and without an excitation pulse were used to calculate ΔT/T. Samples were excited with several different fluences in the range of 3 to 20 μJ/cm^2.

For measuring in the time range of 1 ns to 1 ms with a resolution of 600 ps, the excitation pulse was provided by an actively Q-switched Nd:YVO4 laser (AOT Ltd. MOPA) at 532 nm. The delay between pump and probe in this case was controlled by an electronic delay generator (Stanford Research Systems DG535). TA measurements were performed at room temperature under dynamic vacuum at pressures <10–5 mbar. Similar to the ps-ns measurements, we excited with several different fluences from 5 to 50 μJ/cm^2.

Absorption and Emission spectra

The absorption and emission spectra of the dye in solution using different solvents and on TiO_2 are shown in Figure S 1 and Figure S 2. A strong solvatochromism can be observed, as in the higher polarity solvent DCM the absorption and emission spectra were redshifted. The red shift was even more pronounced for the photoluminescence. On TiO_2 the spectra rather resembled the spectra obtained in the high polarity solvent due to the polarity and anisotropy of the TiO_2 interface, however, the PL was strongly quenched. Upon the addition of Li-TFSI the spectra were further shifted to the red. This strong dependence on the polarity originates from the strong dipole moment of the dye in the ground and excited state (in particular due to the big difference of those two). A higher polar solvent thus stabilizes the excited state leading to a red shift.

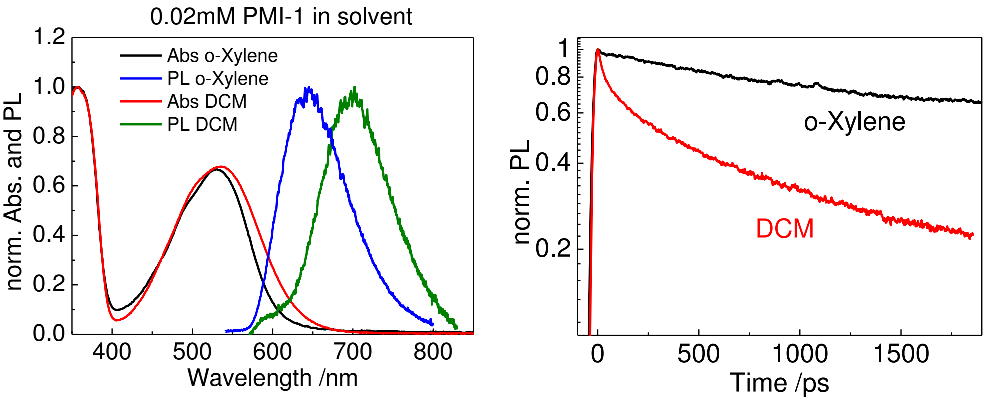

Figure S 1: Absorption and emission spectra of the dye in two different solvents with different polarity (polarity of DCM is larger than of o-xylene). Both spectra are red shifted with higher polarity, stronger emphasized for the PL spectrum.

The PL lifetime in DCM is shorter. A possible explanation is that the oscillator strength of the emissive transition changes with the polarity due to a better coupling of the excited state to the ground state.

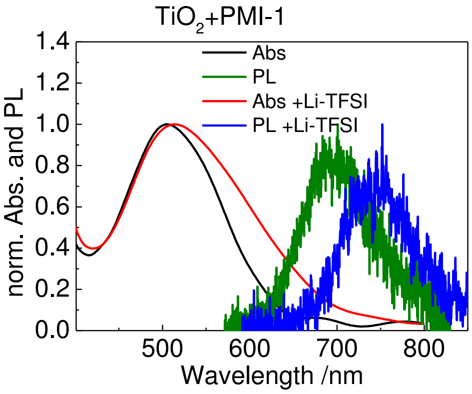

Figure S 2: Absorption and emission spectrum of dye attached to TiO_2 with and without Li-TFSI. The PL is strongly quenched. On TiO_2 the PL spectra resemble the spectra in higher polarity solvents, being more pronounced when Li-TFSI is present.

In the transient absorption spectra obtained from the solutions (Figure S 3), we observed a very fast decay component that could not be observed in the PL measurements and additionally a slow component that somewhat resembled the PL decay in both solvents. The fast component was more pronounced for the more polar solvent DCM and could originate from solvent relaxation or an intramolecular charge transfer.

Dye cation spectrum assignment

In Figure S 4 the 3 ns spectrum of the transient absorption experiment of sample 2 (dye on *TiO_2* with Li-TFSI) is shown in comparison with the spectrum obtained by quasi-steady-state PIA. The agreement of both supports the assignment of this signal to dye cations.

.

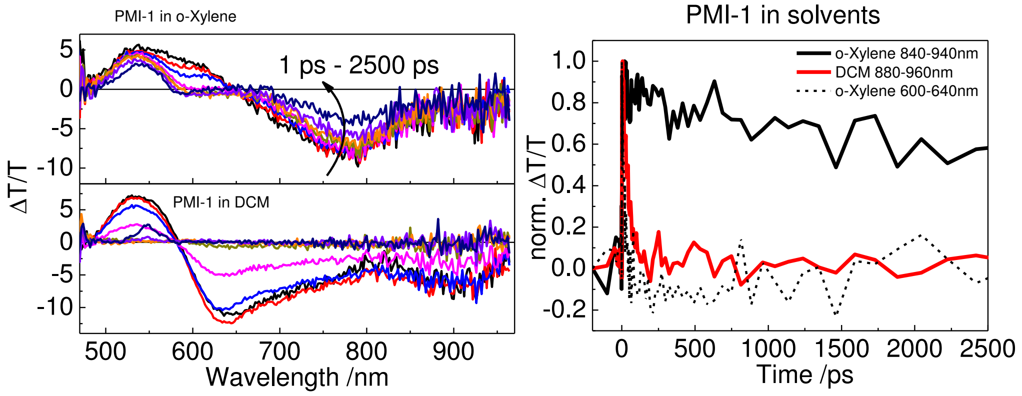

Figure S 3: Transient spectra and kinetics in two different solvents with different polarity (DCM has a higher polarity than o-xylene). Spectra are at times: black: 1.25ps; red: 3.8ps; blue: 11.5ps; magenta: 34ps; olive: 115ps; orange: 335ps; purple: 1020ps; violet: 3125ps.

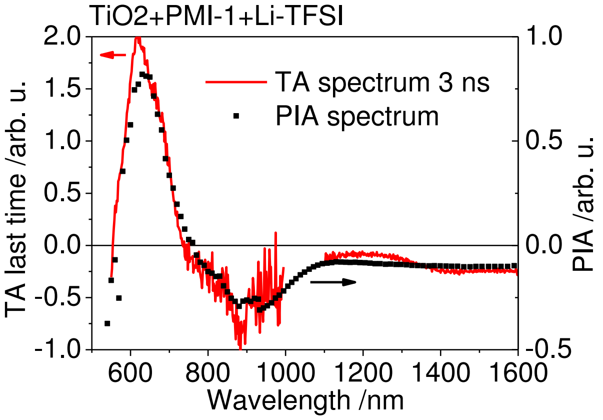

Figure S 4: Comparison of the transient absorption spectrum after 3 ns with the spectrum obtained by quasi-steady state photoinduced absorption spectroscopy (PIA) of sample 2 (*TiO_2*+PMI-1+Li-TFSI). The agreement validates the assignment to created charges.

Fluence dependence of delayed charge recombination

The recombination of electrons in TiO_2 and dye cations was found to be fluence dependent, as can be seen in Figure S 5. A higher fluence led to faster charge recombination indicating non-geminate recombination of free charges. This is clear evidence, that upon the addition of Li-TFSI free charges are created.

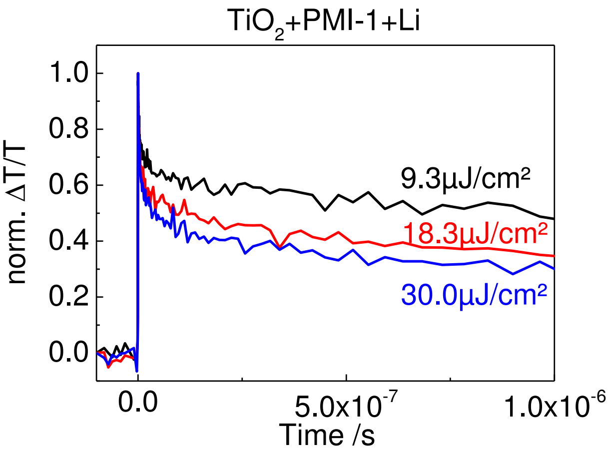

Figure S 5: Fluence dependence of long time recombination of electrons in TiO_2 and dye cations. Higher fluences lead to stronger recombination pointing towards a non-geminate recombination process indicating that free charges are created.

Justification of Regeneration Occurring in The First Two Picoseconds

In Figure S 6 the early-time spectra of the dye attached to TiO_2 in the presence of Li-TFSI. It can be clearly seen that within the first two picoseconds the decaying dye cation signal around 900 nm decreased accompanied by a strong increase of the signal in the NIR, assigned to the generation of spiro cations. Thus the spectra monitor the charge transfer from dye cation to hole transporter within the first two picoseconds.

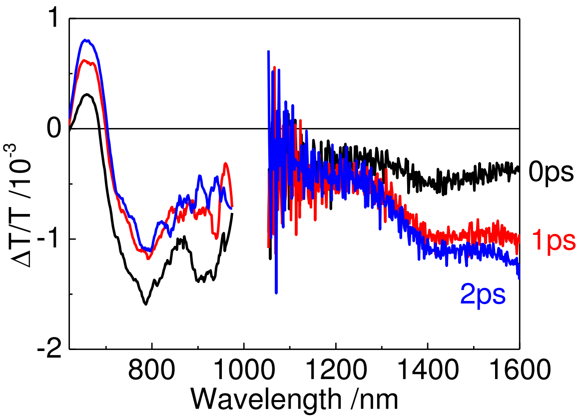

Figure S 6: Comparison of single spectra in the first two picoseconds in the visible and near IR spectral regions. Clearly, the decay of the cation typical feature around 900 nm is coinciding with a steep increase of the NIR signal of spiro cations.

Details of the Fitting

The least square fitting was done with OriginPro 8.5.1G (OriginLab Corporation) with statistical weighting, meaning that $\chi^2 = \sum_{i=1}^{n} \frac{1}{y_i} \left[y_i - f\left(t, \widehat{\Theta}\right)\right]^2$ was reduced, where y_i are the measured values for each time t and $f\left(t, \widehat{\Theta}\right)$ the fit function depending on the independent variable t (time) and the set of parameters $\widehat{\Theta}$. Fluence dependent kinetics were not observed for the short delay measurements (up to 3 ns). The excitation density per cm² was calculated as $N_0 d = \frac{\phi\lambda}{hc}\left(1 - 10^{-A(\lambda)}\right)$. Here, ϕ was the fluence of the excitation beam in J/cm² at the wavelength λ, h the Planck constant, c the speed of light and $A(\lambda)$ the absorbance of the sample as obtained with a Perkin Elmer Lambda 25 UV-VIS absorption spectrometer. Errors for absorbance and fluence were estimated and calculated with Gaussian error propagation. The thickness of all TiO_2 samples was similar and thus not taken into account for the fitting.

Table S 1: Parameters obtained from the fit of the dye attached to TiO_2 (sample 1). Parts of the values are also in the main text in Table 1.

Parameter	805 nm	900 nm	1500 nm
$N_0 d/(10^{13}\ \mathrm{cm}^{-2})$	$2.83 \pm .34$		$4.66 \pm .54$
$A_1^\lambda/(10^{-17}\ \mathrm{cm}^2)$	$6.35 \pm .20$	$3.26 \pm .15$	$0.35 \pm .06$
${k_{dec,1}}^{-1}/\mathrm{ps}$	$3.8 \pm .2$		
$A_2^\lambda/(10^{-17}\mathrm{cm}^2)$	$2.62 \pm .12$	$1.84 \pm .08$	$0.65 \pm .04$
${k_{dec,2}}^{-1}/\mathrm{ps}$	80 ± 5		
$A_3^\lambda/(10^{-17}\mathrm{cm}^2)$	$1.56 \pm .06$	$0.74 \pm .03$	$0.38 \pm .02$
${k_{dec,3}}^{-1}/\mathrm{ps}$	2600 ± 180		

Table S 2: Parameters obtained from fitting the transient absorption dynamics of the device-like sample 3 according to the model described in the text with f as a fixed parameter.

Parameter	805 nm	900 nm	1500 nm
$N_0 d$ /$(10^{13}\mathrm{cm}^{-2})$	$1.78 \pm .20$		$1.88 \pm .26$
${k_{dec}}^{-1}$/ps	187 ± 20		
${k_{D^* \to HT^+}}^{-1}$/ps	15 ± 3		
χ_{II}	$0.44 \pm .03$		
σ_{D^*} /$(10^{-17}\mathrm{cm}^2)$	$17.2 \pm .55$	$7.34 \pm .36$	$0^{+.89}_{-0}$
σ_{HT^+} /$(10^{-17}\mathrm{cm}^2)$	$0.16 \pm .06$	0.83 ± 0.06	12.8 ± 0.25
η	$81 \pm 1\,\%$		

We also fitted the transient absorption decays of the device-like sample 3 with f as a free parameter. It is shown in Figure S 7 as solid lines. The resulting parameters of this fit are given in Table S 3.

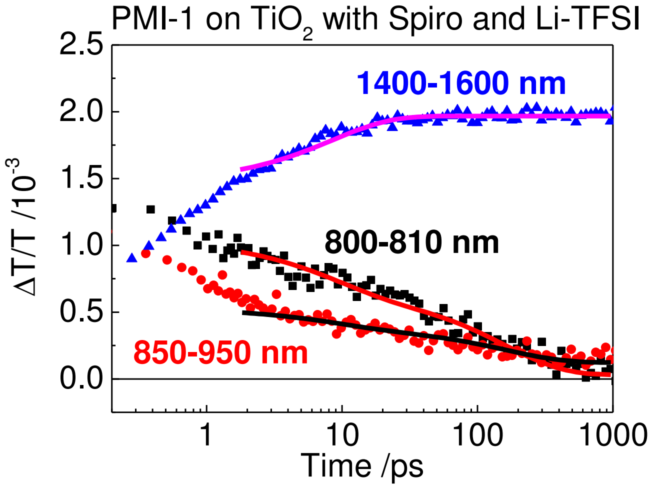

Figure S 7: The same data as presented in the main text in Figure 8 with different fits: the solid lines are fits to the same model as presented in the main text, but with f as a free fitting parameter shared between all three kinetics.

Table S 3: Parameters obtained from fitting the transient absorption dynamics of the device-like sample 3 according to the model described in the main text with f as a free parameter.

Parameter	805 nm	900 nm	1500 nm
$N_0 d/(10^{13}\mathrm{cm}^{-2})$	$1.78 \pm .20$		$1.88 \pm .26$
${k_{dec}}^{-1}/\mathrm{ps}$	160 ± 13		
${k_{D^* \to HT^+}}^{-1}/\mathrm{ps}$	9 ± 2		
χ_{II}	$0.40 \pm .03$		
$\sigma_{D^*}/(10^{-17}\mathrm{cm}^2)$	12.1 ± 1.89	$5.22 \pm .80$	$0^{+1.10}_{-0}$
$\sigma_{HT^+}/(10^{-17}\mathrm{cm}^2)$	$0.24 \pm .06$	0.97 ± 0.09	14.8 ± 0.91
f	$0.53 \pm .07$		
η	$71 \pm 4\ \%$		

The extracted parameters of the dye:spiro blend data fit to the charge transfer model as described in the main text are shown in Table S 4.

Table S 4: Parameters obtained from the fit to the kinetics of the spiro-dye-blend according to the model as explained in the main text.

Parameter	625-635 nm	850-950 nm
${k_{Ex \to CT}}^{-1}/\mathrm{ps}$	$13.5 \pm .7$	
${k_{CT \to GS}}^{-1}/\mathrm{ps}$	787 ± 22	
$\sigma_{Ex}^{eff}/(10^{-4}\ \mathrm{arb.\,u.})$	$-9.1 \pm .2$	$-21.0 \pm .2$
$\sigma_{CT}^{eff}/(10^{-4}\ \mathrm{arb.\,u.})$	$-21.0 \pm .2$	-10.6 ± 0.2

1. Etzold, F.; Howard, I. A.; Forler, N.; Cho, D. M.; Meister, M.; Mangold, H.; Shu, J.; Hansen, M. R.; Müllen, K.; Laquai, F. J. Am. Chem. Soc. 2012, 10.1021/ja303154g.

4.2 Comparison with a Naphthalene Imide Dye (NMI)

The study described in the previous chapter was expanded to another dye that exhibited a blue-shifted absorption. The structure of the naphthalene monoimide based dye NMI is essentially similar to PMI-1 (the dye from the study in the previous chapter 4.1): The perylene imide was replaced by a naphthalene imide, which is connected by a bithiophene spacer unit to the identical donor. The chemical structure of NMI is depicted in Figure 31 together with the photovoltaic performance and UV-VIS absorption of a solid-state DSC in comparison to the data obtained from PMI-1. The overall photovoltaic performance of PMI-1 was better, which can be explained by the stronger and red-shifted absorption spectrum. From the UV-VIS absorption spectrum, the estimated theoretically maximum attainable short circuit current is 14 mA/cm^2 and 9 mA/cm^2 for PMI-1 and NMI, respectively. Note, that in this scenario an internal quantum efficiency of 100% was assumed and the UV-VIS absorption measured in transmission was taken as the total absorption neglecting any reflection, scattering and interference losses. Both assumptions are not valid, but are sufficient for a qualitative comparison: In fact, it shows that the exper-

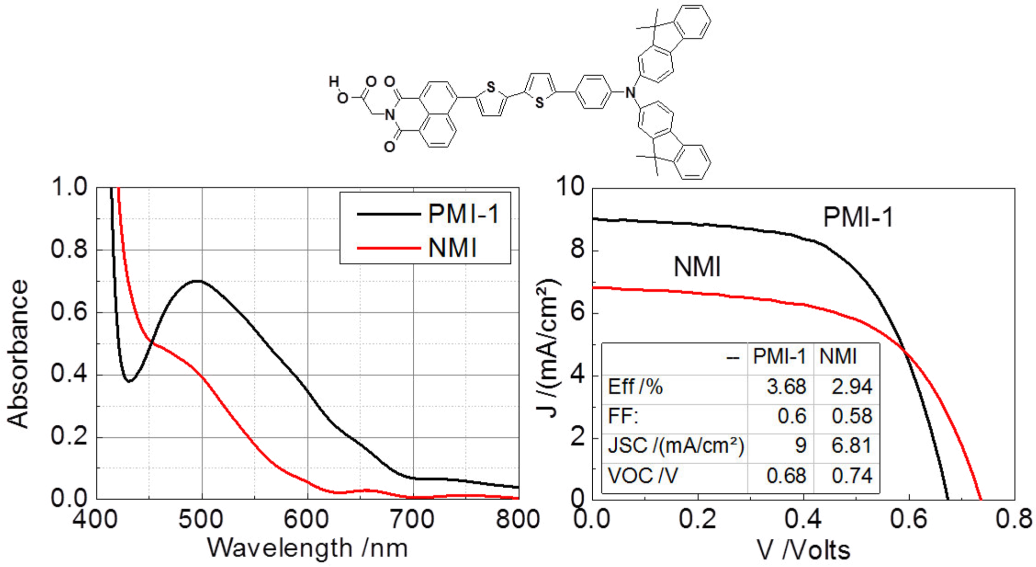

–	PMI-1	NMI
Eff /%	3.68	2.94
FF:	0.6	0.58
JSC /(mA/cm²)	9	6.81
VOC /V	0.68	0.74

Figure 31: Chemical structure of the naphthalene monoimide dye NMI (top) and UV-VIS absorption of the solar cell (left) as well as its J-V-characteristic (right) compared to the data for PMI-1.

imentally measured J_{SC} of NMI is closer to the maximum theoretically possible value (76%) than the J_{SC} of PMI-1 (64%), pointing towards a higher internal quantum efficiency. This is supported by measurements of the internal quantum efficiency yielding 90% for NMI and 67% for PMI-1. [108] In the following, the reasons for this difference is elucidated. All quasi-steady-state PIA and transient absorption data presented in this part were recorded using excitation wavelengths between 530 and 550 nm. Samples for time-resolved photoluminescence measurements were excited at 400 nm, if not otherwise stated.

4.2.1 Observations for NMI

Analogous to the study on PMI-1, results of quasi-steady-state photoinduced absorption spectroscopy (PIA) will be presented first, followed by a more detailed investigation by transient absorption experiments. A similar approach to analyze the transient absorption data as for PMI-1 was pursued to investigate the charge generation of the NMI-dye. However, the above developed analysis and model is not easily applicable to the NMI dye, as discussed below. However, similarities and differences to PMI-1 could be evaluated. Finally, further measurements that were performed on both dyes are presented, which on the one hand show the complexity of the dyes' photophysical behavior but on the other hand also help to better understand the underlying photophysics.

Quasi-steady-state PIA

The PIA spectra of the NMI dye attached to titania in the presence and absence of Li-TFSI and in the device-like structure with the hole transporter spiro-MeOTAD and Li-TFSI are depicted in Figure 32. In contrast to PMI-1, a PIA signal could already be observed even in the absence of Li-TFSI when NMI was attached to TiO_2 (black line upper graph). This is not surprising as the NMI photoexcited state exhibits a lower absolute ionization potential (the excited state energy is higher compared to the TiO_2 conduction band edge) [108] and thus the driving force for electron injection into TiO_2 is higher, because more states in the conduction band can be reached. Here the first problem of the

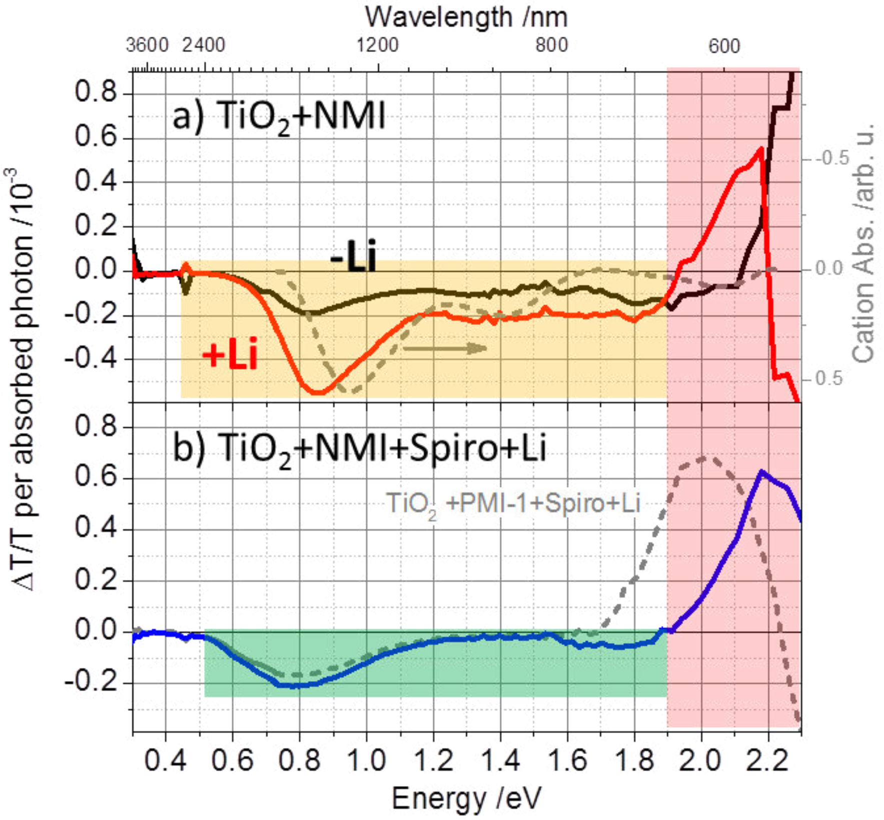

Figure 32: Quasi-steady-state PIA measurement of NMI. a) NMI on TiO$_2$ with (red) and without Li-TFSI (black). In grey, the cation absorption as obtained from oxidation with Iron(III)chloride is shown. b) NMI in a device-like structure with hole transporter and Li-TFSI (blue). In grey, the same measurement for PMI-1 is shown for comparison of the spiro signal strength. The spectral regions of the Stark effect/bleach, of the dye cation and the hole transporter cation are highlighted in red, yellow and green, respectively.

applicability of the model previously used to describe the transient absorption data of PMI-1 arises: For PMI-1, in contrast to NMI, almost solely primary excited states decaying to the ground state were observed in the absence of Li-TFSI, without an appreciable amount of electron injection. This allowed to study the decay of the primary photoexcitations of the dye on TiO$_2$, which was not possible for NMI as injection already occurred without Li-TFSI. The dye cation signal peaked around 0.9 eV (1380 nm) with a tail reaching into the visible spectral region highlighted in yellow in Figure 32a). The spectrum of the cation could be qualitatively reproduced by chemically oxidizing the dye with Iron(III)chloride in chloroform solution (grey dashed line). The absorption of the chemically created cation was slightly shifted to the blue, which can be attributed to the different environment in solution. Upon the addition of Li-TFSI, the PIA signal was again strongly enhanced pointing towards an increased injection efficiency as also seen for PMI-1. On the other hand, this observation also implies that without Li-TFSI not all dyes participated in charge injection. However, it is worth mentioning that not only the injection efficiency seemed to be altered, but also the recombination was slowed down in the presence of Li-TFSI [52], see Figure 33, also leading to a larger signal in the PIA. In the blue spectral region (>1.9 eV), a positive signal was observed, which is highlighted in red in Figure 32. This ground state bleaching originated from dyes that injected and which were present as dye cations before recombination. An interpretation of this signal as a Stark effect feature is also possible, especially in the presence of Li-TFSI, where this signal was shifted to the red and a zero crossing around 2.2 eV (560 nm) could be observed, supporting this interpretation. The red shift was accompanied by a red shift of the ground state absorption when Li-TFSI was added (compare Figure 34). Following the argumentation for PMI-1 in section 4.1, this red shift indicates that Li^+ ions localize at the titania-dye interface. Finally, when the hole transporter was present (Figure 32b), no signatures of the dye cations were observed anymore and the induced absorption of the cations was replaced by the typical broad absorption of spiro cations peaking around 0.8 eV (1550 nm). Additionally, a small signal of spiro cations could be observed around 1.7 eV (730 nm) [109] that was superimposed by strong positive signals in the case of PMI-1. The spiro cation signature is highlighted in green in Figure 32b). Evidently, dye regeneration was very efficient and the pore filling was sufficient to ensure that the majority of dye cations was regenerated. The recombination kinetics of electrons in the TiO_2 and holes in the spiro were similar for both dyes (PMI-1 and NMI), as shown in Figure 35, so that the amplitude of the spiro signals in the NIR can be directly compared. As the absorption cross section of spiro cations is equal in all samples, the relative signal amplitude directly corresponds to the relative amount of spiro cations created. The signal amplitude for PMI-1 was ¾ of the spiro signal in the NMI-sample, indicating that the internal quantum efficiency

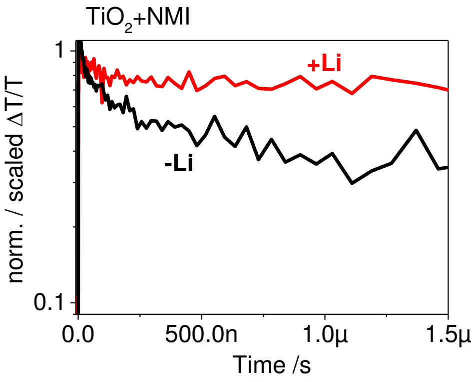

Figure 33: Recombination kinetics at the positive Stark/bleach signal in the visible range for NMI attached to TiO_2 with and without Li-TFSI. The "+Li"-signal is normalized to the maximum and the "–Li"-signal is scaled arbitrarily to allow a better comparison of the decay of the long-lived species. Without Li, the recombination is faster.

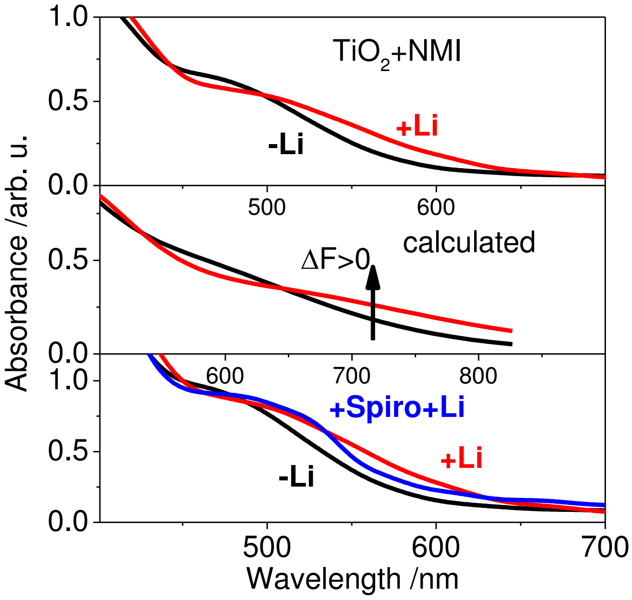

Figure 34: Absorption spectra of NMI attached to TiO_2 and the influence of Li-TFSI (top). The change in absorption can be explained by a more positively charged TiO_2 surface indicating that Li^+ localizes at the TiO_2 interface as shown by TDDFT calculations (middle). [101] Note that the calculated spectra were further shifted to the red. The deviations are caused by the simplifications used for the calculation, e.g. the gas phase. The x-axis for the calculated data is adjusted for better comparability with the measured spectra. The lower panel shows the absorption change when spiro is additionally present. Again, the changes were not as pronounced as for the sample with Li-TFSI only, indicating that less Li^+ localizes at the interface. For further explanation of the localization of Li^+ at the interface see section 4.1.

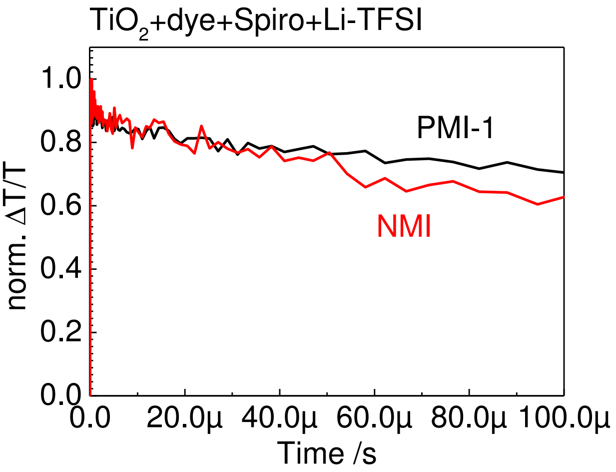

Figure 35: Long-time electron-hole recombination kinetics of the device-like samples in the visible (Stark effect) region measured at lowest fluence. Both dyes show a similar behavior, with a slightly faster recombination for NMI.

at the excitation wavelength (530 nm) was about ¼ less than for PMI-1, which correlates well with the observed differences in internal quantum efficiency and maximum theoretically attainable short circuit current as discussed in the beginning of this subsection. Hence, quasi-steady-state PIA is a valuable tool to study charge generation and evaluate internal quantum efficiencies under the assumptions given, i.e. similar recombination and absorption cross section of spiro cations. To summarize, the measurements for NMI indicated that charge generation on titania was possible even without Li-TFSI in contrast to PMI-1 and that NMI exhibited an overall higher internal quantum efficiency.

Transient Absorption Spectra: Device-like Samples

Having identified the differences in charge generation efficiency between PMI-1 and NMI, the transient absorption studies of the samples containing the NMI dye are presented in the following. First, the transient absorption spectra are evaluated followed by the analysis of the kinetics. From the PIA spectra it had already been clear that the dye cation signals could be expected mainly in the NIR. In Figure 36, the VIS to NIR transient absorption spectra for NMI attached to TiO_2 in the absence and presence of Li-TFSI and in the device-like structure including the hole transporter and Li-TFSI are shown.

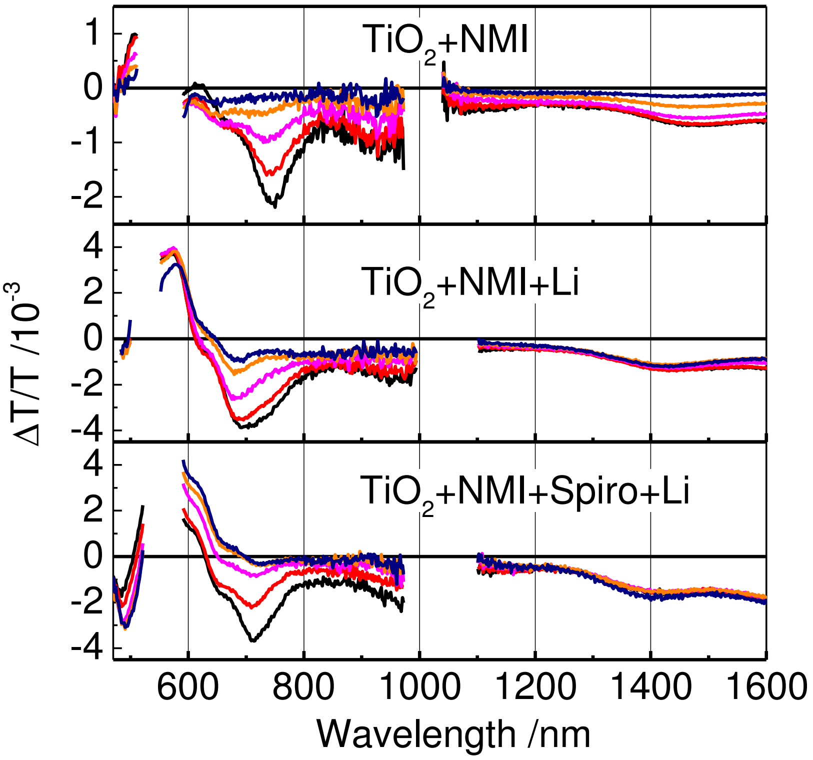

Figure 36: Transient absorption spectra of NMI attached to TiO_2 without Li-TFSI (top panel), with Li-TFSI (middle panel) and in the device-like structure with the hole transporter and Li-TFSI (bottom panel). The colors refer to mean times as: black 1.25 ps; red 3.8 ps; magenta 35 ps; orange 320 ps; dark blue 3 ns.

A clear feature around 700-750 nm mainly assigned to primary photoexcitations (by comparison with measurements of NMI in solution, Figure 38, and on Al_2O_3, Figure 47) was observed in all three samples, which partially shifted with time and additionally was influenced by Li-TFSI. Furthermore, an induced absorption in the NIR around 1500 nm could be observed and was assigned to the primary photoexcited species, which coincided with the cation absorption as identified by PIA. In the absence of Li-TFSI, the whole spectra appeared to be mainly governed by a decay of dyes that could not inject electrons into the titania or that exhibited a delayed injection. A rather small signal survived after the measured time range of 3 ns resembling the spectrum of the dye cation indicating that a small amount of dyes could inject. However, it is also possible, that this induced absorption, especially in the visible spectral region originated from long-lived primary excitations, e.g. an intramolecular charge-transfer state, which exhibited a similar spectrum as the dye cation. In fact, after investigation of the dye attached to alumina in the later course of this study, this became a likely alternative explanation. The NIR spectra showed the typical dye cation feature as identified by PIA even at the shortest delay times. By comparison to the spectra of NMI attached to Al_2O_3 (Figure 50), it became obvious that the feature peaking around 1500 nm uniquely represents dye cations, as the exciton-induced absorption was rather flat in this wavelength region. Thus, the NIR spectra clearly indicate that charges were created in the absence of Li-TFSI. It is however impossible to unambiguously interpret the decay of the signal, which could originate from exciton decay (due to recombination to the ground state or electron injection), represented by a decaying superimposed shapeless exciton-induced absorption, or a fast recombination from previously created cations with electrons in the TiO_2. Regarding the spectral shape that appears to be similar for all times, and the difference of the decay compared to the visible wavelength regions dominated by exciton features especially in the first 35 ps, recombination of charges is a more likely interpretation of the NIR decay.

In the presence of Li-TFSI the spectra changed, but the influence was not as pronounced as for PMI-1. The typical features of the primary photoexcitation were still present in the visible spectral range, whereas the NIR signal showed a less strong change with time and a larger signal amplitude after long delay times. Similar to PMI-1, this indicates that more charges were created in the presence of Li-TFSI. In analogy to the study of PMI-1, it seems reasonable to assume the presence of two pools of dyes, one influenced and the other not influenced by Li-TFSI. However, for NMI, the distinction between injecting and non-injecting dyes due to the presence and absence of Li-TFSI, respectively, is not valid anymore. The minor changes with time in the NIR spectra suggested that the Li-TFSI was suppressing the fast recombination, which is supported by a similar observation in the long-time recombination dynamics, as mentioned earlier (Figure 33) being beneficial for charge generation. Moreover, it also indicates that the possibly observed excitonic decay component was suppressed, as more dyes were able to inject. A closer look at the visible spectra revealed that the induced absorption peak of the primary excitation around 700 nm was broadened and slightly blue-shifted in the presence of Li-TFSI even for the earliest spectra and thus resembled closer the delayed spectra in the absence of Li-TFSI. As some features of the non-affected dyes around 750 nm can be expected, the broadening could originate from a superposition of this signal and a new blue-shifted induced absorption originating from dyes affected by Li-TFSI. This additional signal can be attributed most probably to intramolecular charge-transfer states stabilized by Li-TFSI. The positive ΔT/T-signal below 650 nm does not only originate from bleached dyes but also from a Stark effect signal.

In the presence of the hole transporter and Li-TFSI, the primary photoexcitations were still observed in the visible, but were quenched faster, indicating that preceding hole transfer could play a role for charge generation of the NMI dye. The NIR spectra looked very much like in the other samples, due to the similarity of the dye and spiro cation features in this wavelength region as already observed in the PIA. However, the minor differences, e.g. the increased signal strength at the red edge of the spectrum, suggest that the signals can rather be assigned to spiro cations.

All in all the spectral changes appeared to be rather similar for NMI compared to PMI-1 with the only difference that on TiO_2 even without Li-TFSI a small fraction of longer-lived states were observed, which is elucidated in more detail in the course of the data analysis. In the following part though, the general possibility of preceding hole transfer is investigated first.

Transient Absorption: Dye-spiro Blend and Preceding Hole Transfer

In the previous study on PMI-1, the possibility of preceding hole transfer (termed type II charge generation), was undoubtedly proven by investigating a dye-spiro blend by transient absorption spectroscopy and the observation of absorption signatures of the dye anion. The result of the same experiment for NMI is shown in Figure 37. The chemically produced dye anion exhibited a clear absorption feature at 600 nm. [108] In the transient kinetics, however, this feature did not appear as clearly as for PMI-1. In fact, the spectra were similar to the dye dissolved in dichloromethane (DCM), as shown in Figure 38. In particular the position of the isosbestic point was very alike. As the anion absorption was expected to be rather strong in this wavelength region, the isosbestic point was expected to shift strongly, if a clear anion signal were present. Thus, the spiro-dye-blend spectra did not clearly prove or disprove the possibility of electron transfer from the hole transporter to the excited dye. The kinetics in two distinct wavelength regions, as depicted in the right panel of Figure 37, reflect the kinetics at wavelength regions in which mostly the dye anion was expected to absorb (650-670 nm) and in which the anion was expected to absorb weaker than the primary photoexcitation (850-950 nm). In contrast to the spectra, the kinetics allowed the observation of an electron transfer from the hole transporter to the excited dye. The fit according to the model presented in the previous section 4.1 (subsection 2.2.8 and Figure 8 of the manuscript) qualitatively resembled the data, when the recombination of the charge-transfer state was assumed to be biexponential. All other assumptions were the same as for the model for PMI-1, i.e. that the exciton was much faster quenched due to charge transfer than it could decay to the ground state. The fit resulted in an inverse charge-transfer rate of (0.48 ± 0.03) ps, which is much faster than for PMI-2 and close to the experimental time-resolution, and in two recombination rates of (28 ± 3) ps contributing 33 % and (1899 ± 70) ps contributing 67 %. To conclude, even if the spectra did not unambiguously show the possibility of preceding hole transfer, at least the kinetics indicated that it is a possible pathway. However, the evidence was not as clear as

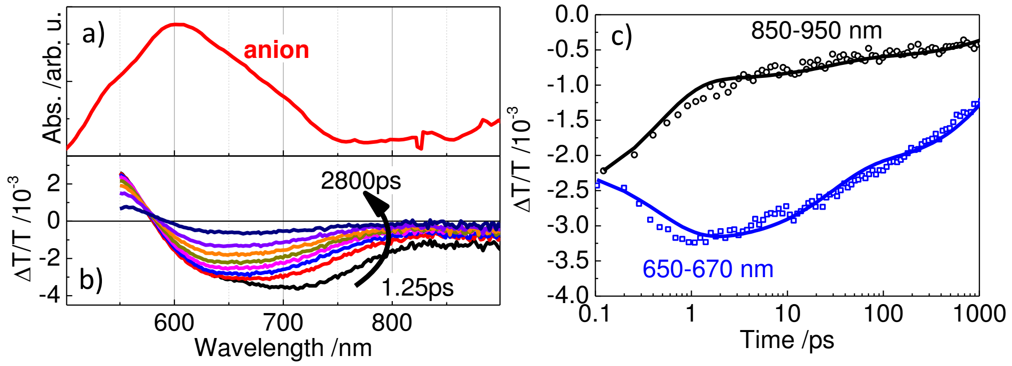

Figure 37: Blend of NMI with spiro-MeOTAD to investigate preceding hole transfer. a) shows the anion absorption spectrum obtained by chemically reducing the dye with Lupasol^{TM} treatment. [108] b) shows the observed transient absorption spectra and c) shows the kinetics at two distinct wavelength regions where dye anion and primary excitation mainly absorb together with a fit to the model described in section 4.1.

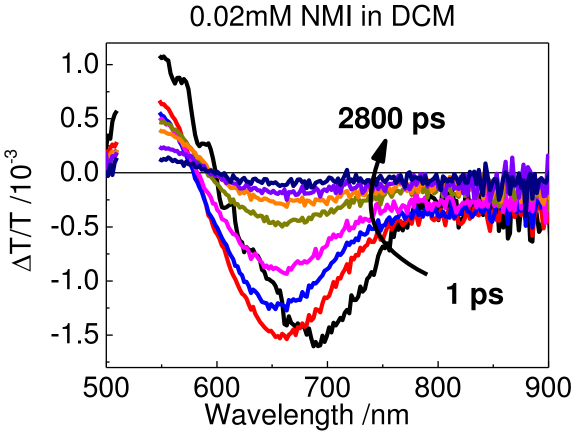

Figure 38: Transient absorption spectra of NMI in DCM. The spectra show similar behavior as the dye in the blend with the hole transporter.

for PMI-1. The obtained charge-transfer rate for preceding hole transfer appears rather high and could be overestimated. The reasons are that the model did not cover all processes, e.g. the complicated photophysics of the primary excitation that also showed kinetics on a similar timescale, as well as spectral shifts with time. Further considerations regarding this charge generation mechanism are taken into account in the next part, where the kinetics in the device-like structures are investigated.

Transient Absorption Kinetics and Modeling: Device-like Samples

Analogue to the previous study on PMI-1, three wavelength regions were chosen to investigate the kinetics of samples of dye molecules attached to TiO_2 in the absence and presence of Li-TFSI and in device-like samples with hole transporter and Li-TFSI. In the visible, two regions were chosen, in which a reasonable amount of primary excitations- and dye cation-induced absorption was expected. In the NIR, one spectral region was chosen, in which additionally the spiro cation absorbed. These regions were 720-760 nm, 850-950 nm and 1400-1600 nm, respectively. The visible wavelength regions were chosen as they were free of a Stark effect.

The kinetics of NMI attached to TiO_2 without and with Li-TFSI are shown in Figure 39 together with fits according to the model developed for PMI-1. Again different dynamics in the VIS and NIR spectral regions were observed for the dye attached to TiO_2 (left graph). Concerning the NMI dye, these differences originated not only from different environments as assumed for PMI-1, but also from the generation of charges. In fact, the slower decay in the first 30 ps in the NIR spectral region together with the spectral shape suggested, as discussed above, that this decay actually came from recombination of charges created previously. Three exponential functions with shared rates were sufficient to describe the data ($\Delta T/T = N_0 d \sum_{i=1}^{3} A_i^{\lambda} \exp(-k_{dec,i} t)$), similarly to

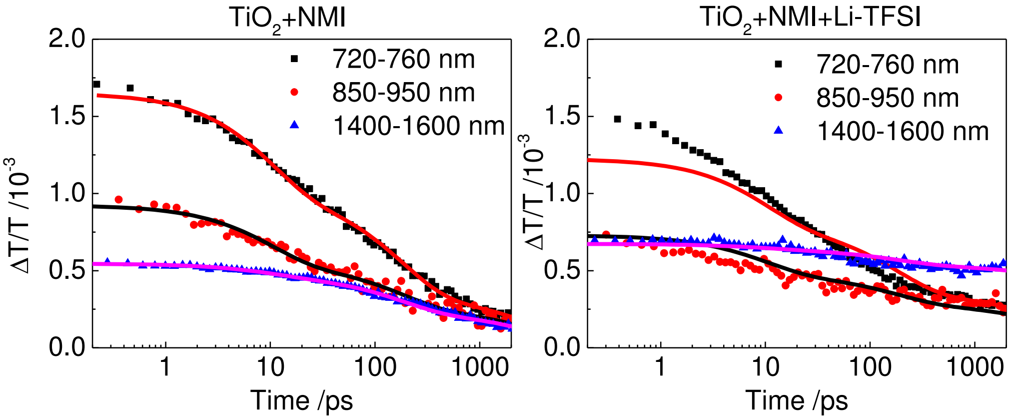

Figure 39: Kinetics normalized to the excitation density at three distinct wavelength regions for NMI attached to TiO_2 without (left) and with Li-TFSI (right) along with fits to the model as developed for PMI-1 in section 4.1.

Table 4: Parameters extracted from the fit to the data of NMI attached to TiO_2 without Li-TFSI according to the same model as used for PMI-1.

Parameters	720-760 nm	850-950 nm	1400-1600 nm
$N_0 d/(10^{13}\mathrm{cm}^{-2})$	$1.0 \pm .5$		$1.9 \pm .8$
$A_1/(10^{-17}\mathrm{cm}^2)$	$6.64 \pm .30$	$3.88 \pm .19$	$0.79 \pm .11$
${k_{dec,1}}^{-1}$ /ps	10 ± 1		
$A_2/(10^{-17}\mathrm{cm}^2)$	$6.87 \pm .21$	$2.97 \pm .15$	$2.45 \pm .10$
${k_{dec,2}}^{-1}$ /ps	177 ± 11		
$A_3/(10^{-17}\mathrm{cm}^2)$	$3.34 \pm .12$	$2.44 \pm .17$	$2.30 \pm .07$
${k_{dec,3}}^{-1}$ /ps	4094 ± 287		

PMI-1. The extracted parameters are shown in Table 4. Again, it should be emphasized that these parameters describe a parameterization of the signal and not the real population decay, as the $A_i^\lambda = A_i \sigma_i$ not only contain the weighting A_i of each rate $k_{dec,i}$ but also the absorption cross sections σ_i of the different states at the respective wavelength, which cannot be further separated. Especially for NMI, for which injection and recombination already played a role in the absence of Li-TFSI, this signal contained contributions of primary photoexcitations as well as charges created. Adding injection to the model to unravel the portion of injected charges, did not lead to any meaningful result, as the absorption cross sections of the individual species were not known. However, the creation of long-lived charges is indicated by the long-time component, which was much slower compared to PMI-1. A major difficulty for this dye was to determine the number of absorbed photons per area $N_0 d$, which is a fixed parameter during the fitting, because of the rather low absorbance of the dye at the excitation wavelength. Additionally, oscillating interference patterns on the order of the absorbance were modulating the absorption spectrum. These deviations were taken into account as an error in the estimation of the number of absorbed photons.

In the presence of Li-TFSI (right graph in Figure 39), the kinetics changed, especially in the NIR. The same model as for PMI-1 was applied to derive the fraction of dyes f influenced by Li-TFSI with all its simplifications, being: i) the

$(1-f)N_0$ dyes not influenced by Li-TFSI were spectroscopically identical to the ones in the sample without Li-TFSI, and ii) the fN_0 dyes influenced by Li-TFSI injected ultrafast and were instantaneously present in the spectra as dye cations. As the constant tail in the kinetics in the NIR indicated that long lived charges were created, which were not recombining on the timescale of the experiment, an additional fast recombination fraction of created charges, as used in the fitting of the data of PMI-1, had not to be taken into account for NMI. Thus the data was fitted according to equation (1) and (2) on page 69 in section 4.1 with $s=0$:

$$\Delta T/T_\lambda\,(\mathrm{t}) = N_0 d\left\{(1-f)\sum_{i=1}^{3} A_i^\lambda \exp\left(-k_{dec,i}t\right) + f\sigma_{D^+}\right\}. \tag{4.1}$$

The resulting fraction f strongly depends on the number of absorbed photons per area $N_0 d$, which could not be determined very precisely as mentioned above. In case of the NMI dye this issue was more severe than for PMI-1, as no recombination of charges occurred and thus the fraction f only contributed a time-independent signal offset to the kinetics. The fit, shown as solid lines in Figure 39 in the right graph, did not entirely describe the data, especially in the visible spectral region in the first 10 ps. The extracted parameters are shown in Table 5. The deviation of the fits in the first 10s of picoseconds can have several reasons: First of all, the model applied is a very simplified description of the actual situation, which appears to be less suitable for NMI as for PMI-1. One particular difference is, that NMI attached to TiO_2 without Li-TFSI already showed charge injection, so that the influence of Li-TFSI was different compared to PMI-1: the Li-TFSI seemed to not only facilitate charge injection for NMI, but also to suppress the fast recombination between electrons in TiO_2 and dye cations. The influence of Li-TFSI on these two processes can be differently

Table 5: Parameters extracted from the fit to the data of NMI attached to TiO_2 with Li-TFSI according to the same model as used for PMI-1 with $\boldsymbol{s} = \mathbf{0}$.

Parameters	720-760 nm	850-950 nm	1400-1600 nm
$N_0 d/(10^{13}\mathrm{cm}^{-2})$	$3.3 \pm .4$		$1.8 \pm .5$
$\sigma_{D^+}\,/(10^{-17}\mathrm{cm}^2)$	$1.49 \pm .30$	$1.33 \pm .28$	$7.83 \pm .35$
f	$0.57 \pm .04$		

depending on the proximity of Li^+-ions. Therefore, the clear difference between dyes influenced and not influenced by Li-TFSI, which is in itself a simplification, cannot be entirely valid anymore. Furthermore, the wavelength region in which the fit deviates the most is the region around 740 nm. Here, the induced absorption was prone to a wavelength shift with time that altered the kinetics in a way not covered by the fitting model. Besides, the origin of the induced absorption is not completely clear. It could originate not only from the primary photoexcitations but also from an intramolecular or even intermolecular (TiO_2^--dye$^+$) charge-transfer state influenced by Li-TFSI in a way not covered by the model, i.e. it could be stabilized or its absorption spectrum could change.

Even though the model failed to describe the data perfectly, the extracted parameter f, representing a measure of the fraction of dyes influenced by Li-TFSI, turned out to be 0.57 ± 0.04. The value of f was expected to be similar for NMI and PMI-1, as the fraction of dyes affected by Li-TFSI does only depend on the sample preparation, which was similar for both dyes. In fact, the extracted values of f of 0.68 ± 0.02 and 0.57 ± 0.04 for PMI-1 and NMI, respectively, agree well, given the experimental uncertainties arising from the sample preparation (spin-coating and soaking time and possible differences in dye coverage) and the uncertainties of the model and excitation densities, especially in case of NMI. Note again that f, in case of NMI, does not describe the fraction of dyes that can inject, which is in contrast to PMI-1.

In the device-like structure the kinetics changed strongly again as depicted in Figure 40. The NIR signal remained almost constant. The fit to the data was reasonable, applying the same simplified model as for the device-like sample incorporating PMI-1 in section 4.1, equation (3). The simplifications were: i) all f_{inj} dyes that injected into TiO_2 were regenerated efficiently within the first two picoseconds and thus only contributed as hole transporter cations to the total signal. For NMI $f_{inj} \neq f$ as f from the previous fit described the amount of dyes affected by Li-TFSI and f_{inj} described the dyes that are able to inject. Injection was however already possible for NMI dyes in the absence of Li-TFSI,

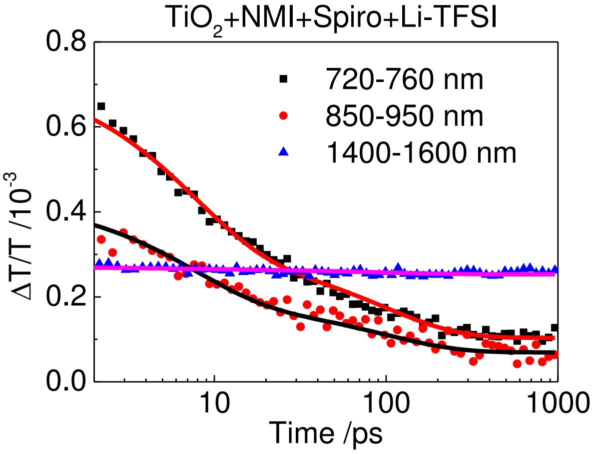

Figure 40: Kinetics normalized to the excitation density at the three wavelength regions in the device-like sample along with fits to the model developed for PMI-1 (solid lines).

so that $f_{inj} > f$, in contrast to PMI-1, were injection was assumed to be solely facilitated by Li-TFSI, so that $f_{inj}^{PMI-1} = f^{PMI-1}$. ii) A fraction χ_{II} of the $(1 - f_{inj})$ dyes that could not inject were able to create charges by type II charge generation (preceding hole transfer) with a rate $k_{D^* \to C}$ competing with recombination of the primary excitation with a rate k_{dec}. The $(1 - \chi_{II})$ portion of the $(1 - f_{inj})$ dyes could not create any charges and just decayed to the ground state with a rate of k_{dec}. Further details to the model and fitting can be found in section 4.1. Similar to PMI-1, the kinetics were fit from 2 ps onwards to fulfill the prerequisite of fast regeneration. The resulting fits depicted in Figure 40 described the data well. The extracted parameters are presented in Table 6.

The most important parameter extracted was $f_{inj} = 0.87 \pm 0.11$, meaning that already 87 % of the primary photoexcitations contribute to the charge generation via ultrafast type I charge generation, and fulfilling the requirement of $f_{inj} > f$. The overall splitting efficiency η turned out to be (95 ± 4) %, determined as for PMI-1 on page 70 ($\eta = f_{inj} + \frac{\chi_{II}(1-f_{inj})k_{D^* \to C}}{k_{dec}+k_{D^* \to C}}$). Thus, the charge generation on the longer timescale contributed only weakly to the exciton splitting efficiency. As this contribution was so small, the cross sections of σ_{D^*}

Table 6: Results of the fits for the device-like structure with the NMI dye.

Parameters	720-760 nm	850-950 nm	1400-1600 nm
$N_0/(10^{13}\mathrm{cm}^{-2})$	$2.47 \pm .66$		$2.35 \pm .50$
${k_{dec}}^{-1}$ /ps	97 ± 9		
${k_{D^*\to C}}^{-1}$ /ps	8 ± 1		
$\sigma_{\mathrm{D}^*}/(10^{-17}\mathrm{cm}^2)$	50 ± 43	29 ± 25	7.7 ± 3.5
$\sigma_C/(10^{-17}\mathrm{cm}^2)$	1.10 ± 0.06	0.74 ± 0.04	$6.8 \pm .3$
f_{inj}	$0.87 \pm .11$		
χ_{II}	$0.68 \pm .02$		
η	(95 ± 4) %		

were rather large and error-prone. Furthermore, as the influence of Li-TFSI is less clear as for PMI-1, the long-time charge generation could also partially originate from dye cations being slowly regenerated. Therefore, the extracted rates of k_{dec} and $k_{D^*\to C}$ should be understood as effective rates that might also contain other processes. However, the rates were reasonable even for the single processes.

In conclusion, preceding hole transfer played a minor role for the charge generation of the NMI dye and it was not as crucial as for PMI-1, because dyes not influenced by Li-TFSI could already undergo electron injection, so that a larger fraction of dyes contributed to the photocurrent by type I charge generation.

In summary, charge generation is efficient in both dyes, PMI-1 and NMI. Whereas PMI-1 requires Li-TFSI and preceding hole transfer to achieve high efficiencies, NMI was not that reliant on the presence of Li-TFSI and type II charge generation.

In the following parts, the photophysical behavior of the dyes in different environments are investigated, which helps to further understand the observations in the device-like samples, especially regarding the complex decay of the exciton to the ground state. Additionally, the problems and difficulties that occur due to these rather complicated photophysical properties will be pointed out.

4.2.2 Solution Measurements: Influence of Solvent Polarity

To gain a deeper insight into the intrinsic photophysical properties of the dyes PMI-1 and NMI, they were studied in solutions of two different solvents, namely dichloromethane (DCM) and o-xylene, which differ in polarity (DCM is more polar than o-xylene, see Table 7).

Table 7: Polarity measures for DCM and o-xylene. [110]

Solvent	Dipole /D	Dielectric constant ε
Dichloromethane (DCM)	1.60	8.93
o-Xylene	0.64	2.56

The UV-VIS absorption and photoluminescence emission spectra as measured with the Streak camera system together with the photoluminescence decay kinetics are shown in Figure 41. A positive solvatochromism was observed for both dyes: A small red shift in the absorption spectrum along with a more pronounced red shift of the photoluminescence due to the solvent polarity and an increased Stokes shift is typically observed for chromophores with strong dipole moments in the excited state, which is the case for both dyes. A straightforward explanation is that the solvent shell is adjusted to the ground state dipole moment and does not change as fast as the electronic transition occurs

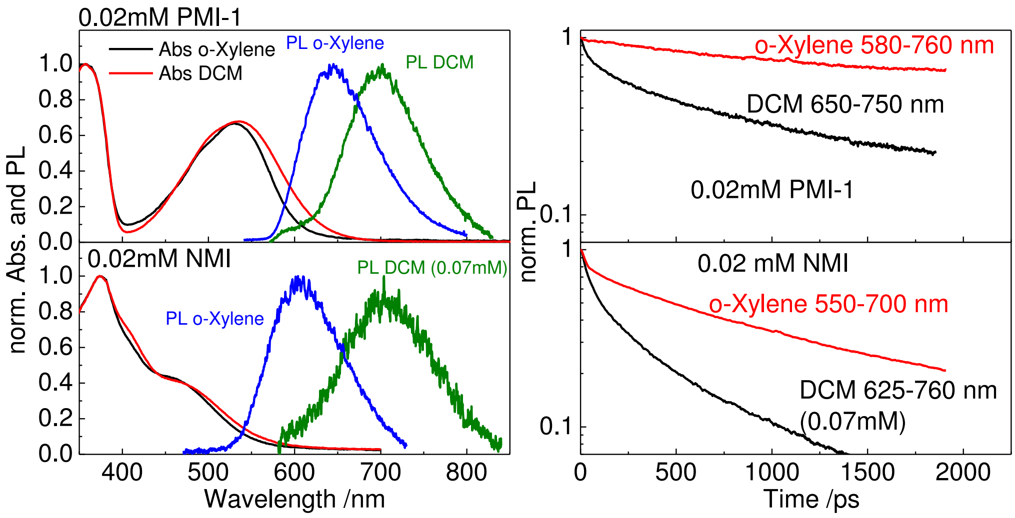

Figure 41: Absorption and emission spectra (left) and photoluminescence decay (right) of PMI-1 (top) and NMI (bottom) in two solvents of different polarity.

upon excitation. The shell then adjusts to the larger excited state dipole moment (typically within less than 10-100 ps) [22], leading to a stabilization of the excited state, which is more pronounced in the more polar solvent. The emission process is again much faster than solvent relaxation, leading to a red-shifted emission in the more polar solvent, as the energy difference between ground and excited state was reduced due to the solvent shell. [22] The photoluminescence decay was faster for the more polar solvent DCM for both dyes. Furthermore, in DCM the measurements implied a decreased photoluminescence quantum efficiency (PLQE), which is typical for dyes exhibiting strong dipole moment changes, leading to an intramolecular charge-transfer state character. [22] The faster measured PL decay arises from an increase of either the non-radiative decay channels or the radiative decay rate, the latter leading not to a decreased PLQE. Such changes can be explained by a more pronounced formation of an intramolecular charge-transfer state in the higher polar solvent. As this state is electronically different from the local exciton formed mainly in the less polar solvent, both rates can be altered. If the fluorescence decay occurs on the order of the solvent relaxation, a time-dependent decay rate of both states can be observed leading to multiexponential decay characteristics. [22] In fact, the more complex behavior in DCM (less monoexponential character) is a sign of the more pronounced solvent relaxation effect. The fluorescence red shift for NMI was stronger than for PMI-1 (see Table 8) and the PL decay was faster for NMI, both indicating a stronger dipole moment change and thus a stronger charge-transfer character for NMI. This agrees very well with TDDFT results on the dipole moment changes, that delivered a $\Delta\mu$ of 32 D for PMI-1 and 45 D for NMI (both pointing away from the anchoring group), i.e. a ~1/3 increase of the dipole moment change for NMI, [101] agreeing qualitatively with the differences in the PL shifts.

Table 8: Photoluminescence maxima of dyes depending on the solvent used.

PL	**PMI-1**	**NMI**
o-Xylene	1.91 eV	2.01 eV
DCM	1.77 eV	1.75 eV
ΔE	0.14 eV	0.26 eV

Having identified the influence of the solvent polarity on the absorption and photoluminescence, the influence of the polarity on the transient absorptions is investigated next.

Figure 42 compares the transient absorption spectra of PMI-1 and NMI in DCM and o-xylene. Depending on the solvents, similar differences were observed in the transient spectra of both dyes. In o-xylene, the spectra exhibited stimulated emission, which becomes apparent when the TA spectra are compared to the PL spectra. At early times, the positive ΔT/T-signal obtained in o-xylene extended further to the red than in DCM. From the red shift of the ground state absorption in DCM compared to o-xylene, a more red-shifted ground state bleach in o-xylene was not expected and thus the signal can only be explained by stimulated emission. Additionally, the PL was stronger in o-xylene so that an increased stimulated emission signal was expected. In case of DCM, stimulated emission was expected to occur further in the red as indicated by the PL spectra. As this region is governed by induced absorption, it is not clear whether stimulated emission was present. Nevertheless, the induced absorption in the region of the PL showed a signal shape that implies a superposition with stimulated emission, indicated by the concave shape. The different spectral shapes of the induced absorption signals in DCM and o-xylene could thus originate from the superposition with the polarity dependent stimulated emission,

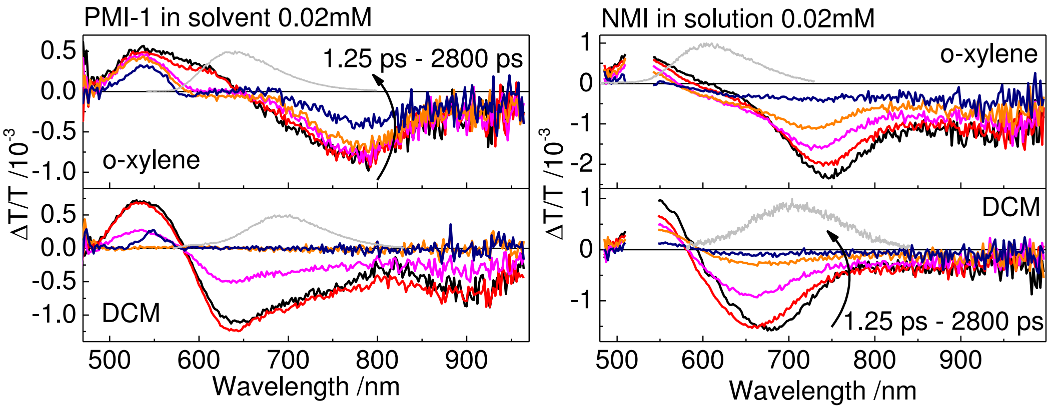

Figure 42: Transient absorption spectra of PMI-1 and NMI in two different solvents. Colors correspond to mean times like: black 1-1.5 ps; red 3-4.5 ps; magenta 27-41 ps; orange 248-372 ps; dark blue 2250-3375 ps. The PL spectra are indicated in grey for comparison.

though an influence of the polarity on the induced absorption spectrum cannot be entirely neglected. Interestingly, spectral shifts of the induced absorption with time were observed for the NMI dye, whereas for PMI-1 only minor spectral changes with time were noticed. The spectral changes could originate from either decays of different unrelated contributions (stimulated emission and induced absorptions) or a more pronounced nuclear relaxation after photoexcitation. [111] A stronger nuclear relaxation is reasonable for NMI as it exhibits a less rigid structure compared to the perylene derivative. Solvent relaxation kinetics are expected to be similar for both dyes, as they mainly depend on the solvent properties and thus cannot explain the shift observed for NMI only. [22]

To further elucidate the dependence of the photophysical properties on solvent polarity, the transient absorption kinetics are compared in Figure 43 and Figure 44. The early-time kinetics of wavelength regions, in which fast changes were observed (usually the region of stimulated emission shown in Figure 44), were comparable in the two solvents, indicating that the kinetics originated from solvent relaxation. This is supported by the indication of a red shift of the PL spectra with time within the first 30-50 ps, which is partially hidden by the instrument response time of the streak camera system and thus not shown. In the entire time range measured, different absorption dynamics were observed depending on the wavelength regions as shown in Figure 43. The differences originate from the overlap of different signals from various species, e.g. stimulated emission, and induced absorption of dark and emissive states, with different charge-transfer character. The presence of different states is obvious, when the kinetics of the photoluminescence decay and the transient absorption are compared, as done in Figure 45. Here, it is evident that the long-time components of the transient absorption signals when scaled properly at least qualitatively resemble the fluorescence decay.

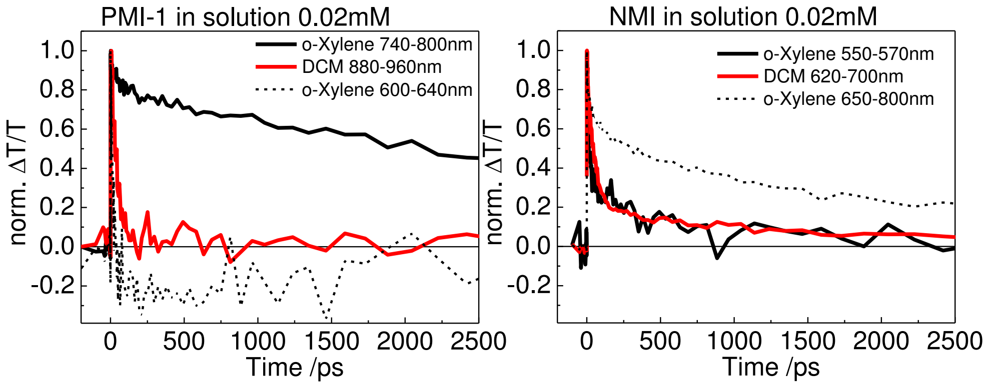

Figure 43: Kinetics at different wavelength regions of PMI-1 (left) and NMI (right) in different solvents.

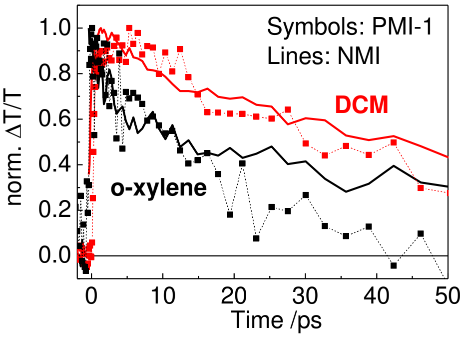

Figure 44: Early-time transient absorption kinetics of NMI and PMI-1 in the two solvents o-xylene (black, 550-570 nm NMI and 600-640 nm PMI-1) and DCM (red, 620-670 nm NMI and 880-960 nm PMI-1), which can be assigned to solvent relaxation.

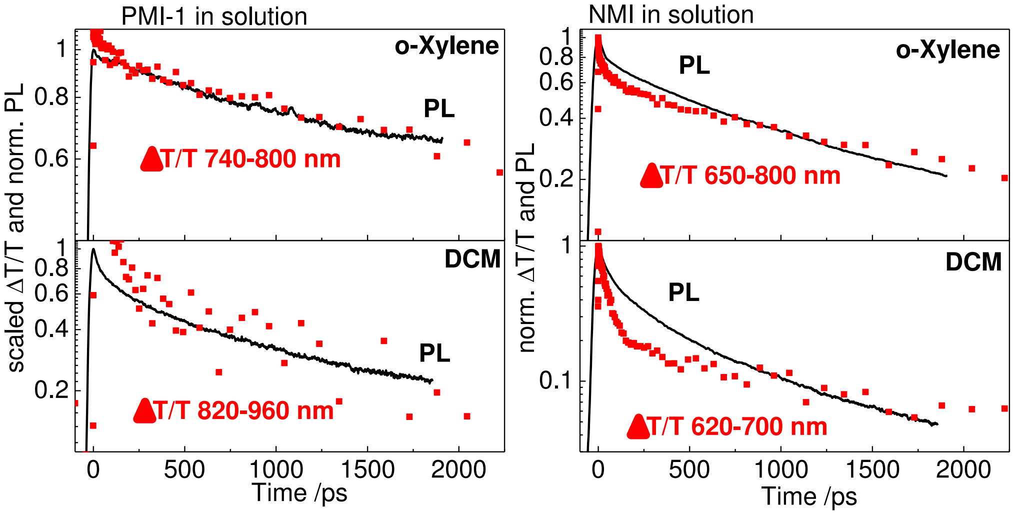

Figure 45: Comparison of transient absorption (scaled arbitrarily to show the similarity of the long-time decay component) and photoluminescence decay (normalized) kinetics of PMI-1 (left) and NMI (right) in the two solvents o-xylene (top) and DCM (bottom).

In summary, the solution measurements showed that both dyes have a strong charge-transfer character as evident by the pronounced influence of the solvent polarity on the photophysical processes. Additionally, the NMI dye exhibited a stronger change of the dipole moment between ground and excited state as determined by the polarity dependent shift in fluorescence and TDDFT calculations, and probably enhanced nuclear relaxation, both indicating a stronger charge-transfer character.

4.2.3 Measurements on Al_2O_3

To further elucidate the photophysical properties of the dyes, especially when attached to a metal oxide, they were investigated on Al_2O_3. Alumina essentially is an insulator rather than a semiconductor and is thus often used as a reference to investigate the dyes' properties when attached to a metal oxide without electronic interaction, i.e. electron injection. [112-114] Its band gap is 8.5-9.9 eV (TiO_2: 3-3.3 eV) and the conduction band edge is much closer to the vacuum level than for TiO_2 (~-0.2 eV for Al_2O_3 vs. ~-4.2 eV for TiO_2). [115]

In Figure 46 and Figure 47, the transient absorption spectra of both PMI-1 and NMI, respectively, attached to Al_2O_3 in absence and presence of Li-TFSI and in the presence of spiro-MeOTAD and Li-TFSI are shown together with the photoluminescence spectra at early and late times. Interestingly, while decaying the PL spectra shift by about 0.1 eV to the red within 1 ns. The delayed PL spectra of PMI-1 on Al_2O_3 closely resembled the spectra observed in DCM. For NMI, the PL spectra on Al_2O_3 with Li-TFSI resembled the spectra in DCM, whereas for PMI-1 the delayed spectra were even further shifted to the red. The shifts between the samples with and without Li-TFSI were attributed to the accumulation of Li^+ at the interface, changing the local electrical environment thereby leading to a red shift of the emission spectra. The positive charge of the Li^+-ions at the interface makes the dipole with the negative charge close to the anchoring group, which is attached to the Al_2O_3, energetically more favorable. The localization of Li-TFSI at the interface is in this case supported by the changes in absorption seen upon the addition of Li-TFSI (see Figure 48), similar to the

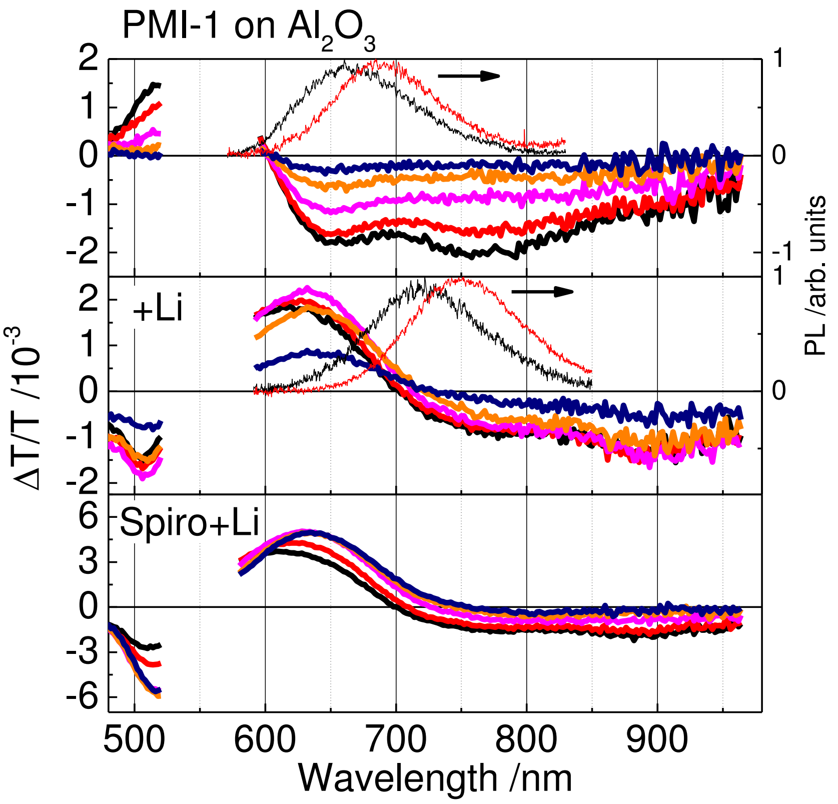

Figure 46: Transient absorption spectra of PMI-1 attached to Al_2O_3 with additives as stated. Colors refer to mean times as: black 1.25 ps, red 3.8 ps, magenta 35.7 ps, orange 334 ps, dark blue 3125 ps. The normalized initial PL spectrum (thin black line) and the normalized PL spectrum after ca. 1.3 ns (thin red line) are shown for the two samples without hole transporter.

argumentation as in section 4.1 and [71]. However, the transient PL shift cannot be explained by the static presence of Li^+ at the interface. A possible explanation is a rearrangement of the neighboring dyes or the dye itself in the local Coulombic field due to the increased dipole moment in the excited state. However, most probably, chromophores embedded in different environments emitting at different wavelengths with different lifetimes led to the impression of a transient shift.

The transient absorption spectra of PMI-1 on Al_2O_3 (Figure 46, top panel) roughly resembled the spectra observed on TiO_2 (Figure 5 of the manuscript in section 4.1), with minor differences in the spectral components that accounted for the three-phasic decay due to the different local environments.

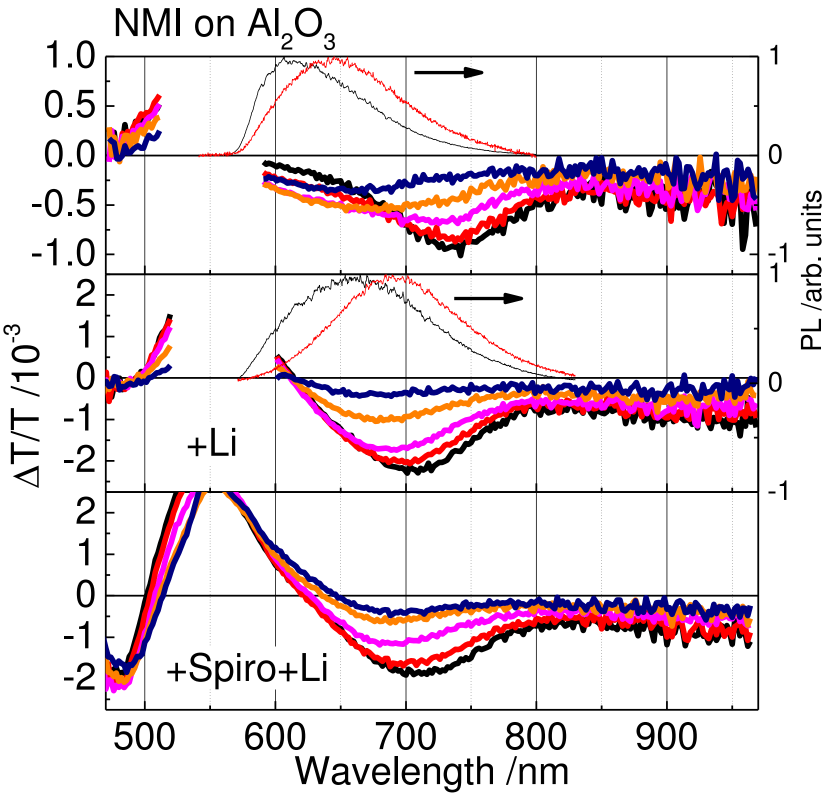

Figure 47: Transient absorption spectra of NMI attached to Al_2O_3 with additives as stated. Colors refer to mean times as: black 1.25 ps, red 3.8 ps, magenta 35.7 ps, orange 334 ps, dark blue 3125 ps. The normalized initial PL spectrum (thin black line) and the normalized PL spectrum after ca. 1.4 ns (thin red line) are shown for the two samples without hole transporter.

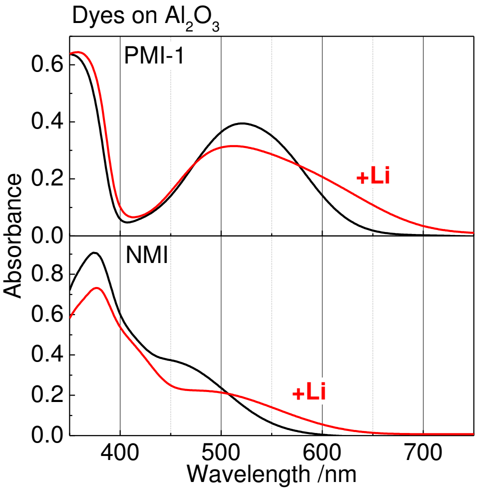

Figure 48: Absorbance of the two dyes attached to Al_2O_3 with and without Li-TFSI.

The NIR spectra and kinetics shown in Figure 49 were very similar for TiO_2 and Al_2O_3, implying that on TiO_2 PMI-1 is unable to inject electrons. For NMI, the spectra and dynamics in the visible on Al_2O_3 (Figure 47, top panel) and TiO_2 (Figure 36, top panel) were similar but the delayed spectra showed a relatively larger amplitude on Al_2O_3, reflecting a longer lived part of the primary excitation that was partially quenched on TiO_2 and replaced by a weaker induced absorption of the dye cation. However, the spectra in the NIR shown in Figure 50, looked different for the two metal oxides. Clearly, a cation signal was observed on TiO_2, whereas on Al_2O_3 the rather flat signature of the exciton was observed. This supports that, in contrast to PMI-1, some NMI dyes were able to inject on TiO_2 even without Li-TFSI. The kinetics in this wavelength region were slightly different for the two metal oxides. Previously, it was argued that the decaying signal in the NIR implied recombination of generated charges. The difference in the kinetics would also support that. However, the differences in the first 30 ps could also point towards delayed injection on TiO_2. Moreover, the fact that only a small difference in dynamics was observed indicates that the main species contributing to the decay could still be excited dyes recombining to the ground state without any injection. Although the origin of

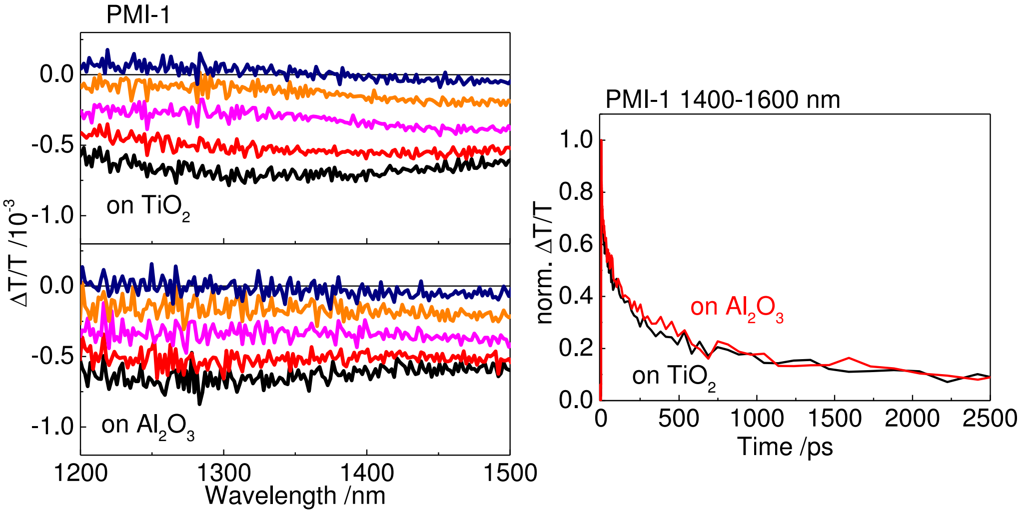

Figure 49: Transient absorption spectra in the near infrared of PMI-1 attached to TiO_2 (left, top) and Al_2O_3 (left, bottom) along with the kinetics (right). Mean times are: black 1.25 ps, red 3.8 ps, magenta 35 ps, orange 320 ps and dark blue 3 ns.

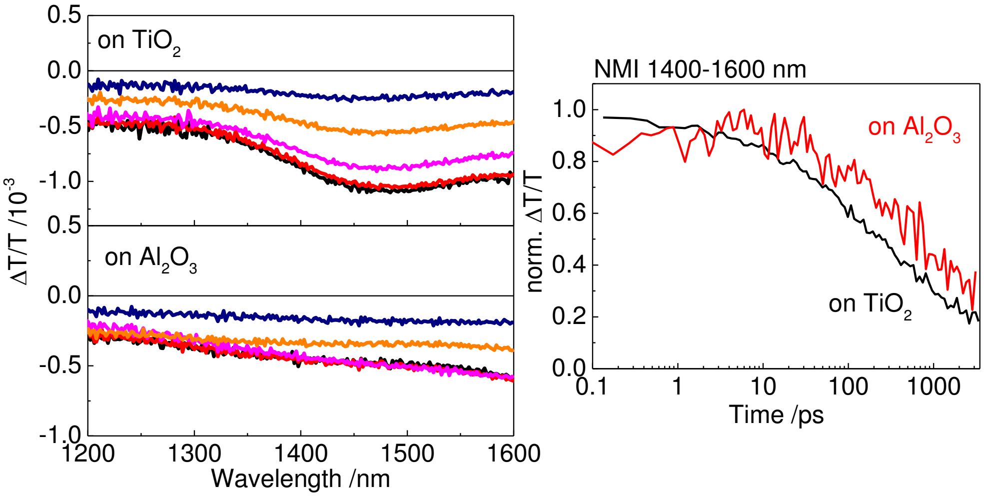

Figure 50: Transient near infrared absorption spectra of NMI attached to TiO$_2$ (left, top) and Al$_2$O$_3$ (left, bottom), along with the respective kinetics (right). Colors in the spectra refer to mean times as: black 1.25 ps, red 3.8 ps, magenta 34 ps, orange 310 ps and dark blue 2.8 ns.

the decaying signal cannot unambiguously be determined, the spectra clearly indicate that some dye cations were formed.

The middle panel of Figure 46 depicts the spectra of PMI-1 attached to Al$_2$O$_3$ in the presence of Li-TFSI. The similarity to the spectrum on TiO$_2$ with Li-TFSI is intriguing (compare to Figure 5 of the manuscript in section 4.1). It has been previously reported that alumina exhibits unoccupied sub-band-gap surface states. [116, 117] Thus, especially if modified with Li$^+$-ions, Al$_2$O$_3$ cannot be treated as an electronically inactive metal oxide anymore and electron injection into trapped surface states can become possible. [118] On the other hand, Li-TFSI changes the local electrical environment, which could lead to changes in the relative contributions of the primary excitations, e.g. stabilize the charge-transfer state character, similar to the observation in the more polar solvent DCM. [119] Therefore, results obtained on samples with dye attached to Al$_2$O$_3$ in the presence of Li-TFSI have to be interpreted carefully. Indications of a possible charge transfer to Al$_2$O$_3$ were: i) The occurrence of long-lived spectral signatures similar to the cation spectrum with a flat peak around 900 nm, ii) the Stark like feature in the blue region that implied a change of the ground state absorption of dyes due to a local electric field that originates from charges in Al_2O_3 or an enhanced charge-transfer state dipole of neighboring excited dyes due to Li-TFSI. On the other hand, the NIR spectra (Figure 51) showed differences between alumina and titania: On TiO_2 the spectra were more structured and had a similar shape throughout the entire timescale, whereas on Al_2O_3 the spectra changed with time and the signals differed to the ones observed on TiO_2 with Li-TFSI. This indicates that on TiO_2 charge injection into the metal oxide and formation of free charges occurred, whereas on Al_2O_3 only an intramolecular charge-transfer state or a charge-transfer state localized between the dye and surface states in Al_2O_3 was observed. This is supported by the difference seen in the kinetics of the two samples, shown in the right graph of Figure 51. Whereas on TiO_2 a decay assigned to dyes not affected by Li-TFSI together with a constant background of induced absorption of charges that had been created instantaneously was observed, on Al_2O_3 a signal increase in the first few picoseconds could be monitored. Assuming a similar situation on Al_2O_3 as for TiO_2, i.e. some dyes being affected by Li-TFSI and some not, kinetics of both pools should be observed. The increase can thus be interpreted either as a delayed charge injection or an internal conversion into

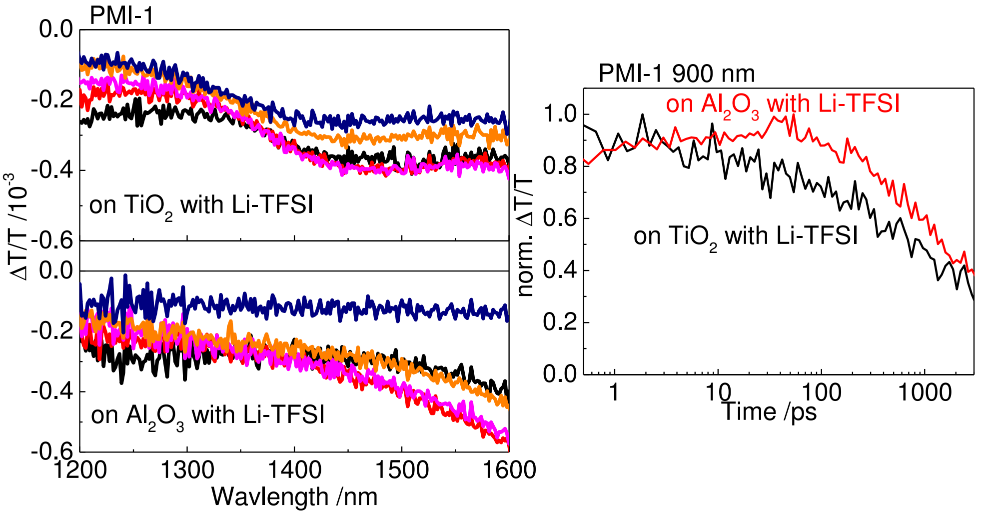

Figure 51: Transient absorption spectra in the NIR of PMI-1 attached to TiO_2 (top left) and Al_2O_3 (bottom left) in the presence of Li-TFSI and kinetics around 900 nm (right). Colors in the spectra refer to mean times as: black 1.25 ps, red 3.8 ps, magenta 34 ps, orange 310 ps and dark blue 2.8 ns.

the charge-transfer state that later recombines, caused by the dyes that were influenced by Li-TFSI. For PMI-1 it is thus not clear if Li-induced charge injection into Al_2O_3, a charge-transfer state between surface states in Al_2O_3 and the dye enabled by Li-TFSI, or an intramolecular charge-transfer state stabilized and enhanced by the presence of Al_2O_3 and Li-TFSI was observed.

For NMI, the situation is comparable. Whereas the spectra in the visible were rather similar in the presence of Li-TFSI for TiO_2 and Al_2O_3 with only subtle differences (compare Figure 47 and Figure 36, middle panels), the NIR spectra were different, as can be seen in Figure 52. The kinetics in the NIR differed strongly, which is caused by the stronger absorbance of the dye cation in this wavelength region. Interestingly, the kinetics in the visible wavelength regions not affected by spectral shifts were similar for the Al_2O_3 samples with and without Li-TFSI (not shown), indicating that they were mainly governed by signals of dyes not influenced by Li-TFSI, or that the Li-TFSI was not affecting the transient absorption kinetics as strongly as in PMI-1. At longer times, the signal from the dye on Al_2O_3 decayed much faster than on TiO_2 as exemplarily shown in Figure 53 for NMI. Together with the observation of fluence depen-

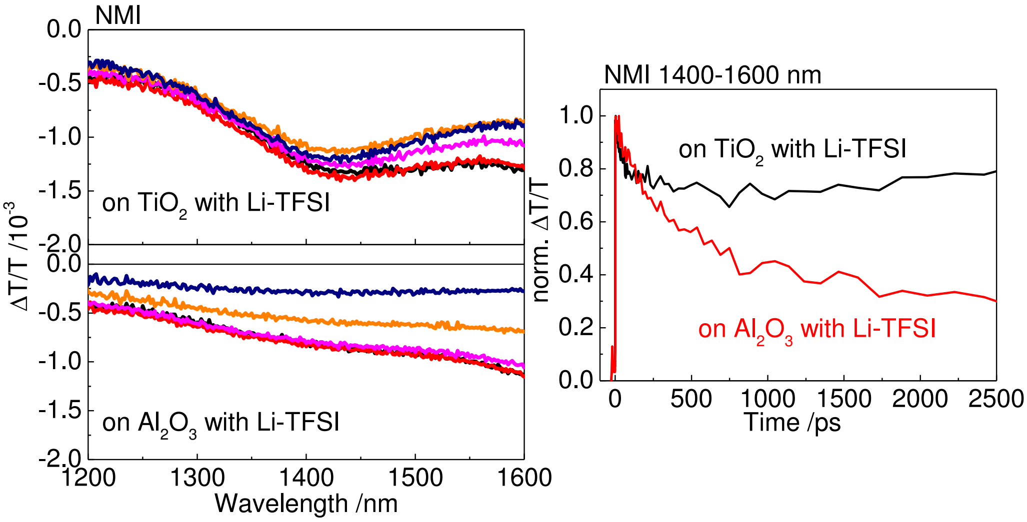

Figure 52: Transient absorption spectra in the NIR of NMI attached to TiO_2 (top left) and Al_2O_3 (bottom left) in the presence of Li-TFSI and kinetics around 1500 nm (right). Colors in the spectra refer to mean times as: black 1.25 ps, red 3.8 ps, magenta 34 ps, orange 310 ps and dark blue 2.8 ns.

dent recombination on TiO_2 but not on Al_2O_3, which is a clear signature of free charges in TiO_2, the assignment to an intramolecular charge-transfer state or a charge-transfer state between Al_2O_3 and the dye, both stabilized by Li-TFSI, becomes more likely. Hence, a charge injection into sub-band-gap surface states in Al_2O_3 generated through Li-TFSI cannot entirely be ruled out. The differences between PMI-1 and NMI point to different effects of the local environment on the charge-transfer character of the dyes induced by Li-TFSI: whereas the addition of Li-TFSI seems not to affect NMI strongly, a pronounced difference for PMI-1 could be observed (especially when the samples Al_2O_3 and Al_2O_3 with Li-TFSI were taken into consideration). The charge-transfer character of NMI appears to be strong upon photoexcitation at the excitation wavelength and thus cannot be further enhanced by Li-TFSI, whereas this is possible for PMI-1. Furthermore, the effect of Li-TFSI can depend on the excitation wavelength. As the excitation wavelength was similar for both dyes and thus rather at the red edge of the absorption spectrum of NMI and in the middle of the absorption spectrum of PMI-1, the observed differences can be explained by a stronger population of the intramolecular charge-transfer state upon photoexcitation of NMI. A dependence of the photophysical properties on the excitation wavelength was not investigated in this thesis, but is interesting for future studies.

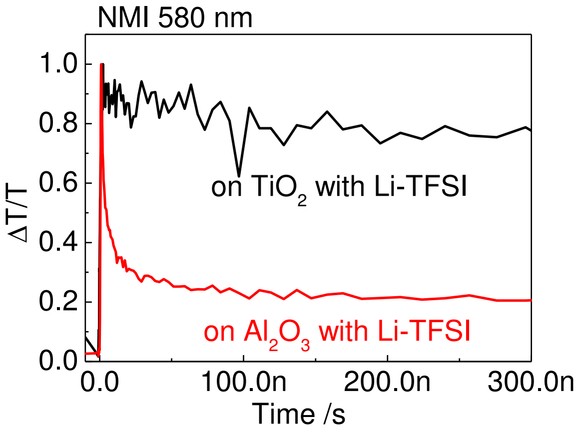

Figure 53: Long-time recombination of NMI on TiO_2 and Al_2O_3 with Li-TFSI.

Finally, in the following part samples of the dye attached to Al_2O_3 in the presence of the hole transporter spiro-MeOTAD and Li-TFSI are investigated. The spectra of both dyes attached to Al_2O_3 in the presence of spiro-MeOTAD and Li-TFSI (Figure 46 and Figure 47 bottom panel) exhibited a strong Stark feature in the blue spectral region. Together with the remaining signal around 700 nm for the NMI sample, which can be assigned to the spiro cation [109], it appears that hole transfer from the excited state of the dye to the hole transporter occurred. However, a feature of the dye anion could not be observed. For PMI-1 the region in which the dye anion absorbs was superimposed by the rather strong Stark signal. For NMI, an induced absorption at 700 nm was observed, that was mainly assigned to the creation of holes in the spiro, although it could also contain contributions of the dye anion. However, due to the possibility of charge transfer to surface states in Al_2O_3 it is possible that the dye anion is not stable and rather injects charges into these states, leaving no optical trace behind. Comparing the normalized kinetics in the NIR as shown in Figure 54, hardly any differences between the traces of PMI-1 attached to TiO_2 or Al_2O_3 in the device-like structure could be observed, indicating that the preceding hole transfer from excited states of the dye to spiro can already account for the charge generation in the solar cell. For NMI, differences pointing towards a more efficient charge generation when the dye is attached to TiO_2 were observed. This difference could be a hint to an explanation for the different

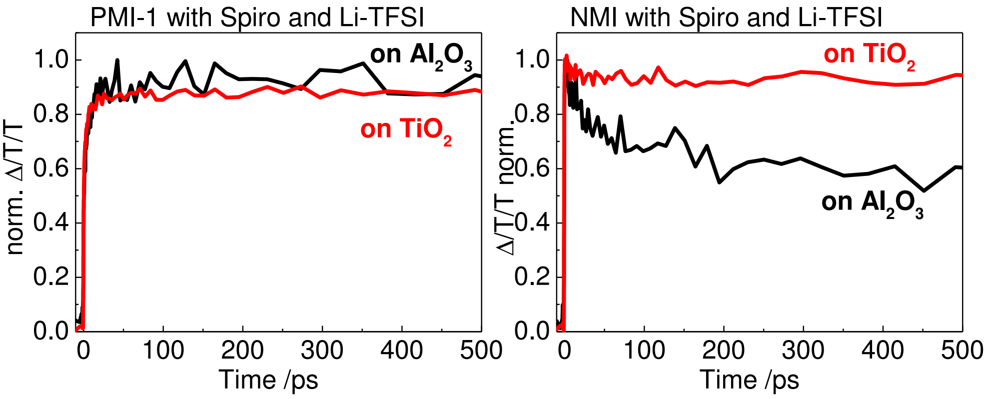

Figure 54: Transient absorption kinetics at the induced absorption from 1400-1600 nm for PMI-1 (left) and NMI (right) attached to TiO_2 and Al_2O_3 in the presence of the hole transporter spiro-MeOTAD and Li-TFSI.

photovoltaic performances of the dyes: Whereas NMI works rather efficiently via the normal route of charge generation, i.e. injection of electrons into the TiO_2 from the excited state and subsequent dye cation regeneration (type I), PMI-1 requires preceding hole transfer (type II) to achieve the observed efficiencies. While the quantum efficiency of this preceding hole transfer can still be high, it is possibly not as effective as the normal charge generation route and thus can, even if it helps to overcome injection problems, account for the differences.

In conclusion, measurements on Al_2O_3 helped to understand the charge generation in more detail, but as the actual electronic interaction of the dyes with Al_2O_3, especially in the presence of Li-TFSI, is not well understood, the results have to be interpreted carefully.

With the knowledge gained in the above sections let us now turn to a short study of the same samples with time-resolved photoluminescence to point out the difficulties of identifying and investigating charge transfer when only the radiative species are considered.

4.2.4 Time-resolved Photoluminescence Measurements and Implications for Charge Generation

In the following, additional time-resolved photoluminescence (PL) data of PMI-1 and NMI is presented. Some of the PL data has already been presented in previous sections, especially the measurements in solution as well as some spectra of films. This part expands these results mainly by considering the kinetics in films along with some additional spectral information not provided previously. The aim of this part is to further support the above findings and to discuss why photoluminescence measurements not necessarily reflect the charge generation dynamics. All samples were measured with the fast sweep unit of the streak camera system with excitation at 400 nm (the system is limited to this excitation wavelength). Thus, differences to the transient absorption measurements can also occur due to the higher photon energy used for excitation. In addition, the samples with hole transporter already show some absorption of the spiro-MeOTAD in the excitation wavelength range, which can also influence the photophysical behavior.

Figure 55 shows the photoluminescence decays of PMI-1 on Al_2O_3 for three different samples (in absence and presence of Li-TFSI and with spiro-MeOTAD and Li-TFSI). The PL is shifted to the red (see Figure 46) and quenched upon the addition of Li-TFSI, contradicting the prolonged transient absorption kinetics shown in Figure 51. The longer-lived signal observed in the absorption kinetics was assigned to delayed generation of cations from a charge-transfer state with surface states in Al_2O_3, or intramolecular charge-transfer states. The PL data agrees, if it is assumed that, for the dyes affected by Li-TFSI, the PL is entirely quenched (due to inter- or intramolecular charge transfer) or shorter-lived and red-shifted. The remaining PL is then caused by both pools (Li-affected and not Li-affected) with an overall faster decay.

In the presence of spiro-MeOTAD, the photoluminescence was strongly quenched and decayed on a much faster timescale, an indication of hole injection from the excited dye to the spiro. The quenching could also arise from stronger non-radiative decay channels due to the different environment of the chromophores. However, supported by the observations in transient absorption spectroscopy, it appears that the hole transfer does play a role in the PL quenching of this sample.

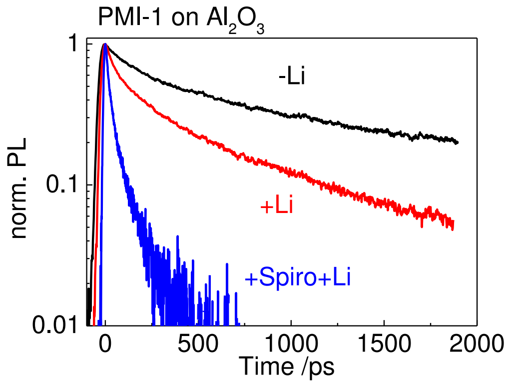

Figure 55: Photoluminescence decays of PMI-1 attached to Al_2O_3 with and without Li-TFSI and with spiro-MeOTAD and Li-TFSI.

For the NMI-dye, the situation was different, as shown in Figure 56. Only a slight difference between the Al_2O_3 sample with and without Li-TFSI was observed. This is in good agreement with the transient kinetics that did not change much upon the addition of Li-TFSI, supporting the idea that Li-TFSI does actually not influence the dye's charge-transfer character as much as for PMI-1. In the presence of the hole transporter, a further red-shifted PL spectrum was observed (Figure 56, left graph). For all other samples, the PL spectra obtained in the presence of spiro and Li-TFSI were similar to the ones with Li only. A reasonable explanation for this red shift is that NMI can form an emissive intermolecular charge-transfer state with spiro (NMI^--$spiro^+$). Even if only a few of those charge-transfer states were able to emit, e.g. due to a particular orientation between dye and spiro molecule or a low oscillator strength of the transition, this is clear evidence for the hole injection from the dye to the spiro on a metal oxide surface. It additionally implies that the negative charge still resides at the dye, as a charge-transfer state emission from an alleged state of $Al_2O_3^-$-$spiro^+$ should be visible in the PMI-1 sample as well and should not depend on the attached dye. It therefore proves the possibility of preceding hole transfer from the excited dye to the hole transporter on the metal oxide.

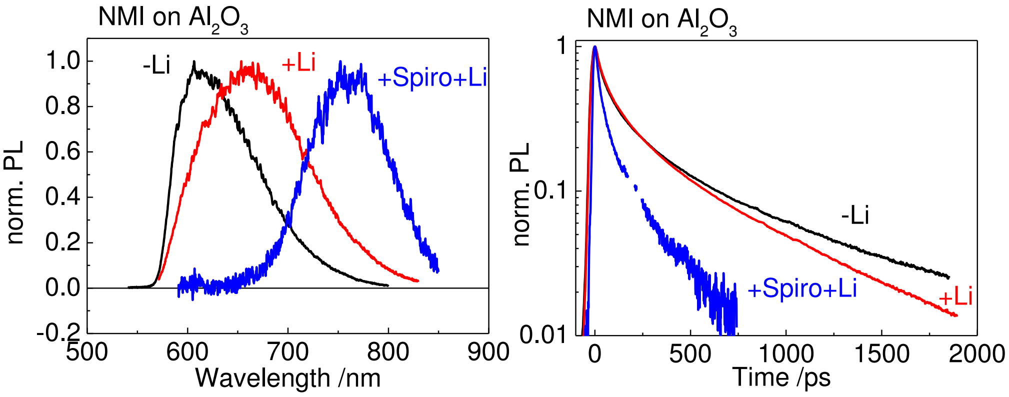

Figure 56: Photoluminescence spectra (at zero time) and PL decays of NMI attached to Al_2O_3 with and without Li-TFSI and with spiro-MeOTAD and Li-TFSI.

The photoluminescence decay on TiO_2 (Figure 57) differed significantly for both dyes compared to the PL decays on Al_2O_3. For all samples, the PL was much faster quenched (note the different time range of the graphs). From this measurement and the difference observed between Al_2O_3 and TiO_2, one can conclude that efficient charge generation took place on TiO_2, which contradicts the findings from the quasi-steady-state PIA and transient absorption measurements. However, it appears that TiO_2 influenced the PL quenching in a different way than Al_2O_3, but not through quenching by free charge generation. Possible reasons can be different binding modes (type of binding, angle and position in general), along with different interactions between the dye molecules or different local electric environments. All these influences can lead to an alteration of the non-radiative and radiative decay channels, thereby changing the observed photoluminescence decay time. [22] Therefore, time-resolved photoluminescence measurements not necessarily reflect the charge injection dynamics leading to free charges in this system, especially considering that they only probe the emissive states that could reside on a minority of molecules. Interestingly, the PL decay of PMI-1 on TiO_2 is not very different for the samples without and with Li-TFSI. A small difference appeared at early times, which can be explained by the instrument response or by background stray light from the excitation pulse that altered the normalization factor. In fact, after 50 ps, the kinetics were similar. This supports the hypothesis that the

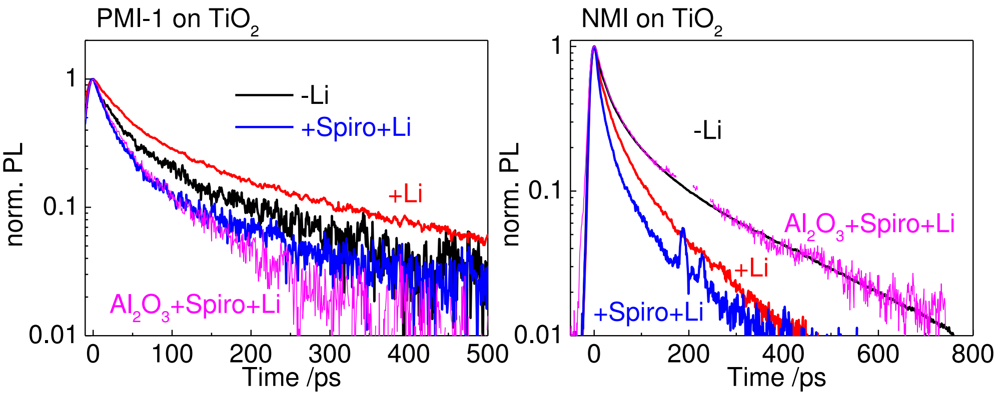

Figure 57: Photoluminescence decays of PMI-1 and NMI attached to TiO_2 with and without Li-TFSI and with spiro-MeOTAD and Li-TFSI. For comparison, the decay of the Al_2O_3 sample with hole transporter and Li-TFSI is shown as well.

dyes that were influenced by Li-TFSI did not show any fluorescence as they were able to inject ultrafast, whereas the second pool of dyes not affected by Li-TFSI showed similar characteristics as the sample without Li-TFSI. A possible explanation for the difference observed in the first 50 ps is that there are some dyes influenced by Li-TFSI that did not inject, e.g. due to a binding site that does not allow injection. Upon the addition of spiro, the PL is further quenched, although the differences were only observed at early times. This indicates a further quenching process. The similarity of the delayed decay shows that only a few dyes that did not have a spiro molecule in the vicinity and thus decayed as if no spiro was present were monitored. Again, the limitations of PL quenching experiments to obtain information on the charge generation in this system became obvious. It may be that the kinetics monitored just reflected a small fraction of dyes that were not participating in any charge generation at all. Compared to the Al_2O_3 sample with spiro and Li-TFSI, the decays were similar, which indicates that the charge generation via preceding hole transfer from the excited dye is similar in both samples.

For NMI the situation is different. The sample with Li-TFSI showed a faster quenching indicating that more dyes might have been affected by Li-TFSI and implying that almost all dyes, i.e. the ones with and the ones without Li-TFSI in the vicinity, were now participating in charge transfer. As the charge transfer was already possible in the absence of Li-TFSI, this appears reasonable. The addition of spiro quenched the remaining dyes leading to a further decrease of the fluorescence. For this particular dye, the PL measurements thus better reflected the injection characteristics observed by the other techniques. For comparison, the decay in the Al_2O_3 device-like structure is also shown in the right panel of Figure 57. It showed a slower decay compared to the sample with TiO_2. As this emission was assigned to a charge-transfer state between spiro and dye, it rather reflects the recombination of this state, which is expected to be longer.

In summary, it could be shown, that even with the limitations of the interpretation of photoluminescence data due to the above mentioned reasons, it can be helpful to support the transient absorption analysis. However, PL quenching experiments alone would not have been sufficient to understand the charge generation of PMI-1.

4.2.5 Influence of Additive ID662

In order to get good efficiencies, the solar cells contain apart from Li-TFSI also other additives such as 4-*tert*-butylpyridine (tBP) or other surface active molecules that increase the open-circuit voltage. The TiO_2 samples used for the studies of PMI-1 and NMI all contained a surface active molecule termed ID662 (BASF) instead of the often used tBP. It is applied to the TiO_2 layer before it is dipped in the dye solution. [120] Its purpose is to increase the open-circuit voltage, usually accompanied by a decrease in short-circuit current, however in sum leading to a higher efficiency. The following short section highlights the most important results regarding the influence of this additive (abbreviated as "add" in the graphs) for PMI-1 and NMI, by comparing quasi-steady-state PIA and ns-µs transient absorption measurements of samples prepared with and without the additive.

Figure 58 shows the quasi-steady-state PIA spectra of PMI-1 and NMI attached to TiO_2 with and without the additive and Li-TFSI. Samples with hole transporter were not considered in this thesis but are in the focus of a further study. Interestingly, the PIA measurement of PMI-1 attached to TiO_2 without any additive showed a signal, even if it was small. The additive (in the absence of Li-TFSI) thus led to a suppression of electron injection, as in the sample with the additive no PIA signal was observed at all (compare section 4.1, manuscript Figure 3). Hence, the acceptor states in TiO_2 or the dye itself were modified in such a way, that injection could not occur any more, indicating a shift in the conduction band [121] or the passivation of sub-band-gap states of TiO_2 [122]. The addition of Li-TFSI, as discussed in the previous section, compensated for this deficiency by facilitating injection. In fact, the effect of Li-TFSI was strong-

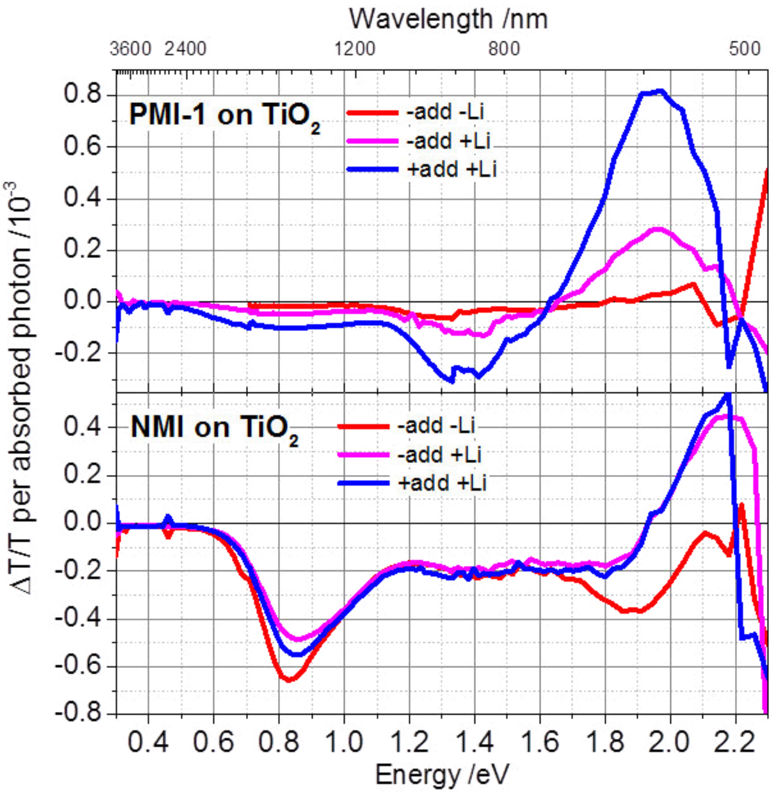

Figure 58: Quasi-steady-state PIA spectra of the two dyes depending on the presence (+) and absence (-) of the additive ID662 (add).

er for the sample with the additive, as indicated by the larger PIA signal. However, the PIA signal strength is not a direct measure of the injection efficiency, as the signal strength depends on the amount of states created (which is a measure for the injection efficiency, if the states are charges), the absorption cross section of the respective states (assumed to be unchanged in all cases) and the recombination dynamics (a faster recombination resulting in smaller signals), so that a change in recombination kinetics can also lead to a change in the signal amplitude in the PIA measurement.

The ns-µs recombination dynamics of electrons in the TiO_2 and the dye cation is depicted in Figure 59. It showed a slightly decreased recombination for the sample with the additive that could account for the increased PIA signal in the presence of the additive (apart from a better injection). For PMI-1 the influence of the additive can thus be summarized as: Decrease (suppression) of injection

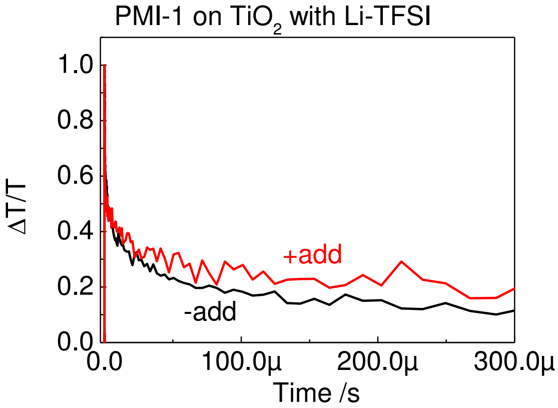

Figure 59: Long-time recombination kinetics of electrons in TiO_2 and dye cations of PMI-1 with and without the additive ID662.

in the absence of Li-TFSI due to the influence on the TiO_2, which is compensated by the addition of Li-TFSI, and reduction of electron-dye-cation recombination. For NMI, the influence of the additive on the PIA signals is rather negligible, probably because the injection potential is higher due to the bluer absorption and lower absolute ionization potential of the photoexcited state. Interestingly, the trend regarding recombination suppression as seen for PMI-1 was not observed for NMI. A suppression of electron-hole recombination in the assembled solar cell, which could also account for a higher open circuit voltage and overall better efficiency, is plausible and has to be investigated in the future. Unfortunately, the influence of Li-TFSI cannot be studied in the solar cell itself, as it not exclusively influences the injection behavior but rather alters the transport properties of the spiro-MeOTAD hole transporter as well, a reason why the solid-state DSCs do not function in the absence of Li-TFSI at all. [73]

4.2.6 Conclusions

The two dyes investigated, namely PMI-1 and NMI, differed in their photophysical and photovoltaic behavior. PMI-1 exhibited a red-shifted absorption spectrum but lower internal quantum efficiency. The investigation of both dyes with quasi-steady-state and transient photoinduced absorption spectroscopy yielded the following results: A strong influence of Li-TFSI on the charge injection was observed, which was stronger for the red-absorbing dye PMI-1. This behavior was assigned to a stronger dependence of the injection ability on the acceptor levels of TiO_2, which were altered by Li-TFSI, and to an effect of the local electric environment on the dye's photophysical properties (charge-transfer character). The findings were supported by measurements on Al_2O_3 and partially by time-resolved photoluminescence measurements. The injection of the blue absorbing dye NMI was less dependent on the presence of Li-TFSI, which was explained by the stronger charge-transfer character in the absence of Li-TFSI and a higher driving force for injection. In case of PMI-1, the photophysics of the dye could be represented by two pools, one of which was influenced by Li-TFSI where the dyes were able to inject and the other which was unaltered as if no Li-TFSI was present and no injection was possible. Interestingly, the second pool could contribute to charge generation via a second route: Instead of electron injection from the excited dye to TiO_2 and subsequent dye regeneration by the hole transporter, the excited state of the dye was quenched by electron transfer from the hole transporter (or equally hole injection from the excited dye into the hole transporter) and subsequent electron injection into TiO_2. This preceding hole transfer (type II charge generation or reductive quenching), thus compensated the lower injection efficiency of PMI-1. NMI was also capable of type II charge generation, but due to its ability to inject electrons into TiO_2 even in the absence of Li-TFSI, did not as much depend on this alternative route of charge generation. This, being the main difference between both dyes, led to the conclusion that the preceding hole transfer, even if it facilitates charge transfer and boosts the exciton splitting efficiency, might not be as efficient as the common way of charge generation, considering the differences in internal quantum efficiency of the two dyes. Besides, the free charge recombination dynamics were similar for the two dyes. However, as will be shown later, even if the recombination appeared to be similar, differences in the efficiency of extracting charges may be present (see chapter 4.4).

4.3 The Effect of Donor Groups at the PMI Bay Position

The following section describes experiments on two perylene monoimide dyes, namely PMI-2 and PMI-2-MeO, of which the latter carries electron-donating methoxy side groups attached to the PMI bay position (see structures in Figure 60). The additional side groups of PMI-2-MeO led to a rise of the HOMO and LUMO level by ~0.2 eV as determined by cyclic voltammetry in solution. The band gap (as determined by UV-VIS absorption) was similar, and the molar extinction coefficients were about 25.000 $M^{-1}cm^{-1}$ for both dyes. [123] The LUMO of PMI-2, also known as ID176, is close to the TiO_2 conduction band edge. [64] By raising the LUMO level as is the case for PMI-2-MeO, the injection into TiO_2 should become more efficient. However, in a solid-state dye-sensitized solar cell the performance of PMI-2-MeO turned out to be much worse than that of PMI-2 (see Figure 60). Furthermore, a strong influence of Li-TFSI on the absorption spectra was observed, as already reported by others. [71] In the following the differences between the two dyes are elucidated by employing steady-state and time-resolved optical spectroscopy in the visible and near-infrared spectral region on device-like structures.

Samples were prepared as described in the experimental section 3.1. For these samples the dye solutions for soaking were prepared at concentrations of 0.5mM in DCM or o-xylene. No obvious influence of the solvent on the photovoltaic performance was observed. The solar cells using one of the two dyes were prepared by the same recipe and sample batch, only the dye solution differed. All samples were soaked overnight. A 15 vol. % spiro solution (177 mg/ml in chlorobenzene with 15 µl 0.6M Li-TFSI in acetonitrile solution per 73 mg of spiro) was used to prepare the hole transporter layer. No additional additives were used. For samples with Li-TFSI and without hole transporter, the spiro was replaced by volume by chlorobenzene in the solution used for spin coating. The measurements were performed by excitation between 520 and 540 nm. Time-resolved photoluminescence was recorded using the streak camera system (section 3.4) with 400 nm excitation.

4.3.1 Steady-state UV-VIS Absorption and Solar Cell Performance

The UV-VIS absorption spectra of the two dyes attached to TiO_2 plus Li-TFSI are shown in Figure 60. Clearly, PMI-2-MeO absorbed less light than PMI-2 when attached to TiO_2. Two likely explanations are: i) the oscillator strength of PMI-2-MeO was weaker compared to PMI-2 when adsorbed to TiO_2, ii) less dye was bound to TiO_2. The typical photovoltaic performance and J-V-curves of both dyes are summarized in Figure 60. The theoretically obtainable short circuit current of PMI-2-MeO was calculated from the absorption spectra to be about ¾ of the short circuit current of PMI-2, which cannot explain the large differences in the measured J_{SC}, as for PMI-2-MeO it is less than half of that of PMI-2. Apart from the J_{SC}, the open circuit voltage was also decreased for PMI-2-MeO, whereas the fill factors were similar. It is worth mentioning, that with PMI-2 better efficiencies have been achieved in solid-state DSCs. [64] In this study, the device efficiency was not entirely optimized, as the aim was a comparative study of the two dyes.

In the following, the question why this efficiency difference is observed is addressed by quasi-steady-state photoinduced and transient absorption spectroscopy. For both dyes the absorption spectra changed upon the addition of Li-TFSI. An explanation for the change is the accumulation of Li^+-ions at the TiO_2-dye interface or the intercalation of Li^+ into TiO_2 as described in sections 4.1 and 4.2. Evidence is again provided by TDDFT [101] calculations that were used to determine the field-induced change in absorption. Figure 61 shows the calculated change of the absorption spectrum for PMI-2 for a positive electric field, i.e. a field pointing away from the TiO_2 surface, as induced by positive ions (Li^+) on TiO_2. Clearly, a second shoulder due to a relative shift of the two absorption peaks occurred as observed in the experimentally measured spectrum shown in Figure 60. The influence of Li-TFSI appeared to be stronger for PMI-2 than for PMI-2-MeO, which can be explained by a smaller ground state dipole moment of PMI-2-MeO, as discussed later.

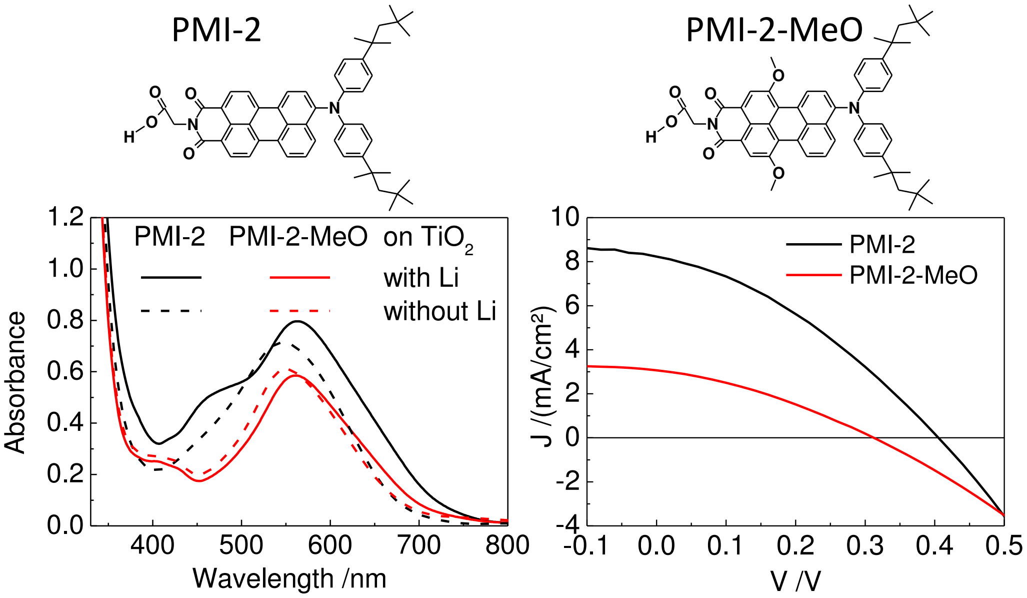

	V_{OC} /V	J_{SC} /(mA/cm²)	FF	Efficiency /%
PMI-2	0.4	8.2	0.35	1.15
PMI-2-MeO	0.32	3.1	0.32	0.31

Figure 60: The structure of the two dyes PMI-2 and PMI-2-MeO together with the absorption spectra of the dyes attached to TiO_2 with and without Li-TFSI and typical current voltage curves and solar cell performance of solid-state DSCs employing the two dyes.

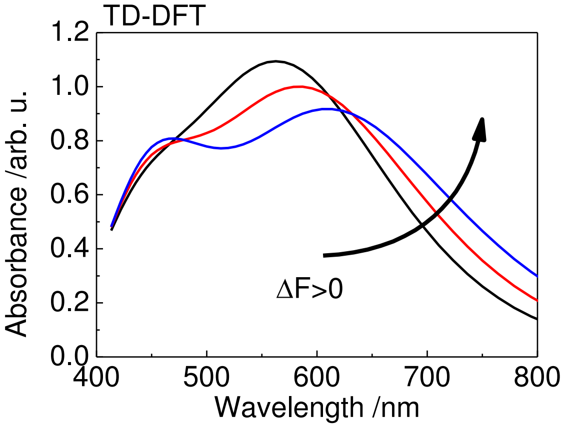

Figure 61: Influence of an electric field change pointing away from the TiO_2, as expected due to the accumulation of Li^+ at the interface, on the absorption spectra of PMI-2 calculated with time-dependent density functional theory. [101]

4.3.2 Quasi-steady-state PIA

The quasi-steady-state PIA spectra of dyed TiO2 without and with Li-TFSI and with spiro-MeOTAD and Li-TFSI normalized to the absorbance of the samples at the excitation wavelength (527 nm, LED) are depicted in Figure 62. Both dyes showed hardly any signal on TiO2 in the absence of Li-TFSI, even at 80K. Thus, no detectable long lived species were present. This is surprising, as a better injection was expected for PMI-2-MeO due to the higher LUMO level. When Li-TFSI was added the situation changed: PMI-2 showed a positive signal up to 750 nm (1.65 eV) followed by an induced absorption peaking around 800 nm (1.55 eV). Additionally, a second broader induced absorption occurred around 1400 nm (0.9 eV). The positive signal either originated from bleaching of ionized dye molecules which absorbed less in this wavelength region or additionally from a Stark effect induced by the electric field of injected electrons, in turn affecting the ground state absorption of non-excited dyes that had already recombined or did not participate in charge generation. [99, 100] Both induced absorptions originate from dye cations created by electron injection from the excited dye molecules. The cation absorption around 800 nm is in good agreement with the data of a recent study by Cappel *et al.* [71] The se-

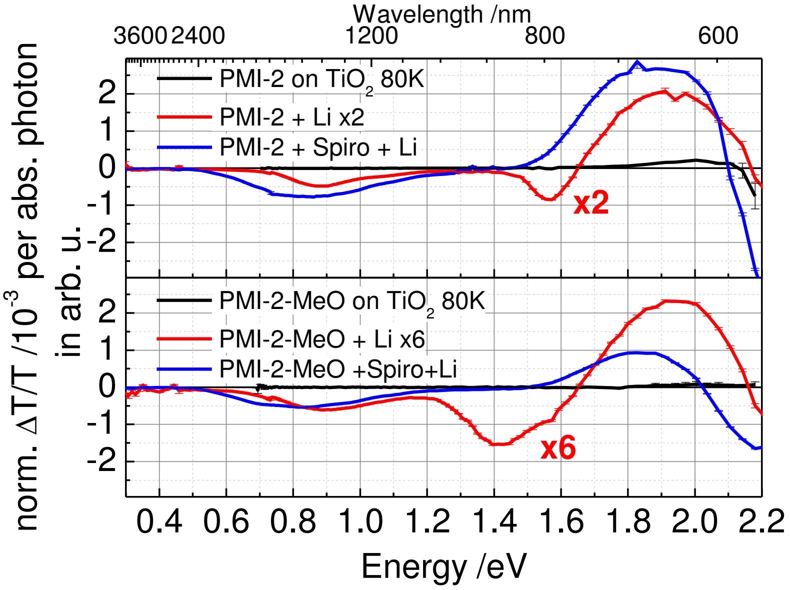

Figure 62: Quasi-steady-state PIA spectra of dyed TiO$_2$ at 80K (black, a room temperature measurement showed the same result), with Li-TFSI at room temperature (red) and with spiro-MeOTAD and Li-TFSI at room temperature (blue) for PMI-2 (top panel) and PMI-2-MeO (bottom panel).

cond induced absorption feature in the near infrared could not be observed in similar measurements using the highly efficient Ruthenium dye Z907 [13] (see Figure 63), and thus it cannot be assigned to electrons in TiO_2. [124] It was therefore also assigned to the dye cation. For PMI-2-MeO the observations were similar, however the main cation-induced absorption was broadened and shifted to the red (1.4 eV, 880 nm). Additionally the signal strength was less than for PMI-2. This could either originate from a less effective injection of electrons, a faster recombination or a smaller absorption cross section of the dye cation as well as a weaker Stark effect due to a different binding of the dye, caused by the smaller ground state dipole moment of PMI-2-MeO (determined by TDDFT) or the higher bulkiness, as the dipole moment changes were similar for both dyes (determined by TDDFT). [101]

When the hole transporter was present, the cation feature vanished for both dyes, pointing towards a complete regeneration of the dye cations by the hole transporter. For PMI-2, a much stronger Stark effect in the presence of spiro was observed, whereas for PMI-2-MeO changes were not that pronounced. Both dyes showed a very broad induced absorption from 950 nm (1.3 eV) towards 2.5 µm (0.5 eV). This feature was assigned to the spiro cation-induced absorption which originates from the regeneration of dye cations. However, for PMI-2-MeO, the induced absorption was not as strong as for PMI-2 (PMI-2 about 1.4 times stronger). As this feature is solely caused by spiro cations, its signal strength is a direct measure of the charge carrier density assuming similar recombination dynamics. Therefore, the charge separation of PMI-2-MeO appeared to be not as efficient as for PMI-2, which is in line with the lower performance in solar cells. Both dyes showed a spiro signal lower than for Z907 (Figure 63), which yielded power conversion efficiencies of more than 2 %. The PIA measurement thus reflected well the overall lower efficiencies of the PMI-2 dyes compared to Z907. At this point no conclusion can be drawn whether this difference is due to a less efficient injection of electrons into TiO_2, a slower regeneration competing with recombination of electron and dye cation or a faster recombination of electrons in the TiO_2 and holes in the spiro. Using transient

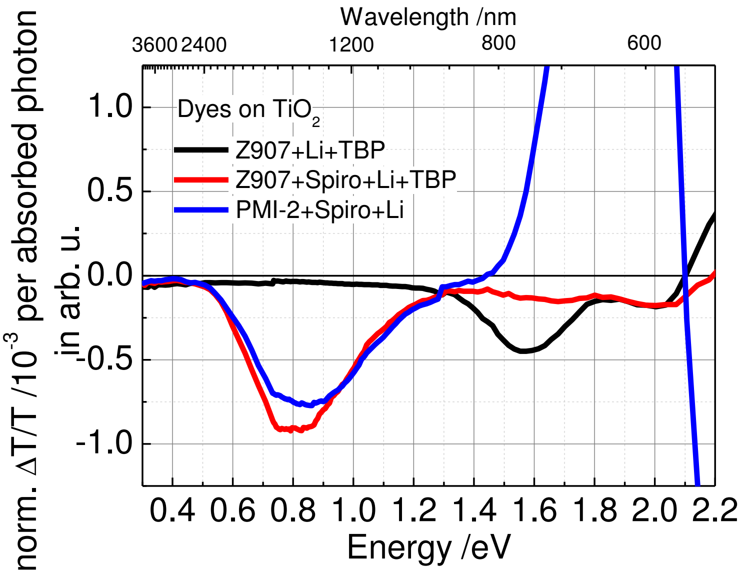

Figure 63: PIA spectra of PMI-2 and Z907, a commonly used Ru-dye that gave more than 2 % efficiency in ssDSCs and was used as a reference system. [13]

absorption spectroscopy these questions are further elucidated in the following sections.

4.3.3 Transient Absorption Spectroscopy: Charge Generation Dynamics

In order to gain a deeper insight into the charge generation processes, the dyes were investigated by ultrafast time-resolved transient absorption spectroscopy. According to a recent publication by Cappel *et al.*, who presented a thorough study on PMI-2 (ID176) [64, 71] a similar line of argumentation is pursued, but extended by measurements covering a broader wavelength range and a longer time scale thereby including also the recombination kinetics. First, the charge generation is examined. Both dyes were studied in different sample compositions to investigate the influence of the metal oxide, the hole transporter spiro-MeOTAD and the additive Li-TFSI. The dyes attached to Al_2O_3, where injection should be suppressed, on TiO_2, which is used in the solar cell, both with and without Li-TFSI and with hole transporter and Li-TFSI were studied. In addition, the differences and similarities of PMI-2 and PMI-2-MeO were investigated.

Samples Prepared without Li-TFSI

In Figure 64, transient absorption data of the dyes attached to TiO_2 and Al_2O_3 are shown together with the kinetics in wavelength regions, in which the absorption of the dye cations was expected from the PIA data. First, the spectra are evaluated followed by a qualitative description of the kinetics. The spectra shown in the top panel of Figure 64 show the dyes on titania and alumina. From a first glance, the spectra differed not much between both metal oxides. A broad photoinduced absorption (PA) in the red part of the spectrum was observed in all cases along with a positive signal in the blue part, which was assigned to bleaching of the ground state. On alumina, no injection and thus pure exciton kinetics of dyes returning to the ground state were expected. Both dyes on Al_2O_3 shared an isosbestic point at around 600 nm indicating the decay of excited states to the ground state. The spectral signatures on Al_2O_3 were thus assigned to the primary excitation of the dye, namely an exciton. This primary

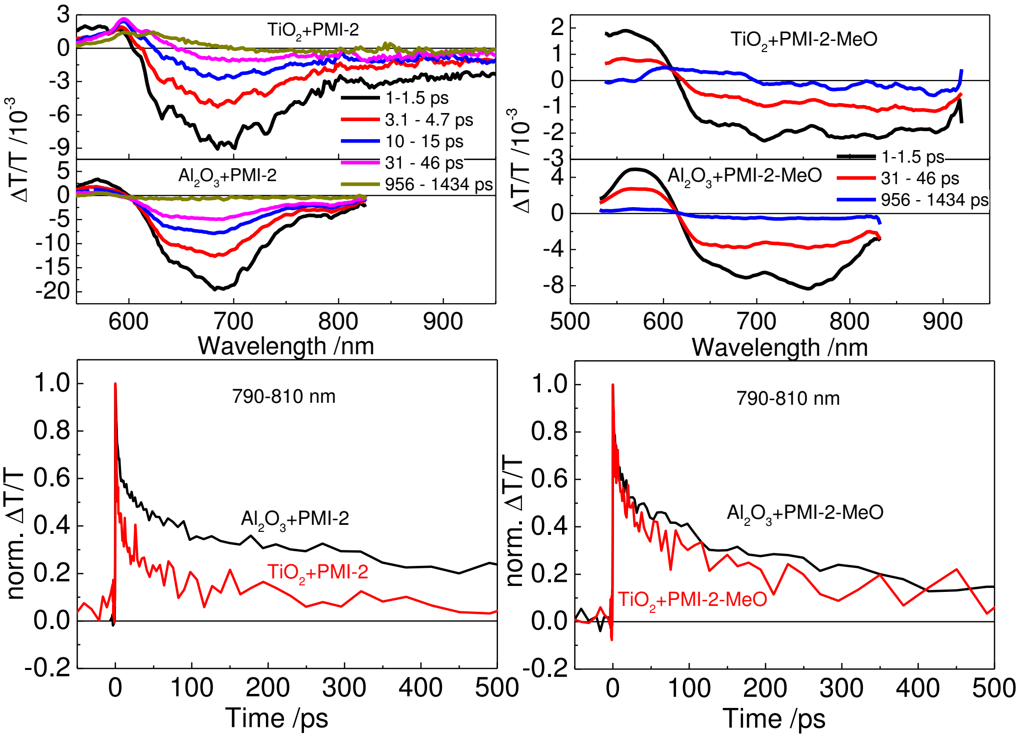

Figure 64: Transient absorption spectra and kinetics of dyes attached to TiO_2 and Al_2O_3 for injection studies. Kinetics were taken at a wavelength, where the cations were expected to absorb.

excitation was not decaying mono-exponentially, indicating a distribution of lifetimes as discussed below. The overall signal shape of the TiO_2 samples was very similar. However, in case of PMI-2 the isosbestic point could not be observed and an additional positive signal emerged up to 700 nm. This new feature was assigned to the creation of some charges on the time scale of the experiment. A clear feature of the dye cation was however not observed, leading to the conclusion that injection was not very effective. PMI-2-MeO still showed an isosbestic point around 600 nm on TiO_2, which was offset by a positive signal, indicating the generation of some charges. This positive signal ranged to 700 nm and was assigned to ground state bleaching or a Stark effect, no longer superimposed by the exciton-induced absorption. The remaining signal decay was found to be similar to the decay on alumina. Thus, it appears that some charges were created on a timescale faster than the experiment's temporal resolution. As no additional induced absorption was observed that could have been assigned to the dye cation, it can be concluded that the ultrafast charge generation does not affect all dyes and is thus not very efficient. The kinetics shown in the lower panel of Figure 64 support these findings: The signal was quenched faster on TiO_2 than on Al_2O_3 for PMI-2 indicating some delayed charge generation, whereas similar kinetics for both metal oxides were observed for PMI-2-MeO. To further support these findings, the transient absorption kinetics in the NIR region (1350-1500 nm) where the dye cations were expected to absorb, were measured and are plotted in Figure 65 together with the photoluminescence decays of the respective samples. First, the kinetics in the NIR differed from the kinetics observed in the visible further supporting the hypothesis, that the decay of the dyes' primary excitation into the ground state is not a simple transition from one excited state into the ground state similar for all dye molecules. These deviations can have different origins: i) The dyes experience different dielectric and electrostatic environments depending on their binding site and binding mode, e.g. due to defects and inhomogeneities in the oxide surface. ii) The dyes themselves have a donor-acceptor structure, which leads to more complex excitation dynamics: The primary photoexcita-

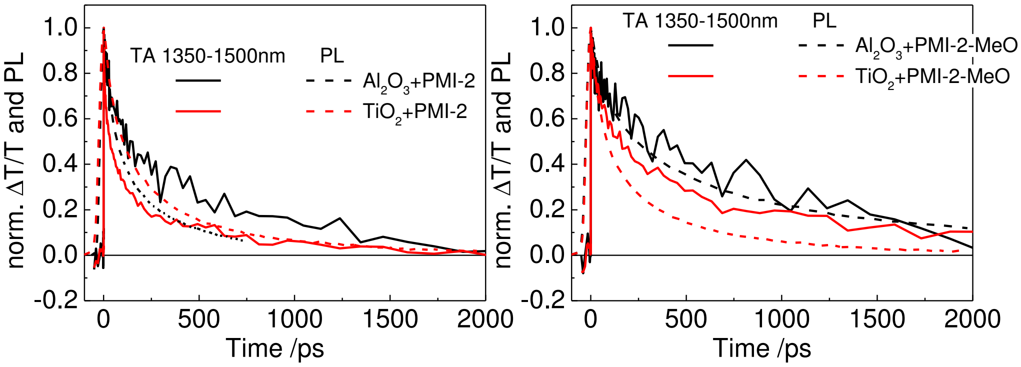

Figure 65: Transient absorption kinetics in the NIR (solid lines) and photoluminescence decays (dashed lines) for PMI-2 (left panel) and PMI-2-MeO (right panel) attached to alumina (black lines) and titania (red lines) mesoporous structures.

tion can relax into an intramolecular charge-transfer state, whose dynamics is different to those of the primary exciton, similar to what was discussed in section 4.2. The intramolecular charge transfer itself depends on the local electric environment. Comparing the NIR kinetics with the photoluminescence decay measured on the same samples, it appears that the NIR spectral region reflects more closely the decay leading to light emission. Besides, the trends observed in the visible were reproduced by the NIR kinetics as the differences between the metal oxides were more pronounced for PMI-2 than for PMI-2-MeO. Interestingly, the PL dynamics of PMI-2 on titania and alumina were very similar, whereas some PL quenching was observed for PMI-2-MeO. This difference could arise from the different surroundings on TiO_2 and Al_2O_3 that influence PMI-2-MeO more. However, more importantly the PL decay shows a very small fraction of dyes that emit, which does not represent the majority of dyes, as the PL quantum efficiencies are typically very low on metal oxides. [71] Thus, the transient absorption experiments are more representative of the entire ensemble of dyes, as they are sensitive to all excitations including those that do not decay radiatively.

In conclusion, it appears that both dyes could inject electrons, however, the majority of dye molecules decayed to the ground state without charge injection. PMI-2-MeO exhibited an ultrafast injection component, whereas PMI-2 showed slower injection, which agrees with its lower-lying LUMO level. The data presented in here is in qualitative agreement with the quasi-steady-state measurements presented above and with the measurements presented by Cappel *et al.* [71]

Samples Prepared with Li-TFSI

Before the results for the complete device-like structure including the hole transporter spiro-MeOTAD and Li-TFSI are presented, the following section reports on the influence of Li-TFSI on the early-time kinetics in samples without spiro-MeOTAD.

Figure 66 shows transient absorption spectra and kinetics of PMI-2 and PMI-2-MeO on titania in the presence of Li-TFSI. PMI-2-MeO exhibited, like the spectrum obtained without Li-TFSI shown in Figure 64, an isosbestic point at a similar wavelength (600 nm). However with Li-TFSI, the isosbestic point was offset by a stronger positive signal extending to 750 nm followed by a negative signal at larger wavelengths, which has already been assigned to charge-induced absorption in the sample without Li-TFSI. This again indicates ultrafast charge transfer occurring on timescales faster than the time resolution of the experiment. The decay originated from some dye molecules that could not inject and hence returned to the ground state. Thus it appears that Li-TFSI facilitated charge injection for more dye molecules. This is supported by the kinetics, as the decay in the first 500 ps was similar for the two PMI-2-MeO samples with and without Li-TFSI, but leveled off at a higher signal offset in the presence of Li-TFSI. No further spectral changes were observed after 500 ps. The situation for PMI-2-MeO is thus comparable to the NMI dye from the previous study.

In case of PMI-2, the situation was more complicated, as shown on the left part of Figure 66. Very complex spectra at different delay times that contained excitonic features, fast kinetics and features originating from the dye cation were observed. In the following, the spectra are disentangled qualitatively.

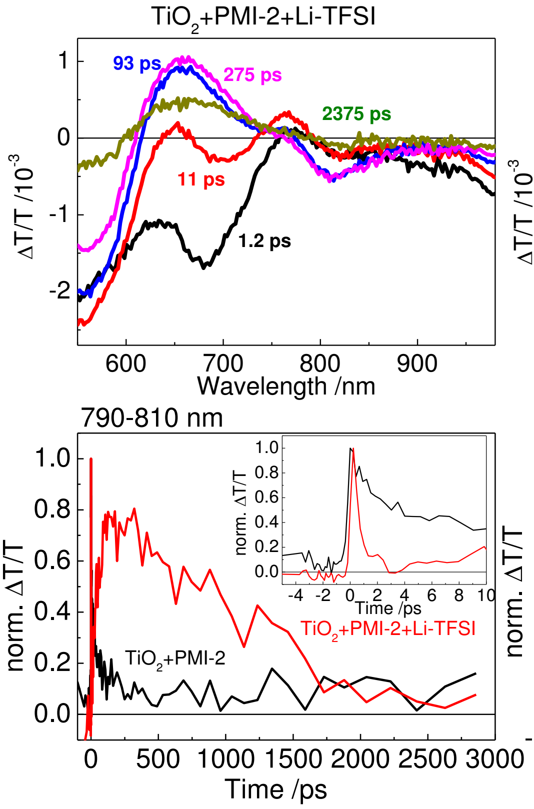

Figure 66: Influence of the addition of Li-TFSI. The two top graphs show the transient absorption spectra of PMI-2 (left) and PMI-2-MeO (right) attached to TiO_2 with Li-TFSI. The lower graphs show kinetics taken at wavelengths where the dye cations were expected to absorb for PMI-2 (left) and PMI-2-MeO (right) on TiO_2 with (red) and without (black) Li-TFSI. The inset in the left graph is a zoom-in of the very early time of the same kinetics.

The very early-time spectra showed spectral features that can be assigned to excitons as observed on Al_2O_3, evident by a photoinduced absorption peak around 680 nm. This signal was superimposed by a positive signal from 600 to 800 nm that clearly rose at later delay times. Additionally, a strong photoinduced absorption below 600 nm and a weaker induced absorption around 800 nm were observed. The further evolution of the spectra resembled a decay of the signal below 600 nm, an increase of the positive signal in the wavelength range from 600 to 750 nm and a build-up of the small induced absorption around 800 nm. The later spectra, after 93 ps, resembled the typical features of charges in close analogy to the quasi-steady-state measurement with the positive signal up to 750 nm and photoinduced absorption at longer wavelength. These signals decayed on longer timescales reflecting a fast recombination process as also observed by Cappel *et al.* [71] However, the early-time evolution was very complex and difficult to disentangle and in the following is elucidated more closely by evaluating the kinetics at distinct wavelengths.

The kinetic traces around 800 nm (Figure 66, bottom left) are considered first. A very fast decay on the order of 1 ps of the induced absorption signal occurred (see inset), followed by an increase on the order of less than 100 ps and a subsequent decay leveling off at a rather low signal amplitude after 2000 ps. The very fast kinetics were previously attributed to electron injection by Cappel et al., however this is not necessarily the case and could actually be an intramolecular process in the dye, which nevertheless can still be followed by injection. Two indications support this hypothesis: Figure 67 shows the kinetics around 800 nm of the dye dissolved in DCM and bound to Al_2O_3 in the presence of Li. Both samples, showed signal changes on the same very short timescale! Note, that solvent relaxation is expected on longer timescales (compare section 4.2.2). The observation of this short process in solution indicates that it is an intrinsic property of the dye. Most likely, it is an intramolecular charge-transfer state that is enhanced in polar solvents or in the presence of Li-TFSI, which is changing the “polarity” of the surrounding. Interestingly, this behavior was not observed on TiO_2 or Al_2O_3 without Li-TFSI, indicating that the change in the locale electric environment induced by Li-TFSI supports the formation of this charge-transfer state. [119] Figure 68 shows the transient absorption spectra of PMI-2 dissolved in DCM (a) and attached to alumina in the presence

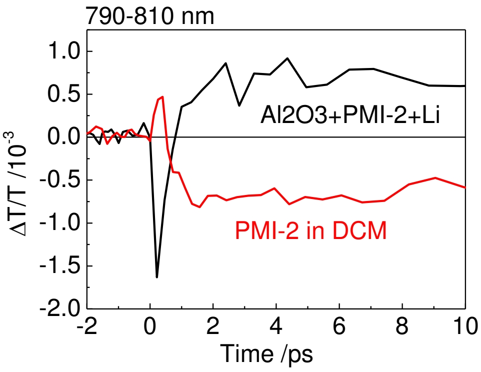

Figure 67: Early kinetics of PMI-2 on Al_2O_3 in the presence of Li-TFSI (black) and in DCM solution (red).

of Li-TFSI (b). Remarkably, the spectral shape observed in DCM above 650 nm resembled the delayed-time spectra of PMI-2 attached to the metal oxides in the presence of Li-TFSI (especially considering the isosbestic point), which was previously assigned to the generation of dye cations. It is very unlikely, that dye cations were formed in DCM upon illumination, leading to the conclusion that the fingerprint of an intramolecular charge-transfer state was observed. It is not surprising that its signature is similar to the dye cation, as in both cases the positive partial charge is localized on the donor of the donor-acceptor structure.

The main difference however, is the negative signal below 600 nm that occurred on both metal oxides in the presence of Li-TFSI. Two possible explanations for this additional signal exist: i) it is a unique photoinduced absorption of the dye cation and not of the intramolecular charge-transfer state, or ii) it is a Stark effect signal originating from the absorption change of the ground state of dyes due to the electric field created by electrons in the metal oxide and the positive charges on neighboring dye molecules or due to the strong dipole of the intramolecular charge-transfer state of nearby dyes. On Al_2O_3 charge injection is not expected, however the Li-TFSI might create sub-band-gap acceptor states that are localized and trapped at the surface, but still can create dye cations. [116-118] Both explanations are possible and cannot be easily distinguished in this wavelength range.

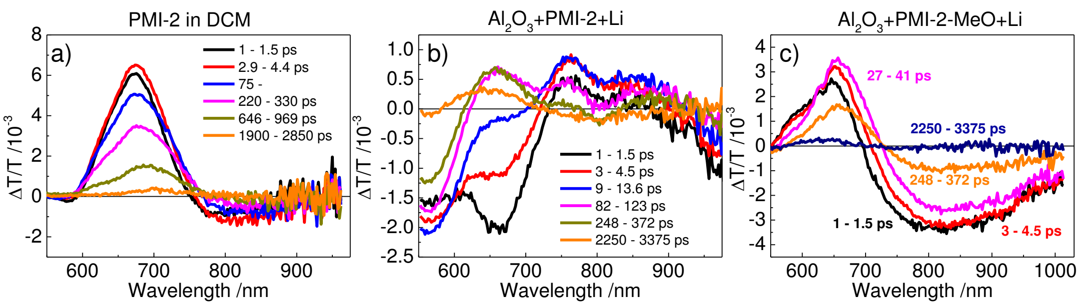

Figure 68: Transient spectra of PMI-2, a) dissolved in DCM and b) attached to Al_2O_3 with Li-TFSI. c) Transient spectra of PMI-2-MeO attached to Al_2O_3 with Li-TFSI.

Due to the similarity of the spectra of PMI-2 on TiO_2 and Al_2O_3 with Li-TFSI, the question remains, whether injection of electrons into TiO_2 occurred. In order to clarify this issue, the transient absorption of dyed Al_2O_3 and TiO_2 samples with Li-TFSI was measured in the near infrared. The kinetics for both dyes are depicted in Figure 69. Here it is evident, that the signal of PMI-2 attached to TiO_2 with Li-TFSI leveled off after about 1000 ps, whereas it vanished on Al_2O_3 on the timescale of 3 ns. In fact, this is evidence showing that on TiO_2 the dye cation was formed, whereas on Al_2O_3 only localized trapped (intramolecular) charge-transfer states were created that quickly recombined. It also exposes, that the kinetics observed in the visible mostly reflected the charge-transfer state dynamics that did not necessarily lead to free charges. Finally, it can also be concluded, that the negative feature in the blue part of the visible spectrum (<600 nm) that was discussed earlier can be assigned to a Stark effect rather than a photoinduced absorption. The Stark effect only occurs in the anisotropic environment of the dye attached to a surface constraining the geometry in one half-space and aligning the dye molecules with respect to the surface. This is supported by the fact that it occurred on both metal oxides, whereas no evidence for injection into Al_2O_3 was observed in the NIR, indicating that it cannot be a unique feature of the dye cation. The origin of the electric field that influences the absorption of dyes in the ground state was thus the dipole of a charge-transfer state (intramolecular or between metal oxide and dye). All in all, the charge generation for PMI-2 is much more efficient in the presence of

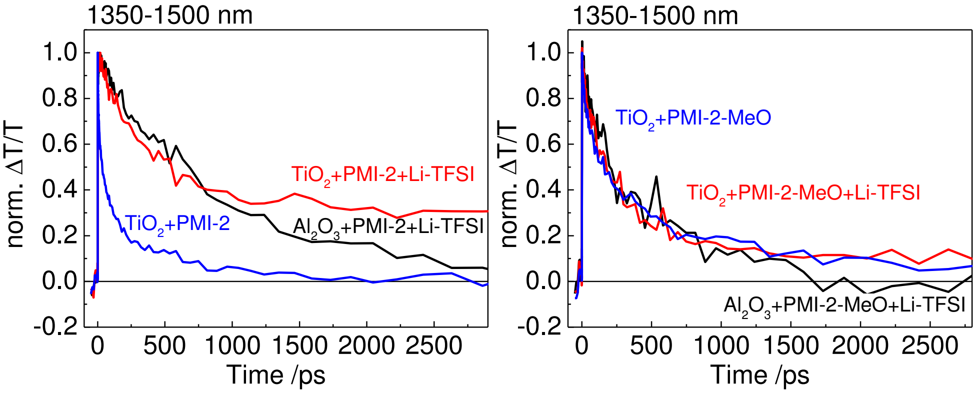

Figure 69: NIR kinetics of PMI-2 (left) and PMI-2-MeO (right) attached to TiO_2 and Al_2O_3 in the presence of Li-TFSI.

Li-TFSI in agreement with the results of Cappel *et al.* [71] However, the data presented in here cannot clarify whether sub-band-gap or surface states of TiO_2 participate in charge injection. Only the difference to Al_2O_3 suggests that surface states available on Al_2O_3 (compare section 4.2.3) also led to slightly different spectroscopic characteristics indicating that the states in TiO_2 are of a different origin, in turn leading to different absorption features of the dye cation or TiO_2 electrons in the NIR.

Taking these findings into consideration, it is also worth evaluating the spectral characteristics of PMI-2-MeO in the NIR, as the visible measurements turned out to be not that conclusive for PMI-2. The right graph in Figure 69 shows the kinetics of PMI-2-MeO in the presence of Li-TFSI on TiO_2 compared to Al_2O_3. The kinetics look similar to PMI-2 apart from the offset of the signal at long delay times. Actually, the differences between TiO_2, TiO_2 with Li-TFSI and Al_2O_3 with Li-TFSI were very subtle. This suggests that the influence of Li-TFSI on PMI-2-MeO was much weaker compared to PMI-2, where it facilitated injection. The NIR data also suggests that the injection efficiency was higher for PMI-2 than for PMI-2-MeO. This is very interesting and unexpected, as despite the higher LUMO of PMI-2-MeO determined in solution, which led to a faster injection in the absence of Li-TFSI, PMI-2 outperformed PMI-2-MeO in the presence of Li-TFSI.

In conclusion, injection occurred for both dyes, PMI-2 showed a very pronounced dependence on the presence of Li-TFSI, caused by an intramolecular charge-transfer state. Additionally the data provided indication of a better injection of PMI-2 in the presence of Li-TFSI. PMI-2-MeO on the other hand showed some injection in the absence of Li-TFSI which appeared to be almost unaltered by Li-TFSI, leading to only a small increase of the exciton splitting efficiency. This discrepancy could cause a significant efficiency difference and might be a reason for the different solar cell performance of PMI-2 and PMI-2-MeO.

Device-like Structure: Regeneration of Dye Cation and Preceding Hole Transfer

Up to now the regeneration of dye cations by the hole transporter spiro-MeOTAD was not taken into account. To this point, it was shown that both dyes were able to inject (some) electrons into TiO_2, so that long-lived cations are available for regeneration. This regeneration is addressed in the following part. Additionally, it is known for perylene dyes, that a preceding hole transfer from the hole transporter to the excited dye prior to electron injection (reductive quenching) is a possible charge generation mechanism (see sections 4.1, 4.2 and [71]). This mechanism is investigated to get a more complete picture of the mechanisms leading to the creation of free charges.

In order to investigate the possibility of a preceding hole transfer, the dyes were blended into the spiro and investigated by transient absorption spectroscopy. The absorption spectrum of the anion of PMI-2 was determined by chemical reduction with Lupasol™ and UV treatment. The obtained spectra can be seen in Figure 70a) in the top panel. [108] The anion absorption differed from the ground state absorption as it was red-shifted and less broad. In the blend with spiro, the difference of ground state and anion absorption spectra was expected to appear transiently as an induced absorption, if electron transfer from the ground state of the hole transporter to the excited dye was possible. This difference spectrum is also shown in Figure 70a), top panel. It showed a clear peak around 630 nm. The bottom graph depicts the observed transient absorption spectra of the dye-spiro blend at different delay times. Clearly, after the very first hundreds of femtoseconds, which were still dominated by the primary excitation (compare Figure 64), the induced absorption spectrum of the dye anion evolved around 630 nm. Figure 70b) shows the kinetics at wavelength regions dominated by the anion and the primary excitation. The anion signal rose very quickly in the first few picoseconds, indicating a fast electron transfer process from the spiro ground state to the excited dye, while the primary excitation simultaneously decayed. Both signals subsequently decayed on the timescale of the experiment, indicating a rather fast recombination of the

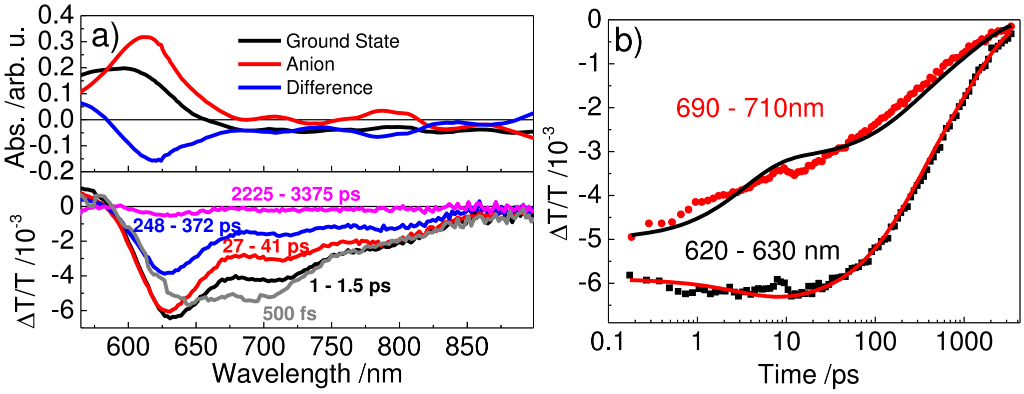

Figure 70: Preceding hole transfer of PMI-2. a) The top graph shows the ground state absorption (black line), the anion absorption (red line) obtained by Lupasol™ treatment [108] and the difference of both (blue line). This is the expected fingerprint to be observed in the transient absorption spectra, if hole transfer from excited dye to the ground state of the hole transporter is possible. The lower graph shows the measured transient absorption spectra of the PMI-2-spiro blend. Clearly, the earliest spectrum shows the excitonic absorption (compare with Figure 64) which is then transformed to a superposition of exciton and anion feature located at a similar position as expected from the blue line in the top graph: Preceding hole transfer is possible! b) Kinetic traces of the transient absorption measurement on the PMI-2-spiro blend at two distinct wavelength regions, in which the dye anion absorbs strongest (620-630 nm) and were the primary excitations absorb (750-760 nm). The quick rise in the bluer region supports that dye anions are formed. Thin lines indicate a fit to a simple model as in section 4.1.

dye$^-$-spiro$^+$ charge-transfer state within a few nanoseconds. These findings are in good agreement with previously published results. [71] Note that a feature at 800 nm previously assigned to localized charge-transfer states was not observed, indicating that this state only occurred when Li-TFSI is present and when the dye is attached to a metal oxide. Similar transient measurements were done for PMI-2-MeO blended with spiro and are shown in Figure 71. Qualitatively the results were similar, showing that PMI-2-MeO is also capable of transferring a hole from the excited state to the hole transporter.

Fitting the kinetics of both dyes to the very simple model for the spiro blend presented in section 4.1, manuscript subsection 2.2.8, only led to meaningful results if the recombination of the dye$^-$-spiro$^+$ charge-transfer state was assumed to be biexponential. The extracted characteristic charge-transfer times of (3.3 ± 0.2)ps and (2.1 ± 0.2)ps for PMI-2 and PMI-2-MeO, respectively, were

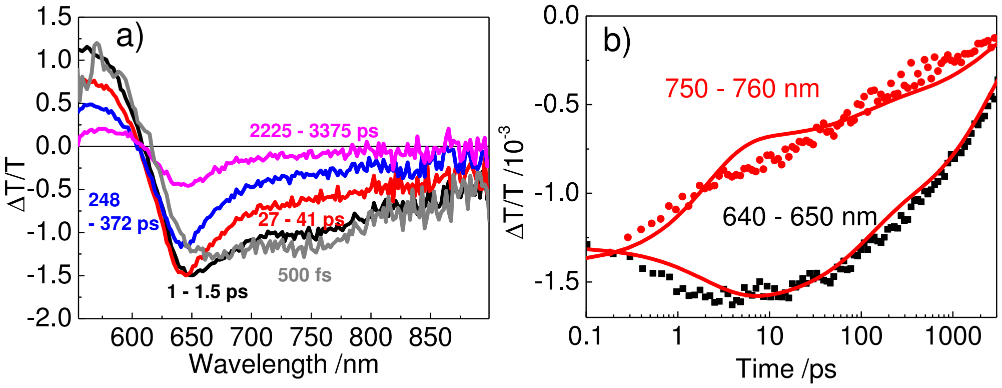

Figure 71: Preceding hole transfer of PMI-2-MeO. Similar spectra (a) and kinetics (b) were observed as for PMI-2 (compare to Figure 70), showing that for PMI-2-MeO electron transfer from the ground state of spiro to the excited dye is possible, when both are blended.

rather fast. The given errors do not take into account the uncertainty of the data and the model itself, so that the two times can be considered roughly similar. Note that it is possible that the model overestimates the splitting, as the charge transfer is assumed to have a quantum efficiency of 100 %. Nevertheless, the model showed that the signals can be explained by a charge transfer between the excited state of the dye and the hole transporter. Keeping in mind, that the situation in the solar cell, where the dyes are attached to a metal oxide and the sample is not as isotropic as in a molecularly-mixed dye-spiro blend, might change the situation, the results of the fitting should not be overrated. The analysis will further be continued by investigating the transient absorption spectra and kinetics in samples with dye molecules attached to a metal oxide and in the presence of the hole transporter and additives, similar to the situation in a functional solar cell.

The transient VIS-IR spectra of both dyes attached to Al_2O_3, which was used as a reference for a non-injecting system, and on TiO_2 with spiro and Li-TFSI are shown in Figure 72. The samples with alumina, Figure 72a) and b), were used to investigate the possibility of a preceding hole transfer from the excited dye to the hole transporter, as electron injection into the metal oxide is expected to

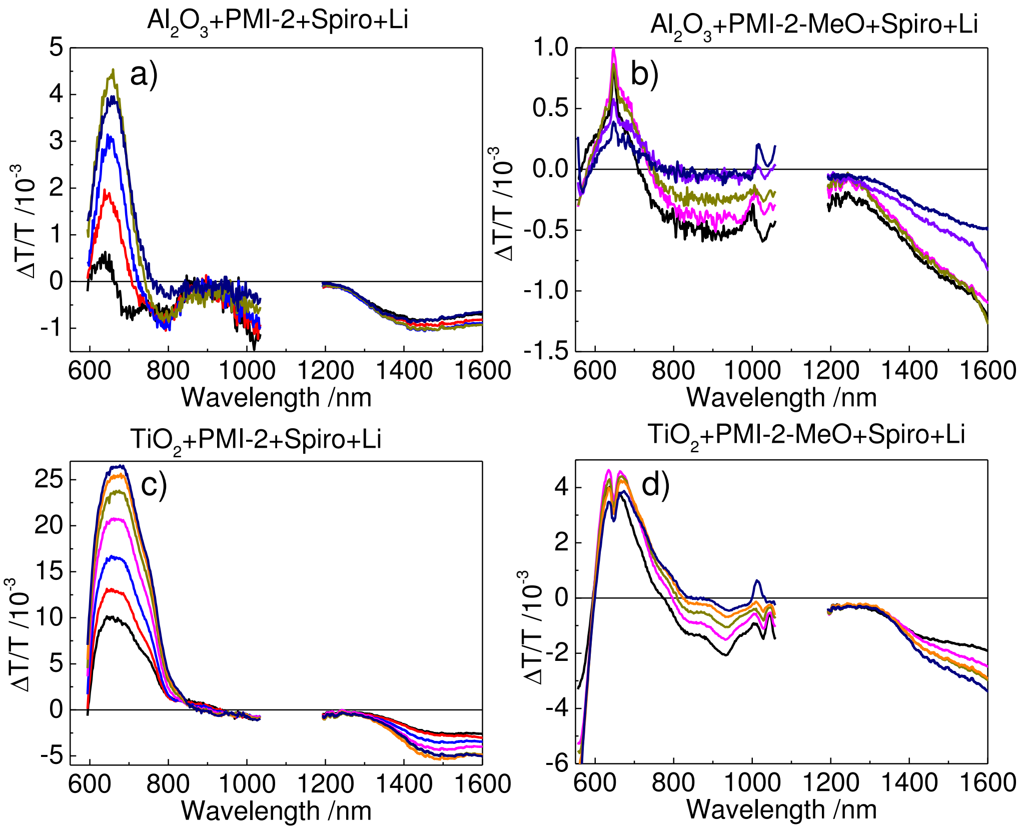

Figure 72: Transient absorption spectra of the dyes PMI-2 and -MeO attached to Al_2O_3 (a) and b), respectively) with spiro and Li-TFSI and PMI-2 and -MeO attached to TiO_2 (c) and d), respectively) with spiro and Li-TFSI as in a solar cell. Colors refer to averaged spectra around mean times as: black 1.3 ps; red 3.8 ps; blue 11.5 ps; magenta 35 ps; green 105 ps; orange 320 ps; violett 1 ns; dark blue 3 ns. Not all times are shown for each sample.

be suppressed. The samples resembling the solar cell composition, Figure 72 c) and d), were investigated to get a conclusive picture of charge generation.

In the following part, these spectra are analyzed along with their kinetics that help to understand the mechanisms of charge generation of both dyes. To begin with, PMI-2 is investigated followed by a similar analysis for PMI-2-MeO. Finally, the differences between both dyes are worked out.

In case of PMI-2 on Al_2O_3 with spiro and Li-TFSI (Figure 72a), the early-time spectrum (in the visible) was similar to the one observed on Al_2O_3 in the presence of Li-TFSI but absence of spiro (compare Figure 68b), especially regarding the induced absorption around 700 nm that was assigned to the primary excitation. The blue part of the spectrum showed a more pronounced positive feature assigned to a Stark effect induced by the electric field between dye anions and holes in the hole transporter. This feature increased strongly in the first 100 ps, indicating charge transfer to the hole transporter via preceding hole transfer. However, a feature of the anion (630 nm) was not observed, which can have several reasons: i) in the presence of Li-TFSI on the metal oxide, the dye anion spectrum can be significantly changed, ii) where the anion-induced absorption was expected from the measurements on the spiro blend, the Stark effect signal was very strong and had a steep slope so that the anion feature was hidden and invisible. Additionally, the anion-induced absorption was expected at the edge of the investigated wavelength region, making it indistinguishable from the rest of the spectrum, and iii) the dye anion was capable to "inject" into the Al_2O_3, and even if no bulk transport sites were available, no spectral indication of the anion would be left behind. Interestingly, all spectra showed a distinct induced absorption around 800 nm that was previously assigned to a localized charge-transfer state and/or the dye cation. As the spiro also absorbs strongly in the NIR, the NIR wavelength region cannot be used to distinguish between those two states, as has been done in the previous part. It is thus impossible to unambiguously assign this feature. However, considering the kinetics it appeared to be related to the preceding hole transfer, as indicated in Figure 73, because of the temporal similarity of the time evolution of the 800 nm-feature (grey line) and the evolution of the NIR signal of the spiro (red line).

The spectra on TiO_2 differed quite substantially. First, the Stark effect was overwhelmingly strong and covered almost the whole visible region, indicating that charge generation was rather efficient and that the electric field between electrons in TiO_2 and holes in spiro at the interface was strong. Besides, no distinct other spectral features were observed in the visible.

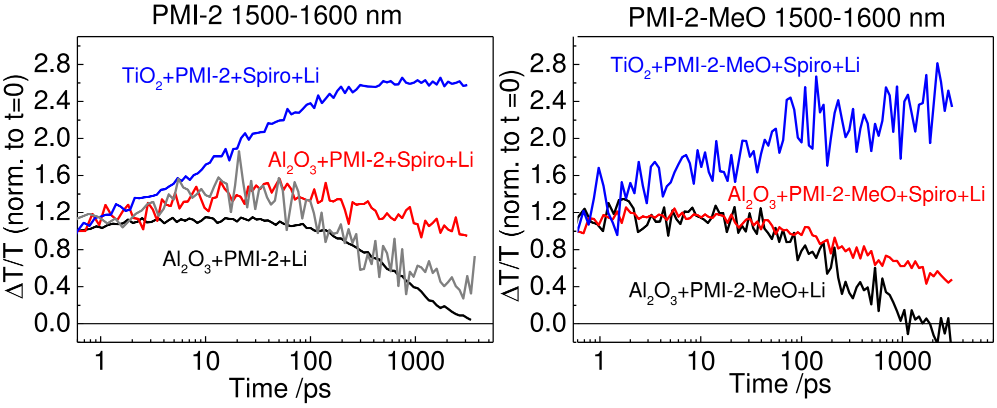

Figure 73: Comparison of NIR kinetics normalized to the signal at zero-time of different sample constitutions for PMI-2 and PMI-2-MeO, where the spiro cation absorbs. The grey kinetic in the left graph is from the same sample as the red curve but at 800 nm, indicating that the origin of the feature at 800 nm is related to the preceding hole transfer.

In the NIR, the signal was stronger and resembled the induced absorption of the holes in spiro-MeOTAD. As Cappel *et al.* already reported [71], it is almost impossible to draw any meaningful conclusions from the visible spectra because it is dominated by a strong Stark feature (for further considerations regarding the Stark feature see section 4.4). Note that the Stark signal increased with time, whereas Cappel *et al.* observed a decreasing signal, [71] which could originate from the different photovoltaic performances and/or different charge movement. However in this case, the NIR spectral region revealed more information about the charge generation. Therefore, the focus of the following part lies on the kinetics of different sample compositions monitored around 1550 nm, where dye exciton, dye cation and spiro cation absorb, but no Stark effect can be observed. Figure 73 (left) depicts these kinetics for the dye attached to alumina in the presence of Li-TFSI only, spiro and Li-TFSI, as well as titania with spiro and Li. From the decay of the NIR signal of PMI-2 on alumina with Li-TFSI (Figure 69), it was derived that the Al_2O_3 sample with Li-TFSI exhibited the decay of the primary excitation (it is deliberately called primary excitation instead of exciton, as it is not clear whether it is an intramolecular charge-transfer state or a charge-transfer state between the dye and Al_2O_3 or a local exciton). Comparing the decay of the primary excitation with the evolution of the signal of the same sample in the presence of spiro, an initial rise in the first few 10s of picoseconds is observed that can be assigned to hole transfer to the spiro. The spiro cation absorption cross section is the largest in this wavelength region and thus the increasing signal represents the increasing population of spiro cations. This process led to longer-lived species compared to the sample without spiro, supporting the idea of a charge transfer and a greater separation of electron and hole. Note that it might be possible, that electrons also resided in trap states at the Al_2O_3 surface. Again, it is evident, that the 800 nm signal (grey line) is related to this charge-transfer process, as it showed an increase and decay on similar timescales, however with different amplitudes. As the feature occurred in the same wavelength region as the dye cation or charge-transfer state absorption, it might originate from the hole being still partially located on the dye, or from the charge-transfer state between spiro and dye. In contrast to the spiro blend, the dielectric and geometrical symmetries were broken due to the metal oxide surface, which can explain why this feature could not be observed in the spiro blend. However, it can also be related to the presence of Li-TFSI. In fact, the induced absorption feature can originate from the red-shifted induced absorption of the dye anion. A red shift in the anion absorption spectrum due to metal oxide and Li-TFSI is realistic, as the ground state absorption also shifts to the red upon adsorption to the metal oxide and especially in the presence of Li-TFSI.

On TiO_2, the increasing signal in the NIR was evolving much stronger and on a longer timescale. Here, not only the preceding hole transfer is possible, but also the regeneration of dye cations that originates from dyes that could inject electrons into the TiO_2. In the previous experiments, it was shown that some electron injection occurred on a longer timescale, which in turn led to a delayed regeneration of dye cations. Hence, the regeneration of the dye cations was efficient and faster than the dye cation recombination. As there was hardly any signal decay observed with spiro, the pore filling must be sufficient so that the majority of dyes were in contact with the hole transporter.

In summary, the charge generation of PMI-2 in the presence of spiro appears to be based on two processes: i) preceding hole transfer from excited states of the dye to the hole transporter and subsequent electron injection, and ii) electron injection from the excited dye into the titania, partially on a longer timescale, followed by efficient regeneration. Note, that the efficiency of the electron injection from the anion could not be determined, as it was not possible to observe features of electrons in TiO_2 in these wavelength regions. However, the fact that the NIR signal was not decaying on the timescale of the experiment for the sample TiO_2+dye+spiro+Li-TFSI suggests that electrons and holes are more separated than in the sample Al_2O_3+dye+spiro+Li, indicating that the electrons did not stay on the dye.

Let us now turn to PMI-2-MeO. The visible spectra of the dye attached to Al_2O_3 with spiro and Li-TFSI, shown in Figure 72b), were not much different from the spectra observed without the hole transporter (compare Figure 68c). The zero crossing of the signal shifted to the red by about 50 nm in about 35 ps. The delayed spectra, where the zero-signal crossing stopped shifting, were also similar to the sample TiO_2+PMI-2-MeO+Li-TFSI. This again supports the hypothesis that the dye did not inject well in the TiO_2+PMI-2-MeO+Li-TFSI sample but rather created a charge-transfer state that not necessarily led to free charge formation. The device-like sample with titania, spiro and Li-TFSI showed some differences (Figure 72d). The zero crossing of the signal shifted even further to the red on longer timescales (300 ps), which was most probably due to a positive Stark effect feature originating from the charges that were created. In contrast to PMI-2, the Stark feature was not that strong, which can be due to the lower dipole moment but can also indicate fewer charge generation. Another difference to PMI-2 is that still some features typical for the primary excitation were observed, that decayed on the timescale of the experiment. Additionally, an induced absorption peak around 900 nm was observed, which remained and closely matched the dye cation-induced absorption feature. In the NIR, a rising signal was observed, indicating the creation of spiro cations, which have a larger absorption cross section than the primary excitations or the dye cation in this wavelength region. No anion features could be observed, though this does not necessarily mean that no anions were created, because the region in which the anion-induced absorption occurred in the spiro blend was superimposed by other signals. Comparing the NIR kinetics shown in Figure 73, right panel, it is evident, that the dynamics in the first 100 ps were very similar in the alumina sample with and without spiro. As the cross section of the spiro cation is larger than of any other species in this wavelength region, this indicates, that preceding hole transfer might not be that efficient, when the dye is attached to a metal oxide in the presence of Li-TFSI! This is supported by the similarity of the spectra of PMI-2-MeO attached to Al_2O_3 in the presence of Li-TFSI without spiro (Figure 68c) and in the presence of both, Li-TFSI and spiro-MeOTAD (Figure 72b). However, the signal in the presence of spiro was longer lived, indicating that the primary excitations were either stabilized in the presence of spiro, or that some preceding hole transfer still occurred, leaving longer-lived charge-transfer states between spiro and dye behind.

In the titania sample, the spiro signal increased almost throughout the entire measured time range, indicating that hole creation was slower compared to PMI-2. It is worth mentioning, that the signal in the visible around 900 nm decayed on the same timescale, indicating that delayed hole transfer rather than recombination to the ground state occurred. However, as the decays of primary excitations were observed to occur on the same timescale (compare Figure 69), it is likely that the slower hole generation is accompanied by additional losses. The signal remaining around 900 nm after the longest time measured indicated that not all dye cations could be regenerated. The pore filling should however be similar in the samples containing both dyes, as they were prepared with the same conditions. In the case of PMI-2, the pore filling appeared to be sufficient to affect almost all dye molecules, so that this remaining PMI-2-MeO cation-induced signal points towards another problem of PMI-2-MeO: The dye might attach to the metal oxide in a different way than PMI-2, so that the hole transporter is not in contact with all cations, e.g. due to aggregation of dyes or dye multilayers, caused by the additional side groups and the smaller dipole moment. Finally, the driving force for regeneration could be altered due to the higher HOMO, which did however not lead to differences between PMI-2 and PMI-2-MeO in the spiro blends.

In summary, the main differences between PMI-2 and PMI-2-MeO in the samples with spiro and Li-TFSI were: i) On alumina, PMI-2-MeO did not exhibit preceding hole transfer as efficiently as PMI-2, and ii) the hole generation in the hole transporter was slower for PMI-2-MeO and seemed not to affect as many dye molecules as for PMI-2. These findings point towards a more efficient regeneration in PMI-2 than in PMI-2-MeO.

Charge Generation: Summary and Discussion

Before the long-time recombination of free charges, which also might have an influence on the performance of the solar cell, is presented in the next part, let us consider the implications of the above findings for the different photovoltaic performances of PMI-2 and PMI-2-MeO.

The main findings were that i) PMI-2 was affected more by Li-TFSI than PMI-2-MeO regarding the efficiency of electron injection into the TiO_2, ii) it showed a better preceding hole transfer ability when attached to metal oxides in the presence of Li-TFSI, and iii) exhibited in general a more efficient charge transfer to the hole transporter.

These observations are counterintuitive, especially taking into account the higher HOMO and LUMO level of PMI-2-MeO, but can be explained as follows:

The two dyes have different ground state dipole moments as obtained by TDDFT calculations. While the calculated dipole of PMI-2 is 7.7 D, PMI-2-MeO has a dipole moment of only 4.3 D, both pointing away from the anchoring group. [101] In general, the dipole moment of the dye attached to TiO_2 leads to an energy level alignment. A dipole pointing away from the TiO_2 surface leads to a relative shift of the TiO_2 conduction band to higher energies with respect to the energy levels of the dye, leading to a reduced driving force for electron injection and higher open circuit voltages in the solar cell. [125, 126] Rühle *et al.* incorporated coadsorbents with different dipole moments and investigated their influence on the open circuit voltage which they assigned to a TiO_2 conduction band shift. [127] They estimated a 9 mV/D upshift for a TiO_2 surface not fully covered with dipoles pointing away from the surface, which would lead to a difference of about 40 mV in the case of PMI-2 and PMI-2-MeO, actually increasing the 0.2 eV higher LUMO of PMI-2-MeO further compared to PMI-2. For a higher surface coverage dipoles shifts as high as 200 mV/D have been reported [128], showing that the impact of the different dipole moments could be even higher. However, such huge changes were not reflected in the V_{OC}, which was about 80 mV lower for PMI-2-MeO, indicating that the dipole moment seemed to play an intermediate role. As this shift actually suggests an even better injection for PMI-2-MeO, it cannot be the origin of the observed differences between PMI-2 and PMI-2-MeO.

In a recent study by Imahori *et al.* [129] it was suggested that the electron injection and recombination of Zn-porphyrin dyes not necessarily occur through the non-conjugated anchor groups that fix the molecule on the TiO_2 surface, but rather through space, so that the orientation of the dyes on the TiO_2 surface plays an important role. The dyes in our study differ by the methoxy group at the bay position, which could influence the binding behavior and angle of the dye with respect to the surface. From the quasi-steady-state PIA, the orientation of the dyes can be roughly estimated. The spiro cation signal in the NIR roughly reflects the amount of generated charges. The Stark signal in the blue part of the spectrum on the other hand reflects the orientation of the dyes with respect to the field, the field strength and the amount of affected dye molecules. As the changes of dipole moment and oscillator strength with field determined by TDDFT calculations were similar for both dyes [101] and under the assumption, that the field created by the charges per spiro cation signal is comparable in both samples, the relative intensities of the Stark and spiro cation signals can be directly compared to reveal differences in the orientation. The Stark signal per spiro cation signal ratio, corrected for the relative dipole moment changes of the two dyes, yields thus a measure for the orientation of the dyes in the field. A higher value then corresponds to an overall more parallel orientation of the dye dipole moments to the field. The extracted values from the PIA are 3.5 for PMI-2 and 1.8 for PMI-2-MeO, indicating that the PMI-2 dipole moments are more parallel to the field and thus more upright on the TiO_2. Together with the observations of more efficient injections and regeneration of PMI-2, this implies that for these dye systems a more upright orientation is beneficial, in contrast to the porphyrin study of Imahori *et al.* [129]

In chapter 4.1 it was shown, that Li^+ mostly localizes at the TiO_2 surface. The different ground state dipole moments of both dyes could imply an influence of Li-TFSI following the previous argument of a better injection when the dye is oriented perpendicular to the TiO_2 surface: As the Li ions positively charge the TiO_2 surface, the orientation of the dyes on the surface could be influenced by interaction with the dipole moment. The dye with a higher ground state dipole moment is thus forced to stand more upright, leading to a better orientation of the dye molecules with respect to the TiO_2 and the spiro molecules and thereby enabling better injection and regeneration. This effect would be stronger for PMI-2 due to the higher dipole moment and is thus a possible explanation for the different influence of Li-TFSI. Therefore, the higher dipole moment of PMI-2 would help to achieve a more beneficial binding orientation on the TiO_2, especially in the presence of Li-TFSI.

Finally, the energy levels were obtained by cyclic voltammetry in solution. Moreover, a strong influence of the local environment of the dye on its photophysical properties was observed. Thus, the influence of, e.g. the metal oxide or the Li-TFSI, on the absolute values of the energy levels remains unknown. Cappel *et al.* showed that Li influences the HOMO level of PMI-2 attached to TiO_2 [71]. This interaction is not known for PMI-2-MeO and could cause a difference.

4.3.4 ns-*µ*s Transient Absorption: Recombination Dynamics

In order to complete the picture of charge generation and recombination, let us now turn to the ns-µs dynamics of separated charges. First, the recombination of electrons and dye cations in the absence of spiro is evaluated before the recombination of electrons and holes in the titania and hole transporter, respectively, is investigated.

ns-µs transient absorption spectra at different delay times for both dyes on TiO_2 with Li-TFSI are depicted in Figure 74. The spectra resembled the quasi-steady-state PIA spectra and the delayed short time spectra very well. In order to compare the kinetics, the fluence and thus the excitation density dependence was investigated and those measurements were analyzed, where no non-linear effects could be observed. The kinetics of the dye-cation photoin-

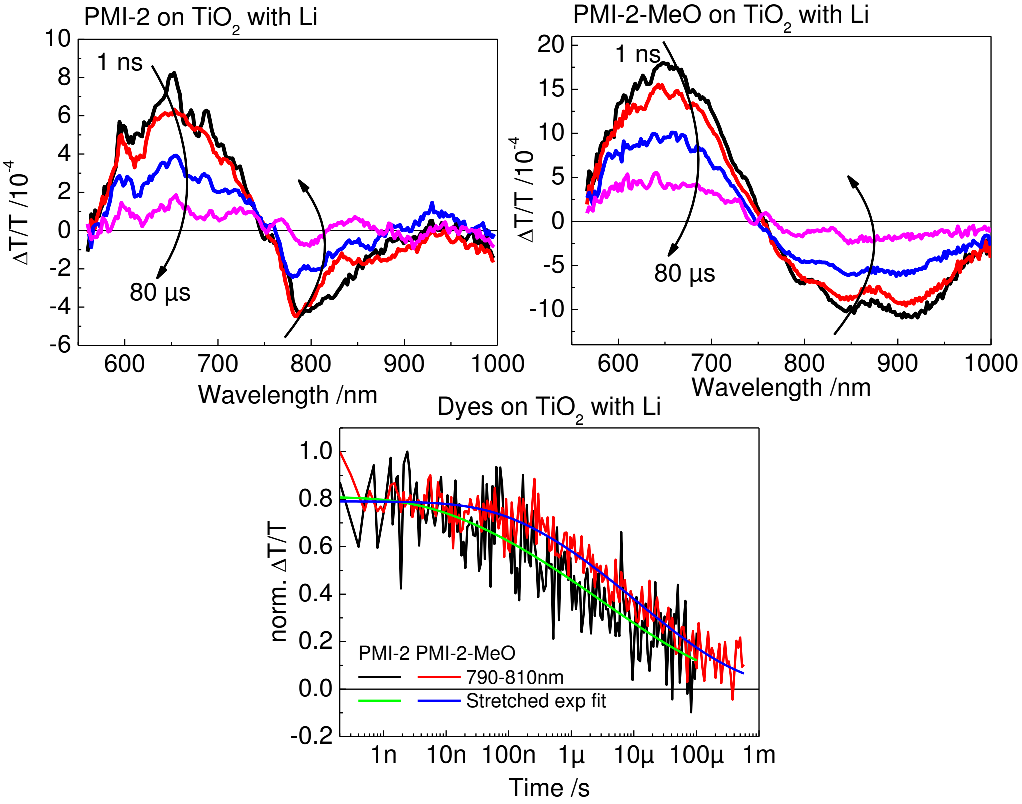

Figure 74: Recombination of electron and dye cation measured for the dye on TiO_2 with Li-TFSI. The spectra resemble the PIA spectra. The kinetics are similar but slower for PMI-2-MeO. The green and blue lines represent fits with a stretched exponential function for PMI-2 and PMI-2-MeO, respectively.

duced absorption showed little differences. PMI-2-MeO exhibited a slower recombination, which is favorable for a good device performance and thus cannot account for the differences in performance. Fitting the data with a stretched exponential function ($\frac{\Delta T}{T} \propto \exp\left(-(t/\tau)^{\beta}\right)$) [130] led to decay times τ of 3 µs and a reasonable width β of 0.22 for PMI-2 and 11 µs with $\beta = 0.26$ for PMI-2-MeO. Keeping in mind that the regeneration occurred on sub-nanosecond timescales even for PMI-2-MeO, this decay will not dramatically alter the device efficiency.

Additionally, the recombination of hole and electron was investigated by applying the same technique on device-like samples including the hole transporter. The main signal observed in the visible was the positive Stark effect feature. As this was the only feature in the wavelength region probed, it was used to estimate electron-hole recombination, assuming that the evolution of this signal solely originated from the decreasing concentration of charges. In Figure 75 the kinetics are shown together with fits using a stretched exponential function. Electron-hole recombination was not much different for both dyes, however, PMI-2-MeO showed slightly faster recombination. The fits yielded inverse decay rates of 400 µs with $\beta = 0.62$ and 880 µs with $\beta = 1$ (monoexponential) for PMI-2-MeO and PMI-2, respectively. Both decay rates

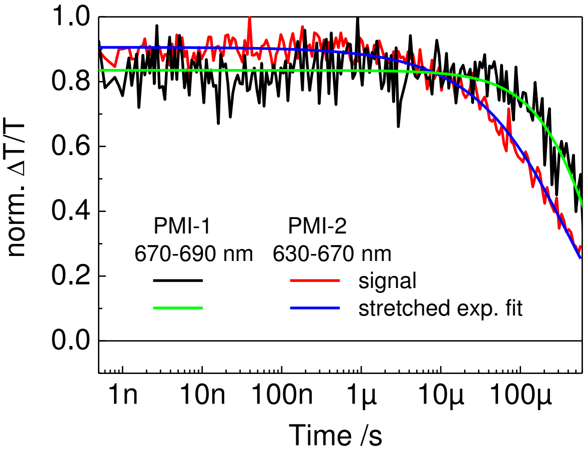

Figure 75: Electron-hole recombination of PMI-2 (black) and PMI-2-MeO (red) on TiO_2 with hole transporter and Li-TFSI at the lowest excitation density. The green and blue lines are fits with a stretched exponential function.

were not much different from those observed with Z907 or other dyes (e.g. NMI or PMI-1 from sections 4.1 and 4.2) and thus could not explain the large performance differences of PMI-2 and PMI-2-MeO. The extracted lifetimes were slightly faster than typically published inverse recombination rates that are on the order of 1 ms [60, 131], which can be due to the different techniques employed (flash photolysis and electronic measurements). It can be concluded that long-time recombination effects do not limit the performance of the PMI-2 dyes compared to other high-performance dyes.

4.3.5 Conclusions

In this chapter two structurally very similar dyes were investigated in solar cells and by steady-state and transient optical spectroscopy. The introduction of electron-donating methoxy groups at the bay position increased the HOMO and LUMO levels, however, leading to huge changes in the solar cell performance and also in the photophysics. HOMO and LUMO were determined in solution by cyclic voltammetry, which not necessarily reflects the situation in the solar cell, when the dyes are attached to a metal oxide and thus are in completely different dielectric environments. [125] Noticeably, the additional methoxy groups in PMI-2-MeO led to a decreased dipole moment (4.3 D vs. 7.7 D) as determined by DFT calculations. [101] It is conceivable that most of the observed differences can be attributed to this difference in dipole moments: i) the presence of Li-TFSI, which alters the local electrostatic environment at the TiO_2 surface has less influence on PMI-2-MeO leading to decreased injection. ii) The smaller dipole moment has a smaller energetic effect on the acceptor states in TiO_2, resulting in a reduced open circuit voltage. iii) As the dipole moment of the excited states differed in a similar manner, an influence on the regeneration due to less separated charge densities of electron and hole on acceptor and donor, respectively, is expected.

The Li-TFSI influence is very crucial in these systems. It has previously been shown, that Li^+ not only influences the TiO_2, but also the excited state of the dye by changing the local Coulomb field [119]. This can also occur in this case, when PMI-2 is stabilized more and influenced more by Li-TFSI. Additionally, in section 4.3.3, it was proposed, that the Li^+ and the $TFSI^-$ can also influence the binding angle and arrangement of the dyes on the TiO_2 surface, again originating from a change in the local Coulombic field of the environment of the dye. This rearrangement leads to a more beneficial positioning for charge generation for PMI-2 with its larger dipole moment.

In summary, it could be shown, that little changes in the chemical structure can have huge influences on the performance of the dyes. It is very essential, that not only the energetics of HOMO and LUMO in solution are considered for dye development, but also the dipole moment, the change in dipole moment and the characteristics of the dye when bound to a metal oxide. In this regard, the influence of Li-TFSI can be very crucial.

4.4 Observing Charge Dynamics in Surface Reactions by Time-Resolved Stark Effects

The following study was submitted to Nature Photonics, but rejected in the peer reviewing. It was resubmitted to the Journal of the American Chemical Society in an adapted version and revision was still in progress at the time this thesis was printed. Note that in the manuscript the dyes PMI-1 and NMI were denoted as D1 and D2, respectively. Coauthors are Björn Baumeier, Neil Pschirer, Rüdiger Sens, Ingmar Bruder, Frédéric Laquai, Denis Andrienko and Ian A. Howard.

Abstract

Surfaces facilitate important chemical reactions occurring in biological and synthetic systems with wide-ranging applications from energy conversion to catalysis and sensing. Microscopic understanding of the structure and dynamics that underpin these reactions is keenly pursued with novel experimental techniques such as sum frequency generation, and laser-assisted photoemission spectroscopy. Herein, we demonstrate that time-resolved observation of the Stark Effect of surface-attached molecules provides an *in-situ* optical probe of the charge dynamics during an interfacial reaction. The technique holds broad potential for investigating charge migration in surface-bound catalysts and sensors, as well as photocenter and retinal proteins, even when explicit knowledge of the material's Stark parameters are unknown. In the current instance, we demonstrate the technique with respect to the energy conversion reaction in solid-state dye-sensitized solar cells. Observing the drift-diffusion of photoinduced holes we find that image charges attract holes back to the interface if dyes are not carefully engineered.

Solid-state dye-sensitized solar cells (SS-DSSCs) are promising candidates for low-cost photovoltaic systems,[1] with power conversion efficiencies reaching 7.2%.[2] In a SS-DSSC, sunlight is absorbed by a monolayer of dye adsorbed on a mesoporous TiO_2 film upon which the photoexcited dye transfers an electron to the TiO_2 and a hole to the hole-transport material (see Figure 1a). The electron and hole transfer are complete within approximately 100 ps of excitation.[3] Thereafter, ideally the electron and hole diffuse to opposite electrodes and are extracted, however in reality some electrons and holes meet at the interface and recombine. Increased significance of this loss mechanism in solid-state cells is proposed to explain why their power conversion efficiency still trails the 12-13% of their liquid electrolyte analogues.[4-6] SS-DSSCs provide an ideal test-case for using time-resolved Stark spectroscopy to track charge dynamics because steady-state measurements have already shown that the surface-bound dyes react strongly to the interfacial field created by photoinduced charges leading to large absorption changes,[7-9] and furthermore the determination of the charge dynamics after injection in SS-DSSCs is highly relevant to understanding the efficiency-limiting recombination. In fact, our time-resolved Stark spectroscopy provides significant new insight into this problem, revealing that fast drift of the hole back to the interface in the field of its image charge enables subsequent recombination (we note that the image charge is caused by the high dielectric contrast at the interface between the organic dye/hole transporter and inorganic nanoparticles). Using time-resolved Stark spectroscopy we can directly characterize the drift of the holes back to the interface, and determine how this efficiency-limiting process is affected by properties of the sensitizing dye.

In ultrafast pump-probe spectroscopy the relative change in transmission of a broadband whitelight laser pulse due to a preceding laser ‘pump’ pulse tuned to excite the sample is measured, $\Delta T/T = (T_{\mathrm{on}} - T_{\mathrm{off}})/T_{\mathrm{off}}$, where T_{on} and T_{off} are the transmission with and without a preceding pump pulse. Therefore, positive signals indicate increased transmission of the sample due to the excitation pulse which, for example, could be caused by excited states bleaching the absorption of chromophores. Negative signals indicate an increased absorption caused by, for instance, the absorption of excited states. Scanning the time delay between the pump and probe pulses allows the time evolution of the photoinduced change in transmissions to be tracked, and from such data the lifetimes and population flow between excited state populations are routinely determined. In the following we show that this technique also reveals transient Stark effects, which, through the general model we develop, allow the transfer dynamics of photoinduced charges to be reconstructed. As an experimental model we compare two representative SS-DSSCs whose quantum efficiency differs because of their sensitization by two different dyes whose structures are shown in Figure 3. More information on the dyes and device performance can be found in the SOI.

Figure 1 c-e shows the measured $\Delta T/T(t,\lambda)$ for the SS-DSSC sensitized with Dye D2. Figure 1c presents an overview of the recorded 2D dataset, while 1d) and 1e) present averaged $\Delta T/T(\lambda)$ spectra for given pump-probe delay times and averaged $\Delta T/T(t)$ kinetics for given wavelength regions. The dominant feature in Figure 1c lies between 480 and 600 nm and has a shape reminiscent of a Gaussian function's first derivative. The signal between 525 and 600 nm remains positive for the entire range of delay times. Because all dyes have returned to the ground state within 200 ps (electron and hole transfer are both complete) this positive feature cannot come from absorption bleaching due to dyes residing in an excited state; it must have another cause. In Figure 1b we show the expected $\Delta T/T(\lambda)$ spectra of a single dye in various electric fields calculated using time-dependent density-functional theory (TDDFT, field orientation was parallel to dye dipole moment, see SOI for further details). Comparing panels b) and d) we find qualitative agreement between the theoretical and experimentally-observed spectra. The 100 nm absolute shift is not significant, as it is a result of the inaccuracy of TDDFT in calculating transition energies and effects of environment. From this result, we can qualitatively hypothesize that the positive feature arises due to the effect of the interfacial field of photoinduced charges on the ground state absorption of nearby dyes.

In order to justify this hypothesis, a few details must be considered. At first in fact, the qualitative similarity of the calculated spectrum of a single dye in an aligned field with the observed signal which is the ensemble average effect of approximately 10^{12} photoinduced charge pairs created throughout a mesoporous film each affecting a distribution of nearby surface bound dyes may be surprising. However, the similarity can be understood by considering the geometry of the system. Firstly, each photoinduced charge pair is created across an interface, which means that although the fields and dyes they influence are disordered in the lab frame, they are similar with respect to the reference of the interface. Secondly, as schematically illustrated in Figure 1a, the surface binding of the dye molecules imposes a constraint on the orientation between the molecular dipole of the dye and the photoinduced electric field (although the dyes azimuthal angle could vary between 0 and 2π, its polar angle is constrained to be between 0 and π). This preferential alignment means that the net Stark effect has a contribution to $\Delta T/T$ that is linear in field leading to first derivative type shapes as observed in the aligned TDDFT calculation. This is contrary the second derivative line shape observed in most Stark spectroscopy performed wherein there is no preferential alignment between the chromophores in amorphous films and the external applied fields.[10] So together, the alignment-caused linear contribution plus the similarity with respect to the interface lead the observed ensemble effect to resemble a superposition of single dye shifts in aligned fields and justify our assignment of the observed signals to transient Stark effects. We note that this assignment is also supported by previous literature,[7-9,11] and also that the observed effect is much smaller in magnitude than that calculated for a single dye because many dyes in the experiment are not affected by photoinduced field since they are not in the vicinity of photoinduced charges.

In Figure 1e) we highlight the temporal evolution $\Delta T/T(t)$ at the peak (560-570 nm) of the positive signal caused by the Stark effect, and in the 740-750 nm wavelength region where both dye excitons and cations on the hole-transporting material show photoinduced absorption (although the cross section of the former is much larger than that of the latter).[11] The photoinduced absorption decreases rapidly in the first few tens picoseconds as the majority of dye excitons are quenched by electron and hole transfer. By 200 ps the last traces of this decrease are complete, as even the slowest injecting photoexcited dyes have returned to the ground state. Thereafter, the photoinduced absorption signal is due to the holes in the hole transport material, and the constancy of the signal over the remaining time indicates that the population of holes does not alter. Despite the absence of generation or recombination, the $\Delta T/T(t)$ at the peak of the positive Stark signal steadily increases on this timescale. As this rise cannot be explained by population change, it must somehow arise due to change in the interfacial field caused by motion of the photoinduced charges.

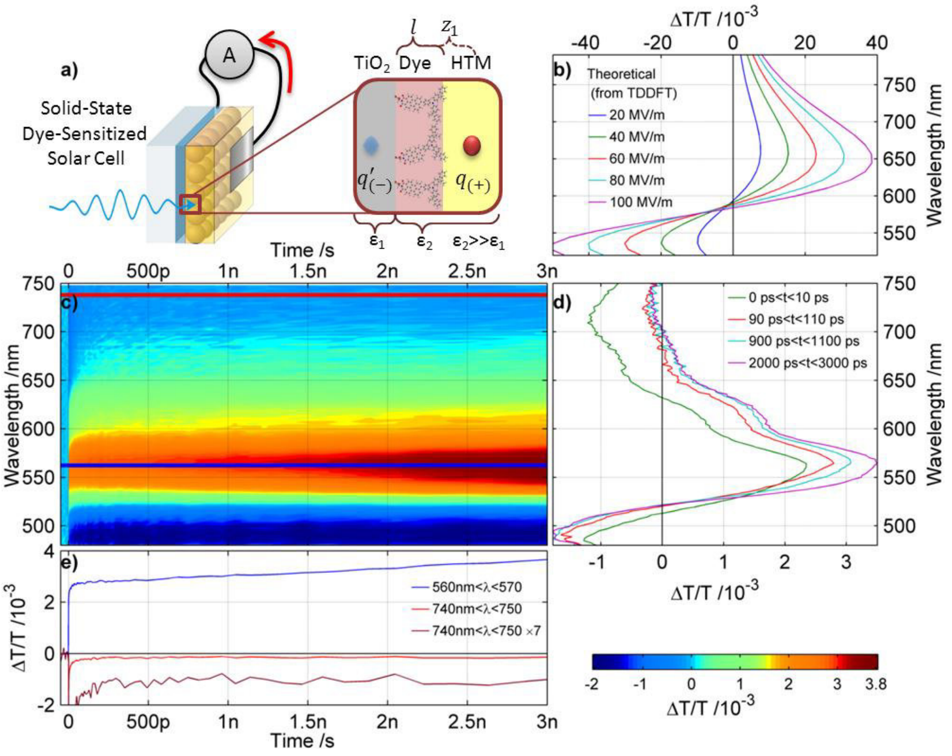

Figure 1: a) Schematic device architecture of a solid-state dye-sensitized solar cell showing, from left to right, the substrate, transparent conductive oxide electrode, dyed mesoporous TiO$_2$, hole-transporting material, and metallic electrode. The inset shows a cross section of the interface after photon absorption. Even if the electron can quickly leave the interface, a hole $\boldsymbol{q_+}$ and its image charge $\boldsymbol{q'_-}$ (which is caused by the high dielectric contrast between the conductive oxide and organic materials) remain. The effective dye length, $\boldsymbol{l}$, and the hole distance, $\boldsymbol{z_1}$, are labeled and will later be shown to strongly influence the charge transfer. Panel b) shows the $\boldsymbol{\Delta T/T(\lambda)}$ expected for a single dye in various fields calculated using TDDFT. Panel c) shows the measured $\boldsymbol{\Delta T/T(t,\lambda)}$ for Dye D2 while d) and e) respectively show spectra at given times and kinetics at given wavelengths. Comparison of b) and d) shows that the feature observed in c) between 480 and 650 nm can be understood in terms of the Stark effect, and that its evolution in time can qualitatively be understood as due to an effective increase in field with time.

Examining Figure 1b) we can already qualitatively say that the signal increase reveals that the strength of the net interfacial field becomes larger with time, indicating that charges are likely returning to the interface. In the following sections we develop a general model that, even without explicit knowledge of material parameters that underlie the Stark effect, allows detailed information regarding the charge dynamics to be easily extracted from these Stark-induced $\Delta T/T(t)$ kinetics.

To perform quantitative analysis of the data, we develop a model which accounts for the distribution of dye orientations relative to the interface, molecular parameters, and charge dynamics at the interface. To do this, we follow classical treatments of the Stark effect[10] and expand the absorption spectrum, $A(E_i, f_i, \vec{F})$, oscillator strengths, f_i, and energies of excited states, E_i, of a single dye up to the second order in external field $\vec{F}$. We then perform several statistical averages. The average over dye orientations with respect to the interface introduces first and second moments (g_1 and g_2) of the dye orientation distribution function, $g(\Omega)$. To perform the second average over the surface area, an explicit expression for the electric field at the interface, $\vec{F}(z=0)$, is required, which is taken to be the field of an electron and a hole at the interface between two dielectrics (i.e. two charges and two image charges). After averaging, the absorption spectrum becomes a function of single dye properties (such as molecular hyperpolarizabilities, oscillator strengths, etc. which could be extracted from experiment or first principles calculations but as we will later show are not explicitly necessary for examining charge dynamics), moments of their orientation distribution function, relative dielectric susceptibilities (ϵ_1 and ϵ_2), and distances of the electron and hole from the interface (z_1 and z_2). See SOI for full derivation.

$$\Delta A(z_1, z_2) = \langle A(\vec{F}=0) - A(\vec{F}) \rangle =$$
$$n S_1(\lambda, \{M\}, g_1) + n \mathrm{Tr}\left[\hat{S}_2(\lambda, \{M\}, g_1) \hat{G}(g_2, z_1, z_2)\right]. \tag{1}$$

Here $\langle \dots \rangle$ denotes surface and ensemble averages, λ is the wavelength, n is the concentration of dyes on a particle surface, $\{M\}$ represents relevant single-molecule properties, S_1 and $\hat{S}_2$ are spectral shapes, and $\hat{G}(g_2, z_1, z_2)$ is a distance-dependent matrix, whose full form is presented in the SOI.

The kinetics of absorption can then be obtained by averaging over the distribution $p(t, z_1, z_2)$ of charge positions at time t

$$\Delta A(t) = \int_0^\infty \Delta A(z_1, z_2)\, p(t, z_1, z_2) \mathrm{d}z_1 \mathrm{d}z_2 \,, \tag{2}$$

where $p(t, z_1, z_2)$ is normalized by the number of charges in the system, $\int_0^\infty p(t, z_1, z_2)\mathrm{d}z_1\mathrm{d}z_2 = n_e + n_h$.

Eqs. (1) and (2) summarize the first important result which follows from our model: in order to gain information about the kinetics of charge drift-diffusion, i.e. how $p(t, z_1 z_2)$ change with time, *explicit knowledge of* S_1 *and* S_2 *is not necessary*, since the distance dependence, and therefore all information regarding the kinetics, is contained exclusively in the distance-dependent matrix $\hat{G}(g_2, z_1, z_2)$. In other words, analysis of the transient absorption kinetics can directly reveal information regarding charge drift-diffusion near chromophores even without knowledge of their specific material properties.

We will now apply this model to the particular case of a SS-DSSC, where the electron is localized in TiO_2, while the hole is in the organic semiconductor. Since the electron mobility in TiO_2 is much higher than the hole mobility in the hole-transport material,[12] we assume that the electron can quickly leave the interface after injection making its contribution to the interfacial field negligible compared to the much closer hole and its associated image charge. With these assumptions the distance dependent matrix simplifies to $\hat{G}(g_2, z_1, z_2) = \hat{G}(g_2, \epsilon_2/\epsilon_1)z_1^{-2}$, where z_1 is the distance between the hole and the interface. In this case the distance dependence of ΔA in equation 1 is given by a single scalar function, which can be tested by normalizing the time-dependent part of the experimental $\Delta T/T(\lambda, t)$ and observing if they all fall on a single master curve. This works for both dyes as shown in the SOI.

In order to determine $p(z_1, t)$ we assume that a hole drift-diffuses in a half-space $z \in [l, \infty]$, where l is the length of the dye (see Figure 1), in the external electrostatic potential of its image charge,

$$U(z_1) = \frac{1}{2\epsilon_1}\frac{\epsilon_2 - \epsilon_1}{\epsilon_2 + \epsilon_1}\frac{q^2}{z_1} \sim k_\mathrm{B}T\frac{z_1 - l_B - l}{l}, \qquad (3)$$

where l_B is the distance at which $U(z)$ is of the order of $k_\mathrm{B}T$. Note that the linearization is valid only for large l.

Solving the Smoluchowski (drift-diffusion) equation with the initial condition $p(z_1, 0) = \delta(z_0 + l)$, that is assuming that a charge is injected at a distance $z_0 + l$ from the interface, and a reflecting boundary condition at $z = l$ (recombination occurs with an inverse rate of hundreds of microseconds and is negligible on this short timescale) we obtain the Green's function $p(z_1, t|z_0, 0)$, or a probability to find a hole at a position z_1 at time t provided it was at position z_0 at time $t = 0$. For the fitting we solve this numerically and considering the full potential, however to gain a general understanding of solution behavior we also find an analytical solution in dimensionless variables for a linearized potential (details in SOI). The distribution of holes at time t then reads, $p(z_1, t) = n_h \int_0^\infty p(z_1, t|z_0, 0) p(z_0, 0) \mathrm{d}z_0$, where $p(z_0, 0)$ is the initial distribution of hole positions.

Substituting $p(z_1, t)$ into eq. (2) we obtain the time evolution of the Stark-induced change in dye absorption due to charge drift-diffusion, which is shown in Figure 2 for varying injection distances. The solutions demonstrate that the form of $\Delta A(t, z_0)$ is very sensitive to the initial injection z_0. When the hole is injected only a small distance into the hole transport material, $\Delta A(t, z_0)$ *decreases* as the moment of the charge distribution net moves away from the interface due to diffusion. On the other hand, if charges are initially injected further from the interface then $\Delta A(t, z_0)$ *increases* as the moment of the charge distribution is pulled back toward the interface due to drift. In both cases the equilibrium distribution is given by the Boltzmann distribution, $p(t = \infty, z) \sim \exp(-U(z)/k_\mathrm{B}T)$, and does not depend on the initial condition.

This is the second conclusion of our model: different injection distances lead to qualitatively different absorption transients, which means that insight into the dynamics of charges can be easily obtained from the measured absorption transients. We note that as we measure the net absorption change due to approximately 10^{12} photogenerated holes, we must average over the initial distribution of charge positions. This averaging, however, will not change the qualitative conclusions.

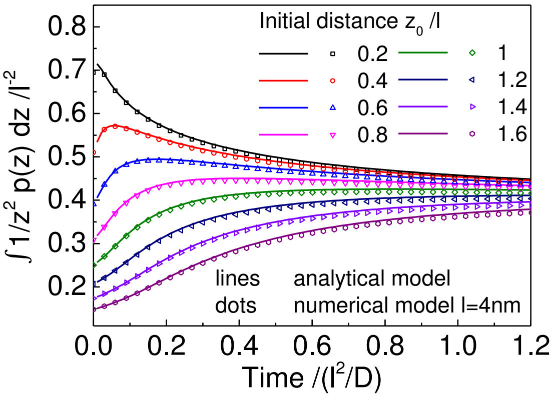

Figure 2: Theoretical evolution due to drift and diffusion of the weighting factor for time-dependent Stark-induced spectrum ($\hat{\boldsymbol{S}}_2(\boldsymbol{\lambda}, \{\boldsymbol{M}\}, \boldsymbol{g_1})$) for a hole and its image charge after hole injection at various distances for dye length $\boldsymbol{l}$ of 4 nm. For short injection distances the spectrum will decrease due to diffusion of the holes away from the interface, while for long injection distances the spectrum will decrease due to drift of the holes back towards the interface.

In order to isolate the ensemble drift-diffusion kinetics from the transient absorption data we chose t_1 to be the latest time in our measurement range, and t_2 the time at which subsequent kinetics are exclusively due to charge motion (i.e. no further population kinetics are observed) and evaluate the following ratio

$$F(t) = \frac{\Delta A(\lambda_m, t) - \Delta A(\lambda_m, t_1)}{\Delta A(\lambda_m, t_2) - \Delta A(\lambda_m, t_1)} \qquad (4)$$

where λ_m corresponds to the peak of $\Delta A(\lambda, t)$. According to eqs. 1, 2 this ratio does not depend on material parameters, only on the injection point z_0 and the thickness of the dye layer, l, and the diffusion constant, D, in the hole-transport material. $F(t)$ is shown in Figure 3 for the two dyes, D1 and D2.

In order to learn about the charge injection and drift-diffusion in our two model dye systems we compute the numerical solutions of $F(t)$ for a uniformly spaced 50×50 mesh of z_0 from 0 to 4 nm and l from 0.5 to 4 nm where we have taken the mobility of the hole transport material to be $\mu = 1 \times 10^{-3}\ \mathrm{V\,s/cm^2}$.[13] The residual between the numerically calculated and measured $F(t)$s are computed for each mesh point, the best fits are shown in Figure 3 along with the residuals and 95% confidence intervals as insets. D1 shows a faster change in the Stark signal which quickly approaches saturation. This indicates a shorter effective dye length, $l_{\mathrm{D1}} = 1.0 - 2.0\ \mathrm{nm}$, and injection distance $z_{D1} = 1\ \mathrm{nm}$ as compared to D2: $l_{\mathrm{D2}} > 2.5\ \mathrm{nm}$ and $z_{D2} > 3\ \mathrm{nm}$. The limited time range of our experiment meant that the saturation of $F(t)$ for D2 was not observed, limiting our ability to constrain the parameters. Nonetheless, we are able to establish clear bounds. Considering the optimized ground state geometries of the dyes shown in Figure 3, the effective dye length parameters extracted by our model are reasonable, and may suggest that D1 lies slightly flatter to the surface perhaps enabled by its more rigid structure. In Figure 3e) and f) we show the extracted probability distributions $p(z_1, t)$ for D1 and D2. The holes are always closer to the interface for D1, the moment of the equilibrium distribution lies closer to the interface, and furthermore the holes return very quickly. The short dye length is primarily responsible for these last two effects, as the short dye means that the hole is in a steep Coulomb potential due to its image charge. D2 has better injection and is slightly longer, leading to a greater initial separation from the interface. The flatter Coulomb potential at this greater distance means that the initial drift back to the interface is much slower. The modestly longer dye length also means that the moment of the equilibrium hole distribution is significantly further from the interface. The enhanced injection length and slower return of the holes to the interface we measure for D2 is also consistent with its greater internal quantum efficiency for D1 ($\mathrm{IQE}_{\mathrm{D1,D2}}$=67%, 90%), demonstrating our technique is applicable to identifying the underlying causes of loss mechanisms that limit the practical application of SS-DSSCs. Our results suggest that overcoming fast drift of the hole back to the interface in the potential of its image charge is necessary for high quantum efficiency, and that this can be achieved by increased dye and hole injection lengths.

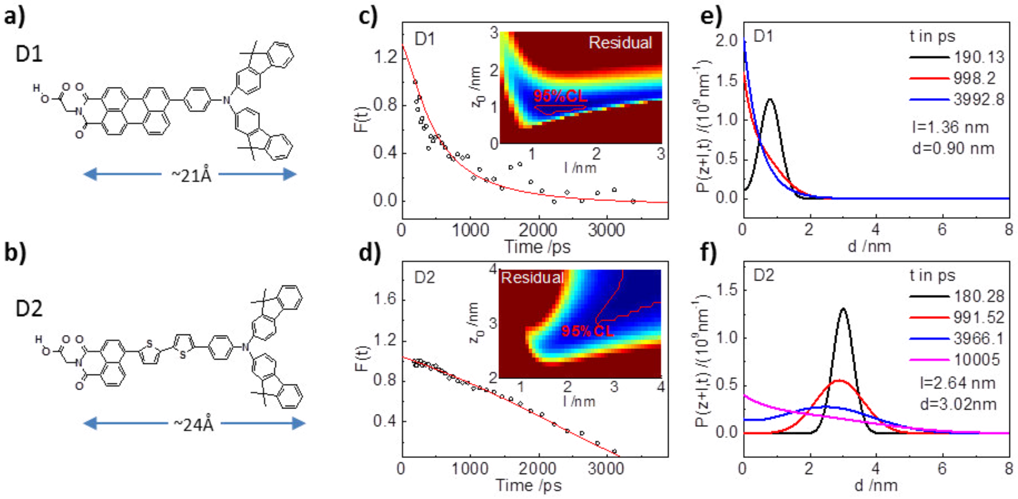

Figure 3: Fits of experimental data to model in order to extract the drift-diffusion of interfacial holes for D1 and D2. Panels c) and d) show $\boldsymbol{F(t)}$ extracted from the experimental data, plus that of the best fit to the numerical solution of the model calculated over a 2500 point mesh. The insets show the residuals (dark blue smaller) along with the 95% confidence intervals. e) and f) show the probability density function to find a hole as a function of distance from the interface for various times. The redder absorbing D1 has a much shorter injection distance, which leads to holes residing much closer to the interface, and returning much more quickly. A longer dye length should theoretically ameliorate this situation.

In conclusion, we have demonstrated that the transient Stark-induced absorption can reveal charge dynamics in systems wherein the geometry constrains the relative orientation of the Stark susceptible molecules and the charge-induced fields, such as at surfaces and in biological proteins. We have developed a general model to interpret the observed signals in these cases, and through our analysis both qualitative and quantitative information regarding charge dynamics can be extracted from the dynamics of the transient Stark spectra, without explicit knowledge of material parameters such as molecular hyperpolarizabilities, oscillator strengths, etc. As such, transient Stark spectroscopy provides access to complementary information to other surface-sensitive techniques such as sum frequency generation,[14,15] laser-assisted photoemission spectroscopy,[16,17] and dynamic-nuclear-polarization-enhanced NMR,[18] allowing the understanding of the physics underlying surface enabled reactions to be approached in ever greater detail. We demonstrated the technique with reference to SS-DSSCs, showing how the motion of photoinduced holes in the hole-conducting material could be reconstructed and finding that the hole injection distance and rate of return to the interface varied between the two dyes measured, with greater separation and slower return correlating with higher device efficiency. This suggests that avoiding drift of the hole back to the interface in the field of its image charge is the final obstacle to address in terms of optimizing quantum efficiency in this class of photovoltaic devices.

Acknowledgements

This work was partially supported by the DFG program IRTG 1404, DFG grant SPP 1355, the Alexander von Humboldt Foundation, the Max Planck Graduate Center, the Max Planck Society for funding a Max Planck Research Group, and the BMBF grant MESOMERIE. We are grateful to Kaphesatz Läser for helping at the early stages of this work.

Competing Financial Interests

The authors declare no competing financial interests.

Contributions

M.M., I.H., and F.L. designed and carried out experiments. R.S., I.B., and N.P., synthesized materials, provided samples, and measured IQE. D.A. and B.B carried out the calculations and developed the model. All authors contributed to the editing of the manuscript.

References

1 Hardin, B. E., Snaith, H. J. & McGehee, M. D. The renaissance of dye-sensitized solar cells. *Nat Photon* **6**, 162-169, (2012).

2 Burschka, J. *et al.* Tris(2-(1H-pyrazol-1-yl)pyridine)cobalt(III) as p-Type Dopant for Organic Semiconductors and Its Application in Highly Efficient Solid-State Dye-Sensitized Solar Cells. *J. Am. Chem. Soc.* **133**, 18042-18045, (2011).

3 Bach, U. *et al.* Solid-state dye-sensitized mesoporous TiO2 solar cells with high photon-to-electron conversion efficiencies. *Nature* **395**, 583-585, (1998).

4 Yella, A. *et al.* Porphyrin-Sensitized Solar Cells with Cobalt (II/III)–Based Redox Electrolyte Exceed 12 Percent Efficiency. *Science* **334**, 629-634, (2011).

5 Snaith, H. J. *et al.* Charge collection and pore filling in solid-state dye-sensitized solar cells. *Nanotechnology* **19**, (2008).

6 Snaith, H. J. *et al.* Efficiency enhancements in solid-state hybrid solar cells via reduced charge recombination and increased light capture. *Nano Lett.* **7**, 3372-3376, (2007).

7 Cappel, U. B. *et al.* Characterization of the Interface Properties and Processes in Solid-state Dye-Sensitized Solar Cells Employing a Perylene Sensitizer. *The Journal of Physical Chemistry C*, null-null, (2011).
8 Cappel, U. B., Feldt, S. M., Schöneboom, J., Hagfeldt, A. & Boschloo, G. The Influence of Local Electric Fields on Photoinduced Absorption in Dye-Sensitized Solar Cells. *J. Am. Chem. Soc.* **132**, 9096-9101, (2010).
9 Ardo, S., Sun, Y., Staniszewski, A., Castellano, F. N. & Meyer, G. J. Stark Effects after Excited-State Interfacial Electron Transfer at Sensitized TiO2 Nanocrystallites. *J. Am. Chem. Soc.* **132**, 6696-6709, (2010).
10 Boxer, S. G. Stark Realities†. *J. Phys. Chem. B* **113**, 2972-2983, (2009).
11 Fantacci, S., De Angelis, F., Nazeeruddin, M. K. & Grätzel, M. Electronic and Optical Properties of the Spiro-MeOTAD Hole Conductor in Its Neutral and Oxidized Forms: A DFT/TDDFT Investigation. *J. Phys. Chem. C* **115**, 23126-23133, (2011).
12 Němec, H. *et al.* Influence of the Electron-Cation Interaction on Electron Mobility in Dye-Sensitized ZnO and TiO_2 Nanocrystals: A Study Using Ultrafast Terahertz Spectroscopy. *Phys. Rev. Lett.* **104**, 197401, (2010).
13 Snaith, H. J. & Gratzel, M. Enhanced charge mobility in a molecular hole transporter via addition of redox inactive ionic dopant: Implication to dye-sensitized solar cells. *Appl. Phys. Lett.* **89**, 262114, (2006).
14 Zhang, Z., Piatkowski, L., Bakker, H. J. & Bonn, M. Ultrafast vibrational energy transfer at the water/air interface revealed by two-dimensional surface vibrational spectroscopy. *Nat Chem* **3**, 888-893, (2011).
15 Tian, C. S. & Shen, Y. R. Structure and charging of hydrophobic material/water interfaces studied by phase-sensitive sum-frequency vibrational spectroscopy. *Proc. Natl. Acad. Sci. USA* **106**, 15148-15153, (2009).
16 Miaja-Avila, L. *et al.* Direct Measurement of Core-Level Relaxation Dynamics on a Surface-Adsorbate System. *Phys. Rev. Lett.* **101**, 046101, (2008).
17 Rohwer, T. *et al.* Collapse of long-range charge order tracked by time-resolved photoemission at high momenta. *Nature* **471**, 490-493, (2011).
18 Lesage, A. *et al.* Surface Enhanced NMR Spectroscopy by Dynamic Nuclear Polarization. *J. Am. Chem. Soc.* **132**, 15459-15461, (2010).

4.4.1 Supporting Information

In what follows, we link charge dynamics, single molecule absorption spectrum, and Stark effect and derive an expression for the absorption spectrum of the system which depends on time, molecular orientation distribution functions, and optical parameters, such as oscillator strengths and energies of excited states. We then discuss a procedure used to analyze experimental data.

Electric field

In a geometry depicted in SOI Figure 1 the electrostatic potential at $z > 0$ is given by the electrostatic potential of the charge q_1, its mirror image q_1', and the screened charge q_2, q_2''

$$\Phi(z > 0) = \frac{1}{\epsilon_1}\left[\frac{q_1}{((z - d_1)^2 + r^2)^{1/2}} + \frac{q_1'}{((z + d_1)^2 + r^2)^{1/2}}\right] + \frac{1}{\epsilon_1}\frac{q_2''}{((z + d_2)^2 + r^2)^{1/2}}$$

where

$$q_1' = -\frac{\epsilon_2 - \epsilon_1}{\epsilon_2 + \epsilon_1} q_1 \,, \qquad q_2'' = \frac{2\epsilon_1}{\epsilon_2 + \epsilon_1} q_2$$

Keeping in mind that $q_1 = -q_2 = q > 0$ (q_2 is an electron) and taking the gradient of Φ we obtain the electric field in the upper half-plane

$$F_z|_{z=0} = -\frac{2q}{\epsilon_2 + \epsilon_1}\left[\frac{\epsilon_2}{\epsilon_1}\frac{d_1}{(d_1^2 + r^2)^{3/2}} + \frac{d_2}{(d_2^2 + r^2)^{3/2}}\right]$$

$$F_r|_{z=0} = \frac{2q}{\epsilon_2 + \epsilon_1}\left[\frac{r}{(d_1^2 + r^2)^{3/2}} - \frac{r}{(d_2^2 + r^2)^{3/2}}\right]$$

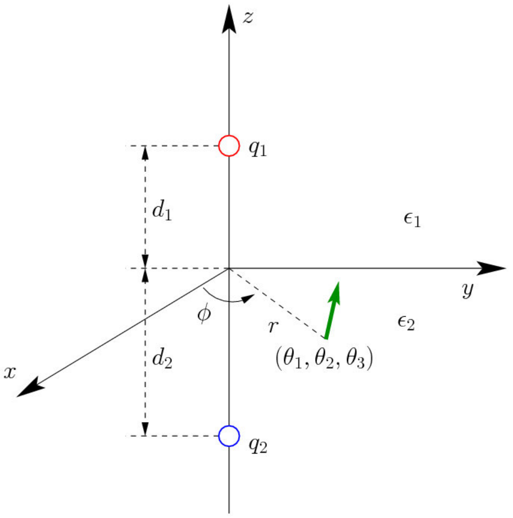

SOI Figure 1. Model geometry: two charges, $\boldsymbol{q_1}$ and $\boldsymbol{q_2}$, are localized at distances $\boldsymbol{d_1} > \boldsymbol{0}$ and $\boldsymbol{d_2} < \boldsymbol{0}$ in two dielectric media with relative susceptibilities $\boldsymbol{\epsilon_1}$ and $\boldsymbol{\epsilon_2}$, correspondingly. Molecules are randomly distributed in the $\boldsymbol{xy}$ plane. One of the molecules, at a position ($\boldsymbol{r\cos\phi}, \boldsymbol{r\sin\phi}$) and orientation given by three Euler angles, $\boldsymbol{\theta_1}, \boldsymbol{\theta_2}, \boldsymbol{\theta_3}$ is shown by a green vector.

Field dependence of the absorption spectrum

To perform the averages, we first expand the transmission spectrum of a single molecule in terms of Gaussian functions

$$A(E, \vec{F}) = \sum_i f_i(\vec{e}_u, \vec{F}) \exp\left[-\frac{1}{2}\left(\frac{E - E_i(\vec{F})}{\sigma}\right)^2\right],$$

where $f_i(\vec{e}_u, \vec{F}) = \frac{4\pi m_e}{3he^2}\mu\left|\vec{e}_u \cdot \vec{M}_{0\to i}\right|^2$ is the molecular oscillator strength, $\vec{e}_u$ is the polarization vector of the incident light, $\vec{M}_{0\to i}$ is the transition dipole moment of state i, $E_i(\vec{F})$ are the corresponding energies of these states.

Since dye molecules are attached to TiO_2 particles and hence their orientations are isotropically distributed in the lab frame, we can average over all directions of the polarization vector $\vec{e}_u$. The averaged oscillator strength, $f_i(\vec{F})$, depends only on the *amplitude* of the transition dipole moment, and hence is a scalar function of field $\vec{F}$.

We now expand oscillator strengths $f_i(\vec{F})$ and energies $E_i(\vec{F})$ up to the second order in field $\vec{F}$

$$E_i(\vec{F}) = E_i + \vec{E}_i \cdot \vec{F} + \frac{1}{2}\vec{F}\,\hat{E}_i\vec{F},$$

$$f_i(\vec{F}) = f_i + \vec{f}_i \cdot \vec{F} + \frac{1}{2}\vec{F}\,\hat{f}_i\,\vec{F}.$$

TDDFT calculations show that the expansion to the second order is sufficient even for fields of the order of 100 MV/m.

To average over molecular orientations and surface area, we will also expand the transmission spectrum up to the second order in field

$$A(E,\vec{F}) = A(E,\vec{F}=0) + \vec{A}(E)\cdot\vec{F} + \vec{F}\hat{A}(E)\vec{F}$$

where

$$\vec{A}(E) = \left.\frac{\partial\vec{A}(E,\vec{F})}{\partial\vec{F}}\right|_{\vec{F}=0}, \quad \hat{A}(E) = \left.\frac{\partial^2\vec{A}(E,\vec{F})}{\partial^2\vec{F}}\right|_{\vec{F}=0}$$

It is convenient to express material parameters in the molecular frame. Let $Q_{\alpha\beta}$ be the transformation matrix from the molecular to the lab frame. Then

$$\vec{A}(E) = \hat{Q}\vec{a}, \quad \hat{A}(E) = \hat{Q}\hat{a}\hat{Q}$$

where

$$\vec{a} = \frac{\partial A}{\partial f_i}\vec{f}_i' + \frac{\partial A}{\partial E_i}\vec{E}_i'$$

$$\hat{a} = \frac{\partial^2 A}{\partial f_i^2}\vec{f}_i'\otimes\vec{f}_i' + \frac{\partial^2 A}{\partial E_i^2}\vec{E}_i'\otimes\vec{E}_i' + \frac{\partial A}{\partial f_i}\hat{f}_i' + \frac{\partial A}{\partial E_i}\hat{E}_i',$$

where all variables in the molecular coordinate frame are primed.

In what follows, we will be interested in the change of the transmission spectrum

$$\Delta A\left(E,\vec{F}\right) = A\left(E,\vec{F}=0\right) - A\left(E,\vec{F}\right) = -\hat{Q}\vec{a}\vec{F} - \frac{1}{2}\vec{F}\hat{Q}\hat{a}\hat{Q}\vec{F}$$

Here $\vec{F} = \vec{F}(x,y)$ is the field in the (x,y) plane and $\hat{Q}$ depends on molecular orientations only.

Averaging over the ensemble of molecules

We further assume that molecules are uniformly distributed on the $z = 0$ surface with the surface density $n = N/S$ and molecular orientations are given by the distribution function $\frac{1}{8\pi^2}g(\Omega)$. Integrating over $d\Omega$ and dS we obtain the ensemble-averaged transmission

$$\langle \Delta A \rangle = n\int d\Omega g(\Omega)\int dS\, \Delta A\left(E,\vec{F}\right) =$$

$$= -na_\beta \int d\Omega g(\Omega) Q_{\alpha\beta} \int dS\, F_\alpha - \frac{n}{2} a_{\gamma\delta} \int d\Omega g(\Omega) Q_{\alpha\gamma} Q_{\beta\delta} \int dS\, F_\alpha\, F_\beta$$

Averaging over the surface area is straightforward. $\int dS\, F_x = 0$ and $\int dS\, F_y = 0$ due to integration over ϕ.

$$\int dS\, F_z = -\frac{2q}{4\pi\epsilon_0(\epsilon_2+\epsilon_1)} \int_0^\infty rdr \int_0^{2\pi} d\phi \left[\frac{\epsilon_2}{\epsilon_1}\frac{d_1}{(d_1^2+r^2)^{\frac{3}{2}}} + \frac{d_2}{(d_2^2+r^2)^{\frac{3}{2}}}\right] = -\frac{q}{\epsilon_0\epsilon_1}$$

$$\int dS\, F_x^2 = \int dS\, F_y^2 = \left(\frac{q}{4\pi\epsilon_0\epsilon}\right)^2 \frac{\pi}{4}\left[\frac{1}{d_2^2} + \frac{1}{d_1^2} - \frac{8}{(d_1+d_2)^2}\right]$$

$$\int dS\, F_z^2 = \left(\frac{q}{4\pi\epsilon_0\epsilon}\right)^2 \frac{\pi}{2}\left[\frac{1}{d_2^2} + \frac{\kappa^2}{d_1^2} + \frac{8\kappa}{(d_1+d_2)^2}\right]$$

Here $\kappa = \epsilon_2/\epsilon_1$, $\epsilon = \frac{\epsilon_1+\epsilon_2}{2}$. Note that the first term depends neither on d_1 nor on d_2.

To average over molecular orientations we rewrite $\hat{Q}$ in terms of Euler angles

$$\hat{Q} = \begin{pmatrix} c_1c_3 - c_2s_1s_3 & -c_1s_3 - c_3c_2s_1 & s_2s_1 \\ c_2c_1s_3 + c_3s_1 & c_1c_2c_3 - s_1s_3 & -c_1s_2 \\ s_3s_2 & c_3s_2 & c_2 \end{pmatrix}$$

where $c_i = \cos\theta_i$ and $s_i = \sin\theta_i$.

The moments of the distribution function $g(\Omega)$ then read

$$g_{\alpha\beta} = \int_0^{2\pi} d\theta_1 \int_0^{\pi} d\theta_2 \sin\theta_2 \int_0^{2\pi} d\theta_3 g(\Omega) Q_{\alpha\beta}$$

$$g_{\alpha\gamma\beta\delta} = \int_0^{2\pi} d\theta_1 \int_0^{\pi} d\theta_2 \sin\theta_2 \int_0^{2\pi} d\theta_3 g(\Omega) Q_{\alpha\gamma} Q_{\beta\delta}$$

We also assume that molecules have preferential polar orientation, while their azimuthal orientations are isotropic, that is $g(\Omega) = g(\theta_2)$. In this case $g_{zz} = g_1$,

$$\begin{array}{lll}
g_{xxxx} = \frac{1}{4}(1+g_2) & g_{xyxy} = \frac{1}{4}(1+g_2) & g_{xzxz} = \frac{1}{2}(1-g_2) \\
g_{yyyy} = \frac{1}{4}(1+g_2) & g_{yxyx} = \frac{1}{4}(1+g_2) & g_{yzyz} = \frac{1}{2}(1-g_2) \\
g_{zzzz} = g_2 & g_{zxzx} = \frac{1}{2}(1-g_2) & g_{zyzy} = \frac{1}{2}(1-g_2) \\
g_{xxyy} = \frac{1}{2} g_1 & g_{xyyx} = -\frac{1}{2} g_1 & g_{yxxy} = -\frac{1}{2} g_1
\end{array}$$

where $g_1 = \frac{1}{2}\int_0^{\pi} d\theta_2 g(\theta_2) \cos\theta_2 \sin\theta_2$, $g_2 = \frac{1}{2}\int_0^{\pi} d\theta_2 g(\theta_2) \cos^2\theta_2 \sin\theta_2$. Note that the rest of the elements are zero. Collecting the terms we obtain

$$\langle \Delta A \rangle = n a_z g_1 \frac{q}{\epsilon_0 \epsilon_1} - \frac{n\pi}{16}\left(\frac{q}{4\pi\epsilon_0\epsilon}\right)^2 \mathrm{Tr}\left(\hat{a}\hat{G}\right)$$

Here we have introduced a distance-dependent matrix

$$\hat{G} = \begin{pmatrix} 1+g_2 & 0 & 0 \\ 0 & 1+g_2 & 0 \\ 0 & 0 & 2(1-g_2) \end{pmatrix} \left[\frac{1}{d_2^2} + \frac{1}{d_1^2} - \frac{8}{(d_1+d_2)^2}\right] + 2\begin{pmatrix} 1-g_2 & 0 & 0 \\ 0 & 1-g_2 & 0 \\ 0 & 0 & 2g_2 \end{pmatrix} \left[\frac{1}{d_2^2} + \frac{\kappa^2}{d_1^2} + \frac{8\kappa}{(d_1+d_2)^2}\right]$$

The expression for $\langle \Delta A \rangle$ is the main result of our derivation and can be rewritten in a compact form presented in the main text

$$\Delta A(d_1, d_2) = nS_1(\lambda, \{M\}, g_1) + n\mathrm{Tr}\left[\hat{S}_2(\lambda, \{M\}, g_1)\hat{G}(g_2, d_1, d_2)\right],$$

where $\{M\}$ represents relevant single-molecule properties, S_1 and $\hat{S}_2$ are spectral shapes, and $\hat{G}$ is the introduced distance-dependent matrix.

Drift-diffusion of a charge in a Coulomb potential: Analytical solution

In this section we will study charge dynamics which is needed to link the distance- to time-dependence of the absorption spectra. We will describe the charge dynamics in terms of a conditional probability function $p(r, t|r_0, t_0)$, which is a probability to find a charge (an electron or a hole) at a position r at time t provided that it was at a position r_0 at time t_0.

Assuming a drift-diffusion type of dynamics for electrons and holes, $p(\vec{r}, t|\vec{r}_0, t_0)$ is a solution of the Smoluchowski equation

$$\frac{\partial p(\vec{r}, t|\vec{r}_0, t_0)}{\partial t} = \vec{\nabla} \cdot De^{-\beta U(\vec{r})}\vec{\nabla} e^{\beta U(\vec{r})} p(\vec{r}, t|\vec{r}_0, t_0),$$

where $U(\vec{r})$ is the external potential at a position $\vec{r}$.

This equation has to be supplemented by appropriate boundary conditions. Here we will be interested in charge dynamics before the recombination, and hence impose a *reflective* boundary condition at $z = 0$

$$\vec{n} \cdot \vec{j}(z = 0, t) = \vec{n} \cdot De^{-\beta U(\vec{r})}\vec{\nabla} e^{\beta U(\vec{r})} p(\vec{r}, t)\Big|_{z=0} = 0,$$

where $\vec{n}$ is a normal to the $z = 0$ plane.

Furthermore, we assume that highly mobile electrons rapidly diffuse away from the interface after they are injected into TiO_2, while significantly less mobile holes drift-diffuse in a half-space $[0, \infty]$. Since a hole interacts with its image charge, the external potential reads

$$U(z) = \frac{1}{2\epsilon_1}\frac{\epsilon_2 - \epsilon_1}{\epsilon_2 + \epsilon_1}\frac{q^2}{z + l},$$

where l is the thickness of the dye layer separating the electron and hole-conducting materials.

It is convenient to introduce a distance l_B at which $U(z)$ is of the order of $k_B T = \beta^{-1}$ and rewrite it in terms of this distance

$$U(z) = k_B T \frac{l_B + l}{z + l}.$$

We now find an approximate solution to this drift-diffusion problem. First, we consider the diffusion in one dimension only, i.e. $p(\vec{r}, t) = p(z, t)$. Second, we approximate $U(z)$ with a linear function on the interval $[0, l_B]$

$$U(z \in [0, l_B]) \sim k_B T \frac{z - l_B + l}{l}.$$

The solution of the Smoluchowski equation in a linear potential with one reflecting boundary is known

$$p(\xi, \tau | \xi_0, 0) = p_1(\xi, \tau | \xi_0, 0) + p_2(\xi, \tau | \xi_0, 0) + p_3(\xi, \tau | \xi_0, 0),$$

where

$$p_1(\xi, \tau | \xi_0, 0) = \frac{1}{\sqrt{4\pi\tau}} \exp\left[-\frac{(\xi - \xi_0 + \tau)^2}{4\tau}\right]$$

$$p_2(\xi, \tau | \xi_0, 0) = \frac{1}{\sqrt{4\pi\tau}} \exp\left[\xi_0 - \frac{(\xi + \xi_0 + \tau)^2}{4\tau}\right]$$

$$p_3(\xi, \tau | \xi_0, 0) = \frac{1}{2} \mathrm{e}^{-\xi} \operatorname{erfc}\left[\frac{\xi + \xi_0 - \tau}{\sqrt{\tau}}\right]$$

Here we introduced a dimensionless unit of length, $= z/l$, and time, $\tau = l^2/D$.

This solution is shown in SOI Figure 2 for two different initial conditions: charge injected directly at a reflecting boundary and charge injected at some distance ($\xi_0 = 1$) from this boundary.

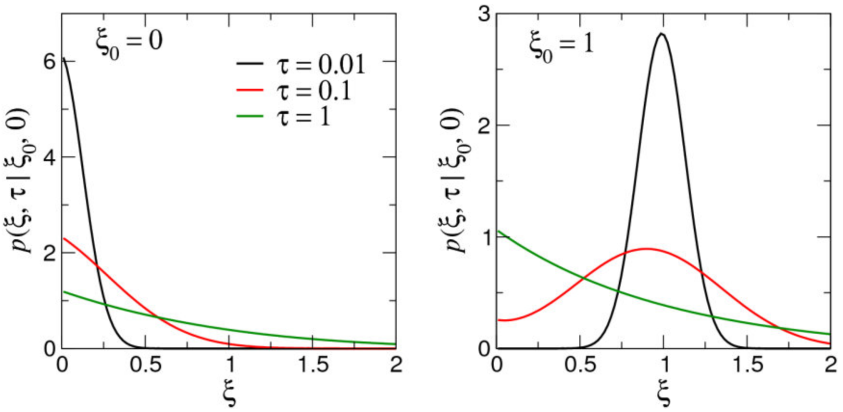

SOI Figure 2. Evolution of the probability distribution for two injection positions: directly at the interface, $\boldsymbol{\xi_0 = 0}$, and far from the interface, $\boldsymbol{\xi_0 = 1}$. In the first case a charge diffuses away from the interface with time, while in the second case it also drifts toward the interface.

Drift-diffusion of a charge in a Coulomb potential: Numerical solution

The analytical approach of solving the Smoluchowski equation helps to understand the influence of initial conditions and it is remarkable that a solution can be written in dimensionless variables. In order to fit the experimental data, we however used the full Coulomb potential, since the linearization might become inaccurate for small surface-charge separations.

The full one dimensional Smoluchowski equation

$$\frac{\partial p(z,t)}{\partial t} = \frac{\partial}{\partial z}\left(D\,\frac{\partial p(z,t)}{\partial z} - \mu F(z)p(z,t)\right),$$

with a Coulomb potential was therefore solved numerically using Matlab, where $F(z) = -\frac{q}{16\pi\epsilon_0\epsilon_1}\frac{\epsilon_2-\epsilon_1}{\epsilon_2+\epsilon_1}\frac{1}{(z+l)^2}$ is the Coulomb field of the image charge and $D = \frac{\mu k_\mathrm{B}T}{q}$ the diffusion constant given by the Einstein relation, μ is the hole mobility, k_B the Boltzmann constant and T the temperature. The equation was solved for $P(z,t)$ on a (z,t)-2500 mesh, which was distributed logarithmically for z and linearly for t. Boundary conditions were chosen to be reflecting similar to the analytical treatment. Size and resolution of the z dimension were set not to lead to finite size effects or uncertainties in the results while keeping the calculation time feasible. The time range was adjusted to the measured time range. Fixed parameters were assigned physically reasonable to be $\epsilon_1 = 3$, $\epsilon_2 = 30$, $\mu = 10^{-3}$ Vs/cm^2 and $T = 300$ K.

Time-dependence of the absorption spectrum

With the solution of the drift-diffusion equation and known dependence of the absorption spectrum on a position of the charge from the interface, ξ, we can now derive explicit time-dependence of the absorption spectrum. As it has been shown above,

$$\langle \Delta A(\xi) \rangle = n a_z g_1 \frac{q}{\epsilon_0 \epsilon_1} - \frac{n\pi}{16} \left(\frac{q}{4\pi\epsilon_0\epsilon} \right)^2 \mathrm{Tr}\left(\hat{a}\hat{G} \right)$$

where, if we neglect the electrons,

$$\hat{G} = \left[\begin{pmatrix} 1+g_2 & 0 & 0 \\ 0 & 1+g_2 & 0 \\ 0 & 0 & 2(1-g_2) \end{pmatrix} + 2\kappa^2 \begin{pmatrix} 1-g_2 & 0 & 0 \\ 0 & 1-g_2 & 0 \\ 0 & 0 & 2g_2 \end{pmatrix} \right] \frac{1}{(\xi+1)^2}.$$

Thus,

$$\langle \Delta A(\tau) \rangle = \int_0^\infty d\xi \, d\xi_0 \langle \Delta A(\xi) \rangle p(\xi, \tau | \xi_0, 0) p(\xi_0)$$

where $p(\xi_0)$ is the distribution of holes at time $t = 0$.

Let us now concentrate on a time-dependent part of the absorption spectrum only (the second term in the expression for $\langle \Delta A(\xi) \rangle$). Rewriting the integrals explicitly and assuming that the initial distribution is $\delta(\xi - \xi_0)$, i.e. all charges are injected at a distance ξ_0, we obtain

$$\langle \Delta A(\lambda, \tau)\rangle = A_1(\lambda) + A_2(\lambda) \int_0^\infty \frac{d\xi}{(\xi+1)^2} p(\xi, \tau | \xi_0, 0).$$

This is the main result of this section: the time-dependence enters the absorption spectrum only via a function

$$\Theta(\tau, \xi_0) = \int_0^\infty \frac{d\xi}{(\xi+1)^2} p(\xi, \tau | \xi_0, 0),$$

which is shown in SOI Figure 3 for several values of injection points ξ_0. The interesting conclusion is that the asymptotic behavior of this function at long times depends on the injection point: if a charge is injected close to the interface, the magnitude of the Stark absorption *decays* with time, since charge *diffuses away* from the interface. If it is injected far from the interface, Stark effect increases with time, which is due to its *drift* towards the interface. In the intermediate region this function is a non-monotonic function of time.

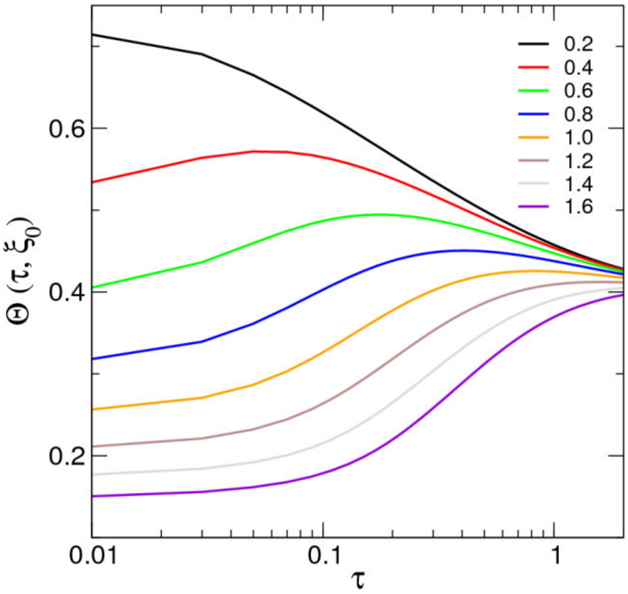

SOI Figure 3. Time-dependent part of the absorption spectrum as a function of dimensionless time $\tau = \frac{l^2}{D} t$ for different charge injection positions $\xi_0 = z_0/l$. Depending on the injection point, the function is either increasing (*charge drift*) or decreases (*charge diffusion*) with time.

First principles calculations

Both the excited states energies $E_i(\vec{F})$ and their associated oscillator strengths $f_i(\vec{F})$ depend on the externally applied electric field $\vec{F}$. Therefore, an explicit determination of the change in the dipole moment $\vec{E}_i$ and polarizability $\hat{E}_i$, as well as their analogues for the quadratic expansion of the oscillator strength, $\vec{f}_i$, $\hat{f}_i$, upon optical excitation of the molecule is required.

To do this, time-dependent density-functional theory (TDDFT) was used to calculate the excited state properties of molecules in an external electric field. Ground state geometry optimizations and excited state calculations have been performed using the B3LYP hybrid functional and 6-311G(d,p) basis set as implemented in the Gaussian 09 package.

First, the direction of the dipole moment of the neutral molecule was aligned with the x-axis. After this calculations with an uniform electric field applied in x, y, and z-directions, whose strength was varied in the range from -2×10^{-3} to 2×10^{-3} a.u. ($1\ \mathrm{a.u.} = \ 5.142206 \cdot 10^{11}\mathrm{V/m}$) were performed. The resulting excitation energies and oscillator strengths for the first three singlet excited states with an electric field in x-direction are shown in SOI Figure 4. Qualitatively similar results are obtained for y and z-directions. Fitting of

$$E_i(\vec{F}) = E_i + \vec{E}_i \ \cdot \vec{F} + \frac{1}{2}\vec{F}\ \hat{E}_i\vec{F},$$

$$f_i(\vec{F}) = f_i + \vec{f}_i \ \cdot \vec{F} + \frac{1}{2}\vec{F}\ \hat{f}_i\ \vec{F}.$$

to the calculated data (shown as lines in SOI Figure 4 for the compound D1) then yields the components of the change in dipole moment as well as the diagonal elements of the change in polarizability, which are summarized in SOI Table 1.

SOI Table 1. Molecular properties of D1 obtained after fitting the field dependence of the excited state energies and oscillator strengths calculated using TDDFT . Similar fit can be done for the compound D2. The factor needed to convert eV/a.u. into Debye is 0.09 (1 Bohr-electron = 2.541756 Debye; 27.2114 eV = 1 Hartree, $\mathbf{1\ a.u.} = \mathbf{5.142206 \cdot 10^{11}\ V/m}$).

E_1 (eV)	2.05
E_2 (eV)	2.55
E_3 (eV)	3.04
$\vec{E}_1$ (eV/a.u.)	346.2
$\vec{E}_2$ (eV/a.u.)	84.3653
$\vec{E}_3$ (eV/a.u.)	384.1
$\hat{E}_1^{xx}, \hat{E}_1^{yy}, \hat{E}_1^{zz}$ (eV/a.u^2)	-146012
$\hat{E}_2^{xx}, \hat{E}_2^{yy}, \hat{E}_2^{zz}$ (eV/a.u^2)	8155.1
$\hat{E}_3^{xx}, \hat{E}_3^{yy}, \hat{E}_3^{zz}$ (eV/a.u^2)	-499173
f_1	0.429376
f_2	0.516711
f_3	0.0
$\vec{f}_1$	308.531
$\vec{f}_2$	-321.834
$\vec{f}_3$	14.3
$\hat{f}_1^{xx}, \hat{f}_1^{yy}, \hat{f}_1^{zz}$	-18976.8
$\hat{f}_2^{xx}, \hat{f}_2^{yy}, \hat{f}_2^{zz}$	34371.2
$\hat{f}_3^{xx}, \hat{f}_3^{yy}, \hat{f}_3^{zz}$	-15624

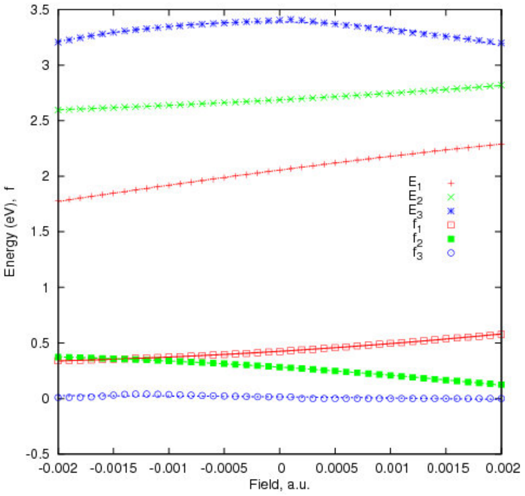

SOI Figure 4. Fit of the field dependence of the three first excitation energies and the corresponding oscillator strengths for the field applied in the x direction. One can see that even for rather high fields the fit with a parabolic function suffices.

Extraction of F(t) from experimental data

In the main text we note that when charges are always equidistant from the interface, i.e. in the case of a hole and its image charge, then the distance dependence becomes a scalar function that can be factored out of $\hat{G}$. In our case the $n\mathrm{Tr}\left[\hat{S}_2(\lambda,\{M\},g_1)\hat{G}(g_2,z_1,z_2)\right]$ simplifies to $n\frac{\epsilon_2}{\epsilon_1}z_1^{-2}\mathrm{Tr}\left[\hat{S}_2(\lambda,\{M\},g_1)\hat{G}(g_2)\right]$, wherein z_1^{-2} expresses the entirety of the distance dependence (and therefore the entirety of the time dependence in the observed data). Should this model be correct, we expect to observe a time invariant Stark signal with a spectrum given by $nS_1(\lambda,\{M\},g_1)$ plus a time varying spectrum given by $\mathrm{Tr}\left[\hat{S}_2(\lambda,\{M\},g_1)\hat{G}(g_2)\right]$ which is weighted by $\frac{\epsilon_2}{\epsilon_1}z_1^{-2}$. Therefore, if we subtract a reference spectrum at a given time from the observed $\Delta T/T(\lambda,t_{1}\,..._{n})$ spectra and normalize the result, we expect to observe a single spectral shape which is proportional to $\mathrm{Tr}\left[\hat{S}_2(\lambda,\{M\},g_1)\hat{G}(g_2)\right]$. In SOI Figure 5, we demonstrate that after subtracting the spectrum measured at 3 ns from each of the other experimentally measured spectrum in the time range within which the kinetics are exclusively due to the Stark effect, the normalized spectra all fall on top of one another. This correct prediction supports the validity of our proposed model. It also allows us to take the kinetics of charge drift diffusion to be extracted from any point within this spectrum. We choose to take it simply from the average of a 10 nm region in the vicinity of its positive peak due to signal-to-noise considerations.

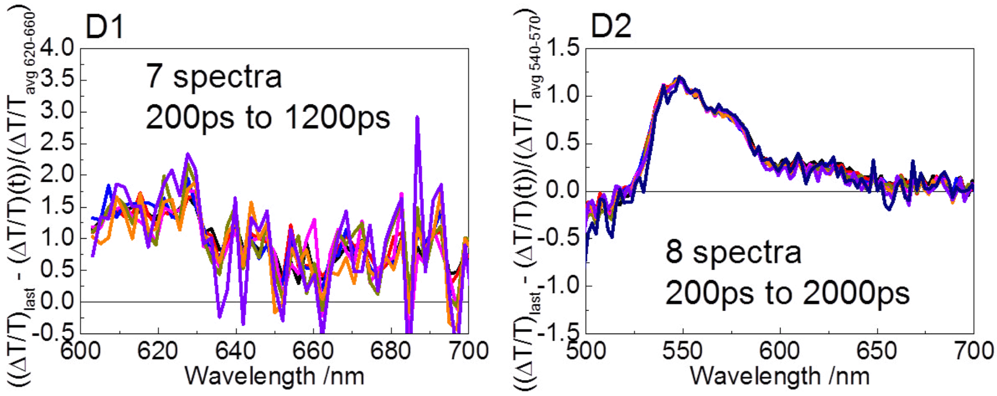

SOI Figure 5: Test of the model. Invariant distance dependent spectral shapes as predicted by our model for D1 and D2 respectively. As discussed in text, this correct prediction supports the validity of our model, and allows us to extract the charge drift/diffusion dynamics from any wavelength region of our choosing.

Solar cell Characteristics for D1 and D2

Solar cell characteristics were measured under simulated AM1.5G conditions in air. The increased absorption of D1 in the red spectral region leads to an increased short circuit current, however the quantum efficiency is decreased.

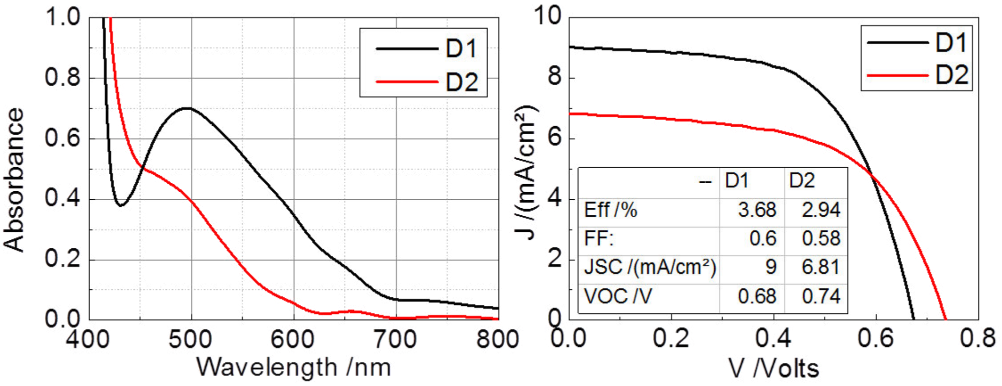

–	D1	D2
Eff /%	3.68	2.94
FF:	0.6	0.58
JSC /(mA/cm²)	9	6.81
VOC /V	0.68	0.74

Transient Absorption Technique

The transient absorption is calculated as

$$\frac{\Delta T}{T} = \frac{T_{\mathrm{on}}\text{-}T_{\mathrm{off}}}{T_{\mathrm{off}}},$$

where T_{on} is the transmission of the white light pulse recorded after an excitation pulse and $\mathrm{T_{off}}$ is that recorded in the absence of a preceding excitation pulse. The white light is produced by focusing a small portion of the 800 nm 100 fs output of a Ti:Saph amplifier operating at 1 kHz (Libra HE, Coherent Inc.) into a sapphire plate to generate a single filament white light continuum. The 700 nm excitation pulse is generated by a TOPAS (Light Conversion Inc.) pumped by the amplifier, chopped to 500 Hz to provide alternating pump on and pump off signals, and mechanically delayed to control the time difference between excitation and probe pulses. The polarization between the pump and probe beams is set to magic angle.

4.5 Parallel Pool Analysis of Transient Spectroscopy Reveals Origins of and Perspectives for ZnO Hybrid Solar Cell Performance Enhancement Using Semiconducting Surfactants

The following letter was published in the Journal of Physical Chemistry Letters by the American Chemical Society on August 27th, 2012.

Reprinted with permission from the Journal of Physical Chemistry Letters, **2012**, *3* (18), pp 2665–2670. Copyright 2012 American Chemical Society.

THE JOURNAL OF PHYSICAL CHEMISTRY Letters
Letter
pubs.acs.org/JPCL

Parallel Pool Analysis of Transient Spectroscopy Reveals Origins of and Perspectives for ZnO Hybrid Solar Cell Performance Enhancement Using Semiconducting Surfactants

Michael Meister,[§,∥] Jason J. Amsden,[*,†,‡,∥,⊥] Ian A. Howard,[*,§,⊥] Insun Park,[‡] Changhee Lee,[†] Do Y. Yoon,[‡] and Frédéric Laquai[*,§,⊥]

[†]School of Electrical and Computer Engineering, Interuniversity Semiconductor Research Center and Center for Multiscale Energy System, Seoul National University, Seoul 151-744, South Korea

[‡]Department of Chemistry, Seoul National University, Seoul 151-747, Korea

[§]Max Planck Research Group for Organic Optoelectronics, Max Planck Institute for Polymer Research, D-55128 Mainz, Germany

Supporting Information

ABSTRACT: Recently, the performance of ZnO nanocrystals as an electron acceptor in a solar cell device was significantly increased by a semiconducting surfactant. Here we show, using transient absorption spectroscopy and a parallel pool analysis, that changes in the quantum efficiency of charge generation account for the performance variation among semiconducting-surfactant-coated, surfactant-coated, and uncoated ZnO nanoparticles. We demonstrate that even better surfactant design to suppress fast recombination could still lead to a further doubling of device efficiency.

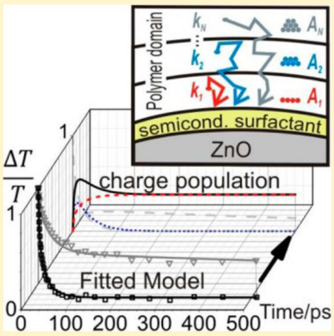

SECTION: Spectroscopy, Photochemistry, and Excited States

Semiconducting nanoparticles such as CdSe,[1] CdS,[2] PbS,[3,4] TiO_2,[5] and ZnO[6] offer alternatives to fullerenes as acceptors in bulk heterojunction photovoltaic devices. The semiconducting nanoparticles have several advantages such as high dielectric constant, tunable band gap (allowing tailoring of energy level alignment and optical absorption), and a wide selection of geometries including particles, rods, and tetrapods. In particular, ZnO is an attractive acceptor due to its nontoxicity, abundance, and ease of synthesis and processing.[7] Typically, bulk heterojunction devices that use conjugated polymers as donors and semiconducting nanoparticles as acceptors have had significantly poorer performance than analogous devices using fullerenes as acceptors. However, it was recently demonstrated that the performance of poly[2-methoxy-5-(3′,7′-dimethyloctyloxyl)-1,4-phenylene vinylene] (MDMO-PPV):ZnO solar cells could be significantly enhanced from ∼0.75 to ∼1.3% by coating the ZnO particles with a semiconducting surfactant,[8] which begins to approach the 2.5% efficiency typical of MDMO-PPV: C_{61}-butyric acid methyl ester (PCBM) devices.[9]

In this letter we demonstrate that time-resolved optical spectroscopy interpreted through a parallel-pool model can fully expose the changes in the device photophysics that lead to the increased efficiency, even when the rate constants are distributed rather than homogeneous. We determine which processes principally limit the internal quantum efficiency for cells prepared with semiconducting-surfactant-coated ZnO, ZnO coated with a nonsemiconducting surfactant, and uncoated ZnO and for each case with which approaches and by how much the internal quantum efficiency might still be increased.

The 3D mesostructure of a hybrid organic:inorganic bulk heterojunction using CdSe nanoparticles with short butylamine ligands has been fully characterized by electron tomography.[10] It was shown that in contrast with the intercalation and mixed phases that can occur in polymer:fullerene blends,[11] the nanoparticles tended to aggregate in the conjugated polymer matrix. This means that quenching of a polymer:nanocrystal blend exciton is strongly influenced by diffusion and therefore sensitively depends on the initial distance between the exciton and the interface. In addition, the quenching is affected by the probability that transfer occurs when an interface is reached. We expect these rates to vary between the three types of ZnO we prepared: One without surfactant, one with a recently developed long-chain semiconducting surfactant 2-(2-ethylhexyl)-1,3-dioxo-2,3-dihydro-1*H*-benzo[de]isoquinoline-6,7-di-

Received: May 16, 2012
Accepted: August 27, 2012

ACS Publications dx.doi.org/10.1021/jz3006207 | J. Phys. Chem. Lett. 2012, 3, 2665−2670

carboxylic acid (BQ),[8] and one with a nonsemiconducting surfactant oleic acid (OA). In previous work, we observed that the dispersion of the nanoparticles drastically increases with the use of the surfactants, but the morphology is similar for both the semiconducting and nonsemiconducting surfactant, so differences in exciton quenching between the surfactants may be primarily influenced by a change in the probability of exciton quenching when the surfactant interface is reached.[8] Blend films of ∼100 nm thickness were prepared on quartz substrates with a 1:2 weight ratio of MDMO-PPV to ZnO for each ZnO type. For the surfactant-coated ZnO, the ZnO contained 3% by weight of the surfactant.

In Figure 1a, we present how we will approach the analysis of the time dependent, diffusion-influenced rate of exciton quenching using the sum of parallel pools. The net effective rate of exciton quenching can be represented by a sum of rates for excitons initially created in parallel population pools each with a unique characteristic exciton quenching rate k_i and population fraction A_i. These reaction rates need not be purely diffusion-limited as the k_i values can also account for a nonunity probability of charge transfer at the interface, which will likely be the case at least for the (OA)ZnO. Our parallel pool method works by analogy to our previous work on determining the phase-domain size in polymer:polymer blends.[12] We either select a set of physically reasonable k_i values and then allow the fractions of the population, the A_i values, to vary to give the best fit to the experimental data or we allow both the k_i values and A_i values to vary.[13] In either case, we can use them to calculate the average decay rate of the entire population as $\tilde{k} = (\sum_i A_i/k_i)^{-1}$. This average rate, $\tilde{k}$, can then be compared with other rates to determine quantitatively population evolutions and quantum efficiencies.

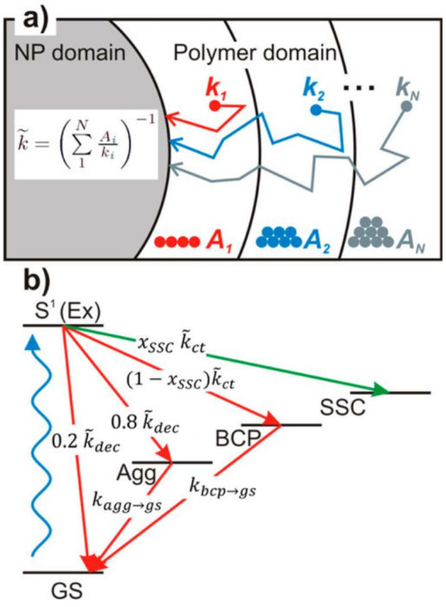

Figure 1. Panel a shows how the distributed rate of exciton quenching at nanoparticle:polymer interfaces can be represented by a sum of parallel population pools. Panel b shows the photophysical model used to fit the transient absorption kinetics of the MDMO-PPV:ZnO blend films. Ex: primary intrachain excitons; Agg: interchain aggregate states; BCP: bound charge pairs that lead to fast recombination to the ground state (GS); SSC: spatially separated free charges that do not recombine on the time scale of the experiment. k_x are rates related to single exponential decays, where x is indicating the transition it refers to; $\tilde{k}_x$ are parallel pool averages used to take into account the distributed or time-dependent rates. Here $x = dec$ denotes the depopulation of Ex due to recombination and energy transfer to aggregate, and $x = ct$ denotes the depopulation of Ex due to charge transfer. x_{SSC} is the fraction of exciton quenching by charge transfer that leads to spatially separated charges.

Our goal is to understand how the surfactant-induced changes affect the internal quantum efficiency of the photovoltaic blends. To achieve this, we will use the aforementioned parallel pool technique alongside the relevant photophysical model as shown in Figure 1b (which we develop and justify in the coming text) to fit the stimulated emission and photoinduced absorption transients measured with ultrafast pump−probe spectroscopy. Examples of the measured transient absorption data are shown in Figure 2 for the neat MDMO-PPV film and the MDMO-PPV:(BQ)ZnO film. The positive signal shown by the blue lines is due to stimulated emission of the exciton species. Because excitons are quenched by charge transfer in the blends, this signal becomes a negative charge-induced absorption. In the photoinduced absorption region shown by the red lines, the photoinduced absorptions of excitons, MDMO-PPV aggregates, and charges all play roles. A slight complication, observable in Figure 2b in the different decay of the red and blue lines, is that exciton quenching occurs even in neat MDMO-PPV films due to energy transfer to aggregate states in MDMO-PPV. We note that the presence of aggregate states in MDMO-PPV has been well-established in previous literature.[14−16] This means, though, that to characterize accurately the charge-transfer-induced exciton quenching, we must take into account this competing aggregate-induced quenching. To establish the rate of aggregate induced quenching, we will begin by examining the kinetics of the neat MDMO-PPV film.

Using a parallel pool model to account for the different rates of exciton quenching by energy transfer to aggregates, the evolution of the emissive exciton population in the neat material (normalized to the initial exciton concentration) can be expressed as $Ex_{\text{neat}}(t) = \sum_{i=1}^{N} A_i \exp(-k_{\text{dec},i}t)$, where N is the number of subsets, A_i is the fraction of the total population that decays with the rate $k_{\text{dec},i}$, and $\sum_{i=1}^{N} A_i = 1$. The population of aggregate states in the neat film is given by $Agg_{\text{neat}}(t) = (1 - PLQE) \times \tilde{k}_{\text{dec}}/(\tilde{k}_{\text{dec}} - k_{\text{agg}\to\text{gs}})[\exp(-k_{\text{agg}\to\text{gs}}t)] - Ex_{\text{neat}}(t))$, where $\tilde{k}_{\text{dec}}$ is the inverse of the weighted average decay lifetime of the exciton ($\tilde{k} = (\sum_i A_i/k_i)^{-1}$), and $k_{\text{agg}\to\text{gs}}$ is the monoexponential rate of aggregate decay to the ground state. The photoluminescence quantum efficiency (PLQE) of MDMO-PPV in film is ∼20%.[17] Making the assumption that aggregate formation is the primary nonradiative decay channel, the rate of aggregate formation is $\tilde{k}_{\text{agg}} = (1 - \text{PLQE}) \times \tilde{k}_{\text{dec}} = 0.8\tilde{k}_{\text{dec}}$. This assumption is justified by the fact that the PLQE is significantly lower in film than in solution. The normalized transient absorption of the neat material shown in Figure 3a can be fit simultaneously in the region of the stimulated emission (610−675 nm) and the photoinduced absorption (900−950 nm, using Origin 8.5, Originlab) with the equations $((\Delta T)/T)_{\text{stim}} = Ex_{\text{neat}}(t)$ and $((\Delta T)/T)_{\text{pia}} = Ex_{\text{neat}}(t) + r^{\text{pia}}_{\text{Agg/Ex}} Agg_{\text{neat}}(t)$, where $r^{\text{pia}}_{\text{Agg/Ex}}$ represents the ratio between the cross-section of the aggregate and the exciton in the photoinduced absorption region. The equation for the stimulated emission region can neglect the influence of aggregates, as we observe that the signal in this region decays

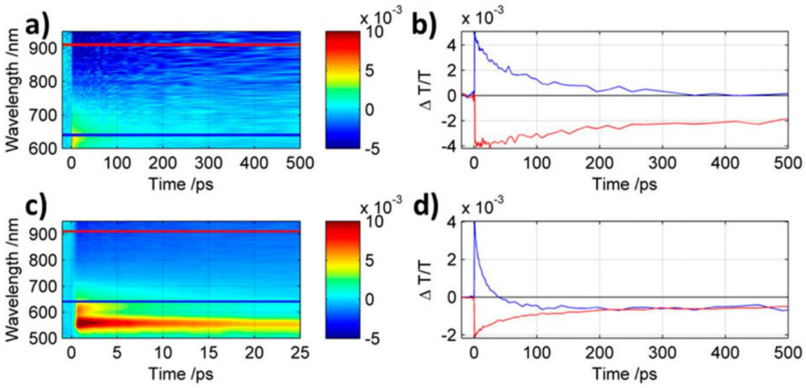

Figure 2. Representative transient absorption data of neat MDMO-PPV (a,b) and MDMO-PPV:(BQ)ZnO blend (c,d). Positive $\Delta T/T$ signals (stimulated emission and absorption bleach) are shown from cyan to red, whereas negative signals (photoinduced absorptions) are shown in blue. Panels a and b show the stimulated emission (600−700 nm, blue line) and photoinduced absorption (700−900 nm, red line) in the neat polymer. The stimulated emission decays more quickly than the photoinduced absorption, indicating, in accordance with previous literature, that dark aggregate states play a role alongside emissive excitons in the neat material and must be taken into account. Panel c shows the absorption bleach (long-lived positive signal centered at 550 nm), the quenched stimulated emission (600−700 nm, blue line), and photoinduced absorption (700−900 nm, red line) in the semiconducting surfactant blend. The efficiency of charge generation will be determined from the stimulated emission quenching, and the alteration of the photoinduced absorption kinetics examples of which are shown in panel d.

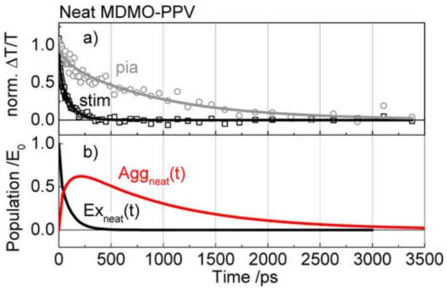

Figure 3. (a) Absorption transients of a neat MDMO-PPV film in the stimulated emission region 610−675 nm (black rectangles) and the photoinduced absorption region 900−950 nm (gray circles) along with a fit (solid lines) according to the model, as described in the text. (b) Population evolutions of primary intrachain excitons ($Ex_{\mathrm{neat}}(t)$) and interchain aggregate states ($Agg_{\mathrm{neat}}(t)$) as derived from the fit.

to zero by 300 ps, indicating that the cross-section of the aggregates is negligible in this wavelength range. Taking two distinct values for $k_{\mathrm{dec},i}$ ($k_{\mathrm{dec},1} = 1 \times 10^{11}$/s and $k_{\mathrm{dec},2} = 1 \times 10^{10}$/s) leads to the parameters shown in Table 1 and the lines shown in Figure 3a. Adding further population subsets did not improve the fitting. In Figure 3b, the extracted population evolutions of excitons and aggregates are shown.

Having established the rate of exciton quenching by transfer to aggregates, we can now examine the data from the blends to examine exciton quenching due to charge transfer. The normalized kinetics of the stimulated emission and photoinduced absorption regions are shown for each blend in the first row of Figure 4. In the stimulated emission region, the signal now becomes negative after a given time due to the non-negligible induced absorption of charges in this wavelength range. The photoinduced absorption now becomes a super-

Table 1. Parameters Determining Exciton Quenching by Energy Transfer to Aggregate States Extracted from Fitting of the Neat-Film-Stimulated Emission and Induced Absorption

parameter	neat fit values
A_1	0.326 ± 0.027
$k_{\mathrm{dec},1}/\mathrm{ps}^{-1}$	0.1 fixed
A_2	0.674 ± 0.016
$k_{dec,2}/ps^{-1}$	0.01 fixed
$k_{\mathrm{agg}\rightarrow\mathrm{gs}}/\mathrm{ps}^{-1}$	(1.04 ± 0.06)x10^{-3}
$r^{\mathrm{pia}}_{\mathrm{Agg/Ex}}$	0.907 ± 0.018

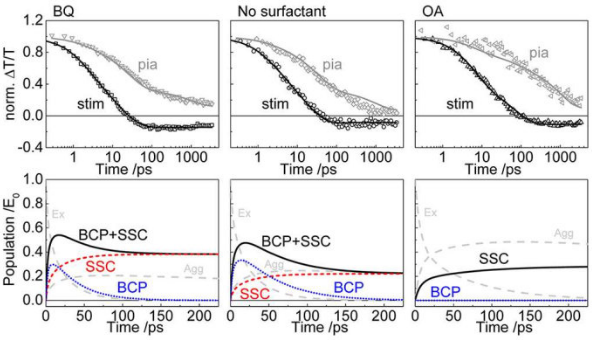

Figure 4. Kinetics of stimulated emission and photoinduced absorption for MDMO-PPV:ZnO blends with the three different surfactants BQ, no surfactant, and OA (upper panels, from left to right). The data are shown as dots along with the fitted curves (solid lines) derived from the model depicted in Figure 1b and described in the text. The lower panels show the population kinetics as obtained from the fitted model for the bound charge pair (BCP, dotted blue lines), the free spatially separated charges (SSC, dashed red lines), and the sum of both accounting for all charges created (solid black lines) for the three ZnO conformations. Populations of excitons (Ex) and aggregate states (Agg) are shown as gray dashed lines. BQ exhibits the highest splitting efficiency and OA exhibits the lowest along with a very low fraction of BCPs, whereas the particles without surfactant have the largest amount of BCPs and a similar splitting efficiency as OA.

position of signals originating from excitons, aggregates, and charges. To describe both wavelength regions in a single fit with shared parameters, a fast charge recombination channel has to be introduced. Without this channel, the photoinduced absorption and the stimulated emission regions of (BQ)ZnO and ZnO could not be described satisfactorily in the first few hundred picoseconds. This fast charge recombination component leads us to postulate that two populations of charges can be created. One, which we name bound charge pairs (BCPs), can undergo fast recombination, likely because the electron remains trapped on the surface of the nanoparticle or perhaps on the semiconducting surfactant. The other population, which we name spatially separated charges (SSCs), cannot decay on the nanosecond time scale because the charges achieve a significant enough initial separation that they no longer influence one another. We will examine the recombination of these free charges later and find that it occurs much more slowly on the time scale of tens of microseconds.

On the basis of the above qualitative observation regarding fast charge recombination, we introduce the factor x_{SSC} to represent the fraction of exciton quenching by charge transfer that leads to SSCs. (See Figure 1b.) For (OA)ZnO, the decay of the photoinduced absorption can be entirely explained by decay of the aggregate pool to the ground state with the rate previously determined in the neat film. (See Figure S4 in the Supporting Information.) Constraining x_{SSC} to 1 for (OA)ZnO is thus a reasonable assumption, whereas for the other two samples, it remains a fitting parameter. Leaving x_{SSC} a free parameter for (OA)ZnO results in over-parametrization and strong cross-correlations without improving the fit, justifying our constraint to the simpler model in this case. With this total model as shown in Figure 1b, the rate equations can be written for each state as:

$$Ex_{\mathrm{blend}}(t) = Ex_{\mathrm{neat}}(t) \sum_{M}^{i=1} C_i \exp(-k_{\mathrm{ct},i}t)$$

$$Agg_{\mathrm{blend}}(t) = \frac{\tilde{k}_{\mathrm{agg}}}{\tilde{k}_{\mathrm{dec}} + \tilde{k}_{\mathrm{ct}} - k_{\mathrm{agg}\to\mathrm{gs}}}(\exp(-k_{\mathrm{agg}\to\mathrm{gs}}t) - Ex_{\mathrm{blend}}(t))$$

$$\mathrm{BCP}(t) = \frac{(1 - x_{\mathrm{SSC}})\tilde{k}_{\mathrm{ct}}}{\tilde{k}_{\mathrm{dec}} + \tilde{k}_{\mathrm{ct}} - k_{\mathrm{bcp}\to\mathrm{gs}}}(\exp(-k_{\mathrm{bcp}\to\mathrm{gs}}t) - \mathrm{Ex}_{\mathrm{blend}}(t))$$

$$SSC(t) = \frac{x_{\mathrm{SSC}}\tilde{k}_{\mathrm{ct}}}{\tilde{k}_{\mathrm{dec}} + \tilde{k}_{\mathrm{ct}}}(1 - Ex_{\mathrm{blend}}(t))$$

Exciton quenching due to charge transfer is diffusion-limited and analogous to the quenching through aggregates described by a multiexponential with subrates $k_{\mathrm{ct},i}$ and their weighting C_i. The transient absorption signals in the stimulated emission and absorption region can be expressed as:

$$\left(\frac{\Delta T}{T}\right)_{\mathrm{stim}} = Ex(t) + r^{\mathrm{stim}}_{\mathrm{CT/Ex}}(BCP(t) + SSC(t))$$

$$\left(\frac{\Delta T}{T}\right)_{\mathrm{pia}} = Ex(t) + r^{\mathrm{pia}}_{\mathrm{Agg/Ex}}Agg(t) + r^{\mathrm{pia}}_{\mathrm{CT/Ex}}(BCP(t) + SSC(t))$$

where $r^{\mathrm{stim}}_{\mathrm{CT/Ex}}$ and $r^{\mathrm{pia}}_{\mathrm{CT/Ex}}$ represent the ratios between the cross-sections of charges and excitons in the stimulated emission and photoinduced absorption region, respectively. All parameters obtained from the neat fit were adopted as fixed parameters. To obtain the most accurate parameter set possible, the stimulated emission together with the photoinduced absorption kinetics were fit at the same time for all three samples. Global variables, like the cross-section ratios, were shared across this global fit to the six data sets. Two subsets ($M = 2$) were sufficient to describe the CT-creation; adding further subsets did not improve the fitting. Further details of the fitting alongside a full table of extracted parameters with uncertainties are given in the Supporting Information. The results of the fitting are shown in the upper part of Figure 4. In the lower part, the evolution of the excited-state populations for each sample extracted from the global fitting is shown. Importantly, we can calculate the probability that a given absorbed photon results in SSCs for each sample as $\eta_{\mathrm{SSC}} = x_{\mathrm{SSC}}\tilde{k}_{\mathrm{CT}}/(\tilde{k}_{\mathrm{dec}} + \tilde{k}_{\mathrm{CT}})$. We compare this probability with the internal photon conversion efficiency measured in the device structure in Table 2.

Table 2. Charge Separation Factors Extracted from the Fitting

sample	k_{ct}^{-1}/ps	x_{SSC} [a]	η_{SSC} [b]	IPCE
(BQ)ZnO	28 ± 7	0.51 ± 0.11	0.38 ± 0.06	0.44
ZnO	37 ± 7	0.31 ± 0.06	0.22 ± 0.04	0.29
(OA)ZnO	178 ± 48	1 [c]	0.28 ± 0.05	0.27

[a] x_{SSC} is the portion of spatially separated charges of all excitons undergoing charge transfer. [b] η_{SSC} is the efficiency of free charge generation extracted from the fitting of the optical spectroscopy. [c] Parameter x_{SSC} of OA was fixed as explained in the text.

The exciton splitting efficiency obtained from the fitting roughly follows the trend of the incident photon to electron conversion efficiency (IPCE) data with the (BQ)ZnO having significantly more SSC generation and also a correspondingly higher IPCE. We note that although we would expect the SSC generation efficiency to be higher than the IPCE, the opposite is observed for ZnO and (BQ)ZnO. However, the IPCE was measured at the built-in field, whereas the spectroscopically determined SSC generation efficiency was measured in the absence of field. A slight field dependence of the SSC generation efficiency (x_{SSC}) would be physically reasonable and explain the underestimation of the quantum efficiency by the spectroscopic measurement in the ZnO and (BQ)ZnO samples.

The cause of the high η_{SSC} in the (BQ)ZnO is due to a fast effective rate of exciton quenching by charge transfer, which can be physically explained by the surfactant creating a good dispersion of ZnO nanocrystals in the polymer matrix and the probability of dissociation for an exciton reaching an interface remaining high.[18] Upon looking at the evolution of the total charge population, we see that it peaks at ~55% around 25 ps after photoexcitation and that the efficiency of SSC generation would be over 60% if x_{SSC} were unity in this sample. In terms of device performance, we see that suppressing the formation of quickly recombining trapped charges could double the efficiency of (BQ)ZnO, and doing this in combination with increasing the rate of exciton quenching by charge transfer so that it was much faster than aggregate formation could increase the efficiency by a factor of 3. So, significant room for improvement remains for the quantum efficiency even in the most efficient (BQ)ZnO sample.

The ZnO sample has a slightly slower average rate of exciton quenching by charge transfer, but the rough similarity with the (BQ)ZnO sample suggests that the dispersion of the nanoparticles in terms of its effect on exciton quenching by charge transfer is not very different between the samples. Given that the morphology shown in ref 8 shows a less-dispersed structure for the uncoated ZnO, it is possible that the charge transfer itself is more effective, as no barrier between ZnO and polymer exists. If x_{SSC} were unity for the ZnO sample, then η_{SSC} would be tripled to a value over 60%. Therefore, our analysis shows that it is not the poor phase separation in the uncoated ZnO samples that is reducing quantum efficiency due to poor exciton quenching but rather that the majority of charges formed by exciton quenching quickly recombine in the absence of a surfactant. This could be due to a high number of surface states in ZnO,[19] leading to fast recombination of trapped charges.

The (OA)ZnO sample has a very much slower effective rate of exciton quenching by charge transfer. Because the OA surfactants do not negatively affect the dispersion of the nanocrystals in the polymer, we hypothesize that the presence of the bulky nonconjugated surfactant introduces a significant tunneling barrier to electron transfer for an exciton reaching the interface and therefore significantly reduces the probability that electron transfer occurs. This means that an exciton could have multiple encounters with the interface without being quenched by charge transfer. The consequence of this slow quenching by charge transfer is that a significant fraction of the exciton population decays into the aggregate state. It is worth noticing that the long chains of the surfactant could also influence the ordering of the polymer altering the exciton diffusion and polymer aggregation.[20,21] However, an advantage of the long inactive surfactant is that if charge transfer does occur, then there is negligible charge recombination on the short time scale. In contrast with the other samples, all quenching by charge transfer leads to free charges. This indicates that the long surfactant is effective in passivating the nanoparticle surface and hindering recombination but that this advantage is overwhelmed by its suppression of the charge-transfer rate.

Finally, to investigate the recombination of SSCs, Figure 5 shows the kinetics of the charge-induced absorption on the time scale of 500 ps to 20 μs. The recombination of free charges in all three cases is very slow. The free carrier lifetime is significantly longer than in PCBM for all ZnO samples, in agreement with previous studies,[22] suggesting that free carrier recombination competing with extraction may not play a significant role in reducing the quantum efficiency of these samples. This is consistent with our previous observation that the efficiency of free charge generation and the internal quantum efficiency were roughly similar. Therefore, we can conclude for all of these samples that the primary quantum efficiency loss mechanisms were the previously discussed limitations of SSC formation.

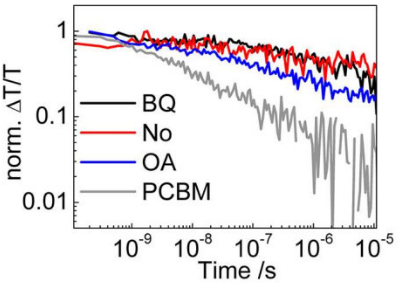

Figure 5. Long-time recombination kinetics of the different blends monitored at the photobleach. With PCBM, recombination is much faster. The ZnO blends exhibit a slower recombination that is in all three cases similar. Only OA has a slightly faster recombination.

In conclusion, our work highlights the importance of continuing to work on nanoparticle surfactant design and synthesis because with the aid of surfactants nanoparticle acceptors should be able to rival the efficiency of fullerenes in bulk heterojunction solar cells. The key functionality that the surfactant must enable appears to be the suppression of fast recombination while not hindering the efficient quenching of excitons by charge transfer.

Along this line, Sargent et al. recently achieved 6% power conversion efficiency using nanocrystal-based inorganic depleted-heterojunction solar cells based on the development of new atomic ligands that passivated surface states while introducing only minimal barriers to transport.[23] Our results suggest that using a similar approach to passivation in the bulk heterojunction device structure may also be fruitful, and with such improvements, the quantum efficiency could theoretically be improved by at least a factor of 2, bringing the power conversion efficiency into the same range as that achieved in this polymer with a fullerene acceptor.

■ ASSOCIATED CONTENT

Ⓢ Supporting Information

Material and sample preparation along with the experimental methods description, device characteristics, quasi-steady-state photoinduced absorption and transient absorption spectra as well as details to the fitting and an alternative fitting model leading to the same conclusions. This information is available free of charge via the Internet at http://pubs.acs.org/.

■ AUTHOR INFORMATION

Corresponding Author

*E-mail: phytrptj@gmail.com (J.J.A.), ian.howard@mpip-mainz.mpg.de (I.A.H.), laquai@mpip-mainz.mpg.de (F.L.).

Author Contributions

‖These authors contributed equally to this work.

Notes

The authors declare no competing financial interest.

⊥Inquiries about surfactant and sample preparation should be addressed to J.J.A. whereas those regarding photophysics should be addressed to F.L. or I.A.H.

■ ACKNOWLEDGMENTS

M.M., C.H.L., and D.Y.Y. thank the IRTG 1404: Selforganized materials for optoelectronic devices, co-funded by the German Research Foundation (DFG) and the National Research Foundation of Korea (NRF), and the Division of Chemistry and Molecular Engineering Program of the Brain Korea 21 Project is gratefully acknowledged. M.M. also thanks the German Research Foundation (DFG) and the and the Max Planck Graduate Center (MPGC) for financial support. J.J.A. is funded by a National Science Foundation International Research Fellowship (OISE-0965057). I.P. thanks the Chemistry and Molecular Engineering Program of BK21 Project.

I.A.H. thanks the Alexander von Humboldt Foundation for a postdoctoral fellowship. F.L. thanks the Max Planck Society for funding a Max Planck Research Group.

■ REFERENCES

(1) Huynh, W. U.; Dittmer, J. J.; Alivisatos, A. P. Hybrid Nanorod-Polymer Solar Cells. *Science* **2002**, *295*, 2425−2427.

(2) Ren, S.; Chang, L.-Y.; Lim, S.-K.; Zhao, J.; Smith, M.; Zhao, N.; Bulović, V.; Bawendi, M.; Gradečak, S. Inorganic−Organic Hybrid Solar Cell: Bridging Quantum Dots to Conjugated Polymer Nanowires. *Nano Lett.* **2011**, 3998−4002.

(3) Seo, J.; Cho, M. J.; Lee, D.; Cartwright, A. N.; Prasad, P. N. Efficient Heterojunction Photovoltaic Cell Utilizing Nanocomposites of Lead Sulfide Nanocrystals and a Low-Bandgap Polymer. *Adv. Mater.* **2011**, 3984−3988.

(4) McDonald, S. A.; Konstantatos, G.; Zhang, S. G.; Cyr, P. W.; Klem, E. J. D.; Levina, L.; Sargent, E. H. Solution-Processed PbS Quantum Dot Infrared Photodetectors and Photovoltaics. *Nat. Mater.* **2005**, *4*, 138−142.

(5) Salafsky, J. S. Exciton Dissociation, Charge Transport, And Recombination in Ultrathin, Conjugated Polymer-TiO_2 Nanocrystal Intermixed Composites. *Phys. Rev. B.* **1999**, *59*, 10885−10894.

(6) Beek, W. J. E.; Slooff, L. H.; Wienk, M. M.; Kroon, J. M.; Janssen, R. A. J. Hybrid Solar Cells Using a Zinc Oxide Precursor and a Conjugated Polymer. *Adv. Funct. Mater* **2005**, *15*, 1703−1707.

(7) Beek, W. J. E.; Wienk, M. M.; Kemerink, M.; Yang, X.; Janssen, R. A. J. Hybrid Zinc Oxide Conjugated Polymer Bulk Heterojunction Solar Cells. *J. Phys. Chem. B* **2005**, *109*, 9505−9516.

(8) Park, I.; Lim, Y.; Noh, S.; Lee, D.; Meister, M.; Amsden, J. J.; Laquai, F.; Lee, C.; Yoon, D. Y. Enhanced Photovoltaic Performance of ZnO Nanoparticle/Poly(phenylene vinylene) Hybrid Photovoltaic Cells by Semiconducting Surfactant. *Org. Electron.* **2011**, *12*, 424−428.

(9) Shaheen, S.; Brabec, C.; Sariciftci, N.; Padinger, F.; Fromherz, T.; Hummelen, J. 2.5% Efficient Organic Plastic Solar Cells. *Appl. Phys. Lett.* **2001**, *78*, 841−843.

(10) Hindson, J. C.; Saghi, Z.; Hernandez-Garrido, J.-C.; Midgley, P. A.; Greenham, N. C. Morphological Study of Nanoparticle−Polymer Solar Cells Using High-Angle Annular Dark-Field Electron Tomography. *Nano Lett.* **2011**, *11*, 904−909.

(11) Cates, N. C.; Gysel, R.; Beiley, Z.; Miller, C. E.; Toney, M. F.; Heeney, M.; McCulloch, I.; McGehee, M. D. Tuning the Properties of Polymer Bulk Heterojunction Solar Cells by Adjusting Fullerene Size to Control Intercalation. *Nano Lett.* **2009**, *9*, 4153−4157.

(12) Westenhoff, S.; Howard, I. A.; Friend, R. H. Probing the Morphology and Energy Landscape of Blends of Conjugated Polymers with Sub-10 nm Resolution. *Phys. Rev. Lett.* **2008**, *101*, 016102.

(13) It is also possible to fix the k_i values to physically reasonable values and fit only the A_i values. Physically, the fixing of the k_i values corresponds to selecting boundaries of the volumes schematically illustrated in Figure 1, then fitting A_i values corresponds to solving for the initial population in the selected volume regions. We do this for the neat film.

(14) Yan, M.; Rothberg, L. J.; Kwock, E. W.; Miller, T. M. Interchain Excitations in Conjugated Polymers. *Phys. Rev. Lett.* **1995**, *75*, 1992−1995.

(15) Schwartz, B. J.; Hide, F.; Andersson, M. R.; Heeger, A. J. Ultrafast Studies of Stimulated Emission and Gain in Solid Films of Conjugated Polymers. *Chem. Phys. Lett.* **1997**, *265*, 327−333.

(16) Collison, C. J.; Rothberg, L. J.; Treemaneekarn, V.; Li, Y. Conformational Effects on the Photophysics of Conjugated Polymers: A Two Species Model for MEH−PPV Spectroscopy and Dynamics. *Macromolecules* **2001**, *34*, 2346−2352.

(17) Cao, Y.; Parker, I. D.; Yu, G.; Zhang, C.; Heeger, A. J. Improved Quantum Efficiency for Electroluminescence in Semiconducting Polymers. *Nature* **1999**, *397*, 414−417.

(18) Oosterhout, S. D.; Wienk, M. M.; van Bavel, S. S.; Thiedmann, R.; Koster, L. J. A.; Gilot, J.; Loos, J.; Schmidt, V.; Janssen, R. A. J. The Effect of Three-Dimensional Morphology on the Efficiency of Hybrid Polymer Solar Cells. *Nat. Mater.* **2009**, *8*, 818−824.

(19) Jianpu, W.; Baoquan, S.; Feng, G.; Greenham, N. C. Memristive Devices Based on Solution-Processed ZnO Nanocrystals. *Phys. Status Solidi A* **2010**, *207*, 484−487.

(20) Monson, T. C.; Lloyd, M. T.; Olson, D. C.; Lee, Y. J.; Hsu, J. W. P. Photocurrent Enhancement in Polythiophene- and Alkanethiol-Modified ZnO Solar Cells. *Adv. Mater.* **2008**, *20*, 4755−4759.

(21) Lloyd, M. T.; Prasankumar, R. P.; Sinclair, M. B.; Mayer, A. C.; Olson, D. C.; Hsu, J. W. P. Impact of Interfacial Polymer Morphology on Photoexcitation Dynamics and Device Performance in P3HT/ZnO Heterojunctions. *J. Mater. Chem.* **2009**, *19*, 4609−4614.

(22) Noone, K. M.; Subramaniyan, S.; Zhang, Q. F.; Cao, G. Z.; Jenekhe, S. A.; Ginger, D. S. Photoinduced Charge Transfer and Polaron Dynamics in Polymer and Hybrid Photovoltaic Thin Films: Organic vs Inorganic Acceptors. *J. Phys. Chem. C* **2011**, *115*, 24403−24410.

(23) Tang, J.; Kemp, K. W.; Hoogland, S.; Jeong, K. S.; Liu, H.; Levina, L.; Furukawa, M.; Wang, X.; Debnath, R.; Cha, D.; et al. Colloidal-Quantum-Dot Photovoltaics Using Atomic-Ligand Passivation. *Nat. Mater.* **2011**, *10*, 765−771.

4.5.1 Supporting Information

This is an abridged version of the supporting information to the letter. It is shortened by the information already provided in the experimental techniques chapter 3 to avoid the repetition of experimental details. The full version is available free of charge via the Internet at http://pubs.acs.org/.

Materials

MDMO-PPV which is known to have its glass transition temperature around 25–50 °C was purchased from COVION (now Merck KGaA), with a molecular weight of M_n 150,000 and polydispersity index of 4.7. PCBM was purchased from nano-C. zinc acetate dihydrate ($Zn(Ac)_2{\cdot}2H_2O$, > 98 % purity) and Oleic acid were obtained from Sigma-Aldrich. Potassium hydroxide (KOH, GR reagent) was obtained from Duksan Pharmaceutical Co. Ltd. All solvents used in this work are of analytical grade or purer. All chemicals mentioned above were used without further purification.

ZnO Synthesis: The synthesis is carried out under N_2 atmosphere. At first, 1.23 g of $Zn(Ac)_2{\cdot}2H_2O$ was dissolved in 55 ml of methanol at room temperature. Then, 25 ml of a methanol solution containing 0.48 g of KOH is added dropwise over a 20 min time interval at 60 ºC with magnetic stirring. After the KOH solution is added, the solution is stirred at 60 °C for 2 hours. The product appears as a white precipitate. After collecting by centrifugation, this white precipitate is washed three times with methanol until it transforms to a gel-like precipitate. Each washing process includes dispersion into methanol by sonication and subsequent centrifugation. Finally, the gel-like precipitate is dispersed in chlorobenzene with 10 vol-% of propanol added for stabilization. The final concentration of ZnO is 100 mg/ml. To verify the size of the ZnO nanoparticles, we checked their visible absorption spectra according to Meulenkamp, et. al.[1] Our ZnO nanoparticles were typically 3.2 nm in diameter.

Surfactant Synthesis: BQ was prepared as described previously.[2] Naphthalene tetracarboxyl dianhydride and 2-ethylhexylamine were purchased from Aldrich. Other reagents were purchased from DaeJung (H_3PO_4), Samchun (KOH, acetic acid), and Dongwoo Fine-Chem (MeOH, electronic use grade). All chemicals mentioned above were used without further purification. To 200 ml of water, naphthalene tetracarboxyl dianhydride (2.00 g, 7.46 mmol) and 1 M KOH aqueous solution (35 ml) were added and stirred. Then 1 M H_3PO_4 aqueous solution was added to adjust pH to 6.4. To the mixture, 2-ethylhexylamine (0.963 g, 1.22 ml, 7.46 mmol) was added and pH was readjusted to 6.4 with 1 M H_3PO_4 aqueous solution. The mixture was refluxed at 120 ^{o}C overnight. After cooling down to room temperature, the reaction mixture was filtered and acetic acid was added to the filtrate until the product was precipitated. To the product was added 200 ml of MeOH (electronic use grade) and stirred for 1 h for purification. The product was filtered and dried under vacuum.

Sample Preparation: All samples were prepared on 12 x 25 mm cleaned quartz substrates. In addition, the ratio of acceptor to donor was chosen based on previous experiments which determined that the optimum ratio for photovoltaic device performance. For ZnO containing samples, the ratio was 2:1 ZnO to polymer.[2,3] Surfactant is added to the ZnO solution after synthesis as described above at 3% by weight. Then 12 μL of 100 mg/ml of the ZnO/surfactant solution was added to 88 μL of 6.8 mg/ml of MDMO-PPV in a 9:1 mixture of chlorobenzene and propanol. After mixing, this blended solution was deposited on the cleaned quartz substrate by spin coating at 2000 rpm for 60s. For PCBM containing samples the optimum ratio was 4:1 PCBM to polymer.[4] For samples containing PCBM, 50 microliters of 40 mg/ml PCBM in chlorobenzene was added to 50 microliters of 10 mg/ml MDMO-PPV in chlorobenzene. After mixing the solution was spun at 500 rpm for 60 s on a cleaned quartz substrate. Typical current voltage characteristics for solar cells made using these recipes are shown in the supplementary information.

Methods

Steady-State PIA: The quasi-steady-state photoinduced absorption spectroscopy (PIA) was performed with a pump–probe setup consisting of a 100 W tungsten-halogen lamp with a LOT-Oriel Omni-λ 300 monochromator as the probe and a Newport LED (LED-527-HP) working at 527 nm with a power density of ca. 100 mW cm^{-2} at the sample used as a pump. The samples were placed in a nitrogen-cooled optical cryostat (Oxford Instruments Optistat CF) at 80 K using helium as a contact gas.

fs-ns TA: Samples were excited with several different fluences in the range of 3 to 50 μJ/cm^2. To analyze, we looked at the intensity dependence of the decay kinetics and picked a fluence below which the decay kinetics were independent of fluence and then picked data sets for each variation where the initial photobleach was similar in size to ensure a similar initial density of photoexcited states.

ns-μs TA: TA measurements were performed at room temperature under dynamic vacuum at pressures <10^{-5} mbar. Similar with the ps-ns measurements, we excited with several different fluences from 3 to 50 μJ/cm^2.

Device Results

1)

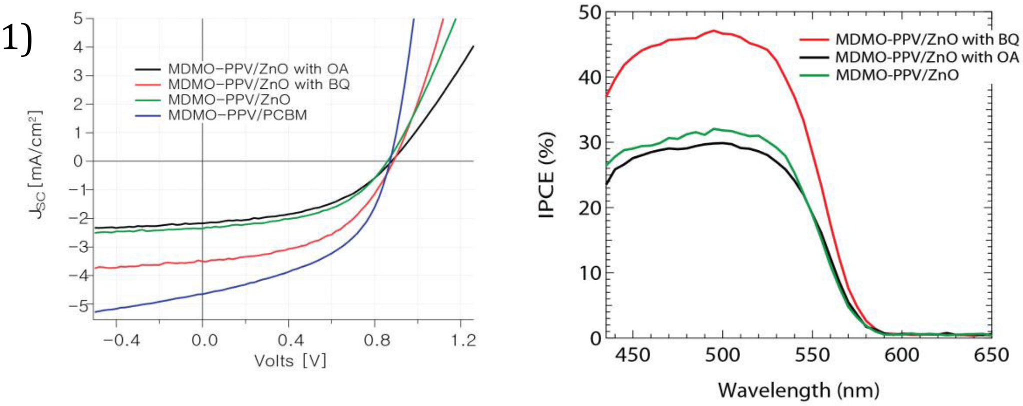

2)

Acceptor	V_{oc}[V]	J_{sc}[mA/cm²]	FF	Efficiency
ZnO+BQ	0.89	3.5	0.5	1.62%
ZnO+OA	0.88	2.17	0.47	0.93%
ZnO	0.86	2.36	0.49	1.04%
PCBM	0.87	4.65	0.47	1.94%

Figure S1: Typical device results. 1), left, 0.2 cm^2 active area devices with the structure indium tin oxide/PEDOT:PSS/active layer/LiF/Al. Illuminated with 100 mW/cm^2 through a 420 nm filter to remove UV irradiation. 1), right, incident photon to current efficiency data from devices in 1). 2) Table summarizing the device results. Note that the device efficiencies reported here are somewhat better than those previously published.[2] As noted in that publication, there tends to be a significant batch to batch variation in ZnO synthesis due in part to the sensitivity of the ZnO surface to humidity.[5]

Quasi-steady-state Photoinduced Absorption

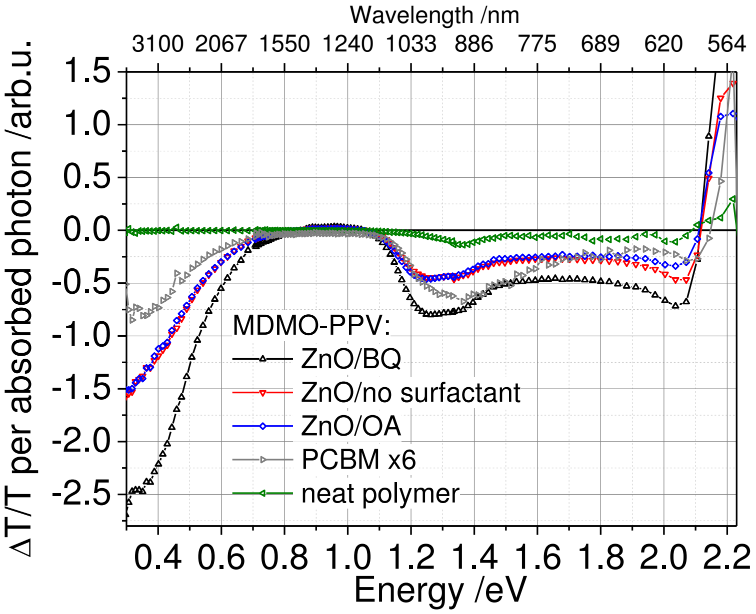

Figure S2: Quasi-steady-state photoinduced absorption showing the induced absorption spectrum of charges excited with a 527 nm ultrabright LED at 317Hz. A broad charge-induced-absorption band is visible between 1.2 and 2.0 eV and charge-induced-absorption peaks are present at 1.2 and 0.3 eV. The signal is proportional to the product of the excited state density and the excited state lifetime. Much faster recombination in the PCBM leads to a shorter lifetime (see Figure 5) and lower signal. The lifetimes in the ZnO sample are similar, meaning that the efficiency of charge generation for the ZnO+BQ sample is roughly twice as large as those for the ZnO and ZnO+OA samples.

The quasi-steady-state photoinduced absorption spectrum for each sample is shown in Figure S2. The spectral shape of all the ZnO samples and the PCBM sample are similar, indicating that the photoinduced absorption primarily arises from the positive polaron of the MDMO-PPV. The measured signal is proportional to the product of the excited-state density and the excited-state lifetime. In the main text we show that the charge lifetimes in the ZnO samples are similar but the lifetime in the PCBM film is much shorter. This explains the smaller signal in the PCBM compared to the ZnO samples, despite the charge density likely being higher (given that the device efficiency is better) in the PCBM sample. As the lifetimes are roughly the same for the ZnO samples, the ratio between the signal magnitudes is roughly proportional to the ratio in the efficiency of exciton quenching by charge transfer. From this we can already qualitatively conclude that the semiconducting surfactant BQ leads to a doubling in the efficiency of exciton quenching by charge transfer as compared to uncoated ZnO or ZnO dispersed with a non-semiconducting surfactant. This is consistent with the device data, and also the detailed description of the quantum efficiency extracted from the analysis of the transient spectroscopy in the main text.

Transient Absorption Spectra

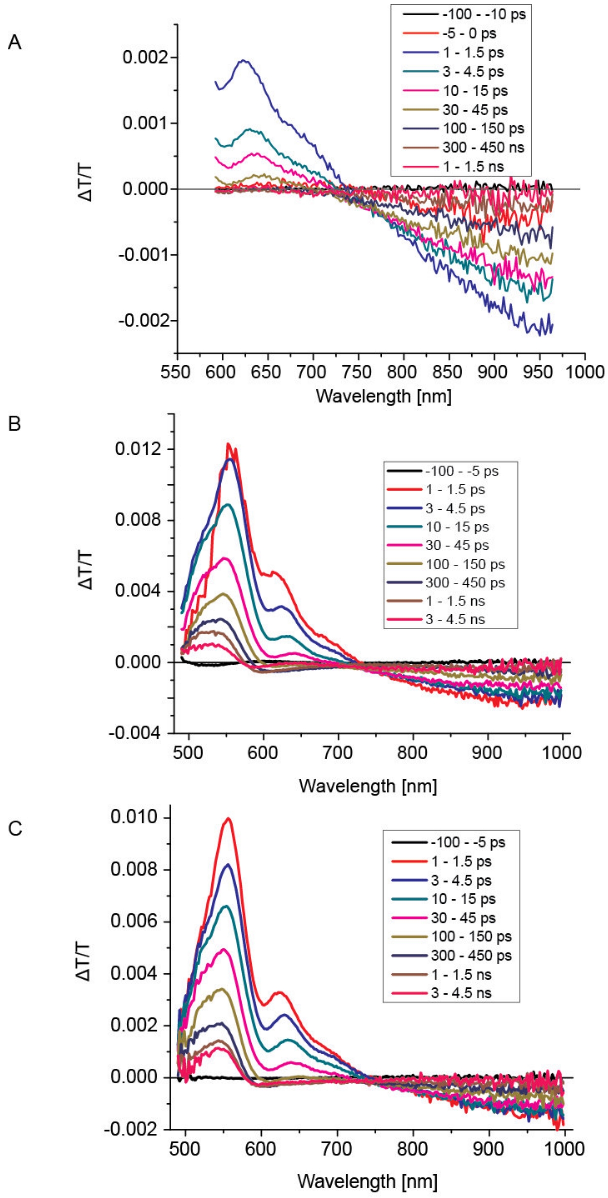

Figure S3 : Transient absorption spectra for A) Neat MDMO-PPV. B) No surfactant. C) Oleic acid surfactant.

Choosing the data for fitting

The kinetics showed a dependence upon the excitation density (fluence). The data for fitting was chosen thus, that the fluence was low enough that the fluence dependence was negligible but high enough to get a sufficient signal to noise ratio. In order to allow a weighting during fitting, error bars were added according to the noise of the white light in the respective wavelength region. Error bars of 0.02 were chosen for the normalized stimulated emission kinetics and 0.05 for the normalized photoinduced absorption kinetics. Weighting was instrumental, meaning that each point entering $\chi^2 = \sum_{i=1}^{N} \omega_i \left(Y_i - f(x_i; \Theta)\right)^2$, which is minimized in the fitting procedure, is weighted by $\omega_i = 1/\sigma_i^2$, where Y_i are the data points, $f(x_i; \Theta)$ is the fit-function, Θ is the set of fit parameters and σ_i are the error bars.

The fitting procedure

All fits were performed using Origin Pro 8.5.1G.

Neat fits: For the fits of the neat kinetics, the two rates for the decay from the intrachain exciton were fixed at educatedly guessed values and only the amplitudes were varied. As the physically reasonable parameters are the combination of rates and amplitudes, this is a reasonable approach. The fit parameters along with errors as derived from the fitting are shown in the main text.

Blend fits: For the blend fits, all rates $k_{ct,i}$ and amplitudes C_i for the transition from excitons to charge transfer were kept as fitting parameters as the kinetics for the different ZnO-surfactant compositions varied strongly. Parameters obtained from the neat fit were adopted as fixed parameters. In order to avoid cross-correlations between the decay rate $k_{ct\to gs}$ of the bound CT state and the fractions of created free charges from the overall created charges x_{SSC} and to regard the fact that the induced absorptions of charges in the stimulated emission region become constant within the time range of the experiment, $k_{ct\to gs}$ was limited to rates >0.002ps^{-1} (which corresponds to an inverse rate of 500ps, being ~1/6 of the time range of the experiment). For OA x_{SSC} was set to 1 as a fixed parameter. Fitting the OA data similar to the other data did not improve the fit.

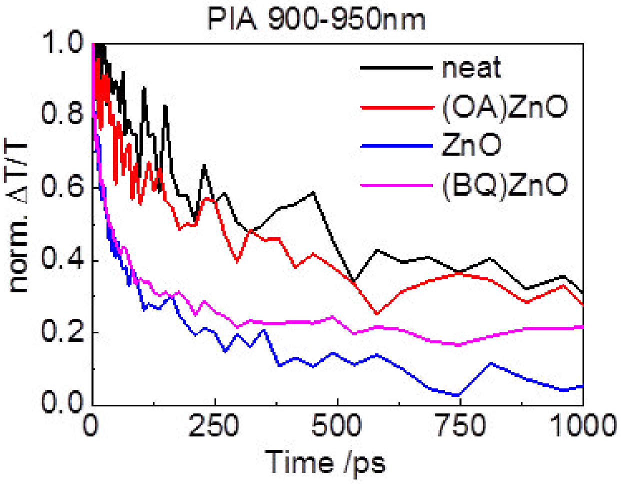

Figure S4: Kinetics of the PIA region, showing that the (OA)ZnO decay is very similar to the aggregate decay in the neat polymer. This justifies fixing the parameter x_{SSC} for (OA)ZnO to 1, meaning that no initial fast recombination that could accelerate this decay is observed. For (BQ)ZnO and ZnO, x_{SSC} and a fast recombination is needed to describe the data (in combination with the stimulated emission region) satisfactory.

Rate equations for the blend model:

$$\frac{dEx(t)}{dt} = -(k_{dec} + k_{ct})Ex(t)$$

$$\frac{dAgg(t)}{dt} = 0.8\, k_{dec}Ex(t) - k_{agg\to gs}Agg(t)$$

$$\frac{dBCP(t)}{dt} = (1 - x_{SSC})k_{ct}Ex(t) - k_{ct\to gs}BCP(t)$$

$$\frac{dSSC(t)}{dt} = x_{SSC}k_{ct}Ex(t)$$

Initial conditions are: $Ex(0) = E_0,\quad Agg(0) = BCP(0) = SSC(0) = 0$

In the solutions, $A_x \exp(-k_x t)$ are replaced by $\sum_{i=1}^{N_x} A_{x,i} \exp\left(-k_{x,i} t\right)$ and k_x are replaced by $\tilde{k}_x = \left(\sum_{i=1}^{N_x} (A_{x,i} / k_{x,i})\right)^{-1}$ for x=ct and x=dec.

The parameters obtained from fitting are depicted in the following table. The best fit reached a reduced chi-square divided by the degrees of freedom of the fit (DOF) of $\frac{\chi^2}{DOF} = 1.53$.

	BQ	No surfactant	OA
C_1	0.262 ± 0.076	0.209 ± 0.045	0.368 ± 0.026
$k_{ct,1}$ /ps^{-1}	0.518 ± 0.108	0.513 ± 0.115	0.149 ± 0.021
C_2	0.738 ± 0.079	0.791 ± 0.047	0.632 ± 0.027
$k_{ct,2}$ /ps^{-1}	0.027 ± 0.006	0.022 ± 0.004	0.0036 ± 0.001
$k_{ct \to gs}$ /ps^{-1}	0.0326 ± 0.012	0.023 ± 0.005	not needed
x_{SSC}	0.533 ± 0.077	0.336 ± 0.050	1 fixed
$r_{CT/Ex}^{stim}$	-0.376 ± 0.072		
$r_{CT/Ex}^{pia}$	0.308 ± 0.034		

Alternative model

The difference to the model presented in the manuscript is, that the primary intrachain excitons (Ex) can only decay into a charge-transfer state (CT) and aggregates (Agg). This intermediate CT state can then split into free spatially separated charges or decay to the ground state.

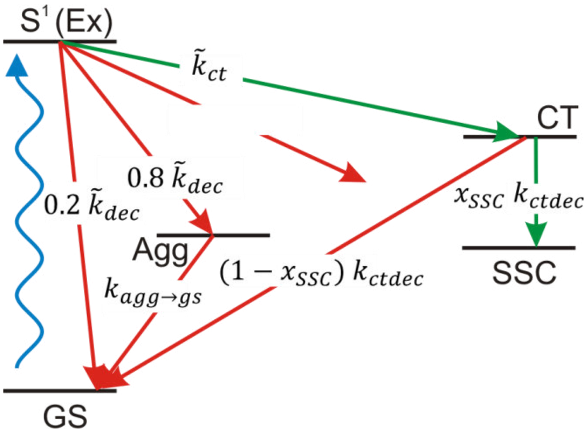

Figure S5: Alternative rate model leading to inferior fits but similar conclusions.

The rate equations read then:

$$\frac{dEx(t)}{dt} = -(k_{dec} + k_{ct})Ex(t)$$

$$\frac{dAgg(t)}{dt} = 0.8\, k_{dec}Ex(t) - k_{agg\to gs}Agg(t)$$

$$\frac{dCT(t)}{dt} = k_{ct}Ex(t) - (1 - x_{SSC})k_{ctdec}CT(t)$$

$$\frac{dSSC(t)}{dt} = x_{SSC}k_{ctdec}CT(t)$$

Initial conditions are: $Ex(0) = E_0,\ \ Agg(0) = CT(0) = SSC(0) = 0$

In the solutions, $A_x \exp(-k_x t)$ are replaced by $\sum_{i=1}^{N_x} A_{x,i} \exp\left(-k_{x,i}t\right)$ and k_x are replaced by $\tilde{k}_x = \left(\sum_{i=1}^{N_x}(A_{x,i}\,/k_{x,i})\right)^{-1}$ for x=ct and x=dec.

The solutions are:

$$Ex_{blend}(t) = Ex_{neat}(t)\sum_{i=1}^{M} C_i \exp\left(-k_{ct,i}t\right)$$

$$Agg_{blend}(t) = \frac{\tilde{k}_{agg}}{\tilde{k}_{dec} + \tilde{k}_{ct} - k_{agg\to gs}}\left(\exp\left(-k_{agg\to gs}t\right)\ - Ex_{blend}(t)\right)$$

$$CT(t) = \frac{(1 - x_{SSC})\tilde{k}_{ct}}{\tilde{k}_{dec} + \tilde{k}_{ct} - k_{ctdec}}\left(\exp(-k_{ctdec}t) - Ex_{blend}(t)\right)$$

$$SSC(t) = \frac{x_{SSC}\tilde{k}_{ct}}{\tilde{k}_{dec} + \tilde{k}_{ct}} + \frac{(1 - x_{SSC})\tilde{k}_{ct}}{\tilde{k}_{dec} + \tilde{k}_{ct} - k_{ctdec}}\exp(-k_{ctdec}t)$$

$$- \frac{\tilde{k}_{ct}\left(\tilde{k}_{dec} + \tilde{k}_{ct} - x_{SSC}k_{ctdec}\right)}{\left(\tilde{k}_{dec} + \tilde{k}_{ct}\right)\left(\tilde{k}_{dec} + \tilde{k}_{ct} - k_{ctdec}\right)}Ex_{blend}(t)$$

The fitting was carried out similar to the other model. The best fit resulted in $\frac{\chi^2}{DOF} = 2.08$. The following graph shows the data along with the alternative fit. The model described in the main text is indicated as dashed lines.

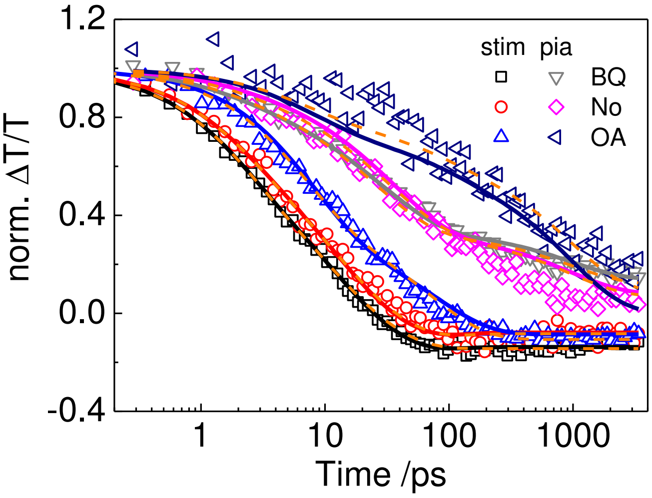

Figure S6: Results of the fits of the alternative model. The results of the model described in the main text are adumbrated in dashed orange lines showing the deviation. The alternative model mainly fails to describe the (OA)ZnO data as satisfactorily as the main model.

The extracted charge generation parameters are summarized in the following table in analogy to Table 2 in the main text.

Sample	k_{ct}^{-1} /ps	x_{SSC}	η_{SSC}	IPCE
(BQ)ZnO	26±6	0.51±.11	0.37±.08	0.44
ZnO	35±8	0.31±.06	0.21±.05	0.29
(OA)ZnO	235±85	1^{A}	0.23±.06	0.27

A similar trend as in the main model is evident, leading to the same conclusions.

(1) Meulenkamp, E. A. Synthesis and growth of ZnO nanoparticles *J. Phys. Chem. B* **1998**, *102*, 5566-5572.

(2) Park, I.; Lim, Y.; Noh, S.; Lee, D.; Meister, M.; Amsden, J. J.; Laquai, F.; Lee, C.; Yoon, D. Y. Enhanced photovoltaic performance of ZnO nanoparticle/poly(phenylene vinylene) hybrid photovoltaic cells by semiconducting surfactant *Org. Electronics* **2011**, *12*, 424-428.

(3) Beek, W. J. E.; Wienk, M. M.; Kemerink, M.; Yang, X.; Janssen, R. A. J. Hybrid Zinc Oxide Conjugated Polymer Bulk Heterojunction Solar Cells *J. Phys. Chem. B* **2005**, *109*, 9505-9516.

(4) Shaheen, S. 2.5% efficient organic plastic solar cells *Appl. Phys. Lett.* **2001**, *78*, 841-843.

(5) Qiu, Y. F.; Yang, S. H. ZnO nanotetrapods: Controlled vapor-phase synthesis and application for humidity sensing *Adv. Funct. Mater.* **2007**, *17*, 1345-1352.

5

Conclusions & Outlook

In this thesis, four organic push-pull (donor-acceptor) dyes were investigated in solid-state dye-sensitized solar cells by means of optical spectroscopy to correlate the photophysical properties with their photovoltaic performance. Specifically, broadband quasi-steady-state and transient absorption spectroscopy in the visible and especially the near-infrared spectral region, combined with time-resolved photoluminescence spectroscopy, were used to gain a better understanding of the charge generation and recombination processes. The interpretation of the results obtained helped to elucidate the advantages and disadvantages of the solid hole transporter spiro-MeOTAD and the use of broadly absorbing organic donor-π-spacer-acceptor dyes as sensitizers. The extension of the study to polymer-metal oxide nanoparticle hybrid bulk heterojunction solar cells further showed the potential of transient absorption spectroscopy to unravel the efficiency-limiting processes in hybrid solar cells.

The aim of this chapter is to summarize the similarities and differences between the dyes examined, in order to identify trends and to draw general conclusions regarding the applicability of organic dyes in ssDSCs. Additionally, design rules and figures of merit to be considered for novel high performance dyes are developed and suggestions regarding further studies are made.

5.1 Influence of Additives

One important and recurring theme was the influence of Li-TFSI on the photophysics and performance of the studied DSCs. The additive Li-TFSI is usually added to the hole transporter solution before preparation of the sample. Clearly, this additive played an important role in the electron injection from the excited dye to TiO_2 for all investigated dyes. It was shown that Li-TFSI positively charged the TiO_2 surface. A reasonable explanation for this is the intercalation of Li^+-ions into the TiO_2 surface [132]. However, as intercalation mostly occurs when Li ions are electrochemically inserted and not just applied from solution, a more likely explanation is the accumulation of Li^+-ions on the surface. [133] It is known that the Li^+-ions shift the TiO_2 conduction band edge to lower energies, thereby enabling injection, [42] a likely explanation for the increased injection efficiency observed for the investigated dyes. However, on Al_2O_3 similar effects were observed, which shows that the Li-TFSI not only affected the TiO_2, but also the dye itself. In fact, the push-pull dyes are very sensitive to their dielectric environment due to their high ground state dipole moments, and dipole moment changes from the ground to the excited state. Thus, a change in the local electric field ("polarity") due to the presence of Li cations clearly influences the dye [119]. The benefit of a more pronounced intramolecular charge-transfer state is obvious: If the electron density of the excited state in the acceptor part of the dye, which is close to the anchoring group, is increased, the electron density is closer to the TiO_2 surface and thus electron coupling is enhanced. The same argument holds for the holes and the hole transporter at the donor side. Moreover, the influence of Li-TFSI on the attachment of the dyes, which can affect the charge-transfer efficiency, was discussed. Interestingly, the Li-influence appeared not to be the same for all dyes. This suggests that the above-mentioned benefits for charge injection induced by Li-TFSI were weighted differently for the different dyes. For instance, the charge injection of the dye absorbing at higher energy was less influenced by Li-TFSI lowering the conduction band, whereas the dye with a lower dipole moment was less influenced by the stabilization effect. All in all, the role of Li-

TFSI is very crucial and its influence should be considered in the development of new dyes. It is very interesting to study the dependence of the photophysical properties on the amount of Li-TFSI present, which could also help to further elucidate the different contributions of conduction band level or stabilization to the total Li-influence. In this regard, it would be very useful to study the electronic properties of titania nanoparticles more thoroughly, for instance the density of unoccupied acceptor states and the influence of Li-TFSI and the dye itself. A possible experiment is two photon photoemission spectroscopy (2PPE), which probes unoccupied electronic states, [134] or time-resolved terahertz spectroscopy, which probes the electrons injected into TiO_2 and their mobility [135-138] and is thus a complementary technique to transient absorption spectroscopy, which can probe the charges in the dye and the organic hole transporter but not in TiO_2.

Other additives, such as dopants or dipolar additives (tBP etc.) that affect the interface and the bulk hole transporter also strongly affect the efficiency, and their influence has to be studied in more detail in future work. Interface engineering is of great importance for the performance of the solar cell, as it influences the fundamental steps in charge generation, by enhancing separation or by suppressing recombination.

5.2 Dipole Moments of Dyes: A Parameter to Consider

The dipole moment of molecules attached to metal oxide interfaces influences the electronic properties of the metal oxide and, in dye-sensitized solar cells, of the metal oxide:dye:hole transporter heterojunction. [127, 128] Evidently, the dipole moment of the dye itself also influences these properties. [125, 126] Therefore, the dipole moment needs to be taken into account when the potential of dyes for use in DSCs is evaluated. In section 4.3, the differences in the performance of the two dyes PMI-2 and PMI-2-MeO were attributed to the difference in the ground state dipole moment, which led to a different influence of the additive Li-TFSI. Additionally, evidence for a different orientation of the higher dipole moment dye PMI-2, facilitating charge injection, was presented. Table 9 summarizes the ground state dipole moments of the four investigated dyes together with the dipole moment changes from ground to excited state. Evidently, the poorest performing dye possessed the smallest ground state dipole moment and the smallest dipole moment change, resulting in the weakest push-pull character. The best performing dyes exhibited not only a high ground state dipole moment, but also a large change in dipole moment from the ground to the excited state, indicating strong intramolecular charge-transfer character. Therefore, it appears to be crucial to maintain the strong push-pull character of the dyes, when novel structures or modifications, such as side chains, are introduced.

Table 9: Absolute ground state dipole moments $|\vec{\mu}|$ and dipole moment changes from ground to excited state of the studied dyes $|\Delta\vec{\mu}|$ as calculated by TDDFT. [101] The main direction of both vectors points away from the anchoring group (left to right in the chemical structure).

Compound	$\|\vec{\mu}\|$ /D	$\|\Delta\vec{\mu}\|$ /D	Chemical structure
PMI-1	8.7	32	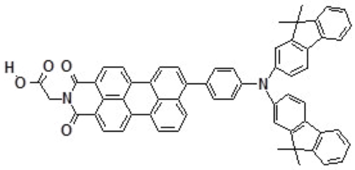
NMI	7.4	45	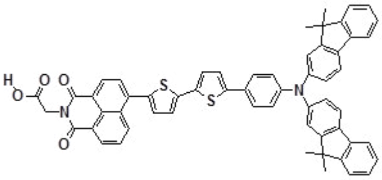
PMI-2	7.7	13	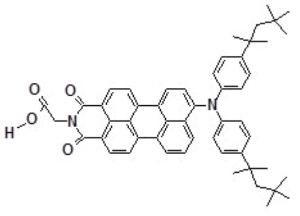
PMI-2-MeO	4.3	12	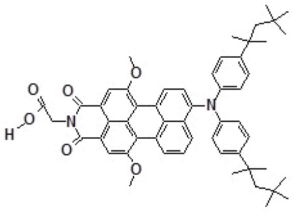

5.3 Recombination Issues

After their generation in the solar cell, charges have to be extracted to contribute to the photocurrent. The loss mechanism for charges is recombination. Two recombination processes lead to the majority of the losses in DSCs, namely, the recombination of a dye cation and an electron in TiO_2 prior to regeneration, or the recombination of already separated charges in TiO_2 and the hole transporter. By interface modification, recombination can be suppressed. This interface modification can be realized in different ways, for instance by using coadsorbents, additives in the hole transporter or by introducing thin blocking layers on the TiO_2 surface. [6]

In chapter 4.2.1, it was shown that the additive Li-TFSI can also lead to the suppression of recombination of dye cations and electrons in TiO_2. The recombination of free charges is however not only influenced by these additives, but also by the dye layer itself. [60, 139]. In chapter 4.4, it was shown that charges are attracted back to the interface by their image charge, due to the dielectric contrast between hole transporter and TiO_2. This is a major drawback of organic solid hole transporters. This loss channel can be suppressed by introducing a thicker passivation layer between hole transporter and titania, e.g. by shells or longer dye molecules, leading to further separation of the charges from the dielectric boundary and thus decreasing the Coulombic attractive force. Increasing the dielectric shielding of the dye and the hole transporter, as discussed below (section 5.5), could help by decreasing the dielectric contrast and thereby the attractive force of the image charge.

Furthermore, the recombination suppressing effect of a surface modifier molecule (ID662), investigated in chapter 4.2.5, could help to increase the efficiency of solar cells using already available hole transporter materials. In general, solid-state dye-sensitized solar cells are prone to faster recombination than their liquid electrolyte analogues, requiring the use of thinner TiO_2 layers. [9] Therefore, the suppression of recombination allows the use of thicker layers, allowing more of the incoming photons to be harvested. On the other hand, if dyes absorb as much light as possible so that a thinner TiO_2 layer is sufficient, recombination might not play such a crucial role any more. Along these lines, perovskite materials, used in place of dyes, have recently proven to be interesting absorber materials, as they are strongly absorbing [82], work well as a hole transporter replacement [12] and are even capable of achieving high efficiencies as absorber and electron transporter simultaneously [83]. Additionally, the possibly higher (and anisotropic) dielectric constant of perovskite could also lead to a better screening and channeling of charges to the electrodes and avoiding recombination.

5.4 Design Rules for Dyes

The observed differences in efficiency and charge generation between the four dyes, even if the dyes cannot be easily compared due to the different photophysical properties, can be translated into a set of design rules for the development of novel dyes, some of which have to be further investigated:

1. A large dipole moment helps to overcome injection problems due to the interaction with the additive Li-TFSI. The ground state dipole moment should however not be too strong, otherwise the physical properties of the metal oxide are changed detrimentally. The optimum depends on the energy level alignment when the dye is attached to the metal oxide.
2. The dipole moment change from ground to excited state (the push-pull character) should be large.
3. The dyes should cover the TiO_2 in a way that they passivate the interface between hole transporter and TiO_2 to avoid direct recombination. This layer should be as thick as possible to reduce the attraction of charges back to the interface.
4. To clarify the role of the binding angle, the binding groups should define the angle with respect to the metal oxide, so that the influence of dye orientation on charge generation can be evaluated.
5. Energy levels determined in solution do not necessarily reflect the situation on the metal oxide, especially in the presence of Li-TFSI. There-

fore, at least the energy levels when attached to TiO_2 should be considered.

5.5 Hole Transporter and Preceding Hole Transfer

The replacement of the liquid electrolyte by a solid hole transporter in DSCs has tremendous advantages for industrial applications. However, solid hole transporters are underdeveloped and present much room for improvement. Within this thesis it was shown that the solid hole transporter has advantages but also severe disadvantages. An advantage is that it enables a novel path of charge generation, namely preceding hole transfer (or reductive quenching). In contrast to the conventional charge generation mechanism, i.e. the injection of an electron from the excited state of the dye into the TiO_2 and subsequent regeneration of the thereby formed dye cation by the hole transporter, preceding hole transfer allows the excited dye to inject a hole into the hole transporter followed by injection of an electron into the TiO_2 from the thereby formed dye anion. By modeling the transient absorption data, it could be shown that this additional charge-transfer mechanism clearly helped to overcome injection problems of a particular dye (PMI-1) and boosted the charge generation efficiency.

However, by monitoring the transient Stark effect it could be shown that the low dielectric constant of the organic hole transporter and the high dielectric contrast to TiO_2 is a strong disadvantage: the negative image charge, induced in the TiO_2 by a positively charged hole in the hole transporter due to the dielectric constant contrast, exhibits enough force to attract the free charge back to the interface and thereby prevent extraction. This is perhaps the biggest drawback of organic solid-state hole transporters compared to their liquid analogues. The liquid electrolyte is able to shield the charges effectively, although recent publications suggest that the effect is smaller than previously predicted. [100] Thus, novel hole transporters with better adjusted energy levels and higher dielectric constants are required to achieve higher efficiencies. The previously mentioned perovskite-based materials already pave the way in this direction. [12]

The use of additives to increase the dielectric constant is also feasible. Further investigations regarding the hole transporter are required to better understand the physics of solid-state DSCs and to eventually achieve higher efficiencies.

5.6 Surfactants in Polymer-Metal Oxide BHJ Solar Cells

In chapter 4.5, it was shown that the development of novel surfactants attached to ZnO in polymer:ZnO hybrid bulk heterojunction (BHJ) solar cells helps to increase photocurrent generation. By applying a parallel pool analysis on the transient absorption data in two distinct wavelength regions, it was shown that MDMO-PPV:ZnO suffers from energy transfer from the photoexcited polymer to polymer aggregates. The exciton diffusion and charge transfer to the ZnO must be faster than this energy transfer in order to avoid losses. Additionally, it was shown that a fast recombination channel, arising from recombination of bound charge pairs, likely because electrons remain trapped on the surface of the ZnO nanoparticles, led to losses of already created charges. The addition of surfactants, in addition to improving the dispersion of the nanoparticles, reduced the influence of this fast recombination channel, which is beneficial for the creation of free charges. Compared to the metal oxide nanoparticles without any surfactant, an insulating surfactant (oleic acid) was able to suppress the fast recombination completely, however it suffered from reduced charge generation induced by an injection barrier, leading to inferior photovoltaic performance as more excitons were lost by energy transfer to aggregates or exciton recombination. A semiconducting surfactant on the other hand could suppress the fast recombination whilst maintaining the exciton splitting efficiency leading to higher power conversion efficiencies. A further suppression of the fast recombination channel could lead to a more than doubling of the photocurrent, eventually leading to similar efficiencies as observed for the commonly used organic acceptor PCBM, by the design of novel surfactants.

Furthermore, the use of polymers which do not form aggregates that can act as quenching sites appears promising.

5.7 Spectroscopic Challenges

Studying the photophysics of dye-sensitized solar cells or polymer-metal oxide hybrid BHJ solar cells by optical spectroscopy is a complicated task, as many transient species of the individual components of the heterojunction can be present at the same time (in ssDSCs for instance dye excitons, dye anion, dye cation, spiro cation, charge-transfer states, Stark effect and potentially other signals that are not assigned). Furthermore, the sample itself is not homogeneous, so that several spectroscopically different situations may be probed at the same time. Disentangling these quantitatively is very complicated (e.g. compare the quantitative analysis of PMI-1 and NMI in sections 4.1 and 4.2) and does not always lead to results that can be directly correlated to the efficiency. The problem occurs that the kinetics do not contain enough information with respect to the number of unknown parameters, thereby causing an over-parameterization of the description of the data. A common approach to circumvent this issue is to describe the kinetics by an arbitrary function such as a multiexponential function and to compare the different contributions for different sample compositions. [71] This however is rather a qualitative approach, not differing much from the simple comparison of the kinetics. However, in this thesis a different approach was presented, namely, a multi-wavelength analysis that covers the most important wavelength regions. Applied to ssDSCs (chapters 4.1 and 4.2) and polymer-metal oxide hybrid bulk heterojunction solar cells (chapter 4.5), more detailed insights into the efficiency-limiting processes in these solar cells were achieved. This way of describing the obtained data is a first step towards a more general analysis of the data that could in fact be achieved by a full matrix analysis. The data-matrix contains the entire spectroscopic $\Delta T/T$-information as a function of wavelength in one, and time in the other, dimension. In order to constrain as many parameters as possible, the spectral region has to be as broad as possible so that it contains the maximum amount of information. With matrix algebra, the basic components (spectra) and their kinetics can be extracted. This analysis will not be presented in detail here, however, it shows great promise in giving a better understanding of the spectroscopic data and the physical processes in hybrid organic/inorganic solar cells. [140-142] This, together with further studies by different (complementary) experimental techniques performed on the same samples, such as time-resolved THz-spectroscopy, is the way forward to finally understand the efficiency-limiting processes of ssDSCs and hybrid BHJ solar cells and to determine ways to overcome these issues.

Finally, the analysis of Stark features observed in solid-state DSCs could be extended to reveal charge dynamics in systems in which the molecules that are affected by the Stark effect, and the electric field that causes the Stark effect, are geometrically constrained. For instance surface-bound molecules or biological proteins could be investigated by studying the Stark effect. The method's advantage of being independent of explicit knowledge of material parameters such as molecular hyperpolarizabilities or oscillator strengths is promising and needs to be further investigated. Other dye systems that exhibit ultrafast charge generation and a strong Stark effect combined with novel hole transporters are possible highly interesting candidates for further investigations, to develop as well as to support this method.

References

[1] IEA, International Energy Agency, http://www.iea.org/newsroomandevents/news/2012/may/name,27216,en.html (July 2012).

[2] G. Dennler and C. J. Brabec, in Organic Photovoltaics, Wiley-VCH Verlag GmbH & Co. KGaA, 2009, p. 531.

[3] US Energy Information Administration, International Energy Outlook 2011, DOE/EIA-0484(2011), 2011

[4] Q. Schiermeier, J. Tollefson, T. Scully, A. Witze, and O. Morton, Electricity without carbon, Nature 454 (2008) 816.

[5] IEA, International Energy Agency, Technology Roadmap - Solar photovoltaic energy, 2010

[6] A. Hagfeldt, G. Boschloo, L. Sun, L. Kloo, and H. Pettersson, Dye-Sensitized Solar Cells, Chem. Rev. 110 (2010) 6595.

[7] Logitech, Solar Keyboard Folio, http://www.logitech.com/de-de/tablet-accessories/keyboards/solar-keyboard-folio (July 2012).

[8] G24 Innovations, G24i Bicycle Panniers, http://www.g24i.com/pages,g24i-bicycle-panniers,92.html (July 2012).

[9] B. E. Hardin, H. J. Snaith, and M. D. McGehee, The renaissance of dye-sensitized solar cells, Nat. Photonics 6 (2012) 162.

[10] U. Bach, D. Lupo, P. Comte, J. E. Moser, F. Weissortel, J. Salbeck, H. Spreitzer, and M. Grätzel, Solid-state dye-sensitized mesoporous TiO_2 solar cells with high photon-to-electron conversion efficiencies, Nature 395 (1998) 583.

[11] J. Burschka, A. Dualeh, F. Kessler, E. Baranoff, N.-L. Cevey-Ha, C. Yi, M. K. Nazeeruddin, and M. Grätzel, Tris(2-(1H-pyrazol-1-yl)pyridine)cobalt(III) as p-Type Dopant for Organic Semiconductors and Its Application in Highly Efficient Solid-State Dye-Sensitized Solar Cells, J. Am. Chem. Soc. 133 (2011) 18042.

[12] I. Chung, B. Lee, J. Q. He, R. P. H. Chang, and M. G. Kanatzidis, All-solid-state dye-sensitized solar cells with high efficiency, Nature 485 (2012) 486.

[13] L. Schmidt-Mende, S. M. Zakeeruddin, and M. Grätzel, Efficiency improvement in solid-state-dye-sensitized photovoltaics with an amphiphilic Ruthenium-dye, Appl. Phys. Lett. 86 (2005)

[14] H. J. Snaith, R. Humphry-Baker, P. Chen, I. Cesar, S. M. Zakeeruddin, and M. Grätzel, Charge collection and pore filling in solid-state dye-sensitized solar cells, Nanotechnology 19 (2008)

[15] I.-K. Ding, N. Tétreault, J. Brillet, B. E. Hardin, E. H. Smith, S. J. Rosenthal, F. Sauvage, M. Grätzel, and M. D. McGehee, Pore-Filling of Spiro-OMeTAD in Solid-State Dye Sensitized Solar Cells: Quantification, Mechanism, and Consequences for Device Performance, Adv. Funct. Mater. 19 (2009) 2431.

[16] I. A. Howard and F. Laquai, Optical Probes of Charge Generation and Recombination in Bulk Heterojunction Organic Solar Cells, Macromol. Chem. Phys. 211 (2010) 2063.

[17] M. Pope and C. E. Swenberg, Electronic Processes in Organic Crystals and Polymers, Oxford University Press, 1999.

[18] H. Haken and C. W. Wolf, Molekülphysik und Quantenchemie, Springer-Verlag, 2006.

[19] M. Schwoerer and H. C. Wolf, Organic Molecular Solids, Wiley-VCH, 2007.

[20] H. Ibach and H. Lüth, Solid-State Physics, Springer-Verlag, 2009.

[21] B. Valeur and M. N. Berberan-Santos, Molecular Fluorescence: Principles and Applications, Wiley-VCH Verlag GmbH, 2012.

[22] J. R. Lakowicz, Principles of Fluorescence Spectroscopy, Springer, 2006.

[23] J. Stark, Observation of the separation of spectral lines by an electric field., Nature 92 (1914) 401.

[24] D. Meschede, Gerthsen Physik, Springer-Verlag, 2004.

[25] S. G. Boxer, Stark Realities, J. Phys. Chem. B 113 (2009) 2972.

[26] W. Liptay, Electrochromism and Solvatochromism, Angew. Chem., Int. Ed. Engl. 8 (1969) 177.

[27] P. A. Cox, The Electronic Structure and Chemistry of Solids, Oxford University Press, 1987.

[28] S. Na-Phattalung, M. F. Smith, K. Kim, M.-H. Du, S.-H. Wei, S. B. Zhang, and S. Limpijumnong, First-principles study of native defects in anatase TiO_2, Phys. Rev. B 73 (2006) 125205.

[29] R. A. Marcus, On the Theory of Oxidation-Reduction Reactions Involving Electron Transfer, J. Chem. Phys. 24 (1956) 966.

[30] T. M. Clarke and J. R. Durrant, Charge Photogeneration in Organic Solar Cells, Chem. Rev. 110 (2010) 6736.

[31] J. Jortner, Temperature dependent activation energy for electron transfer between biological molecules, J. Chem. Phys. 64 (1976) 4860.

[32] P. Siders and R. A. Marcus, Quantum effects for electron-transfer reactions in the "inverted region", J. Am. Chem. Soc. 103 (1981) 748.

[33] B. A. Gregg, Excitonic solar cells, J. Phys. Chem. B 107 (2003) 4688.

[34] D. Mori, H. Benten, H. Ohkita, S. Ito, and K. Miyake, Polymer/Polymer Blend Solar Cells Improved by Using High-Molecular-Weight Fluorene-Based Copolymer as Electron Acceptor, ACS Appl. Mater. Interfaces 4 (2012) 3325.

[35] H.-Y. Chen, J. Hou, S. Zhang, Y. Liang, G. Yang, Y. Yang, L. Yu, Y. Wu, and G. Li, Polymer solar cells with enhanced open-circuit voltage and efficiency, Nat. Photonics 3 (2009) 649.

[36] Y. Sun, G. C. Welch, W. L. Leong, C. J. Takacs, G. C. Bazan, and A. J. Heeger, Solution-processed small-molecule solar cells with 6.7% efficiency, Nat. Mater. 11 (2012) 44.

[37] S. D. Oosterhout, M. M. Wienk, S. S. van Bavel, R. Thiedmann, L. J. A. Koster, J. Gilot, J. Loos, V. Schmidt, and R. A. J. Janssen, The effect of three-dimensional morphology on the efficiency of hybrid polymer solar cells, Nat. Mater. 8 (2009) 818.

[38] A. Yella, H.-W. Lee, H. N. Tsao, C. Yi, A. K. Chandiran, M. K. Nazeeruddin, E. W.-G. Diau, C.-Y. Yeh, S. M. Zakeeruddin, and M. Grätzel, Porphyrin-Sensitized Solar Cells with Cobalt (II/III)–Based Redox Electrolyte Exceed 12 Percent Efficiency, Science 334 (2011) 629.

[39] A. W. Hains, Z. Liang, M. A. Woodhouse, and B. A. Gregg, Molecular Semiconductors in Organic Photovoltaic Cells, Chem. Rev. 110 (2010) 6689.

[40] R. Katoh, A. Furube, A. V. Barzykin, H. Arakawa, and M. Tachiya, Kinetics and mechanism of electron injection and charge recombination in dye-sensitized nanocrystalline semiconductors, Coord. Chem. Rev. 248 (2004) 1195.

[41] S. A. Haque, Y. Tachibana, R. L. Willis, J. E. Moser, M. Grätzel, D. R. Klug, and J. R. Durrant, Parameters Influencing Charge Recombination Kinetics in Dye-Sensitized Nanocrystalline Titanium Dioxide Films, J. Phys. Chem. B 104 (1999) 538.

[42] S. Ardo and G. J. Meyer, Photodriven heterogeneous charge transfer with transition-metal compounds anchored to TiO_2 semiconductor surfaces, Chem. Soc. Rev. 38 (2009) 115.

[43] S. E. Koops, B. C. O'Regan, P. R. F. Barnes, and J. R. Durrant, Parameters Influencing the Efficiency of Electron Injection in Dye-Sensitized Solar Cells, J. Am. Chem. Soc. 131 (2009) 4808.

[44] J. N. Clifford, E. Palomares, M. K. Nazeeruddin, M. Grätzel, J. Nelson, X. Li, N. J. Long, and J. R. Durrant, Molecular Control of Recombination Dynamics in Dye-Sensitized Nanocrystalline TiO_2 Films: Free Energy vs Distance Dependence, J. Am. Chem. Soc. 126 (2004) 5225.

[45] G. M. Hasselmann and G. J. Meyer, Diffusion-Limited Interfacial Electron Transfer with Large Apparent Driving Forces, J. Phys. Chem. B 103 (1999) 7671.

[46] J. N. Clifford, E. Palomares, M. K. Nazeeruddin, M. Grätzel, and J. R. Durrant, Dye Dependent Regeneration Dynamics in Dye Sensitized Nanocrystalline Solar Cells: Evidence for the Formation of a Ruthenium Bipyridyl Cation/Iodide Intermediate, J. Phys. Chem. C 111 (2007) 6561.

[47] U. Bach, Y. Tachibana, J.-E. Moser, S. A. Haque, J. R. Durrant, M. Grätzel, and D. R. Klug, Charge Separation in Solid-State Dye-Sensitized Heterojunction Solar Cells, J. Am. Chem. Soc. 121 (1999) 7445.

[48] A. Solbrand, H. Lindström, H. Rensmo, A. Hagfeldt, S.-E. Lindquist, and S. Södergren, Electron Transport in the Nanostructured TiO_2–Electrolyte System Studied with Time-Resolved Photocurrents, J. Phys. Chem. B 101 (1997) 2514.

[49] J. van de Lagemaat, N. G. Park, and A. J. Frank, Influence of Electrical Potential Distribution, Charge Transport, and Recombination on the Photopotential and Photocurrent Conversion Efficiency of Dye-Sensitized Nanocrystalline TiO_2 Solar Cells: A Study by Electrical Impedance and Optical Modulation Techniques, J. Phys. Chem. B 104 (2000) 2044.

[50] B. C. O'Regan, K. Bakker, J. Kroeze, H. Smit, P. Sommeling, and J. R. Durrant, Measuring Charge Transport from Transient Photovoltage Rise Times. A New Tool To Investigate Electron Transport in Nanoparticle Films, J. Phys. Chem. B 110 (2006) 17155.

[51] F. Fabregat-Santiago, J. Bisquert, L. Cevey, P. Chen, M. Wang, S. M. Zakeeruddin, and M. Grätzel, Electron transport and recombination in solid-state dye solar cell with spiro-OMeTAD as hole conductor, J. Am. Chem. Soc. 131 (2009) 558.

[52] J. Krüger, R. Plass, L. Cevey, M. Piccirelli, M. Grätzel, and U. Bach, High efficiency solid-state photovoltaic device due to inhibition of interface charge recombination, Appl. Phys. Lett. 79 (2001) 2085.

[53] B. O'regan and M. Grätzel, A Low-Cost, High-Efficiency Solar-Cell Based on Dye-Sensitized Colloidal TiO_2 Films, Nature 353 (1991) 737.

[54] M. Saito and S. Fujihara, Large photocurrent generation in dye-sensitized ZnO solar cells, Energy Environ. Sci. 1 (2008) 280.

[55] A. Kay and M. Grätzel, Dye-sensitized core-shell nanocrystals: Improved efficiency of mesoporous tin oxide electrodes coated with a thin layer of an insulating oxide, Chem. Mater. 14 (2002) 2930.

[56] A. Birkel, Y. G. Lee, D. Koll, X. Van Meerbeek, S. Frank, M. J. Choi, Y. S. Kang, K. Char, and W. Tremel, Highly efficient and stable dye-sensitized solar cells based on

SnO_2 nanocrystals prepared by microwave-assisted synthesis, Energy Environ. Sci. 5 (2012) 5392.

[57] K. Shankar, G. K. Mor, H. E. Prakasam, S. Yoriya, M. Paulose, O. K. Varghese, and C. A. Grimes, Highly-ordered TiO_2 nanotube arrays up to 220 μm in length: use in water photoelectrolysis and dye-sensitized solar cells, Nanotechnology 18 (2007)

[58] M. K. Nazeeruddin, A. Kay, I. Rodicio, R. Humphrybaker, E. Muller, P. Liska, N. Vlachopoulos, and M. Grätzel, Conversion of Light to Electricity by *Cis*-X_2bis(2,2'-Bipyridyl-4,4'-Dicarboxylate)Ruthenium(II) Charge-Transfer Sensitizers (X = Cl^-, Br^-, I^-, Cn^-, and Scn^-) on Nanocrystalline TiO_2 Electrodes, J. Am. Chem. Soc. 115 (1993) 6382.

[59] F. Gao, Y. Wang, D. Shi, J. Zhang, M. K. Wang, X. Y. Jing, R. Humphry-Baker, P. Wang, S. M. Zakeeruddin, and M. Grätzel, Enhance the optical absorptivity of nanocrystalline TiO_2 film with high molar extinction coefficient ruthenium sensitizers for high performance dye-sensitized solar cells, J. Am. Chem. Soc. 130 (2008) 10720.

[60] H. J. Snaith, A. J. Moule, C. Klein, K. Meerholz, R. H. Friend, and M. Grätzel, Efficiency enhancements in solid-state hybrid solar cells via reduced charge recombination and increased light capture, Nano Lett. 7 (2007) 3372.

[61] J. H. Yum, E. Baranoff, F. Kessler, T. Moehl, S. Ahmad, T. Bessho, A. Marchioro, E. Ghadiri, J. E. Moser, C. Y. Yi, M. K. Nazeeruddin, and M. Grätzel, A cobalt complex redox shuttle for dye-sensitized solar cells with high open-circuit potentials, Nat. Commun. 3 (2012)

[62] C. Li and H. Wonneberger, Perylene Imides for Organic Photovoltaics: Yesterday, Today, and Tomorrow, Adv. Mater. 24 (2012) 613.

[63] V. Kamm, G. Battagliarin, I. A. Howard, W. Pisula, A. Mavrinskiy, C. Li, K. Müllen, and F. Laquai, Polythiophene:Perylene Diimide Solar Cells - the Impact of Alkyl-Substitution on the Photovoltaic Performance, Adv. Energy Mater. 1 (2011) 297.

[64] U. B. Cappel, M. H. Karlsson, N. G. Pschirer, F. Eickemeyer, J. Schöneboom, P. Erk, G. Boschloo, and A. Hagfeldt, A Broadly Absorbing Perylene Dye for Solid-State Dye-Sensitized Solar Cells, J. Phys. Chem. C 113 (2009) 14595.

[65] P. Wang, Q. Dai, S. M. Zakeeruddin, M. Forsyth, D. R. MacFarlane, and M. Grätzel, Ambient temperature plastic crystal electrolyte for efficient, all-solid-state dye-sensitized solar cell, J. Am. Chem. Soc. 126 (2004) 13590.

[66] J. H. Wu, S. Hao, Z. Lan, J. M. Lin, M. L. Huang, Y. F. Huang, P. J. Li, S. Yin, and T. Satot, An all-solid-state dye-sensitized solar cell-based poly(N-alkyl-4-vinyl-pyridine iodide) electrolyte with efficiency of 5.64%, J. Am. Chem. Soc. 130 (2008) 11568.

[67] P. Wang, S. M. Zakeeruddin, J. E. Moser, R. Humphry-Baker, and M. Grätzel, A solvent-free, $SeCN^-/(SeCN)_3^-$ based ionic liquid electrolyte for high-efficiency dye-sensitized nanocrystalline solar cells, J. Am. Chem. Soc. 126 (2004) 7164.

[68] Y. Bai, Y. Cao, J. Zhang, M. Wang, R. Li, P. Wang, S. M. Zakeeruddin, and M. Grätzel, High-performance dye-sensitized solar cells based on solvent-free electrolytes produced from eutectic melts, Nat. Mater. 7 (2008) 626.

[69] J. A. Chang, J. H. Rhee, S. H. Im, Y. H. Lee, H.-j. Kim, S. I. Seok, M. K. Nazeeruddin, and M. Grätzel, High-Performance Nanostructured Inorganic−Organic Heterojunction Solar Cells, Nano Lett. 10 (2010) 2609.

[70] T. Leijtens, I. K. Ding, T. Giovenzana, J. T. Bloking, M. D. McGehee, and A. Sellinger, Hole Transport Materials with Low Glass Transition Temperatures and High

Solubility for Application in Solid-State Dye-Sensitized Solar Cells, ACS Nano 6 (2012) 1455.

[71] U. B. Cappel, A. L. Smeigh, S. Plogmaker, E. M. J. Johansson, H. k. Rensmo, L. Hammarström, A. Hagfeldt, and G. Boschloo, Characterization of the Interface Properties and Processes in Solid State Dye-Sensitized Solar Cells Employing a Perylene Sensitizer, J. Phys. Chem. C 115 (2011) 4345.

[72] Y. Liu, A. Hagfeldt, X. R. Xiao, and S. E. Lindquist, Investigation of influence of redox species on the interfacial energetics of a dye-sensitized nanoporous TiO_2 solar cell, Sol. Energy Mater. Sol. Cells 55 (1998) 267.

[73] H. J. Snaith and M. Grätzel, Enhanced charge mobility in a molecular hole transporter via addition of redox inactive ionic dopant: Implication to dye-sensitized solar cells, Appl. Phys. Lett. 89 (2006) 3.

[74] C. Y. Chen, M. K. Wang, J. Y. Li, N. Pootrakulchote, L. Alibabaei, C. H. Ngoc-le, J. D. Decoppet, J. H. Tsai, C. Grätzel, C. G. Wu, S. M. Zakeeruddin, and M. Grätzel, Highly Efficient Light-Harvesting Ruthenium Sensitizer for Thin-Film Dye-Sensitized Solar Cells, ACS Nano 3 (2009) 3103.

[75] P. Lellig, M. A. Niedermeier, M. Rawolle, M. Meister, F. Laquai, P. Müller-Buschbaum, and J. S. Gutmann, Comparative study of conventional and hybrid blocking layers for solid-state dye-sensitized solar cells, Phys. Chem. Chem. Phys. 14 (2012) 1607.

[76] M. D. Brown, T. Suteewong, R. S. S. Kumar, V. D'Innocenzo, A. Petrozza, M. Lee, U. Wiesner, and H. J. Snaith, Plasmonic Dye-Sensitized Solar Cells Using Core−Shell Metal−Insulator Nanoparticles, Nano Lett. 11 (2010) 438.

[77] M. D. Brown, P. Parkinson, T. Torres, H. Miura, L. M. Herz, and H. J. Snaith, Surface Energy Relay Between Cosensitized Molecules in Solid-State Dye-Sensitized Solar Cells, J. Phys. Chem. C 115 (2011) 23204.

[78] B. E. Hardin, E. T. Hoke, P. B. Armstrong, J.-H. Yum, P. Comte, T. Torres, J. M. J. Frechet, M. K. Nazeeruddin, M. Grätzel, and M. D. McGehee, Increased light harvesting in dye-sensitized solar cells with energy relay dyes, Nat. Photonics 3 (2009) 406.

[79] J. H. Yum, B. E. Hardin, S. J. Moon, E. Baranoff, F. Nuesch, M. D. McGehee, M. Grätzel, and M. K. Nazeeruddin, Panchromatic Response in Solid-State Dye-Sensitized Solar Cells Containing Phosphorescent Energy Relay Dyes, Angew. Chem., Int. Ed. 48 (2009) 9277.

[80] A. G. Pattantyus-Abraham, I. J. Kramer, A. R. Barkhouse, X. Wang, G. Konstantatos, R. Debnath, L. Levina, I. Raabe, M. K. Nazeeruddin, M. Grätzel, and E. H. Sargent, Depleted-Heterojunction Colloidal Quantum Dot Solar Cells, ACS Nano 4 (2010) 3374.

[81] A. Nattestad, A. J. Mozer, M. K. R. Fischer, Y. B. Cheng, A. Mishra, P. Bäuerle, and U. Bach, Highly efficient photocathodes for dye-sensitized tandem solar cells, Nat. Mater. 9 (2010) 31.

[82] H.-S. Kim, C.-R. Lee, J.-H. Im, K.-B. Lee, T. Moehl, A. Marchioro, S.-J. Moon, R. Humphry-Baker, J.-H. Yum, J. E. Moser, M. Grätzel, and N.-G. Park, Lead Iodide Perovskite Sensitized All-Solid-State Submicron Thin Film Mesoscopic Solar Cell with Efficiency Exceeding 9%, Sci. Rep. 2 (2012) 591.

[83] M. M. Lee, J. Teuscher, T. Miyasaka, T. N. Murakami, and H. J. Snaith, Efficient Hybrid Solar Cells Based on Meso-Superstructured Organometal Halide Perovskites, Science (2012)

[84] W. J. E. Beek, M. M. Wienk, M. Kemerink, X. Yang, and R. A. J. Janssen, Hybrid Zinc Oxide Conjugated Polymer Bulk Heterojunction Solar Cells, J. Phys. Chem. B 109 (2005) 9505.

[85] W. U. Huynh, J. J. Dittmer, and A. P. Alivisatos, Hybrid Nanorod-Polymer Solar Cells, Science 295 (2002) 2425.

[86] S. Ren, L.-Y. Chang, S.-K. Lim, J. Zhao, M. Smith, N. Zhao, V. Bulović, M. Bawendi, and S. Gradečak, Inorganic–Organic Hybrid Solar Cell: Bridging Quantum Dots to Conjugated Polymer Nanowires, Nano Lett. (2011) 3998.

[87] J. Seo, M. J. Cho, D. Lee, A. N. Cartwright, and P. N. Prasad, Efficient Heterojunction Photovoltaic Cell Utilizing Nanocomposites of Lead Sulfide Nanocrystals and a Low-Bandgap Polymer, Adv. Mater. (2011) 3984.

[88] C. H. Chang, T. K. Huang, Y. T. Lin, Y. Y. Lin, C. W. Chen, T. H. Chu, and W. F. Su, Improved charge separation and transport efficiency in poly(3-hexylthiophene)-TiO_2 nanorod bulk heterojunction solar cells, J. Mater. Chem. 18 (2008) 2201.

[89] W. J. E. Beek, M. M. Wienk, and R. A. J. Janssen, Efficient hybrid solar cells from zinc oxide nanoparticles and a conjugated polymer, Adv. Mater. 16 (2004) 1009.

[90] J. Bouclé and J. Ackermann, Solid-state dye-sensitized and bulk heterojunction solar cells using TiO_2 and ZnO nanostructures: recent progress and new concepts at the borderline, Polym. Int. 61 (2012) 355.

[91] I. Park, Y. Lim, S. Noh, D. Lee, M. Meister, J. J. Amsden, F. Laquai, C. Lee, and D. Y. Yoon, Enhanced photovoltaic performance of ZnO nanoparticle/poly(phenylene vinylene) hybrid photovoltaic cells by semiconducting surfactant, Org. Electronics 12 (2011) 424.

[92] J. Weickert, R. B. Dunbar, H. C. Hesse, W. Wiedemann, and L. Schmidt-Mende, Nanostructured Organic and Hybrid Solar Cells, Adv. Mater. 23 (2011) 1810.

[93] F. Träger, ed., Handbook of Lasers and Optics, Springer, 2007.

[94] R. Menzel, Photonics, Springer, 2007.

[95] B. E. A. Saleh and M. C. Teich, Fundamentals of Photonics, John Wiley & Sons, 2007.

[96] R. Paschotta, Encyclopedia of Laser Physics and Technology, http://www.rp-photonics.com/encyclopedia.html

[97] D. Meschede, Optik, Licht und Laser, Vieweg+Teubner, 2008.

[98] J. Cabanillas-Gonzalez, G. Grancini, and G. Lanzani, Pump-Probe Spectroscopy in Organic Semiconductors: Monitoring Fundamental Processes of Relevance in Optoelectronics, Adv. Mater. 23 (2011) 5468.

[99] U. B. Cappel, S. M. Feldt, J. Schöneboom, A. Hagfeldt, and G. Boschloo, The Influence of Local Electric Fields on Photoinduced Absorption in Dye-Sensitized Solar Cells, J. Am. Chem. Soc. 132 (2010) 9096.

[100] S. Ardo, Y. Sun, A. Staniszewski, F. N. Castellano, and G. J. Meyer, Stark Effects after Excited-State Interfacial Electron Transfer at Sensitized TiO_2 Nanocrystallites, J. Am. Chem. Soc. 132 (2010) 6696.

[101] Provided by D. Andrienko and B. Baumeier, Polymer Theory Group, MPI for Polymer Research, (2012)

[102] S. Ito, P. Chen, P. Comte, M. K. Nazeeruddin, P. Liska, P. Pechy, and M. Grätzel, Fabrication of screen-printing pastes from TiO_2 powders for dye-sensitised solar cells, Prog. Photovoltaics 15 (2007) 603.

[103] NREL, http://rredc.nrel.gov/solar/spectra/am1.5/ (July 2012).

[104] R. Mauer, Charge generation, transport and recombination in organic solar cells, Universität Mainz, Zentralbibliothek / MAG [Signatur: 4º BE 7471], 2012

[105] M. Westerling, C. Vijila, R. Osterbacka, and H. Stubb, Optical studies of excited-state relaxation in poly(9,9-dihexylfluorene-co-benzothiadiazole), Phys. Rev. B 67 (2003) 6.

[106] G. Dellepiane, C. Cuniberti, D. Comoretto, G. F. Musso, G. Figari, A. Piaggi, and A. Borghesi, Long-Lived Photoexcited States in Symmetrical Polydicarbazolyldiacetylene, Phys. Rev. B 48 (1993) 7850.

[107] S. Voigt, U. Zhokhavets, M. Al-Ibrahim, H. Hoppe, O. Ambacher, and G. Gobsch, Dynamical optical investigation of polymer/fullerene composite solar cells, Phys. Status Solidi B 245 (2008) 714.

[108] Provided by R. Sens, BASF, 2012.

[109] S. Fantacci, F. De Angelis, M. K. Nazeeruddin, and M. Grätzel, Electronic and Optical Properties of the Spiro-MeOTAD Hole Conductor in Its Neutral and Oxidized Forms: A DFT/TDDFT Investigation, J. Phys. Chem. C 115 (2011) 23126.

[110] W. M. Haynes, ed., CRC Handbook of Chemistry and Physics Internet Version, 2012.

[111] A. Petrozza, F. Laquai, I. A. Howard, J.-S. Kim, and R. H. Friend, Dielectric switching of the nature of excited singlet state in a donor-acceptor-type polyfluorene copolymer, Phys. Rev. B 81 (2010) 205421.

[112] L. Dworak, V. V. Matylitsky, and J. Wachtveitl, Ultrafast Photoinduced Processes in Alizarin-Sensitized Metal Oxide Mesoporous Films, ChemPhysChem 10 (2009) 384.

[113] M. Ziolek, B. Cohen, X. Yang, L. Sun, M. Paulose, O. K. Varghese, C. A. Grimes, and A. Douhal, Femtosecond to millisecond studies of electron transfer processes in a donor-(π-spacer)-acceptor series of organic dyes for solar cells interacting with titania nanoparticles and ordered nanotube array films, Phys. Chem. Chem. Phys. 14 (2012) 2816.

[114] K. Vinodgopal, X. Hua, R. L. Dahlgren, A. G. Lappin, L. K. Patterson, and P. V. Kamat, Photochemistry of Ru(bpy)2(dcbpy)$^{2+}$ on Al_2O_3 and TiO_2 Surfaces. An Insight into the Mechanism of Photosensitization, J. Phys. Chem. 99 (1995) 10883.

[115] E. Palomares, J. N. Clifford, S. A. Haque, T. Lutz, and J. R. Durrant, Control of Charge Recombination Dynamics in Dye Sensitized Solar Cells by the Use of Conformally Deposited Metal Oxide Blocking Layers, J. Am. Chem. Soc. 125 (2002) 475.

[116] M. Gautier, J. P. Duraud, L. P. Van, and M. J. Guittet, Modifications of Alpha-Al_2O_3(0001) Surfaces Induced by Thermal Treatments or Ion-Bombardment, Surf. Sci. 250 (1991) 71.

[117] T. Kurita, K. Uchida, and A. Oshiyama, Atomic and electronic structures of α-Al_2O_3 surfaces, Phys. Rev. B 82 (2010) 155319.

[118] J. B. Asbury, R. J. Ellingson, H. N. Ghosh, S. Ferrere, A. J. Nozik, and T. Q. Lian, Femtosecond IR study of excited-state relaxation and electron-injection dynamics of $Ru(dcbpy)_2(NCS)_2$ in solution and on nanocrystalline TiO_2 and Al_2O_3 thin films, J. Phys. Chem. B 103 (1999) 3110.

[119] A. Abrusci, R. S. S. Kumar, M. Al-Hashimi, M. Heeney, A. Petrozza, and H. J. Snaith, Influence of Ion Induced Local Coulomb Field and Polarity on Charge Generation and Efficiency in Poly(3-Hexylthiophene)-Based Solid-State Dye-Sensitized Solar Cells, Adv. Funct. Mater. 21 (2011) 2571.

[120] Personal Correspondence with BASF, 2012.

[121] R. Katoh, M. Kasuya, S. Kodate, A. Furube, N. Fuke, and N. Koide, Effects of 4-tert-Butylpyridine and Li Ions on Photoinduced Electron Injection Efficiency in Black-Dye-Sensitized Nanocrystalline TiO_2 Films, J. Phys. Chem. C 113 (2009) 20738.

[122] S. Yu, S. Ahmadi, C. H. Sun, P. Palmgren, F. Hennies, M. Zuleta, and M. Gothelid, 4-tert-Butyl Pyridine Bond Site and Band Bending on TiO_2(110), J. Phys. Chem. C 114 (2010) 2315.

[123] Provided by H. Wonneberger, BASF, 2012.

[124] G. Boschloo and A. Hagfeldt, Photoinduced absorption spectroscopy as a tool in the study of dye-sensitized solar cells, Inorg. Chim. Acta 361 (2008) 729.

[125] U. B. Cappel, S. Plogmaker, E. M. J. Johansson, A. Hagfeldt, G. Boschloo, and H. Rensmo, Energy alignment and surface dipoles of rylene dyes adsorbed to TiO_2 nanoparticles, Phys. Chem. Chem. Phys. 13 (2011) 14767.

[126] P. Chen, J. H. Yum, F. D. Angelis, E. Mosconi, S. Fantacci, S.-J. Moon, R. H. Baker, J. Ko, M. K. Nazeeruddin, and M. Grätzel, High Open-Circuit Voltage Solid-State Dye-Sensitized Solar Cells with Organic Dye, Nano Lett. 9 (2009) 2487.

[127] S. Rühle, M. Greenshtein, S. G. Chen, A. Merson, H. Pizem, C. S. Sukenik, D. Cahen, and A. Zaban, Molecular Adjustment of the Electronic Properties of Nanoporous Electrodes in Dye-Sensitized Solar Cells, J. Phys. Chem. B 109 (2005) 18907.

[128] J. Krüger, U. Bach, and M. Grätzel, Modification of TiO_2 heterojunctions with benzoic acid derivatives in hybrid molecular solid-state devices, Adv. Mater. 12 (2000) 447.

[129] H. Imahori, S. Kang, H. Hayashi, M. Haruta, H. Kurata, S. Isoda, S. E. Canton, Y. Infahsaeng, A. Kathiravan, T. r. Pascher, P. Chábera, A. P. Yartsev, and V. Sundström, Photoinduced Charge Carrier Dynamics of Zn−Porphyrin−TiO_2 Electrodes: The Key Role of Charge Recombination for Solar Cell Performance, J. Phys. Chem. A 115 (2010) 3679.

[130] J. Nelson, S. A. Haque, D. R. Klug, and J. R. Durrant, Trap-limited recombination in dye-sensitized nanocrystalline metal oxide electrodes, Phys. Rev. B 63 (2001) 205321.

[131] S. Handa, H. Wietasch, M. Thelakkat, J. R. Durrant, and S. A. Haque, Reducing charge recombination losses in solid state dye sensitized solar cells: the use of donor-acceptor sensitizer dyes, Chem. Commun. (2007) 1725.

[132] U. Diebold, The surface science of titanium dioxide, Surf. Sci. Rep. 48 (2003) 53.

[133] K. Westermark, A. Henningsson, H. Rensmo, S. Sodergren, H. Siegbahn, and A. Hagfeldt, Determination of the electronic density of states at a nanostructured TiO_2/Ru-dye/electrolyte interface by means of photoelectron spectroscopy, Chem. Phys. 285 (2002) 157.

[134] D. Ino, K. Watanabe, N. Takagi, and Y. Matsumoto, Electron transfer dynamics from organic adsorbate to a semiconductor surface: Zinc phthalocyanine on TiO_2(110), J. Phys. Chem. B 109 (2005) 18018.

[135] R. Ulbricht, E. Hendry, J. Shan, T. F. Heinz, and M. Bonn, Carrier dynamics in semiconductors studied with time-resolved terahertz spectroscopy, Rev. Mod. Phys. 83 (2011) 543.

[136] J. J. H. Pijpers, R. Ulbricht, S. Derossi, J. N. H. Reek, and M. Bonn, Picosecond Electron Injection Dynamics in Dye-Sensitized Oxides in the Presence of Electrolyte, J. Phys. Chem. C 115 (2011) 2578.

[137] P. Tiwana, P. Parkinson, M. B. Johnston, H. J. Snaith, and L. M. Herz, Ultrafast Terahertz Conductivity Dynamics in Mesoporous TiO_2: Influence of Dye Sensitization and Surface Treatment in Solid-State Dye-Sensitized Solar Cells, J. Phys. Chem. C 114 (2010) 1365.

[138] P. Tiwana, P. Docampo, M. B. Johnston, H. J. Snaith, and L. M. Herz, Electron Mobility and Injection Dynamics in Mesoporous ZnO, SnO_2, and TiO_2 Films Used in Dye-Sensitized Solar Cells, ACS Nano 5 (2011) 5158.

[139] S. Ito, P. Liska, P. Comte, R. Charvet, P. Pechy, U. Bach, L. Schmidt-Mende, S. M. Zakeeruddin, A. Kay, M. K. Nazeeruddin, and M. Grätzel, Control of dark current in photoelectrochemical (TiO_2/I^--I^{3-}) and dye-sensitized solar cells, Chem. Commun. (2005) 4351.

[140] L. J. G. W. van Wilderen, C. N. Lincoln, and J. J. van Thor, Modelling Multi-Pulse Population Dynamics from Ultrafast Spectroscopy, PLoS One 6 (2011) e17373.

[141] J. Jaumot, R. Gargallo, A. de Juan, and R. Tauler, A graphical user-friendly interface for MCR-ALS: a new tool for multivariate curve resolution in MATLAB, Chemom. Intell. Lab. Syst. 76 (2005) 101.

[142] N. Mouton, M. Sliwa, G. Buntinx, and C. Ruckebusch, Deconvolution of femtosecond time-resolved spectroscopy data in multivariate curve resolution. Application to the characterization of ultrafast photo-induced intramolecular proton transfer, J. Chemom. 24 (2010) 424.

List of Acronyms

2PPE	Two Photon Photoemission Spectroscopy
add	Additive, see ID662
Ag	Silver
Al	Aluminium
Al_2O_3	Aluminium Oxide, Sapphire, Alumina
AM1.5G	Air Mass 1.5 Global Solar Spectrum Norm
AOM	Acousto-optical Modulator
BASF	The Chemical Company
BBO	Barium Borate
BHJ	Bulk Heterojunction
CB	Conduction Band
CCD	Charge-coupled Device Camera Sensor
CdTe	Cadmium Telluride
CIGS	$CuIn_xGa_{(1-x)}(S,Se)_2$ solar cell technology
CO_2	Carbon Dioxide
CT	Charge Transfer
D	Debye (Dipole moment strength, $1\ D \approx 3.336 \cdot 10^{-30}$ Cm)
D/A	Donor/Acceptor
D1	Dye PMI-1
D2	Dye NMI
DCM	Dichloromethane
D-π-A	Donor-π-Bridge-Acceptor
DSC	Dye-sensitized Solar Cell

ε	Dielectric Constant of a Medium
EQE	External Quantum Efficiency
ET	Electron Transfer
eV	Electronvolt (Energy, $1\ eV \approx 1.602 \cdot 10^{-19}$ J)
FF	Fill Factor
FTO	Fluorinated Tin Oxide (a TCO)
η	Power conversion efficiency or exciton splitting efficiency
GSB	Ground State Bleach
HOMO	Highest Occupied Molecular Orbital
IC	Internal Conversion
ID662	Acronym for BASF Additive
IPCE	Incident Photon to Current Efficiency (same as EQE)
IQE	Internal Quantum Efficiency
IR	Infrared (referring to the wavelength range >1800 nm)
ISC	Intersystem Crossing
ITO	Indium Tin Oxide (a TCO)
J_{SC}	Short Circuit Current Density
J-V	Current-Voltage Characteristics
KLM	Kerr-lens Modelocking
LCAO	Linear Combination of Atomic Orbitals
LED	Light Emitting Diode
Li-TFSI	Lithium bis(trifluoromethanesulphonyl)imide salt
LUMO	Lowest Unoccupied Molecular Orbital
M	Concentration: molar (mol/L)
MDMO-PPV	poly[2-methoxy-5-(3′,7′-dimethyloctyloxyl)-1,4-phenylene vinylene], Donor Polymer

MeO	Methoxy Side Group
MPP	Maximum Power Point
NIR	Near-Infrared (referring to the wavelength range ~800-1800 nm)
NLM	Non-linear Medium
NMI	Naphthalene Monoimide based dye
OD	Optical Density
OPA	Optical Parametric Amplifier
opt	optical
OPV	Organic Photovoltaics
P3HT	Poly(3-hexylthiophene)
PA	Photoinduced Absorption
PCBM	[6,6] Phenyl C61 Butyric Acid Methyl Ester
PEDOT:PSS	Poly(3,4-ethylenedioxythiophene) poly(styrenesulfonate)
PIA	Quasi-steady-state Photoinduced Absorption Spectroscopy
PL	Photoluminescence
PLQE	Photoluminescence Quantum Efficiency
PMI	Perylene Monoimide based dye
Pt	Platinum
PV	Photovoltaics
rpm	Rounds per Minute
Ru	Ruthenium
SE	Stimulated Emission
SnO_2	Tin Oxide
spiro	see spiro-MeOTAD
spiro-MeOTAD	(2,2′7,7′-tetrakis-(N,N-di-p-methoxyphenyl-amine)-9,9′-spirobifluorene, Hole Transporter

ssDSC	Solid-state Dye-sensitized Solar Cell
TA	Transient Absorption Spectroscopy
tBP	4-tert-butylpyridine
TCO	Transparent Conductive Oxide
TDDFT	Time-dependent Density Functional Theory
TiO_2	Titanium Dioxide, Titania
UV	Ultraviolet (referring to the wavelength range ~200-400 nm)
UV-VIS	Ultraviolet to Visible wavelength range (~200-800 nm) or steady-state Absorption Spectroscopy
V_{OC}	Open Circuit Voltage
VIS	Visible (referring to the wavelength range ~400-800 nm)
VIS-IR	Visible to Infrared (referring to the wavelength range 400- >1800 nm)
YAG	Yttrium Aluminium Garnet
YVO_4	Yttrium Orthovanadate
Z907	Acronym for a Ru based dye: cis-Bis(isothiocyanato)(2,2’-bipyridyl-4,4’-dicarboxylato)(4,4’-di-nonyl-2’-bipyridyl) ruthenium(II)
ZnO	Zinc Oxide

List of Scientific Contributions

Publications in Peer-Reviewed Journals

- **I.A. Howard, R. Mauer, M. Meister, F. Laquai,** "Effect of Morphology on Ultrafast Free Carrier Generation in Polythiophene:Fullerene Organic Solar Cells", *J. Am. Chem. Soc.* **2010**, , 132, (42), 14866-14876
- **I. Park, Y. Lim, S. Noh, D. Lee, M. Meister, J.J. Amsden, F. Laquai, C. Lee, D.Y. Yoon**, "Enhanced photovoltaic performance of ZnO nanoparticle/poly(phenylene vinylene) hybrid photovoltaic cells by semiconducting surfactant", *Org. Electronics* **2011**, 12, (3), 424-428
- **F. Etzold, I.A. Howard, R. Mauer, M. Meister, T.-D. Kim, K.-S. Lee, N.S. Baek, F. Laquai**, "Ultrafast Exciton Dissociation Followed by Nongeminate Charge Recombination in PCDTBT:PCBM Photovoltaic Blends", *J. Am. Chem. Soc.* **2011**, 133, (24), 9469-9479
- **P. Lellig, M.A. Niedermeier, M. Rawolle, M. Meister, F. Laquai, P. Müller-Buschbaum, J.S. Gutmann**, "Comparative study of conventional and hybrid blocking layers for solid-state dye-sensitized solar cells", *Phys. Chem. Chem. Phys.* **2012,** 14, (5), 1607-1613
- **F. Etzold, I. A. Howard, N. Forler, D. M. Cho, M. Meister, H. Mangold, J. Shu, M. R. Hansen, K. Müllen and F. Laquai,** "The Effect of Solvent Additives on Morphology and Excited-State Dynamics in PCPDTBT:PCBM Photovoltaic Blends", J. Am. Chem. Soc. **2012**, 134, (25), 10569-10583
- **M. Meister, J. J. Amsden, I. A. Howard, I. Park, C. Lee, D. Y. Yoon and F. Laquai,** "Parallel Pool Analysis of Transient Spectroscopy Reveals Origins of and Perspectives for ZnO Hybrid Solar Cell Performance Enhancement Using Semiconducting Surfactants", J. Phys. Chem. Lett. 2012, 3, (18), 2665-2670
- **M. Meister, B. Baumeier, N. Pschirer, R. Sens, I. Bruder, F. Laquai, D. Andrienko, I. A. Howard**, "Observing Charge Dynamics in Surface Reactions by Time-Resolved Stark Effects", *submitted to J. Am. Chem. Soc.*
- **M. Meister, B. Baumeier, N. Pschirer, R. Sens, I. Bruder, D. Andrienko, I. A. Howard, F. Laquai,** "Two Channels for Charge Generation in Perylene Monoimide Solid-state Dye-Sensitized Solar Cells", *submitted to Energy & Environmental Science*
- **P. Lellig, M. Meister, J. W. Ochsmann, M. A. Niedermeier, M. Rawolle, F. Laquai, P. Müller-Buschbaum, J. S. Gutmann**, "Application of a Hybrid Blocking Layer in Solid-state Dye-sensitized Solar Cells", *in preparation*

Conference Contributions

- **M. Meister,** B. Baumeier, I. A. Howard, D. Andrienko, N. Pschirer, R. Sens, I. Bruder, F. Laquai, “Optimizing Charge Generation in Solid-State Dye-Sensitized Solar Cells: the Role of Interfacial Ions and Reductive Quenching”; MRS Fall Meeting, Boston, USA, 25th - 30th November 2012
- **M. Meister**, Y. Kim, I. A. Howard, H. Wonneberger, C. Li, K. Müllen, F. Laquai, “Charge Generation and Recombination in Perylene Solid-state Dye-sensitized Solar Cells”; DPG Spring Meeting, Berlin, 25th - 30th March 2012
- **M. Meister**, B. Nölscher, I. A. Howard, H. Wonneberger, C. Li, K. Müllen, F. Laquai, “Charge Generation and Recombination in Perylene-imide Solid-state Dye-Sensitized Solar Cells”; Pacific Polymer Conference, Jeju, Korea, 13th - 17th November 2011
- **M. Meister**, B. Nölscher, I. A. Howard, H. Wonneberger, C. Li, K. Müllen, F. Laquai, “Charge Generation and Recombination in Perylene Imide Dye-sensitized Solar Cells”; Interdisciplinary Workshop on Fundamental Function of Organic Solar Cells, Munich, 19th July 2011
- **M. Meister**, B. Nölscher, I. A. Howard, H. Wonneberger, C. Li, K. Müllen, F. Laquai, “Charge Generation and Recombination in Perylene Imide Dye-sensitized Solar Cells”; 10th IRTG Conference on Organic Optoelectronics Meeting, Mainz, 5th – 7th July 2011
- **M. Meister**, B. Nölscher, I. A. Howard, H. Wonneberger, C. Li, K. Müllen, F. Laquai, “Charge Generation and Recombination in Perylene Dye-sensitized Solar Cells”; DPG Spring Meeting, Dresden, 13th - 18th March 2011
- **M. Meister**, H. Wonneberger, C. Li, K. Müllen, F. Laquai, “Charge Generation and Recombination in Perylene Dye-sensitized Solar Cells”; Korea-Germany IRTG Workshop, Seoul, Korea, 16th – 24th January 2011
- **M. Meister**, H. Wonneberger, C. Li, K. Müllen, F. Laquai, “Perylene Monoimides as Efficient Sensitizers for Dye-sensitized Solar Cells”; Pacifichem 2010, Honolulu, USA, 15th – 20th December 2010
- **M. Meister**, H. Wonneberger, C. Li, K. Müllen, F. Laquai, “Perylene Monoimides as Efficient Sensitizers for Dye-sensitized Solar Cells: A Photophysical Study”; IRTG Summer Meeting 2010, Mainz, 21th – 24th June 2010
- **M. Meister**, H. Wonneberger, C. Li, K. Müllen, F. Laquai, “Charge Generation and Recombination in Perylene Dye-sensitized Solar Cells”; DPG Spring Meeting, Regensburg, 21th - 26th March 2010
- **M. Meister**, F. Laquai, “Studying Excited States in Dye-sensitized Solar Cells with Photoinduced Absorption Spectroscopy (PIA)”; IRTG International Workshop on Self-organized Materials for Optoelectronics, Mainz, 24th – 25th August 2009

Supplementary Information (added after print)

A revised version of the manuscript in Chapter 4.1 is published in Advanced Energy Materials:

Meister, M., Howard, I. A., Baumeier, B., Wonneberger, H., Pschirer, N., Sens, R., Bruder, I., Li, C., Müllen, K., Andrienko, D. and Laquai, F., Two Channels of Charge Generation in Perylene Monoimide Solid-State Dye-Sensitized Solar Cells. Adv. Energy Mater., 2013, DOI: 10.1002/aenm.201300640

A revised version of the manuscript in Chapter 4.4 is published in The Journal of Physical Chemistry C:

Meister, M., Baumeier, B., Pschirer, N., Sens, R., Bruder, I., Laquai, F., Andrienko, D., and Howard, I. A., Observing Charge Dynamics in Surface Reactions by Time-Resolved Stark Effects, J. Phys. Chem. C, 2013, 117 (18), pp 9171–9177, DOI: 10.1021/jp403268c